SPECTRAL ANALYSIS AND QUANTITATION IN MALDI-MS IMAGING

A THESIS SUBMITTED TO THE UNIVERSITY OF MANCHESTER
FOR THE DEGREE OF DOCTOR OF PHILOSOPHY
IN THE FACULTY OF BIOLOGY, MEDICINE AND HEALTH

2019

SOMRUDEE DEEPAISARN

SCHOOL OF HEALTH SCIENCES

DIVISION OF INFORMATICS, IMAGING AND DATA SCIENCES

‘Blank page’

Contents

Word count: 63,901

List of Tables

List of Figures

List of Abbreviations

ACN	Acetonitrile
AD	Alzheimer's disease
ADC	Apparent diffusion coefficient
ANOVA	Analysis of variance
CFR	Curved field reflectron
CHCA	α-cyano-4-hydroxycinnamic acid
CI	Chemical ionisation
CID	Collision induced dissociation
CLASS	Comprehensive lipidomics analysis by separation simplification
CNS	Central nervous system
CSF	Cerebrospinal fluid
DC	Direct current
DESI	Desorption electrospray ionisation
DHA	Docosahexaenoic acid
DHB	Dihydroxybenzoic acid
DI	Desorption ionisation
EI	Electron ionisation
EM	Expectation maximisation
ESI	Electrospray ionisation
FA	Factor analysis
FAB	Fast atom bombardment
FOV	Field of view
FT-ICR	Fourier transform ion cyclotron resonance
FWHM	Full-width half maximum
HPLC	High performance liquid chromatography
ICA	Independent component analysis
iCAT	Isotope-coded affinity tags
iid	Independent, identically distributed

IR	Infrared
ITO	Indium tin oxide
iTRAQ	Isobaric tag for relative and absolute quantification
LAESI	Laser ablation electrospray ionisation
LD	Laser desorption
LP-ICA	Linear Poisson independent component analysis
LPM	Linear Poisson modelling
LSIMS	Liquid secondary ion mass spectrometry
m/z	Mass-to-charge ratio
MALDI	Matrix-assisted laser desorption/ionisation
MAX SEP	Maximisation separation
MCP	Microchannel plate
MRI	Magnetic resonance imaging
MS	Mass spectrometry
MS/MS or MS^n	Tandem mass spectrometry
MSI	Mass spectrometry imaging
NMR	Nuclear magnetic resonance spectroscopy
NNMF	Non-negative matrix factorisation
PC	Phosphatidylcholine
PCA	Principal component analysis
PCoA	Principal coordinate analysis
PD	Plasma desorption
PE	Phosphatidylethanolamine
PET	Positron emission tomography
PG	Phosphatidylglycerol
pLSA	Probabilistic latent semantic analysis
PMF	Probability mass function
PNA	Paranitroaniline
PNS	Peripheral nervous system
PSD	Post-source decay
REIMS	Rapid evaporative ionisation mass spectrometry

RF	Radiofrequency
RGB	Red-green-blue
RMS	Root mean square
S/N	Signal-to-noise ratio
SA	Sinapinic acid
SALDI	Surface-assisted laser desorption/ionisation
SILAC	Stable isotope labelling of amino acids in cell culture
SIMS	Secondary ion mass spectrometry
SM	Sphingomyelin
SRM	Selected reaction monitoring
SSIMS	Static secondary ion mass spectrometry
SVM	Support vector machine
t-SNE	t-distributed stochastic neighbour embedding
TAG	Triacylglycerol
TFA	Trifluoroacetic acid
TIC	Total ion count
TLC	Thin layer chromatography
TOF	Time-of-flight
UV	Ultraviolet
YAG	Yttrium aluminium garnet
YLF	Yttrium lithium fluoride

Abstract

Name of University: The University of Manchester
Name of Candidate: Somrudee Deepaisarn
Degree Title: Doctor of Philosophy
Thesis Title: Spectral Analysis and Quantitation in MALDI-MS Imaging
Date: 9th April 2019

Matrix-assisted laser desorption/ionisation (MALDI) mass spectrometry is an analytical technique used for identifying molecules on the basis of their mass-to-charge ratio, facilitating the analyses of intact large biomolecules through soft ionisation. The technique suits a wide range of biomedical applications, with potential for biomarker discovery. However, quantitative MALDI analysis is very difficult because of the complex variations introduced during sample preparation, the ionisation process and data acquisition. An analysis method was therefore developed based on linear Poisson independent component analysis (LP-ICA) that appropriately addresses signal and noise statistical modelling. It was validated on real MALDI mass spectra that have been pre-processed using in-house algorithms. LP-ICA works by extracting independent components within the mass spectral data set, describing underlying variations in the mass spectra.

In order to validate the LP-ICA approach, three data sets were acquired using different binary mixtures of complex biological lipid samples, chosen to mimic the complexity of different types of biological tissues that might be imaged by MALDI-MS. These include cow and goat's milk, lamb brain and liver, and lamb brain's white and grey matter, at varied relative concentrations to provide known "ground truth" data sets for the analysis. The resulting quantitative analysis achieved twice the accuracy of the conventional approach using a single mass-to-charge peak associated with a particular biological sample composition. Moreover, it made use of information from the entire mass spectrum, without bias.

The application of LP-ICA analysis was then extended to MALDI-MS imaging data, where mass spectra are acquired at an array of locations across a thin tissue section. Extraction of mass spectral components from a post-ischemic stroke rat brain tissue cross-section image was successful, where the component images can distinguish sub-types of brain tissue. The brain contains a number of different types of lipid-rich tissue phenotypes which can be differentiated by biomolecules found to be specific to distinct anatomical regions. LP-ICA is also shown to have potential for the automatic identification and characterisation of healthy and diseased tissue regions.

Declaration

No portion of the work referred to in the thesis has been submitted in support of an application for another degree or qualification of this or any other university or other institute of learning.

Copyright Statement

i. The author of this thesis (including any appendices and/or schedules to this thesis) owns certain copyright or related rights in it (the "Copyright") and s/he has given The University of Manchester certain rights to use such Copyright, including for administrative purposes.

ii. Copies of this thesis, either in full or in extracts and whether in hard or electronic copy, may be made **only** in accordance with the Copyright, Designs and Patents Act 1988 (as amended) and regulations issued under it or, where appropriate, in accordance with licensing agreements which the University has from time to time. This page must form part of any such copies made.

iii. The ownership of certain Copyright, patents, designs, trademarks and other intellectual property (the "Intellectual Property") and any reproductions of copyright works in the thesis, for example graphs and tables ("Reproductions"), which may be described in this thesis, may not be owned by the author and may be owned by third parties. Such Intellectual Property and Reproductions cannot and must not be made available for use without the prior written permission of the owner(s) of the relevant Intellectual Property and/or Reproductions.

iv. Further information on the conditions under which disclosure, publication and commercialisation of this thesis, the Copyright and any Intellectual Property and/or Reproductions described in it may take place is available in the University IP Policy (see http://documents.manchester.ac.uk/DocuInfo.aspx?DocID=24420), in any relevant Thesis restriction declarations deposited in the University Library, The University Library's regulations (see http://www.library.manchester.ac.uk/about/regulations/) and in The University's policy on Presentation of Theses.

Acknowledgement

I would like to extend my sincere appreciation to my supervisors, Dr Adam McMahon and Dr Neil Thacker, firstly for warmly welcoming me to the programme, PhD Medicine (Imaging), and most importantly, for always providing me with excellent supervision, academic support, professional/personal trainings, and kindness. A very special thank goes to Dr Paul Tar who developed the LP-ICA analysis tool used in this project, and who gave great contributions and advice on the project. The completion of this thesis would not have been possible without them.

My gratitude goes to Dr Fiona Henderson for training me to use the laboratory instrumentation, and for acquiring the rat brain MALDI-MS image data set that was analysed in Chapter 6. I feel thankful to Dr Herve Boutin who provided with the rat brain model and trained me to do the brain tissue dissection. I would also like to acknowledge Dr Ashley Seepujak, who took part in developing the mass spectral pre-processing tool and preparation of the lamb brain:liver mixtures. My heartfelt thanks are extended to my colleagues based at the Wolfson Molecular Imaging Centre (WMIC) and Stopford Building, University of Manchester, for their generosity and friendship, particularly Dr Jingduo Tian, who gave me occasional software support, and Dr Duncan Forster and Dr Roberto Paredes, who provided me with necessary equipment and related trainings.

Furthermore, I am indebted to Miss Amaia Carrascal Minino for always assisting me in the laboratory and giving fruitful advice on many aspects of my work, and Mr. Jaruphat Wongpanich for his useful discussions about some of the work contexts. I also appreciate best friendship from them, as well as from all my friends with whom I enjoyed spending time after work.

I would like to express my gratitude to the University of Manchester for educating me in the undergraduate and postgraduate levels; to all teachers who taught me in those years and in the past; the Royal Thai Government scholarship provided by the Development and Promotion of Science and Technology Talents Project (DPST) for the financial funding from secondary school until doctorate levels; Office of Educational Affairs, the Royal Thai Embassy, London, for taking good care of me throughout 9 years of my studies in the UK; Kratos (Shimadzu, Manchester) for granting me the opportunity to use the 7090 MALDI-TOF-MS instrument based at their company; and finally, TINA open source image analysis environment for the access to analysis tools which were essential to my work.

In addition, I have to thank all the examiners who assessed my work in the first year of the PhD programme and who assessed my final thesis in the viva voce, namely, Dr James Graham (first year), Professor Jamie Gilmour (first year and final thesis) and Professor Josephine Bunch (final thesis).

My deepest gratefulness goes to my beloved parents, Mr. Suroj Deepaisarn and Mrs. Somporn Deepaisarn, for their true love, care, endless support, and encouragement. I would also like to thank my family members for always being kind and supportive. Last but not least, I always remember my late grandfather, Mr. Kimsuang Sae-Bae, who inspired me to go study abroad.

Chapter 1

Introduction

1.1 Important Concepts

Mass spectrometry (MS) is an analytical tool for molecular characterisation by the measurement of the mass-to-charge ratio (m/z) of gas-phase ions. MS technologies have been actively developed throughout recent decades for higher performance, including, mass resolution, precision and sample throughput. A variety of ionisation methods coupled with appropriate mass analysers can be selected, to give optimal performance, matched to the analytical application.

Matrix-assisted laser desorption/ionisation (MALDI) is a soft ionisation mass spectrometry technique, invented by Karas and Hillenkamp (1988). Koichi Tanaka and co-workers (1988) made key developments leading to intact ionisation of the large proteins with masses above 30 kDa. Tanaka was later awarded a share in the Nobel Prize in Chemistry in 2002, sharing with John Bennett Fenn who developed electrospray ionisation (ESI) and Kurt Wüthrich who used nuclear magnetic resonance spectroscopy for determining the three-dimensional structure of biological macromolecules in solution. MALDI has particular usage in analysing biomolecules, which are normally large and involatile. When a laser irradiates a sample surface, the energy is preferentially absorbed by a matrix compound which has been deposited and co-crystallised with the analytes in the sample. The matrix assists in ionisation of analytes with which they have been co-crystallised. The use of

a matrix prevents unwanted damage to large molecular structures, yielding intact ions of the analytes of interest. MALDI-TOF-MS is well-known for its ability to acquire spectra across a wide mass range, and is a powerful qualitative analytical tool. The technique is increasingly used in proteomics, lipidomics, metabolomics, and studies of other large organic/inorganic molecules such as polymers, with a wide range of applications, including medical, pharmaceutical, forensic, food and environmental sciences (Fuh *et al.*, 2017; Bonnel *et al.*, 2018; Li *et al.*, 2017; de Koster and Brul, 2016; Avanzi *et al.*, 2017). One of the strengths of MS is that it can determine the m/z ratio for multiple analytes in a sample within the same acquisition. Thus, MS data is very informative, containing many m/z peaks, which allows flexibility in targeting the molecules to be investigated.

Biomolecules can be large, complex, and challenging to characterise. The advantages of MALDI mass spectrometry outlined above, make the technique able to bridge the gaps and/or complement other well-established *in-vitro* analysis techniques. Immunohistochemistry, is a widely used imaging technique to detect an antigen-antibody binding site for protein within cells or tissues, providing microscopic views of biological samples. Note that more than one antibody is often required to target a particular protein as one might not be specific enough to that protein. Other standard analytic spectroscopy techniques such as nuclear magnetic resonance (NMR) or infrared (IR) spectroscopy, are widely used too. Relative to MS, NMR is considered a better method for structural identification, whereas IR, shows only the functional groups of molecules within the sample but IR is also capable of direct tissue imaging. However, NMR requires the analytes to be purified. Biomolecules are unlike synthetic polymers, which are composed of identical serially repeated units throughout their molecules. Instead, greater variation of monomers is observed within large biomolecules of typically >1000 Da (Jacobsen, 2016). This usually reduces the specificity of the NMR to determine molecules. For this reason, NMR typically only works well when analysing smaller peptides of a few repeated amino units. On the other hand, tandem MS or MS^n with n multiple MS stages, can provide structural information for an analyte based on its fragmentation. Furthermore, MALDI-MS together with other soft MS methods, e.g. desorption electrospray ionisation (DESI),

laser ablation electrospray ionisation (LAESI), secondary ion mass spectrometry (SIMS), are capable of molecular imaging on thin tissue slices.

MS in medicine and biology has grown rapidly since the developments of MALDI and ESI. Current research has major focuses in oncology and neurology (Liu *et al.*, 2018; Kaya *et al.*, 2017), uncovering the biology/pathology that can guide treatment directions for diseases. Given that MS techniques are sensitive to trace analytes within small volumes of sample, it has potential for biomarker discovery, toxicological studies, etc. Expanding the medical applications of MS from routine clinical laboratories, to use during surgical operations, is also becoming a promising possibility (Phelps *et al.*, 2018). This approach could provide rapid and accurate diagnoses, directing personalised medicine and influencing clinical decision making in real time. Medical imaging using MALDI-MS, can give local information of chemical compositions in tissue sections, and hence normal or abnormal regions can be recognised. Combining results of mass spectrometry imaging (MSI) with other medical imaging modalities, e.g. magnetic resonance imaging (MRI), positron emission tomography (PET) is possible, when available, to study the biology associated with stages of disease and understand the causes (Lohöfer *et al.*, 2018; Henderson *et al.*, 2018). The complexity of the technical procedures used requires experienced users to perform the experiments, and gain optimal outcomes – i.e. from appropriate parameter adjustment.

However, analysis of MALDI-MS results is complicated by a number of sources of variance produced before, during, and post-acquisition. These may come from complex MALDI ionisation processes, contaminants, chemical noise, suppression effects, and other uncontrollable parameters, such as a drift in the flight-time measurement of same ion species. Sample preparation techniques can also introduce significant variability. Typically, a time-of-flight (TOF) mass analyser is coupled to a MALDI ion source, providing reasonably good mass resolution, which varies across m/z values. For example the 7090 MALDI-TOF-MS (Shimadzu) can achieve a mass resolution of 10,000 (full-width half maximum) at m/z 1200 (Shimadzu, 2013). However, mass shift can be observed between acquisitions due to misalignment, which happens to be within around 1 Da for simple instruments. All these factors

contribute to variation in the resultant mass spectra, causing problems for data analysis, and especially quantification.

Scientific analyses can either be qualitative or quantitative. Qualitative analysis refers to descriptive interpretations of data via observation of a process, which is therefore considered subjective. On the other hand, quantitative analysis involves numerical measurements, allowing for further investigation such as in-depth statistical assessments and mathematical modelling. Quantitative or semi-quantitative measurements are essential to some experiments, where numerical values are required to confirm the basis of theory. In mass spectrometry experiments, the measurements usually involve determination of how much of a substance or material is present, in absolute or relative terms. Some indicators, generally a change in amount of specific analyte detected relative to some form of standards, would characterise and/or distinguish complex samples. Several approaches have been described for quantitative analysis of MALDI-MS, including computational multivariate analysis methods. However, the statistical properties of the data have not normally been considered, despite the fact that appropriate assumptions about the statistical properties of the data are necessary to form a mathematical solution that matches the data behaviour. Also, as measurements cannot be exact, an understanding of associated errors and uncertainties is particularly important, so that the closest estimation/approximation is obtained when the right assumptions are made. An analysis method should be testable by comparing predictions from a hypothesis against the measured values from experiments. This topic is still open to improvement.

The aim of this PhD project is therefore to develop a reliable method for quantifying the relative signal contributions of the underlying components found in complex biological mixtures measured by MALDI-MS, looking deeply into the nature of the acquired mass spectra and their sources of variation, aiming for a more accurate quantitative MS analysis. This can be related to the absolute concentration of the component through the use of an internal or external reference standard. The method should look for the source of mixture signal variability and extract components (based upon the correlated set of signals) which best describe the

relative proportions of molecules present in the sample. This is a model of the underlying material as a whole, not focusing only on an individual m/z peak. A mass spectrum is normally recorded in the format of histogram, showing the frequency of ion counts as a function of m/z. In the case of mass spectra produced on a MALDI-MS instrument, they are confirmed to have a Poisson error distribution (Deepaisarn *et al.*, 2018), in contrast, many data analysis algorithms assume Gaussian errors for convenience. Due to the complex characteristics of MALDI-MS, as described above, with expected contamination and instability of signal detection, spectral pre-processing is clearly needed prior to performing further analysis. In-house pre-processing algorithms employed include resolution reduction, alignment, baseline correction (background subtraction) and peak detection. The mass spectral data set is not only huge and complex, but it is also high in dimensionality – i.e. each mass peak represents the presence of one or a few molecules and thousands of molecules may be present in a tissue sample. Spatial variations in signal intensity are also taken into account in MS imaging. However, a commonly used approach to quantitative analysis using MS data is based on a change in a single peak through multiple samples of interest. Other approaches including principal component analysis (PCA) and conventional independent component analysis (ICA) are very often used with the assumption of Gaussian noise statistics of signal variability (errors of the measurements) for the ease of calculation (Gut *et al.*, 2015). If a robust error model is to be established, this Gaussian assumption is found statistically inappropriate for analysing MALDI-MS data which are expected to have a Poisson behaviour due to their sampling process. Therefore, an in-house computational modelling method called linear Poisson independent component analysis (LP-ICA) was applied to extract the most information contained in the MS data set quantitatively, dealing appropriately with the spectral signal and noise statistics. Available modelling options are discussed in terms of assumptions on data properties as summarised in Table 3.2 – see Section 3.4.3 of Chapter 3, showing the suitability of the LP-ICA assumptions to mass spectral data. LP-ICA was initially developed for quantitative analysis of planetary images, by Paul Tar (2013) (TINA vision). The method works for quantitative analysis of histogram data in general (Tar and Thacker, 2014). It has proven to be applicable to the analysis of the MRI parameter: apparent diffusion

coefficient (ADC) with applications in cancer imaging. The method was also applied to time-of-flight mass spectrometry data, produced by the RELAX system (Gilmour *et al.*, 1994), which generates relatively simple mass spectra with only few peak of xenon isotopes. This resulted in the quantitation accuracy being doubled in a contaminated peak (Tar *et al*., 2017). On this basis, it was anticipated that the LP-ICA method would be applicable for use with MALDI-TOF-MS data which has appropriate signal and noise statistical behaviour. By fitting the model to the data, the noise distribution shape was confirmed as matching the Poisson assumption via the Bland-Altman plot (Figure 5.6 – see Section 5.4.2 of Chapter 5).

1.2 Aims and Objectives

The aims of the research project are;

- To demonstrate that variability in the MALDI-MS data follows Poisson statistics,
- to develop and validate a quantitative approach for the analysis of MALDI-TOF-MS / MSI data, using LP-ICA algorithms as a standard platform to obtain numerical results and errors,
- and to demonstrate the use of this approach in biomedical applications.

These aims break down into the following objectives:

- Optimisation of the mass spectral signal-to-noise by improving preparation protocols for the selected samples, and finding optimal acquisition parameters for the MALDI-MS instrumentation used
- Testing the statistical characteristics of MALDI mass spectra to confirm agreement with the assumption on LP-ICA
- Creation of the LP-ICA routine to model underlying sub-components within MALDI mass spectra of biological mixtures (simulated concentrations of known biological materials were used to mimic the complexity in real biological systems)

- Application of the LP-ICA to MALDI mass spectra of a real-world sample: MS imaging data of biological tissues
- Prediction of quantities of underlying sub-spectra which can be linearly summed to have a biologically meaningful interpretation
- Measurement of errors associated with the model's quantity estimates, minimising the errors using an automatic approach, and evaluating the resultant model based on theoretical errors
- Identifying classes of underlying variables in biological samples as modelled by LP-ICA – i.e. the ability to classify extracted ICA components as belonging to some specific tissue types, and comparing these results with the literature

1.3 Thesis Overview

The relevant background provided for this thesis includes mass spectrometry instrumentation and applications (Chapter 2), and quantitative mass spectrometry (Chapter 3). The experimental work was divided into 3 main parts, set out in Chapter 4, 5 and 6. At the end, the overall summary of the work is discussed with suggestions for potential future work (Chapter 7).

Brief Experimental Description

Chapter 4**:** Sample preparation protocols and data acquisition parameters were assessed for the Kratos AXIMA MALDI-TOF-MS instrument in order that the signal-to-noise characterisation for mass spectra (for non-imaging, and some aspects related to imaging) of selected lipid mass range were optimised. The ability to quantify MALDI mass spectra was initially assessed. The general instrumental specification of the AXIMA was compared with the superior Kratos 7090 MALDI-TOF-MS used in acquiring the imaging data presented in Chapter 6.

***Chapter 5*:** Binary mixtures of biological samples that varied in proportion, including lipid extracts of cow and goat's milk, of lamb brain and liver, and of lamb brain's white and grey matter, were selected as examples of complex lipid mixtures for generation of mass spectral data sets. They are used as artificial samples of complex lipid mixtures that mimic real-world variations that might be expected within tissue samples but prepared with known relative quantities of underlying composition. The analysis is therefore performed on a set of known samples and hence the errors can be assessed accordingly. The in-house pre-processing steps were applied to the mass spectral data sets prior to the LP-ICA analysis. From these data sets, the LP-ICA method of modelling and quantifying variability within the mass spectra can be tested and validated. A model was fitted using an extended maximum likelihood estimation, based on an expectation maximisation algorithm. Weighted linear combinations of certain components provided the quantity estimates for underlying biological samples. The prediction accuracy using the model can be calculated and assessed with respect to the ground truth.

Out of the three data sets, white and grey matter samples were considered the most sophisticated choice of binary mixtures to test the capacity of the LP-ICA. Dissected white and grey matter of lamb's brain was expected to be more relevant to the goal of imaging a brain section, and was used as a final test for the LP-ICA to justify sub-spectral components of biologically similar samples.

***Chapter 6*:** The LP-ICA analysis was applied to mass spectrometry imaging of a brain tissue section taken from a rat model of ischemic stroke where mass spectra were acquired on a grid of locations across the brain tissue section. As the brain contains different types of lipid-rich tissue which can be differentiated by biomolecules specific to anatomical regions, a set of component images showing sub-types of brain tissue were extracted. If the identification and characterisation of various tissues in brain regions can be automated, the application is likely to move on toward identification of other tissue types.

Overview of the work done in this PhD thesis is summarised in the flow chart (Figure 1.1) below.

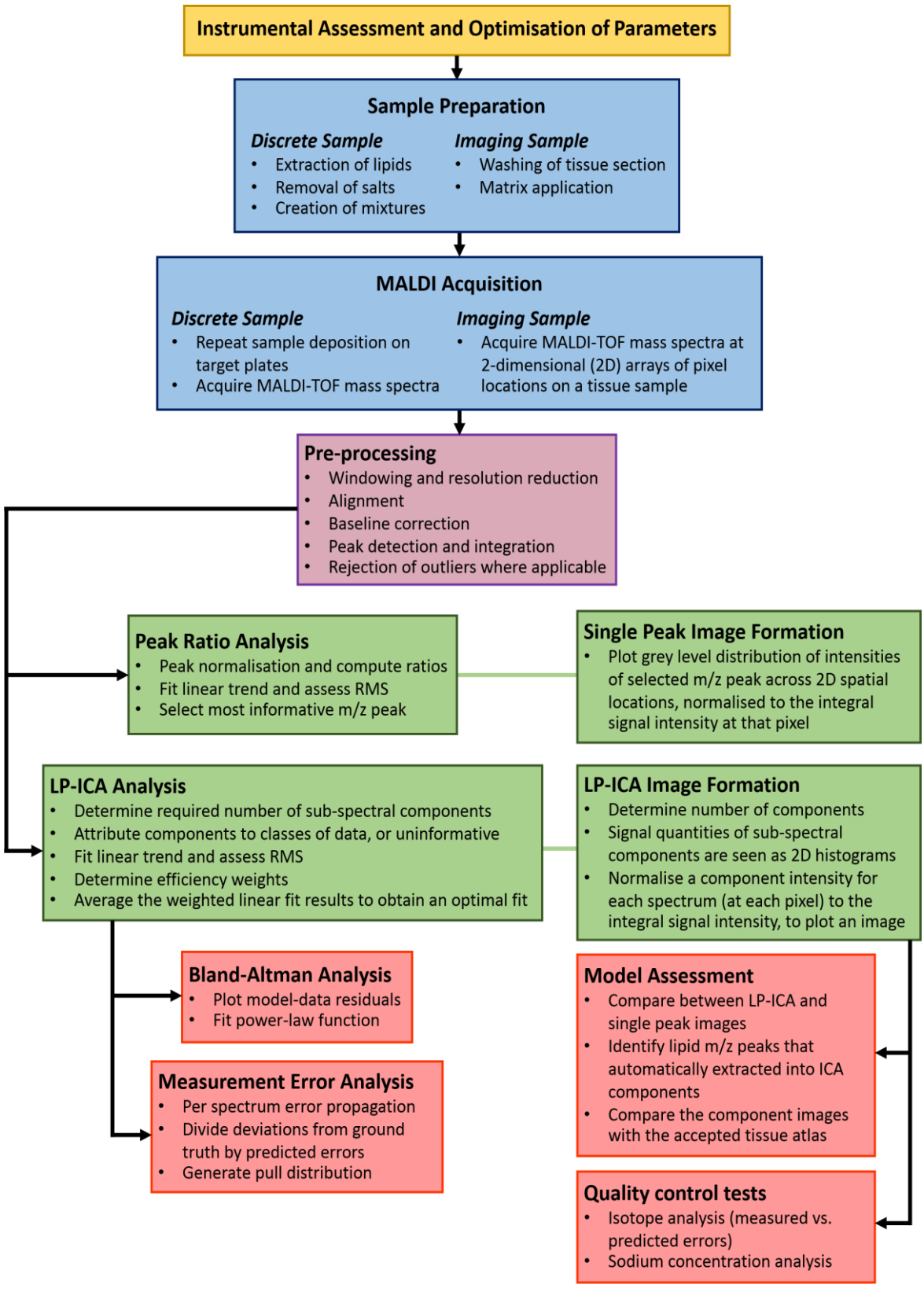

Figure 1.1 Work flow chart: Outline of the experiments

1.4 List of Outputs

The outputs from research reported in this thesis are listed here as journal publications and international conference posters. Other relevant document (internal reports, TINA memos: accessible via http://www.tina-vision.net/docs/memos.php), including my first and second year PhD continuation reports, are also listed. Note that some materials in this thesis, mainly in Chapter 5 and parts of Chapter 6, are mostly covered in the published work. The contributions to these are noted on the list of co-authors named below.

***Chapter 4*:**

- Deepaisarn, S., *'First year PhD continuation report: Spectral analysis and quantitation in MALDI-MS imaging'*; Internal report, TINA memos, 2015-016: University of Manchester – Nov 2015

***Chapter 5*:**

- Deepaisarn S., Paul D. Tar, Neil A. Thacker, Ashley Seepujak and Adam W. McMahon; *'Quantifying biological samples using linear Poisson independent component analysis for MALDI-TOF mass spectra'*; Bioinformatics journal, Oxford University Press – OCT 2017

- Deepaisarn S., Adam W. McMahon, Neil A. Thacker, Paul D. Tar and Ashley Seepujak; *'Towards quantitative analysis of MALDI mass spectral data using linear Poisson independent component analysis'*; 65th ASMS Conference on Mass Spectrometry and Allied Topics, American Society for Mass Spectrometry (ASMS), Indiana, USA – JUN 2017

- Deepaisarn S., Neil A. Thacker, Paul D. Tar, Ashley Seepujak and Adam W. McMahon; *'Quantitative MALDI mass spectrometry analysis of brain tissues using linear Poisson ICA modelling'*; 38th British Mass Spectrometry Society Annual Meeting, Manchester, UK – SEP 2017

- Deepaisarn S., Neil A. Thacker, Paul D. Tar, Ashley Seepujak, Adam W. McMahon; *'Quantitative MALDI mass spectrometry of biological mixtures using linear Poisson independent component analysis'*; 7th Asia-Oceania Mass Spectrometry Conference, Singapore – DEC 2017

- Deepaisarn, S., *'Second year PhD continuation report: Spectral analysis and quantitation in MALDI-MS imaging'*; Internal report, TINA memos, 2016-017: University of Manchester – DEC 2016

***Chapter 6*:**

- Paul D. Tar, Neil A. Thacker, Deepaisarn S. and Adam W. McMahon; *'A reformulation of pLSA for mass spectra imaging, uncertainty estimation and hypothesis testing'*; Submitted to Bioinformatics journal, Oxford University Press

- Thacker, N. A., Deepaisarn, S. and McMahon, A.W. 2016; *'Estimating noise models for arbitrary images'*, Internal report, TINA memos, 2016-009: University of Manchester – APR 2016

Chapter 2

Background I:

Mass Spectrometry

Instrumentation and Applications

Generally, mass spectrometers comprise 4 main parts: an ion generator, an ion accelerator, a mass analyser, and a detector. There are many combinations and varieties of these components suitable for specific analyses. In Section 2.1, a broad but brief overview of mass spectrometry is provided, including the types of ionisation techniques and mass analysers. MALDI-MS, which is frequently combined with a TOF mass analyser, will be discussed thoroughly in Section 2.2 because of its specific relevance to this work. A basic introduction to lipidomics and the application of MALDI-MS in lipidomics are reviewed in Section 2.3. Finally, the application of MS imaging to lipid analysis, which is the focus of the experimental work in Chapter 6 of this thesis, is introduced in Section 2.4.

2.1 Fundamentals of Mass Spectrometry

Mass spectrometry is an instrumental/analytical method for identifying and quantifying a range of types of analyte. Mass spectrometry (MS), involves the separation of charged molecules, in the gas phase, on the basis of their mass-to-charge ratios. These data are presented as a mass spectrum; a plot of ion signal intensity against mass-to-charge ratio.

The principles of mass spectrometry have developed from the work of Eugen Goldstein (1886), a German Physicist in late 19^{th} century who observed (positively charged) "anode rays" in a gas discharge tube made from glass containing low-pressured gas. The rays were accelerated along the direction of the applied electric field. Wien (1897) investigated the deflection of anode rays when projected through either electric or magnetic fields. He found that the degree of bending varied when different types of gas were present. One of Wien's experiments using parallel electric and magnetic fields in a discharge tube had led towards the first mass spectrometer constructed by J.J. Thomson (1907) and improved by Aston, which could record mass-to-charge information in a mass photograph. J.J. Thomson reduced the pressure in an observation tube so that it reduced scattering of the beam of charged particle before reaching the detecting wall. Also, he improved sensitivity by using a Zn_2SiO_4 (Willemite) detector that could emit relatively intense visible radiation onto a photograph compared to normal glass fluorescence (Münzenberg, 2013). This set-up produced the mass spectrograph with the expected parabolic paths for a beam of ionised hydrogen atoms (H^+) and ionised hydrogen gas molecules (H_2^+) that were deflected in electromagnetic fields, according to their mass-to-charge ratios (Münzenberg, 2013). His invention of the mass spectrometer with the assistance of Aston led to Thomson's discovery of neon isotopes in 1913. Later, Aston (1919) found that separate regions of electric and magnetic fields aligned at 90° was a preferred design and managed to build the first quantitative mass spectrograph. The literature reviews by Karl Wien (1999) and Münzenberg (2013) provide a detailed history of mass spectrometry development in the early dates with clear explanations of those early experiments.

Being an excellent tool for the study of isotopes is not the only advantage of mass spectrometry. Today, it plays an important role in analytical chemistry with applications in many branches of science such as biology, nuclear physics, pharmacokinetics, forensic science, medical imaging, etc. Mass spectrometry techniques continue to be developed since its invention. Many types of mass spectrometer have been produced for research and also for commercial purposes.

2.1.1 General Background

The mass-to-charge ratio in mass spectrometry is typically represented by the abbreviation m/z indicating a relative molecular mass per net charge number of an ion – The unit is the Thomson (Th), 1 Th = 1.04×10^{-8} kg/C. Where the mass of an atomic nucleon is equivalent to 1 Dalton (Da) (or 1.66×10^{-27} kg), and the electronic charge is 1.60×10^{-19} C.

The term ionisation describes a method to turn atoms or molecules into an ionic state where they carry net positive or negative charge(s). In mass spectrometry, molecules require enough energy to both vapourise and then ionise, perhaps in a vacuum, which allows them to be accelerated in an electric field. The ionisation and acceleration regions together comprise the ion source which generates an ion beam that enters the mass analyser. The ionisation method should be matched with an appropriate mass analyser. Selection of both ion source and mass analyser should suit the applications and analyte types, taking into account the required level of sensitivity and selectivity. The ions are separated according to their mass-to-charge ratios and then passed to the ion detector separated in space and/or time. The ability to distinguish the signals from different mass-to-charge ratio ions is expressed in terms of mass resolution, or mass resolving power. The definition can vary as will be mentioned in Section 2.2.6. The value of the mass resolution is affected by many factors including ionisation method, ion energy distribution and the detection system. All types of mass analysers have their relative strong and weak points.

Hard and soft ionisation refers to the amount of energy absorbed by the analyte excess to that required for ionisation. Hard ionisation means that energy beyond the ionisation threshold energy level is given to analyte molecules, where the excess energy can pool to break the bonds within an ion, causing ion fragmentation (Sun, 2009). A widely used hard ionisation technique is the electron ionisation method, where the fragmentation pattern aids in identification of the analyte. Soft ionisation is a more gentle method that results in a higher yield of molecular ions. Such methods include spray ionisation and desorption/ionisation methods. They also allow ionisation of involatile molecules. In general, such ionisation processes involve cation adduct formation transferring little energy to the analyte and causing little-fragmentation, thereby allowing molecular weight determinations but giving no structural details. Chemical structure can be studied by adding further dissociation energy to ions of selected m/z through collisions, reactions or irradiation, and operating in tandem mass spectrometry mode.

Scanning mass analysers detect a mass-filtered ion m/z value at a time. They are most suitable for continuous ion sources. In contrast, time-of-flight mass analysers are better suited to pulses of ions. Ion trap devices can store ions and enable scanned or pulsed mass analysis from a continuous ion source (Dolnikowski *et al.*, 1988).

2.1.2 Ionisation Techniques

There are a number of ionisation techniques available for use with mass spectrometry. Each specific technique has its own characteristics and suits appropriate applications. The principle and uses of some of the major ionisation techniques, including, electron ionisation, chemical ionisation, fast atom bombardment and electrospray ionisation are discussed in this section.

2.1.2.1 Electron Ionisation

Electron (impact) ionisation (EI) is classified as a hard ionisation method. A high energy (70 eV) electron beam from a heated filament collides with gas-phase analyte molecules. The collision allows energy transfer from the moving electron to a valance electron of an analyte molecule. Given that the energy is greater than the first ionisation energy, an electron of the analyte molecule is removed causing the molecule to have a net positive charge. Multiply charged ions are also possible but less common. The physical process is straightforward and its characteristics are simple and almost fully-understood. Mass spectra generated from an EI source are usually better for structural determination of the analyte using the typical 70 eV electron beam where significant fragmentation takes place, whilst molecular weight determination can be performed using a 20 eV electron beam where the molecular ion is more likely to be observed (Dagan and Amirav, 1995). Many databases are available for EI spectra, as they have been widely used in research. However, it is limited to the formation of radical cation ions (Gross and Roepstorff, 2011) which are not formed in large quantities during soft ionisation of biomolecules.

2.1.2.2 Chemical Ionisation

Tal'roze and Ljubimova (1952) introduced a softer method of ionisation called chemical ionisation (CI) as seen in the republished paper (Tal'roze and Ljubimova, 1998). Detailed MS analysis of hydrocarbon compounds can be obtained in either positive or negative ionisation modes, which is particularly useful for studying biological materials (Harrison, 1980; 1992). This is classified as a soft ionisation method in which a proton is transferred to the analyte molecule via a reagent gas, leading to less fragmentation than using a direct EI process. Whilst typical energies transferred in EI are greater than 10 eV, in CI they are less than 5 eV (Chapman, 1995). CI involves electron impact ionisation of the reagent gas. Examples of such reagent gases are methane, ammonia, isobutane, acetone, benzene, etc. (Gross, 2004). Then, secondary reactions between gaseous reagent, ions and molecules create more ion species. Analyte molecules subsequently participate in a chemical reaction with

these reagent gas ions to form analyte ions. Positive ions are produced by proton transfer, anion abstraction, charge exchange, or electrophilic addition, whereas negative ions can be created via electron capture or proton abstraction (Gross, 2004). Collision rates can be increased with a combination of sufficiently high pressures, and ion source residence time, which then give a sufficient ion yield (Field and Munson, 1965; Griffith and Gellene, 1993).

2.1.2.3 Fast Atom Bombardment

Fast atom bombardment (FAB) is a soft ionisation technique developed at the University of Manchester by Barber and coworkers in 1981 to help ionise thermo-labile and involatile biological molecules in mass spectrometry. A neutral particle beam, normally a noble gas such as Ar, is directed onto the sample surface at the rate of about 10^{10}-10^{11} atoms·s^{-1}·cm^{-2} (Barber *et al.*, 1981). The sample is usually dispersed in a glycerol matrix. The matrix is a host material which prevents instant transfer of high energy from fast atoms to the analyte that could cause unnecessary degradation. During ionisation, the ion chamber is under high vacuum. This ionisation method does not require prior sample vapourisation, allowing the analysis of non-volatile samples by mass spectrometry. The characteristics of the analyte ions are defined by the nature of analyte and any added chemicals, such as the matrix components. The technique is useful for molecular mass determination and possibly structural analysis of high mass organic and inorganic molecules of up to 5.7 kDa and 25.8 kDa, respectively (Rinehart, 1982). However, high chemical background is a significant problem to be avoided. The development of FAB ionisation paved the way for the very similar, more sensitive and widely applicable, matrix-assisted laser desorption/ionisation method which will be discussed in Section 2.2.1, to the point that FAB-MS is now little used.

2.1.2.4 Electrospray Ionisation

Electrospray ionisation (ESI) is another soft ionisation technique where the ionisation process differs considerably from the others. In 1914, Zeleny carried out an experiment by applying positive electrical potential to ethanol in a glass capillary tube and negative potential at a small distance from the tube. He observed positively charged ethanol droplets released from the tube towards the negative electrode. Electric field strength, sample flow rate, the tube's diameter and gas pressure are important factors, which affect the elongation of the charged sample at the end of the tube. All of these influence the size of the droplets, that form from what is known as Taylor cone as illustrated by the diagram in Figure 2.1 (Taylor, 1964). The fluid droplets evaporate during their flight to the opposite electrode which makes charge density increase, until the Coulombic repulsion forces overcome the cohesive surface tension of the liquid as expected from Rayleigh's limit estimation (Rayleigh, 1882). The typical voltage applied is around 2 - 4 kV (Standford, 2013). As a result, the smaller singly or multiple charged droplets are generated at atmospheric pressure. This ionisation method produces a low chemical background. This allows the application of electrospray as an ionisation process in mass spectrometry invented by Yamashita and Fenn (1984) and the method is still widely used. However, it is difficult to control the charge state of the ions formed. Also, the modality requires many steps and is selective towards high-polarity analytes. A sample is often introduced to the electrospray mass spectrometer via liquid chromatography.

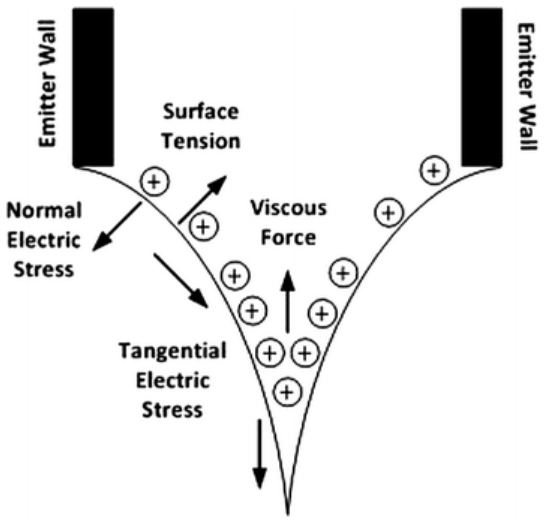

Figure 2.1 Taylor cone (Reproduced from: Wu et al., 2012)

2.1.3 Types of Mass Analysers

The mass analyser is a core part of the mass spectrometer where separation of different m/z ions take place. The main methods of mass analysis are electric/magnetic sectors, transmission quadrupole, time-of-flight, and various types of ion trap.

Table 2.1 below provides a summary of some features for the 5 types of mass analysers. The overviews of principles of these different instruments are given in the following parts of this section. However, the mass range and accuracy will depend on the instrumental design. Typical values are provided here in the table based on literature values.

Table 2.1 Main features for different types of optimised mass analysers

Mass analyser	Detection mode	Physical quantity for ion separation	Upper mass range (m/z)	Mass accuracy
Sector	Continuous	Momentum/ kinetic energy	10,000	Sub-ppm
Quadrupole	Continuous	Path stability	10,000	20 ppm
Orbitrap	Pulsed	Axial frequency	6,000	2-5 ppm
Fourier transform ion cyclotron resonance	Pulsed	Orbital frequency	Varies with trap size and field strengths	Sub-ppm
Time-of-flight	Pulsed	Velocity	Unlimited	2-5 ppm

(Information from: Standford (2013); Marshall *et al.* (1998); Pedder *et al.* (1999); Hu *et al.* (2005))

2.1.3.1 Electric/Magnetic Sectors

Sector instruments are types of scanning mass analysers. In a magnetic sector instrument, a magnetic field is applied perpendicular to the plane of ion motion so that the ions experience centripetal force leading to circular motion. The 180° magnetic sector design by Dempster (1918) is the simplest example. At a constant magnetic field strength, the ion accelerating voltage is altered in order to scan through different values of m/z (Pacey, 1976). In this way, it is possible to adjust ion velocities which determine the flight path. In an electric sector instrument, ions with

different kinetic energies are dispersed in circular paths when experiencing a centripetal force due to the static electric field in a cylindrically symmetric electrode (Herbert and Johnstone, 2002). Ions with the same energy are focused together. Much greater mass resolution is achieved using this combined electric and magnetic sector design to filter the energy of an ion beam. Various combinations of electric and magnetic sectors are possible.

2.1.3.2 Transmission Quadrupole

For this type of scanned mass analyser, instead of using a magnetic field to disperse the ion beam according to mass-to-charge ratios of ions, ions are allowed to pass through a quadrupole field (Paul and Steinwedel 1953; 1960). A quadrupole mass analyser is composed of 4 parallel rods of monopoles at varying electrical potentials (see the diagram presented in Figure 2.2). Opposite pairs of rods at sides have the same polarity. They are electrically connected having direct current (DC) voltage and radiofrequency (RF) alternating current voltage applied across the pairs of rods. This results in an oscillating electric field which can be adjusted to allow only ions with a selected mass-to-charge ratio to pass all the way through the gap between parallel rods. Quadrupole instruments can apply ion trapping to temporally store ions at a given mass-to-charge ratio with use of appropriate Mathieu's equation parameters (March *et al*., 1989; March, 1997).

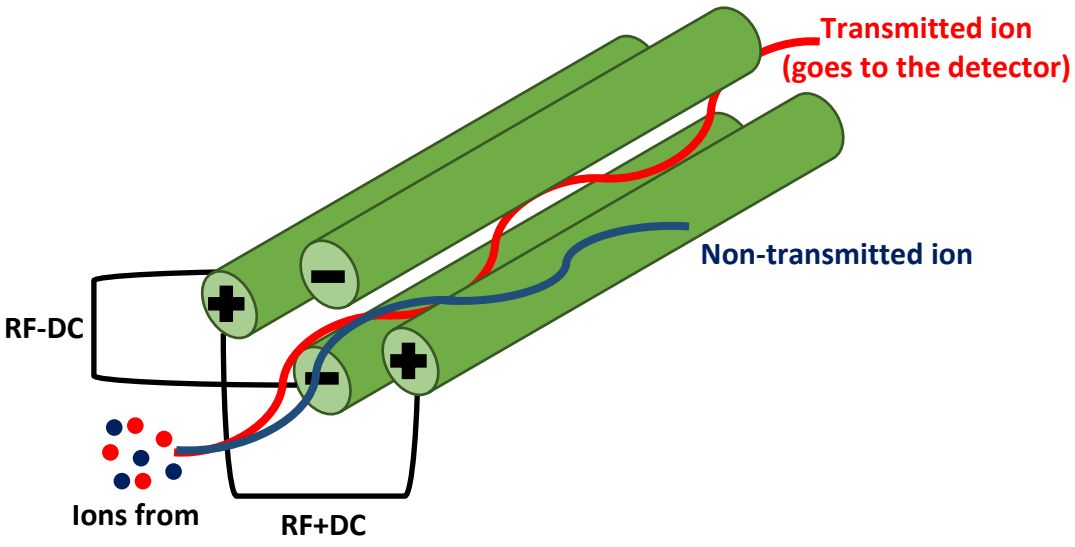

Figure 2.2 Quadrupole mass analyser

2.1.3.3 Orbitrap

The orbitrap is a modified Kingdon trap. The Kingdon trap is a cylindrical capacitor which has a tungsten cathode wire, aligned on the central axis of the anode tube made of molybdenum (Kingdon, 1923). The dynamic Kingdon trap has an alternating voltage added across the capacitor to trap ions for longer period of time compared to the original Kingdon trap which had only a static voltage applied (Blümel, 1995). Knight (1981) adapted the shell of the electrodes to be spindle-like where direct current voltage is applied such that the centripetal force due to electrostatic energy balances the centrifugal force due to ion's kinetic energy (Perry *et al*., 2008). This induces ion orbits around the wire axis and harmonic oscillation in the longitudinal direction. Ions are trapped and their m/z can be determined based upon Fourier transform of the axial harmonic oscillation frequency of each ion detected in time domain (Hu *et al*., 2005; Perry *et al.*, 2008), see the diagram shown in Figure 2.3.

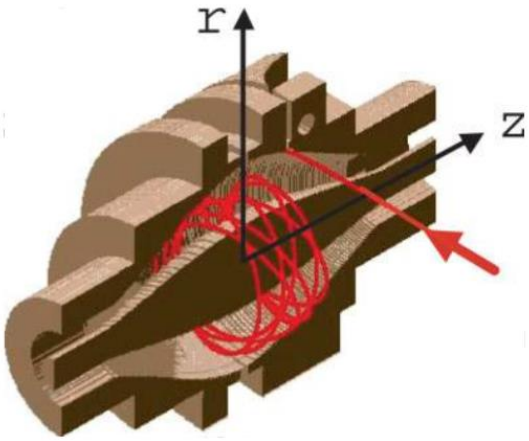

Figure 2.3 Orbitrap mass analyser (Reproduced from: Hu et al. (2005))

2.1.3.4 Fourier Transform Ion Cyclotron Resonance

Fourier transform ion cyclotron resonance (FT-ICR) can achieve the highest mass resolution of all available types of mass analyser. The FT-ICR technique is suitable for almost all ionisation methods. A cyclotron frequency is defined as the angular frequency at which an ion orbits in a constant magnetic field. This quantity is a function of magnetic field strength and ion mass-to-charge ratio. The kinetic energy distribution does not influence the cyclotron frequencies. Therefore, high precision

and high resolution can be achieved without any energy focusing (Marshall and Hendrickson, 2002). The ion cyclotron resonance is then excited by an RF voltage pulse causing the charge particles in the detector to oscillate at the resonance frequency. Ion image currents detected in the time domain can be converted into the frequency domain spectra by a Fourier transform operation. The mass resolution of FT-ICR spectra is mass-to-charge dependent. Exceptional resolution is achieved using the multi-electrode ICR cell (Nagornov *et al.*, 2014). However, FT-ICR MS is relatively time consuming and expensive, as a superconducting device is required to produce such a strong magnetic field. Also, the sensitivity is limited since its measurements rely on image currents, not a multiplier detector.

2.2 MALDI Mass Spectrometry

This section aims to give an overview of MALDI mass spectrometry which was developed to allow the ionisation of very large biological molecules. Understanding MALDI-TOF-MS instrumentation is crucial to describing the nature of mass spectra generated and to optimising experimental parameters. The mass spectra not only contain useful information associated to analytes, but can also indicate the performance of specific instrumental settings and experimental protocols via signals and noise behaviour. Obtaining appropriate laboratory methods/conditions are key to every analysis, especially in quantitative tasks, where reproducible results are necessary. In what follows, the invention, instrumental design, mass resolution, matrices and sample preparation of MALDI-MS will be reviewed, with discussion of imaging aspect comes later in Section 2.4.

2.2.1 Invention

Matrix-assisted laser desorption/ionisation is one of the techniques in the desorption ionisation family. Desorption ionisation (DI) techniques are classified as soft ionisation techniques and include spray methods as well as laser desorption. The

processes involve quick transfer of energy to the sample by interactions between incoming particles (charged or uncharged) or photons, and analyte molecules in the sample, influencing molecular excitations and ionisation state (Busch, 1995). Excitation, evaporation and ionisation are almost simultaneous. The desorption ionisation techniques were developed specifically to enable vapourisation and ionisation of molecules with low volatility that is not possible using EI or CI methods. Also, typical methods to bring about sample volatilisation to initiate ionisation might introduce too much internal energy to the analyte molecules causing unnecessary fragmentation and/or rearrangement. In mass spectrometry applications, the softer DI techniques tend to improve the ability to ionise large polymers especially biological molecules.

FAB as discussed in Section 2.1.2.3, is a type of desorption ionisation technique which uses fast-moving atoms, as an energetic incident beam. Similar sorts of ionisation processes are involved, as for liquid secondary ion mass spectrometry (LSIMS) (Ross and Colton, 1983) that was inspired by the previously-developed static secondary ion mass spectrometry (SSIMS) (Benninghoven, 1969), except that incident ions are used instead of neutral particles. In contrast, plasma desorption (PD) activates sample ionisation using high energy ions derived from nuclear fission of the ^{252}Cf isotope (MacFarlane and Torgerson, 1976). A time-of-flight mass analyser measures the mass-to-charge ratios of the produced sample ions. Typical PD energy is of the order of MeV whereas FAB, SIMS and LSIMS use keV energies (Busch, 1995). Moreover, primary collision events of the high energy ion beam with a sample molecule could trigger secondary impulses with neighbouring molecules, thus increase the ionisation and the variety of ion species. In FAB and LSIMS, a matrix material can be added or dissolved in the sample solution. The sample-matrix could be removed from the deposited area when exposed to the incident beam. Matrix molecules help to absorb incident energy and impart the right amount of energy to the sample such that the analyte molecules are ionised and separated from the rest of the solvent without significant fragmentation.

Laser desorption (LD) is a distinct approach relative to other desorption ionisation techniques where energy exchange is brought about by a beam of photons rather

than of particles. LD energy is adjustable and is controlled by choosing the corresponding wavelength and fluence of the laser pulses. This method is generally used with time-of-flight mass analysers. In mass spectrometry analysis of very large biological molecules, a matrix is usually provided so as to mitigate degradation problems. The two best-known techniques are matrix-assisted laser desorption/ ionisation (MALDI) and surface-assisted laser desorption/ionisation (SALDI) mass spectrometry. However, the matrix-free approach is available for light molecules of ideally less than 1 kDa (Peterson, 2007).

MALDI became an ionisation method for mass spectrometry analysis of larger molecules, introduced in late 1980s following the interesting work of Japanese (Tanaka *et al*., 1988) and also German (Karas and Hillenkamp, 1988) groups. They added matrix substrate into the analyte in such a way that they would form a solution. Suitable solvents were added as required. The selected matrix must co-crystallise with the analytes after solvents are evaporated. Tanaka *et al.* (1988) developed the "ultra-fine metal plus liquid matrix method", where a mixture of fine cobalt powder and glycerol is selected as a matrix in this experiment, which improved the capability for producing ions of up to 25 kDa. Karas and Hillenkamp (1988) reported the use of nicotinic acid solution as a matrix that enabled 67 kDa bovine albumin to be measured. Nitrogen and neodimium-doped yttrium aluminium garnet (Nd:YAG) ultraviolet lasers at wavelengths 337 nm and 266 nm were used in Tanaka's and Hillenkamp's experiments, respectively. The photon-induced MALDI method might be used for large polymers e.g. biomolecules with low volatility and usually form closed-shell ions. (Li, 2009). The concept is that instead of giving a direct dose of laser energy to ionise the analyte, the laser will increase the energy of the matrix substance which can then be dissipated to the surrounding analytes in solution. Firstly, an energetic fragment of sample-matrix crystal is removed from the sample surface. Then, the matrix desorbs, causing itself to evaporate and induces electron-proton transfers in the analyte molecules. This indirect absorption of laser energy by the analyte reduces the damage caused to the molecular structure of analytes, and hence, increases the number of useful ions and their stability. However, the mechanism behind the MALDI ionisation process is not yet totally interpretable.

Typical MALDI-TOF instruments have a mass resolution of more or less 10,000 (Köfeler *et al*., 2012). It also tends to have limitations at very high mass due to the sensitivity of ion detection systems (see Section 2.2.5) and the complex desorption ionisation characteristics of sample-matrix crystals. Therefore, fundamental MALDI research focuses on understanding and enhancing its mechanism and performance.

2.2.2 MALDI Ionisation

The energy source for ion generation in MALDI is the laser photons. Different laser sources give different photon wavelengths ranging from the ultraviolet (UV) to infrared (IR) regions of electromagnetic radiation. Examples of laser sources and their characteristics are provided in Table 2.2.

Table 2.2 Laser sources for MALDI-MS

Laser type	**Nitrogen (gas laser)**	**Neodymium:YAG (solid-state laser)**			**Erbium:YAG (solid-state laser)**
		Fundamental	**Frequency-tripled**	**Frequency-quadrupled**	
Wavelength	337 nm	1.06 µm	355 nm	266 nm	2.94 µm
Pulse width	Few ns	Few ns			Few tens ps

(Information from: O'Connor and Hillenkamp (2007); Menzel *et al*. (2002); Soltwisch and Dreisewerd, (2011))

A laser shot fired onto a small volume of matrix-analyte crystals on the sample surface initiates evaporation and sudden plume expansion due to an increase in temperature. This involves electronic, vibrational and kinetic energy excitations, with exchange of energy over a short period of time. Energy propagation for MALDI has to be completed within a period shorter than the sample's thermal diffusion time to promote proton transfer during the quasi-equilibrium state of the plume, and to prevent ions from neutralisation (Knochenmuss, 2013). A pulsed laser generally has higher fluence compared to a continuous laser design. It creates ion packets in pulses, which works well with the time-of-flight analyser because it allows enough time for a packet of ions ionised by a previous laser shot to reach the detector before the next one comes. This makes the energy per pulse a more important consideration than

that of an individual photon. Therefore, not only the laser wavelength but also the pulse width (duration of a pulse) and fluence are taken into account to evaluate the energy available for ionisation in each laser pulse. The beam passes through focusing optics, in order to generate a near-Gaussian or Top-Hat distribution of energy at the surface, to filter out hot spots and to adjust the spot size of the beam on the sample.

The process of desorption/ionisation is illustrated by the diagram in Figure 2.4. When a laser beam is fired at the sample-matrix mixture deposited on a target, some fraction of energy is absorbed by the matrix and associated sample molecules. The absorbed energy, E_a in the irradiated sample volume, V (determined by spot size and penetration depth of beam into the sample), can be expressed in terms of laser fluence as follows.

$$\frac{E_a}{V} = \alpha H \tag{2.1}$$

Where laser fluence, H which is defined as energy per unit area at depth, z from sample surface decays exponentially as a function of z as shown in Equation (2.2) (Hillenkamp *et al.*, 2013).

$$H = H_0 e^{-\alpha z} \tag{2.2}$$

With H_0 being the fluence at $z = 0$ and α being absorption coefficient of sample-matrix at a specific laser wavelength (Hillenkamp *et al.*, 2013). Therefore, by integrating Equation (2.2), Equation (2.1) is obtained.

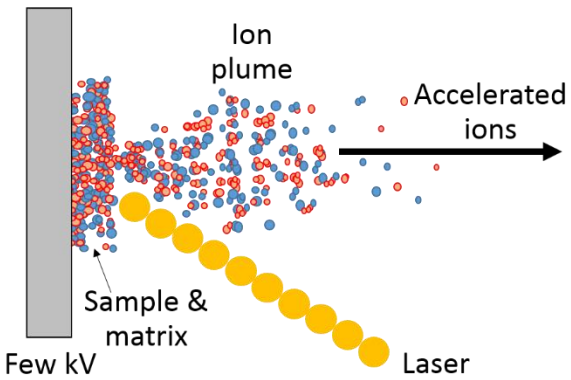

Figure 2.4 Desorption/ionisation process in MALDI (Adapted from: Lewis et al. (2006))

As a co-crystallised structure is formed, including molecules of the matrix and the sample, energy absorbed by matrix molecules can be pooled in matrix clusters and transferred to analyte molecules. Whilst escaping the sample surface, the matrix molecules evaporate from sample, some forming matrix clusters, and which are involved in ionisation of some of the sample molecules (analytes) as illustrated in Figure 2.4. However, the majority of energetic sample molecules are non-ionised and leave the sample source as neutrals. Following ionisation and acceleration, an Einzel lens brings a divergent ion beam into focus. The ion beam experiences electric fields whilst passing through a series of component lenses, causing the ion beam to diverge and re-focus (Sise *et al*., 2005).

2.2.3 Ion Acceleration

The very first ion accelerator for TOF-MS applications dates back to a simple two-plate capacitor (Stephens, 1946; Cameron and Eggers, 1948; Wolff and Stephens, 1953). Where a voltage is applied across the two parallel plates resulting in acceleration of ions produced between the plates. The ion potential energy changes when an electric field is applied. The sum of the potential energy and the initial energy obtained from ionisation procedure (left hand side of Equation (2.3)) will be fully converted into kinetic energy (right hand side of Equation (2.3)) after leaving an exit grid of the accelerator into the mass analyser, following the law of conservation of energy.

$$qV + U_0 = \frac{1}{2}mv^2 \qquad (2.3)$$

Where q is ion charge, V is electric potential difference at the ion source (typically 20 kV), m is ion mass, v is speed of ion when leaving electric field and U_0 is an initial energy after ionisation (translational energy).

However, individual molecules with identical mass-to-charge ratio are rarely ionised at exactly the same time or distance, nor do they carry the same momenta. There exists some shift in flight-time measurements from ion to ion even though their masses are equal. Positional differences at which the ions are formed, transforms to

a kinetic energy distribution of ions in the mass analyser (drift) region which expands the flight-time distribution (see more details in Section 2.2.4). Applying the Newton's second law of motion, Equation (2.4) determines a value for acceleration in the accelerating region.

$$\boldsymbol{a} = \frac{q\boldsymbol{E}}{m} \tag{2.4}$$

Where $\boldsymbol{a}$ is acceleration in the electric field direction and $\boldsymbol{E}$ is electric field.

Accordingly, the time an ion takes to leave the acceleration region, t'_a is given by Equation (2.5) (Guilhaus, 1995). Assuming that sample molecules are ionised in the same plane relative to the electric field direction.

$$t'_a = -\frac{\sqrt{2mU_0}}{Eq} \pm \frac{\sqrt{2m(U_0+Eqs)}}{Eq} \tag{2.5}$$

Where s is a displacement of ion while being accelerated (only the displacement along the axis of accelerating field is important). Given that the direction of acceleration is positive, the sign of t'_a indicates whether the direction of ion's initial velocity is the same as that of acceleration. In other words, positive valued t'_as refer to ions that continue to travel in the same direction as their initial velocity. On the other hand, those with negative values have initial velocities which oppose the accelerating field. So they undergo deceleration prior to acceleration which results in change in trajectory direction and some extra flight-time over the ones with same initial energy which initially travelled downstream. In reality, the time an ion spends in acceleration region, $t_a = |t'_a|$. Where two times the first term of Equation (2.5) is known as the turn-around time an opposing ion needs to catch up its original position that often occurs in ionisation events (Guilhaus, 1995).

Space focus is arranged such that ions with different kinetic energies are spread over the smallest possible displacement along the acceleration field. This removes the spatial and energy shifts to some extent which leads to improvement of the overall flight-time resolution. Furthermore, even better temporal resolutions can be achieved via additional energy correction steps (see Section 2.2.6).

2.2.4 The Time-of-flight Mass Analyser

Ideally, a group of ions is generated starting from the same position at the same time and ions are then accelerated to the same kinetic energy. Their transit time through a field-free flight tube can then be measured. However, in reality, “the same position”, “the same time” and “the same kinetic energy” are all approximations. The relevant parameters and techniques to correct for each are discussed in this section. MALDI-MS is usually coupled with a time-of-flight mass analyser. Other types of mass analysers such as quadrupole, ion cyclotron resonance are also available but are less commonly built for commercial purposes. The reasons which make time-of-flight instrument a preferred mass analyser for MALDI-MS is that it is designed to detect pulsed ions with ideally no limit in mass range, and no ions are wasted by scanning. Also, TOF with a subsequent mass analyser of same or other types can be constructed to perform multiple MS analysis. Therefore, in this instrumental design section, only MALDI-TOF-MS instruments will be considered.

In time-of-flight instruments, flight-time is a parameter to be quantified and converted into m/z information. The total flight-time can be expressed as the overall time spent in acceleration region, t_a, drift region, t_D and also any delayed time during ionisation and detection processes.

The time-of-flight mass analyser is a simple yet effective tool for determining ion m/z. Charged particles from the ion source are accelerated through an appropriate path inside the mass spectrometer. The time taken to reach the detector called “time-of-flight” or “flight-time” is the main parameter to be measured. Suitable detectors can measure the flight-time of ion packets with different masses. This information is then passed for computer processing to obtain mass spectra (plots of signal intensity vs. m/z).

2.2.4.1 Linear Time-of-flight Mass Spectrometer

An ion enters the drift region of length, D with a final velocity from the accelerator that can be worked out from the equation of conservation of energy, Equation (2.3).

The ion exerts no force in the vacuum drift region. It therefore travels with the constant velocity throughout the drift region. The time it takes to pass the drift region, t_D is derived in Equation (2.6).

$$t_D = \frac{D}{2}\sqrt{\frac{2m}{(U_0+qEs)}} \tag{2.6}$$

From Equations (2.5) and (2.6), the total flight-time, t is directly proportional to the square root of mass ($t \propto m^{\frac{1}{2}}$). Finally, the ion beam hits a detector device which generates signals from the distribution of flight-times of the different ions in the beam, and the mass-to-charge ratios of the ions are calculated. A diagram for this type of mass spectrometer is shown in Figure 2.5.

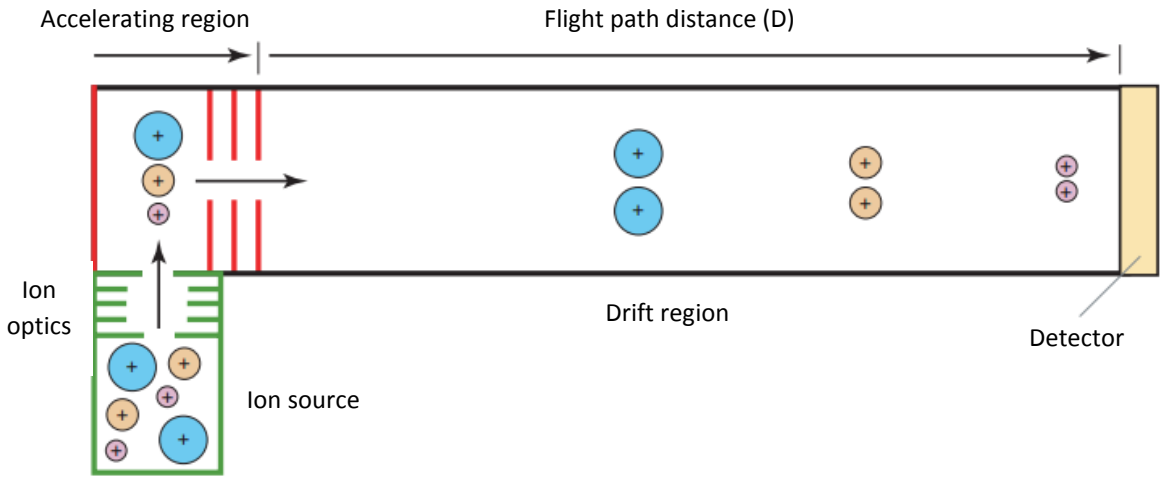

Figure 2.5 A simple diagram for orthogonal acceleration time-of-flight mass spectrometer (Picture from: Fjeldsted (2003))

In this simplest time-of-flight mass spectrometer, there is a limitation due to the fact that ions are created in slightly different locations in space as mentioned earlier in Section 2.2.3. The spatial variation in the position of ions in the direction of electric field affects velocities and therefore the flight-time of ions of the same mass-to-charge ratio leaving the exit plate of the capacitor. Each ion with the same mass and carrying equal charge is accelerated at the same rate in the static electric field between the capacitor plates, as described in Equation (2.4). The potential difference

in static electric field varies as a function of distance to be accelerated. Thus, the final velocity of same ion varies as a function of distance being accelerated within the capacitor as a result of differences in kinetic energy. This causes time-of-flight m/z peaks in mass spectra to be broaden, influencing the mass resolution (see Section 2.2.6 for the definition of mass resolution). The uses of linear and curved field reflectrons are approaches to overcome this distribution of flight-times.

2.2.4.2 Reflectron Time-of-flight Mass Spectrometer

The reflectron also known as the ion mirror, retards the incoming ions and causes them to reverse their initial direction. This was first designed by Mamyrin *et al*. (1973). It makes use of electrostatic lens components which create a retarding electric field gradient.

Ions with identical mass-to-charge ratio in the drift region have a small kinetic energy distribution caused mostly by initial energy when ions are formed. The longer the flight path, the more significant shift in flight-time of these same ions would be observed as a result of their variation in velocity. Higher velocity ions have a relatively short flight-time in the drift region compared to lower velocity ions. To reduce the flight-time shift, these ions must be introduced into a reflectron (Cornish and Cotter, 1993). The reflectron's electric field decelerates the ions when they are travelling inbound until they stop, then reaccelerates them in the outbound direction (Cornish and Cotter, 1993). Faster ions (i.e. with greater than average kinetic energy) spend more time in the reflectron region as they penetrate slightly deeper than slower ones, this corrects for different time spent in the drift region. Also, a focus is made at the point where the ion packet is most compressed (in time). This results in far better mass resolving power than linear instruments with same drift length. It therefore gives high performance without the need to build larger mass spectrometers.

2.2.4.3 Curved Field Reflectron Mass Spectrometer

The curved field reflectron (CFR) is a subsequent generation of reflectron developed by Cotter and Cornish (1993). This aims specifically to remove imperfections in MS/MS time-of-flight mass analysis. When ions are fragmented via collision induced dissociation (CID), the kinetic energy of product ions depend solely on their mass, leading to separations of focal points associated with the depth travelled by ions into a linear field reflectron as from SIMION trajectory simulations (Cornish and Cotter, 1993). In contrast, a curved field reflectron incrementally reduces the strength of the electric field as it goes deeper into the reflectron. In other words, the potential used to create the field goes down at a constant rate with the form of "the arc of a circle" to satisfy conditions determined by SIMION simulations (Cornish and Cotter, 1993). Thus, the focal points of different products (and their parent) ions are brought to focus more tightly than with the linear field reflectron.

2.2.5 Ion Detection

The detection system includes the ion detector, signal amplifier and signal acquisition electronics. The output of ion signal vs. mass-dependent flight-time variations of ions is recorded and turned into a mass spectrum. A microchannel plate (MCP) detector is often used as an ion detector in MALDI-TOF-MS instruments. An incident ion collides with the detection surface and activates secondary electrons in parallel electron multiplier tubes of few micrometres diameter in order to amplify signals. The quality of mass measurements can be affected significantly by the design of the detector (e.g. having a planar detector is useful for a time-of-flight mass analyser).

At a certain kinetic energy, ions with higher masses will travel with lower velocities which might not be sufficient for secondary electron emission to occur and can result in a decay of MCP detection sensitivity. For example, Liu *et al*. (2014) reported that the detection of immunoglobulin G dimer whose mass is about 300 kDa can be more than 10% less sensitive than the detection of the 1 kDa angiotensin ion. If ions are accelerated with higher voltage, the kinetic energy and therefore velocity of all ions

increase and the sensitivity is then improved. On the other hand, detection of fast moving, lower mass ions with high incident energy might be limited by the saturation of the detector which can give rise to a poorer resolution. Temporal events can currently be resolved down to the order of nanosecond or less (Li and Whittal, 2009). In addition to the conventional approach, the ion conversion detector and superconducting tunnel junction are attempts to overcome these sensitivity limitations as velocity-dependence no longer applies (Wenzel *et al.*, 2006). Higher sensitivity can be attained by increasing detector voltage, however, would raise the level of electrical background noise at the detector and lead to a corresponding reduction of signal-to-noise (Wetzel *et al.*, 2006).

2.2.6 Mass Resolution

The mass resolution is defined by Equation (2.7).

$$mass\ resolution = \frac{m}{\Delta m} \tag{2.7}$$

Where Δm is the width of m/z peak centred at m in a mass spectrum (width values at full width half maximum or at 10% of the peak height may be used). Δm represents the extent to which the m/z measurements are distributed for that peak. Therefore, the mass resolution represents an ability to tell apart different peaks in a mass spectrum.

Mass resolution can be calculated from the flight-time resolution. For time-of-flight instruments, flight-time is defined by the relationship $t \propto m^{\frac{1}{2}}$ (see equation (2.6)), given that flight-time is approximately equal to drift time providing that accelerating time is much smaller than drift time ($t_a \ll t_D$). Therefore, mass resolution can also be derived using Equation (2.6) and its derivative with respect to m and U_0. In addition, the kinetic energy resulting from accelerating an ion through the electric field dominates the initial translational energy ($U_0 \ll qV$) such that U_0 can be ignored in the numerator of Equation (2.8). Therefore, the mass resolution for time-

of-flight mass spectrometer is estimated as in Equation (2.8) in terms of flight-time and internal energy, respectively.

$$\frac{m}{\Delta m} = \frac{t}{2\Delta t} = \frac{U_0 + qV}{\Delta U_0} \approx \frac{qV}{\Delta U_0} \tag{2.8}$$

Note that the electric field is in fact not perfectly uniform.

Further improvements of space focus in the acceleration region, include placing another electric field next to the initial space focus field following an instrument designed by Wiley and McLaren (1955), taking into account appropriate ratios of the two electric field strengths and acceleration distances (Weinkauf *et al*., 1989; Karas, 1997). These designs eliminate up to the first and the second terms of Equation (2.9) of Taylor's expansion which express the inverse flight-time resolution as a function of kinetic energy distribution, respectively (Weickhardt *et al.*, 1996). The results predict a much better mass resolution compared to the single field design (see Section 2.2.3) without having to extend too far the space focus distance.

$$\frac{\Delta t}{t} = a\frac{\Delta U}{U} + b\left(\frac{\Delta U}{U}\right)^2 + c\left(\frac{\Delta U}{U}\right)^3 + \cdots \tag{2.9}$$

Where t is the overall flight-time, U is the ion's kinetic energy and a, b, c are constants.

The arrangements of linear and curved field reflectrons as discussed in Sections 2.2.4.2 and 2.2.4.3 that lead to better flight-time focus would offer similar improvements in temporal resolution.

2.2.7 MALDI Matrices

The matrix is core to the process of MALDI as described in Sections 2.2.1 and 2.2.2. A matrix is selected such that sample and matrix co-crystallise in an analyte-specific manner, to suit a particular experiment. Key properties include the ability to incorporate a chromophore to absorb the laser light and the ability to generate an appropriate ionisation environment for the formation of positive or negative ions. Standard matrices for MALDI-MS of biological molecules include α-cyano-4-

hydroxycinnamic acid (CHCA), dihydroxybenzoic acid (DHB) and sinapinic acid (SA). They are able to absorb energy from ultraviolet frequency lasers. The structure of the ions created from samples with the use of DHB matrix are more preserved compared to ones with CHCA matrix which normally causes significant degradation (Hazama *et al*., 2008). Therefore, CHCA matrix is well-suited for analytes of lower mass range whereas DHB as well as SA can be used with higher mass range to avoid fragmentations. In contrast, Luo *et al*. (2002) reported that greater internal energy was observed in analytes ionised using DHB, where internal energy influences fragmentation and stability of ion signals after shots of laser. However, this is highly subject to the laser fluence and depends upon the analyte's characteristics.

The more acidic a matrix is, the better positive ion yields are obtained (Schiller *et al.*, 2007; Dashtiev *et al*., 2007). Additional trifluoroacetic acid (TFA) could enhance signal-to-noise ratios of mass spectra (Damnjanovic *et al*., 2011). DHB is used as a matrix to prepare most lipid samples, especially the 2,5-DHB type which gives the best quality mass spectra of all the isomers, as a result of relatively high positive ion yield and small crystal size (which gives homogeneous preparation surface – good for imaging in particular) relative to other available types, i.e. 2,3-DHB, 2,4-DHB, 2,6-DHB, 3,4-DHB and 3,5-DHB (Schiller *et al*., 2007).

It is possible to make up a matrix compound of more than one component. For example, DHB/CHCA as reported in Laugesen and Roepstorff (2003) could combine the advantages of the two which accounted for a more complete set of analytes within a sample, in a single acquisition.

2.2.8 Sample Preparation (Sample-matrix Depositions)

Appropriate matrix type and sample preparation methods are selected for each analyte and sample type. The main consideration in matrix selection is to optimise the signal-to-noise of the analyte signals. This requires increasing ionisation efficiency without introducing background signals. Along with appropriate signal intensity, the optimal mass accuracy, resolution and reproducibility are desired in

each MALDI-MS experiment. These can be achieved by optimising sample preparation, together with adjusting instrumental parameters and calibration. In general, a sample should be prepared in suitable conditions to form significant numbers of analyte-containing matrix crystals. Such crystals should be distributed homogeneously throughout the dried drop on the sample target with uniform shape and size. Also, the target supporting the sample must be cleaned properly to minimise impurities. Optional purification methods of hydration/recrystallisation or sublimation/recrystallisation (Yang and Caprioli, 2011) can be used. Contaminants that are highly soluble in water will be dissolved and can be removed, and then purer crystals remain on the target plate. Solvents can be added to re-dissolve and recrystallise which can purify the sample and change crystal morphology.

The original dried-droplet sample preparation method (Karas and Hillenkamp, 1988) involves spotting a sample solution spotted onto the target surface and leaving it to dry and then spotting the matrix solution on top of the sample spot. Another approach is to make a mixture of saturated matrix and sample solutions, then a small droplet of this is spotted onto a metal target. The dried-droplet technique results in large crystal sizes. Therefore, useful spectra can be acquired repeatedly from the large crystals at selected spatial locations. MALDI targets are usually designed to hold an array of sample droplets that can be conveniently analysed in the same session.

The homogeneity of the MALDI sample surface depends in part on size of the crystals being formed which is affected by the type of matrix and analyte concentrations, and could be improved by selecting a solvent with high evaporation rate. When crystals formed are small in size, better homogeneity of the preparation is achieved but fewer ions (lower intensity mass spectra) are produced per crystal. To minimise this disadvantage, the dried-droplet can be applied again on top of the preparation to increase the crystal size for discrete (non-imaging) MALDI sample. Note that, for imaging, a finer and consistent crystal size would be preferred for a uniform spread on the prepared surface. This is achieved by appropriate preparation, choice of matrix and matrix deposition parameters. Matrix deposition methods for MALDI-MS imaging will be mentioned in Section 2.4.3.

2.2.9 Tandem Mass Spectrometry

A tandem mass spectrometry system refers to the use of two or more mass analysers each subsequently perform mass spectrometry analysis – MS^n where n is the number of MS stages. Usually 2 mass analysers are used, referred to as: MS/MS or MS^2. Between the 2 consecutive analysers, there can be a collision chamber containing neutral gas, usually helium, argon and nitrogen. Collision with neutral gas molecules can fragment a parent ion (Wells and McLuckey, 2005). The process is called collision induced dissociation (CID), which can be used in TOF/TOF instruments. More fragmentation occurs when target gas of heavier molecular weight is used, providing higher centre-of-mass collision energy (Bordas-Nagy *et al.*, 1992). The purpose of tandem MS is to extract structural information from the analyte. First of all, the analytes' m/z(s) in the mixture (within a defined mass range) needs to be identified in order to select the ion of interest. This can be achieved in a TOF instrument using the ion mass spectrum resulting from the first mass analyser by gating a narrow mass range that includes the mass peak of interest. Only ions with the selected mass range, called precursor ions, undergo decomposition into product ions and suffer neutral losses. These product ions then go on to the second mass analyser for further mass analysis. The mass spectra of product ions provide the masses of component fragments of the precursor (parent) ions. Alternatively, MS/MS spectra of the whole mass range can be scanned to observe specific product ions resulting from CID and metastable decays which could indicate the possible precursor. For increased selectivity, selected reaction monitoring (SRM) is performed at specific precursor's and product's m/z values (Lange *et al.*, 2008). The other method called a neutral loss scan is also applicable by observing for a specific interval between mass peaks, then all possible products of a precursor can be determined and vice versa.

An early tandem MS instrument was the magnetic/electric sector. Ions pass the magnetic sector component (constant field) followed by scanning field in the electrostatic sector where the mass of product ions are determined based on their kinetic energy (Beynon *et al.*, 1973). This paved the way for generations of MS/MS instruments. Triple quadrupole (Yost and Enke, 1979) and more accurate FT-ICR

instruments, both select precursor ions prior to CID. Not only space separated tandem mass spectrometry using multiple mass analysers, but also time separated tandem mass spectrometry using ion traps can be performed (Payne and Glish, 2005). Tandem mass spectrometry based on the TOF/TOF instrument configuration is another fast improving method due to its simplicity, robustness and wide mass range. The correction for the varying focal length of different mass ions was solved by Cornish and Cotter (1993) who developed the curved field reflectron as discussed in section 2.2.4.3. A diagram for this design of tandem reflectron TOF MS/MS is illustrated in Figure 2.6.

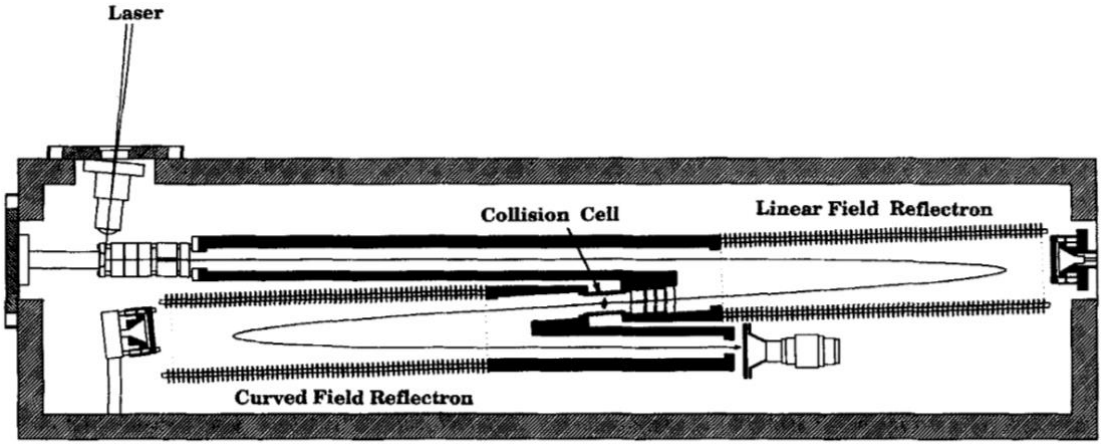

Figure 2.6 Tandem TOF/TOF mass spectrometer combining linear and curved field reflectron TOF mass analysers (Picture from: Cornish and Cotter (1993))

Note that hybrid systems that combine different types of analysers are also available such as sector/quadrupole, sector/TOF and the commercially most abundant quadrupole/TOF (Glish and Burinsky, 2008).

2.3 Lipidomics and the Application of MALDI-MS in Lipidomics

2.3.1 Lipid Types and Functions

Fahy *et al.* (2005) divided lipids into 8 main classes, "fatty acyls, glycerolipids, glycerophospholipids, sphingolipids, sterol lipids, prenol lipids, saccharolipids, and polyketides". As a result of the diversity of lipid classes, their masses vary across a wide range from few hundred daltons to kilodaltons. In general, lipids are organic molecules that are present in biological systems and can be produced via biosynthesis. Most lipids are highly soluble in organic and other low polarity solvents as a result of highly hydrophobic components of these molecules, frequently having an alkyl "tail", see the structure of a fatty acid depicted in Figure 2.7 (a). Fatty acids are the most fundamental lipids composed of carbon, hydrogen and oxygen atoms. A fatty acid has the structure of carboxylic acid where a long chain hydrocarbon is connected to a carboxyl group. They can be attached to functional groups to form various head-tail structure of more complex lipid molecules. Fatty acid derivatives also count as lipids (Adibhatla *et al*., 2006).

Lipids are involved in metabolic and other biological activities as energy storage, vitamins, neurological signalling and can function as hormones. Phospholipids are major structural components of cells, forming of cell membranes and protein binding sites. Most biological cell membranes consist largely of phosphatidylcholine (PC). Normal cells differ in the lipid components and distributions of specific organelles and cell types (van Meer *et al.*, 2008). Hence, lipid mass spectra might be good indicators for tissue phenotypes and some pathological disorders. There have been attempts to perform quantitative studies of lipids to possibly trace lipid metabolism in cancer tissues that could identify cellular activities stated as hallmarks of cancers (Hanahan and Weinberg, 2000; 2011; Santos and Schulze, 2012). As brain tissues are lipid-rich, observing the correlations between lipid concentrations and brain diseases, disorders and damage has become an interesting topic of research (Adibhatla *et al*., 2006).

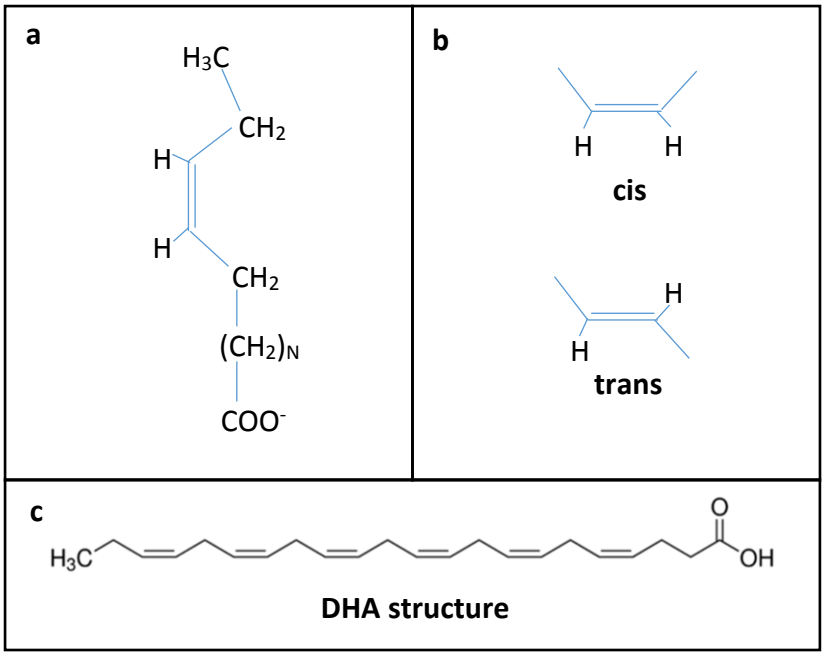

Figure 2.7 (a) A ω-3 fatty acid where N indicates a number of repeated CH_2 (with single bond C-C) (Adapted from: Berg et al. (2002)), (b) cis and trans structures, and (c) DHA structure (from: www.sigmaaldrich.com)

2.3.2 Cellular Lipids

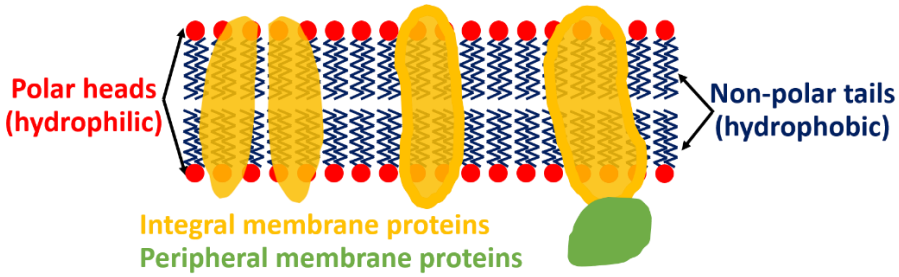

Figure 2.8 Lipid bilayer in cell membrane

Animal cells (eukaryote) are protected by the outer structure called membranes which create the boundaries that separate the cell's contents from its surrounding environments. The membrane has a bilayer structure as seen in Figure 2.8 where two layers of lipid are aligned such that the hydrophilic parts face inside of the bilayer while the hydrophobic parts face outside. The major lipids found in membranes are phosphatidylcholine whose structure is shown in Figure 2.9. Glycolipids and

glycoproteins are strongly adhesive (via hydrogen bonds) to water part of the inner and outer cell environments, assisting the cell structure to retain. Proteins are attached to the bilayer and take part in several interactions – e.g. function as channels for controlling transportation of molecules in and out of the cell, as receptors for different enzymes. The polarity and electrical potential difference across the membrane are designed to allow the exchange of ions through the cell. Energy storage and cell communication are also fundamental roles of membrane lipids. Some organelles within the cell are also surrounded by membrane, for example, mitochondria (double-layer membrane with the internal layer responsible for energy conversion and storage), lysosome (single-layer membrane with a receptor at its surface for as binding site for specific proteins/nutrition/toxins/dead cells which can then turn into small bag of phosphatidylcholine vesicles to be digested by the associated enzymes). In neurons, the membrane at the axon can send signals via electrical transmission to trigger neuronal activity and hence communication between cells. Note that local lipids in the membranes are associated with specific types of proteins that perform different tasks. Therefore, the lipid contents could potentially be used to suggest main functionalities and types of biological cell/tissue. Extracellular matrix also consists of various biological molecules. In order to analyse all these complex biological components, mass spectrometry can be employed.

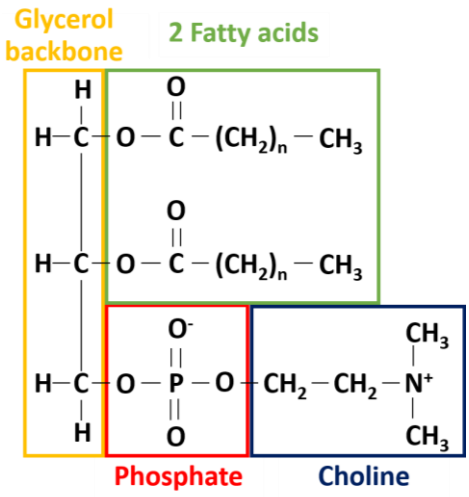

Figure 2.9 Phosphatidylcholine structure

Phosphatidylcholines consist of 2 fatty acids structured as hydrocarbon chains (hydrophobic tails) attached to the acyl groups. Both fatty acids are linked to the glycerol backbone which links to a phosphate that carries the hydrophilic choline head group. Each part of the phosphatidylcholine structure is marked in Figure 2.9 with different colours.

2.3.3 Lipid Extraction Techniques

An extraction method using chloroform and methanol has been widely used in several applications due to its simplicity and robustness. Chloroform, methanol and deionised water in an appropriate ratio can be added to a biological compound to allow lipid extraction with no need to heat or evaporate the sample (Bligh and Dyer, 1959). Chloroform and lipids form a solution that sets itself apart from water, methanol and other polar substances in the mixture which is seen as a separated top layer. This extraction method requires only a small quantity of sample. In comparison with the previous methods e.g. Dyer and Morton (1956), Folch *et al.* (1957), rapidity of the procedure is maintained but the yield and purity of lipid extracts are significantly improved. Chloroform can be added, followed by adding water to the lipid extracts to repeat extractions until a satisfactory level of purification is achieved. The use of water is to effectively wash the chloroform-based lipid extract, to remove water soluble substances, such as salts. In tissue sample applications, the tissue sample could be blended to facilitate extraction.

Thin layer chromatography (TLC) is a technique to separate components in the lipid extracts based on their mass and polarity properties. Lipids move different distances on a chromatography plate. Note that silica gel is often used as a stationary phase and the chloroform-methanol mixture is a mobile phase solvent. Furthermore, liquid-solid extraction can be applied by dissolving sample compound in different solvents of varying polarity and pH. This allows filtering out the undissolved parts at each step, and hence separation for different compound classes before introducing them into analysis system.

2.3.4 Spectral Analysis (in Lipid Classification)

Mass spectrometry is widely used in proteomic studies, but can also be used for lipidomics. In particular, MALDI is one of the soft ionisation methods that was shown to generate useful ions for qualitative (and some quantitative) analysis of a wide mass range of biological molecules. MALDI-TOF-MS analysis of phospholipids and triacylglycerols by Emerson *et al*. (2010) requires as tiny portion as 1 µl of extracted lipids from beef and egg yolk samples. Mass determination together with structural information can be obtained by performing MS/MS (or MS^n) which is very useful to deal with complex lipid molecules.

Lipidomics covers the structural and functional study of lipids in living cells, and their role in supporting metabolic processes, including interactions between lipids and other fundamental biomolecules – i.e. generic and protein molecules contained in the cells. There are 2 main aspects for lipid mass spectrometry analysis. The classical one is when lipid extracts are separated through appropriate gas or liquid chromatography before being introduced to a mass spectrometer. This is so-called "comprehensive lipidomics analysis by separation simplification" (CLASS) allows selected classes of lipids to be analysed by the mass spectrometer, one at a time (Harkewicz and Dennis, 2011). Whereas another method called "shotgun lipidomics" applies ESI mass spectrometry to the lipid extracts directly (Han and Gross, 2005).

The common shorthand notation for fatty acid (carboxylic acid) isomers can be written as $C:D$ representing *number of carbon atoms : number of double bonds* in the fatty acid components of the molecule. This reduces the complexity of writing the lipid structure as a standard chemical formula. Molecular information about complex lipids can be described by quoting each fatty acid component along with its head group. To add clarity, if D is non-zero in a fatty acid isomer, the symbol n-x or ω-x is used with the x being the numerical order of the first double carbon-to-carbon bond counting from its methyl end (Harwood and Scrimgeour, 2007), e.g. an essential fatty acid, Docosahexaenoic acid (DHA) can be expressed as 22:6 (n-3) means that it has 22 carbon atoms with 6 double bonds in the carbon chain, the first double bond is at ω-3 position – see the structure in Figure 2.7 (c). If there is a double (or triple)

bond between carbon atoms in the molecule, the fatty acid is said to be unsaturated; otherwise, it is saturated. Metabolism rates in the organic tissue are thought to be increased with the degree of phospholipid unsaturation in membrane (Hulbert and Else, 1999). The conformation at each double bond could be either “trans” or “cis” as illustrated in Figure 2.7 (b) which are reflected in the properties of lipid molecules such as polarity, thermal stability. However, current mass spectrometers might not provide enough information to distinguish between these two.

Typical lipids are saturated and have an even number of carbons, as shown in the mass spectrum of lipids from a milk sample presented in Figure 2.10.

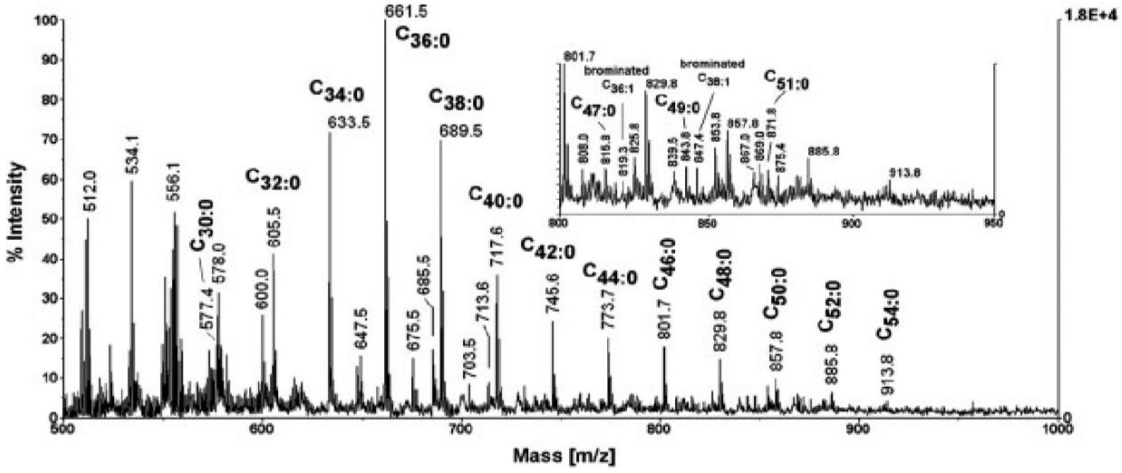

Figure 2.10 MALDI-MS spectrum of milk sample with an expanded view appearing brominated C(36:1) and C(38:1) (Picture from: Picariello et al. (2007))

If the sample is treated with bromine, a brominated lipid would show up in a mass spectrum as a shift in peak with an additional mass per double bond equal to molecular mass of Br_2 of approximately 160 Da and displaying a bromine isotope pattern (Picariello *et al*., 2007). From the mass spectrum provided in Figure 2.10, peaks for brominated C(36:1) and C(38:1) are well illustrated. A determination of double bonds can be done by observing degrees of oxygenation as in a study of unsaturated oils using MALDI-MS (van den Berg *et al*., 2004).

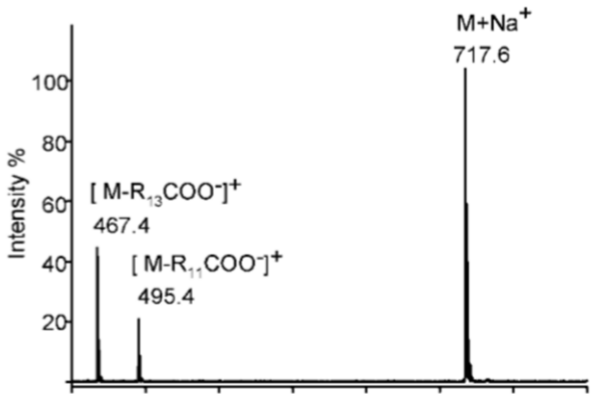

Figure 2.11 MALDI-MS spectrum for triacylglecerol (12:0/14:0/14:0) using positive ion mode (Picture from: Al-Saad et al. (2003))

Loss of the different carboxylate groups during post-source decay (PSD) in a triacylglycerol (TAG) is equally likely. The intensity ratio of the positive ion fragment peaks agree with the stoichiometry of these carboxylate groups in the lipid – i.e. the intensity of the remaining fragment from loss of C(14:0) is twice as much than loss of C(12:0) following the spectrum in Figure 2.11, at m/z 467.4 and 495.4, respectively. Therefore, the relative intensities of the fragments can be used to determine the relative abundance of each carboxylate group contained in a molecule (Al-Saad *et al*., 2003). Phospholipids have a phosphate head group attached to more than one carboxylate tails. The phosphate groups are components of the polar part of phospholipids. Al-Saad *et al*. (2003) also reported that only the fragmentations of polar heads occurred with the protonated phospholipids whereas salted phospholipids rather showed other fragmentations of the molecular structure as well.

2.3.5 Limitations and Challenges

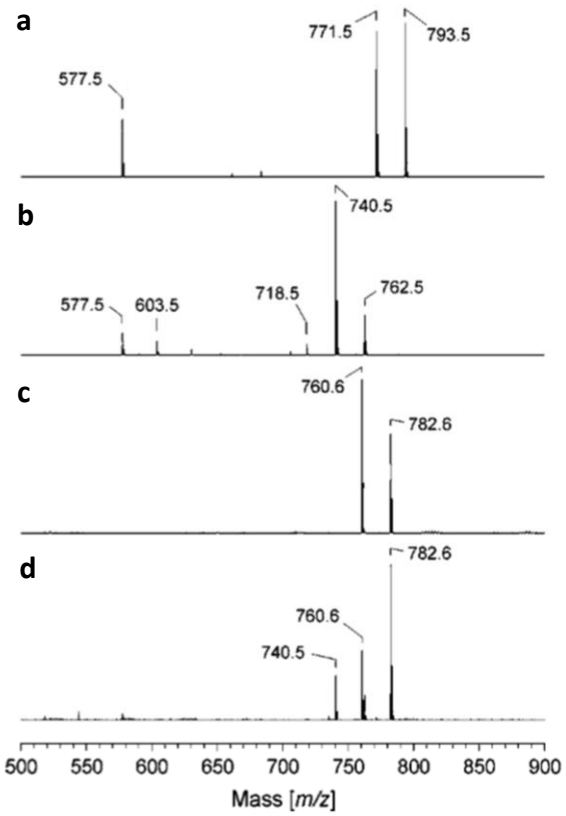

Figure 2.12 MALDI-MS spectra of phospholipids samples (a) 1-palmitoyl-2-oleoyl-sn-phosphatidylglycerol, (b) 1-palmitoyl-2-oleoyl-sn-phosphatidylethanoamine, (c) 1-palmitoyl-2-oleoyl-sn-phosphatidylcholine, and (d) mixture of equal fractions of these 3 lipids with DHB matrix, acquired using positive ion mode (Picture from: Fuchs et al. (2009))

In phospholipids, the phosphatidylcholine (PC) head group can cause severe signal suppression to fragment ion signals of other head groups, especially in phosphatidylethanolamine (PE) which is also commonly present in biological compounds (Emerson *et al.*, 2010). The spectrum presented in Figure 2.12 (d) shows the suppression effect of PCs acting on PEs and phosphatidylglycerols (PG) when the PC:PE:PG lipid mixture mass spectrum was acquired. This was compared to each individual mass spectrum of PGs, PEs and PCs in Figure 2.12 (a), (b) and (c), respectively, in a positive ion mode. For example, all m/z peaks appeared in Figure 2.12 (a) and in Figure 2.12 (b) apart from m/z 740.5 were not observed in the mixture mass spectrum. The negative molecular ions of PC cannot be detected using MALDI-MS (Al-Saad *et al.*, 2003). The negative ion mode is then favored for a detection of PE and PG which is normally suppressed by the PC in positive mode arrangements. Paranitroaniline (PNA) as a matrix substance would give non-acidic environment that enhances the detection of the negative molecular PE ions (Fuchs *et al.*, 2009).

Matrix and analyte suppression effects occur in the presence of significant amounts of salts as they also give rise to positive ions (Lou *et al.*, 2009). In MALDI-MS

experiments, alkali metal salts of proteins can be washed after depositing samples onto a target in order to minimise the chemical background noise they caused (Smirnov *et al.*, 2004). This might be applicable to remove lipid salts as well.

Nowadays, interest in lipidomics seems to be growing as lipid metabolism can diagnose cellular dysfunction (Pirman *et al*., 2013). However, due to the complexity of lipid analyses, there is relatively little research leading to a lower availability of lipidomic databases compared to that of proteomics. There are many classes of lipid occupying a wide mass range and the MS analysis is difficult to do at high masses. However, mass spectrometry technology is continuously evolving. MS/MS analysis of lipids with a mass resolution of greater than 30,000 can be achieved using a quadrupole mass analyser to select lipids at an increment of 1 Da to pass to a CID system and then proceed through a time-of-flight mass analyser for final mass analysis (Simons *et al.*, 2011). The "LIPID MAPS Lipidomic Gateway" website (http://www.lipidmaps.org/) is a good resource for lipid identification whose information is based on lipid classification studies as updated in 2009 by Fahy and coworkers which provides a database of lipid structures and MS peaks of all lipid classes. This has been reviewed every year. Nevertheless, numerous variations in hydrocarbon chain length and bonding could cause a lot of confusion to mass spectral analysis of large lipids (Fahy *et al.*, 2005). Therefore, careful TLC or gas chromatography separation methods are needed for full resolution.

2.3.6 Lipids in the Brain

As discussed earlier, a variety of lipids are found in biological cells as structural and functional components. Brain tissues in general have very high lipid concentrations. Lipid types and distributions should be consistent in normal brains in order to perform their proper activities. Therefore, unusually distributed lipids in some parts of the brain may link strongly to diseases, disorders and damage. Quantitative imaging is therefore a powerful tool to investigate pathological changes giving

biochemical composition as well as anatomical information. Uses of MALDI imaging will be discussed in Section 2.4.

There are similarities between human and rat brains that make a rat brain a reasonable model for the study of brain disorders relevant to humans. Since the 1960s (Bayer *et al*., 1993), it was confirmed that human and rat brains show very close correlation with processes of central nervous system (brain and spinal cord) development since their embryonic stages. Where same developmental stage occurs in the same order but at different time scales. They described details of brain structure as a result of cells/neurons generations, tissue formations at different parts of the brain. The appearance of human and rat brains have similarities as seen in the pictures provided in Figure 2.13.

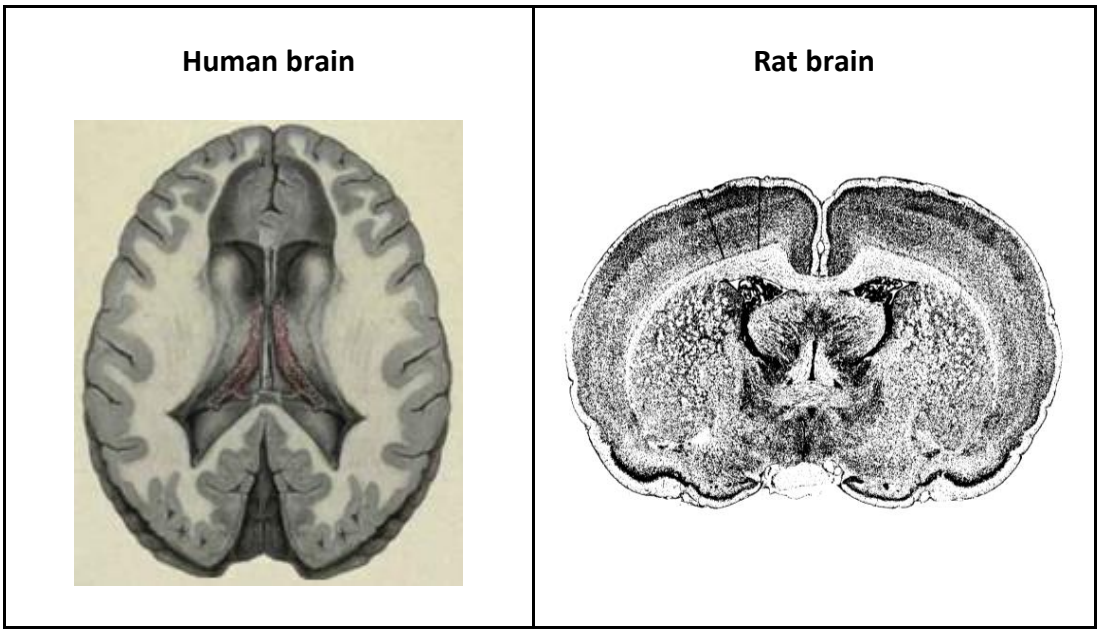

Figure 2.13 Coronal section of Human vs. rat brains (Pictures from: Davis (1913) and Bennett et al. (1964), respectively)

From these correlations during early brain development, they are believed to show comparable pathological and physical changes in response to brain diseases. Rat brains can be modified to better mimic human brain diseases by altering parts of brain either in terms of biochemical composition and/or physical degradation.

2.4 Mass Spectrometry Imaging for Lipid Analysis

Mass spectrometry imaging (MSI) allows MS information to be represented as an image, mapping distribution of analytes in each of its pixels in correspondence with the spatial positions on the actual sample. Hence, applications can be in structural observations of biological molecule distributions in tissues and their change due to pathological conditions. MALDI-MS imaging is widely used to image drug and drug metabolite distributions as well as peptides, proteins, and lipids which is the main emphasis of this section, will be extensively discussed in Section 2.4.3.

2.4.1 General MS Imaging Instrumentation

A simple microprobe MSI controls the trajectory of the laser beam relative to spatial coordinates of the plane of the sample either by moving the laser beam across the sample area, or vice versa. A series of mass spectra is recorded at each point in space. The size of the focusing beam influences the spatial precision (McDonnell and Heeren, 2007). The number of scans per dimension determines the spatial resolution. In contrast, microscope type MSI collects both MS and spatial coordinate data at a position-sensitive detector. This allows measurement without the need to determine the location at which each MS spectrum is acquired in the initial stage.

2.4.2 Understanding the Mass Spectrometry Imaging Data Formats

All mass spectrometry images in this work were acquired using a Shimadzu 7090 TOF^2 mass spectrometer (Kratos, Manchester). Each image data set was exported as two separate files, with filename extensions: .imzML (hundreds of Mb) containing the header information, and the accompanying .ibd (few Gb) which containing the spectral information acquired at each pixel. This is one of the standard formats for

MS image used in commercial instruments. Other major formats include mzXML, mzML, RAW, Analyze 7.5, ASCII and HDF5. Data sets are convertible among these available formats but it is important to know the data structure or to have conversion software to enable analysis. The MS image data can be thought of as contained in a cubic matrix format. The diagram drawn in Figure 2.14 illustrates the typical components of an MS image data set including: 2-dimensional pixel locations i.e. x-pixel and y-pixel, specifying a spatial location on the imaging plane where a mass spectrum was recorded and the number of mass-to-charge (m/z) bins determines the length of the 1-dimensional mass spectral array holding the intensity value at every m/z.

Both mass resolution and spatial resolution are factors influencing the MS image size. Reducing these could arise from parameter adjustment either during or post acquisition. Most of the time, mass spectrometry imaging data are usually acquired by selecting maximum mass and spatial resolutions available for the instrument, given a reasonable acquisition time taken. Believing that the higher acquired resolution provides higher quality information, is not always the best approach in terms of data interpretation for several reasons. For example, there will be an enormously large data set to process, and this requires long calculation time which scales linearly with the data size. Increasing numbers of data points in both mass and spatial dimensions can raise peak-to-peak / pixel area overlapping which can introduce additional source of noise into signal. If the acquiring step (pixel size) is set smaller than the laser diameter, the acquired area will overlap between pixels. The signals would degrade and become inconsistent as the matrix in the acquired area has been used unevenly.

A simple approach to solve these problems is to fix the data after acquisition with some appropriate pre-processing to reduce the data size. In the mass dimension, this is conventionally done by directly reducing the mass resolution by combining adjacent bins and/or filtering to keep only the main peaks with strong signal amplitude. Similarly, in the spatial dimension, adjacent pixels can be combined into a larger pixel obtaining a coarser spatial structure throughout the image with

improved signal quality at each pixel. Clearly, poorer spatial resolution is achieved since pixels are combined.

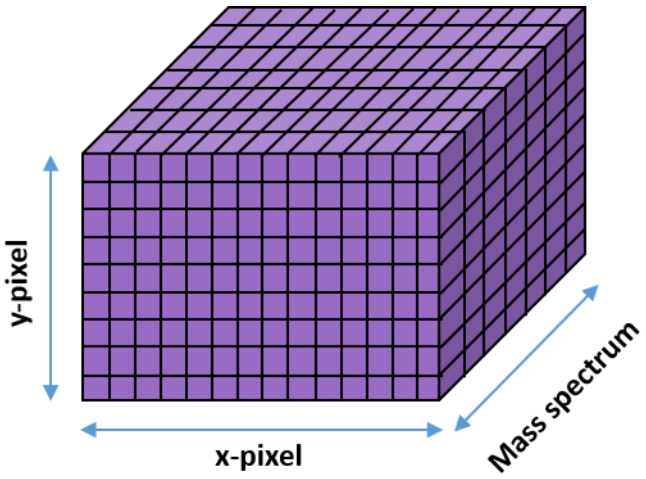

Figure 2.14 Diagram for mass spectrometry imaging data structure

2.4.3 MALDI-MS Imaging of Lipids

Lipids are important in biological systems, and it makes more sense to observe lipid distributions in tissue samples. This can be done by mass spectrometry imaging (MSI). Using either microprobe or microscope methods (see Section 2.4.1), mass spectra at particular spatial locations can be obtained. For each mass-to-charge ratio of interest, a map of ion distribution within a tissue slice is acquired. A diagram outlining the steps required to obtain MALDI-MS images of tissue samples at a specific m/z values is shown in Figure 2.15. Results from all slices of tissue can be combined to create a 3-dimentional MS image. Note that a tandem MS mode can be applied using collision induced dissociation for more specified molecular information (Steven and Bunch, 2013).

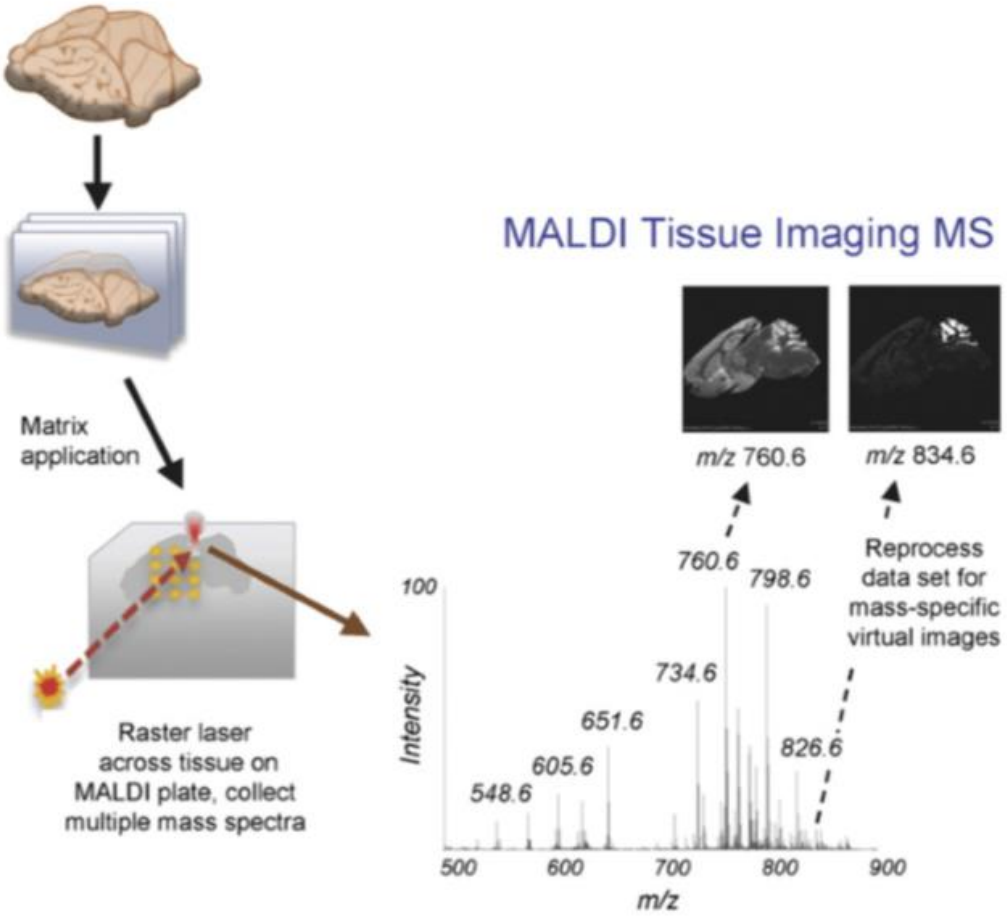

Figure 2.15 MALDI-MS imaging steps
(Diagram from: Murphy and Merrill (2011))

Matrix must be carefully applied such that it deposits uniformly with suitable thickness over the thin section of sample. The application methods range from using airbrushes (which are hand-held apparatus and therefore difficult to control uniform spread of matrix solution), TLC sprayers, inkjet printers, oscillating capillary nebulisers (which usually have a moving nozzle that enable automatic application of matrix with selected parameters, e.g. rate of application, number of layers) or sublimation methods (which give the most uniform and smallest matrix crystals) (Zaima *et al*., 2010), or other purpose designed instrumentation.

Mouse brain contains significant lipid concentrations with the main types being phospholipids, sphingolipids and glycerolipids (Murphy *et al.*, 2009). Murphy *et al.* (2009) observed concentrations of potassiated PC(16:0a/16:0) to vary from pixel to

pixel over the tissue section. The quantitative representation of the PC distribution as the relative intensity level of each pixel in the MSI image at m/z 772.5 is seen in Figure 2.16.

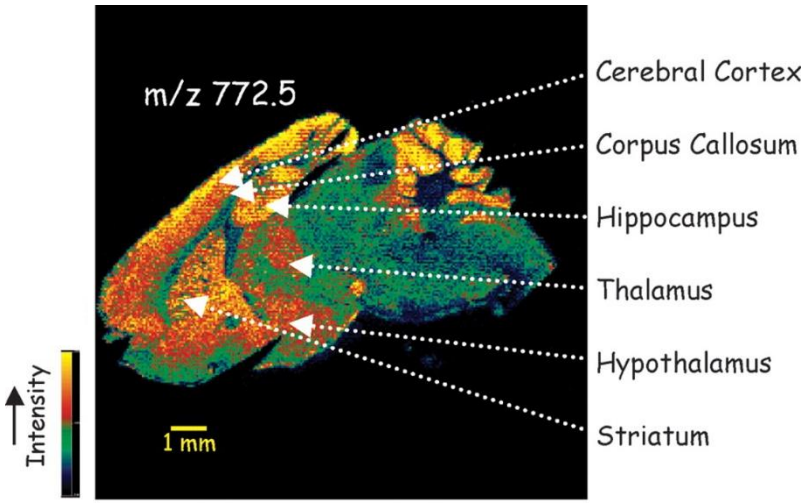

Figure 2.16 A mass spectrometry image indicating potassiated PC(16:0a/16:0) distributions for sagittal slice of mouse brain with labels of brain parts (Picture from: Murphy et al. (2009))

Deterioration of the brain can be involved in various diseases which decrease capabilities to carry out normal lipid metabolism at specific brain regions (Adibhatla *et al.*, 2006). Lipid MSI analysis can be performed at a target brain region to trace for the abnormalities. Alzheimer's disease (AD) is a common brain diseases in the elderly which can cause serious neurodegeneration. It induces abnormal lipid metabolism in the central nervous system where a variety of lipids in the tissues are involved in neurotransmission. Mass spectra hold molecular phenotyping information. If this information was extracted, it could yield better understanding of the physiology and pathology with respect to the anatomical structure, and help suggest disease stages. However, the accuracy of the spatial mapping is subject to imaging resolution. Also, sufficient concentrations of analyte must be present at a location to be detected by MS imaging. Veloso *et al.* (2011) carried out research on real human brain samples and studied particularly the lipid distributions of the central nervous system. The hippocampus is a part in the central nervous system (located at the prosencephalon

of the brain) one of the primary sites attacked by Alzheimer's (Mu and Gage, 2011). For hippocampus MSI, to 100 µm imaging resolution was required due to the complexity of the structure (Veloso *et al.*, 2011).

2.4.4 Other Mass Spectrometry Imaging Techniques

The key mass spectrometry ionisation techniques used in tissue imaging beside MALDI, include secondary ion mass spectrometry (SIMS), desorption electrospray ionisation (DESI) and laser ablation electrospray ionisation (LAESI). The main features and typical parameters of these techniques according to Bodzon-Kulakowska and Suder (2016) are summarised in Table 2.3 below.

Table 2.3 Comparison of mass spectrometry imaging techniques (Reproduced from: Bodzon-Kulakowska and Suder (2016))

Technique	Ionisation source	Soft/ hard	Analytes	Spatial resolution (µm)	Upper mass range (Da)
SIMS	Ion gun	Hard	Elemental ions, small molecules, lipids	< 10	1,000
DESI	Solvent spray	Soft	Small molecules, lipids, peptides	100	2,000
LAESI	Mid-IR laser beam, solvent spray	Soft	Small molecules, Lipids, peptides, proteins	200	2,000
MALDI	UV laser beam	Soft	Lipids, peptides, proteins	20	100,000

SIMS has an advantage of spatial resolution over other techniques, allowing cell imaging applications (Passarelli and Ewing, 2013). However, its hard ionisation due to the energetic incident ion beam causes fragmentation to larger molecules, hence the acquisition is limited to only some smaller analytes. In contrast, MALDI ionisation is soft which specifically is good for ionising intact biomolecules up to a very high

mass, and can still preserve a reasonably good spatial resolution if coupled with a laser source of small diameter.

DESI is an adaption of ESI used for imaging, works by introducing electrospray droplets to carry away analytes from a sample surface (Takáts *et al.*, 2004). It can produce cleaner mass spectra compared to those acquired by MALDI because of the expected greater stability of the technique (where there is no need to deal with the variability due to matrix and laser). Another adaption to DESI called nano-DESI, which uses two very thin separate capillaries, one for delivering the solvent to contact on the sample surface, and immediately, another one for transportation and electrospray ionisation of the analyte solution. This technique resulted in a factor of 10 - 20 improvement on the spatial resolution, e.g. Laskin *et al.* (2012). LAESI requires two steps to allow ionisation; the mid-IR laser is fired locally onto a sample, allowing extraction of analytes via evaporation of existing moisture on the sample, which then undergoes ESI (Nemes and Vertes, 2007). Less precision in spatial location can be achieved compared to DESI. With DESI, and LAESI, the main limitation is that multiply charged ions are largely generated for molecules of higher mass as is normally seen in ESI; therefore, the technique are efficient when observing smaller biomolecules.

Chapter 3

Background II:

Quantitative Mass Spectrometry

This chapter sets out the general scope of quantitative mass spectrometry, outlining the challenges and conventional approaches used (see Section 3.1). Some common computational methods (pattern recognition) are described in Section 3.2, with examples of their uses in analysing mass spectrometry data discussed. The other approaches of clustering and linear component decomposition specific to MS imaging data analysis are discussed in Section 6.1.3 of Chapter 6. The background specific to the analytical approach used in Chapters 5 and 6 of this thesis is described in Section 3.3 and Section 3.4. Together, this demonstrates a new, alternative approach to data analysis that comprises an error model that is especially important for addressing a number of scientific questions.

3.1 The Scope of Quantitative Mass Spectrometry

Mass spectrometry has been used by a range of scientific disciplines as a technique to acquire information on a variety of molecules within a range of sample types. The technical development of today's spectrometers is based on research in a number of fields, particularly, in chemistry and particle/atomic physics. The development of mass spectrometry led to the discovery of isotopes – i.e. Francis William Aston received a Nobel Prize in Chemistry in 1922, for the development of the mass spectrograph (early mass spectrometer) which led to consequent discovery of many isotopes. An example of MS use in biological sciences is the use of stable isotope tracers such as ^{13}C-enriched tracer. The investigation of isotope ratios, e.g. $^{207}Pb/^{206}Pb$ can help predicting the age of a planet, hence the application of MS to geology. Many other applications lie in applied fields such as medical, pharmaceutical, forensic, and food sciences. More routinely, the technique is often used in industry for routine quality control and contaminant assessments.

Improvement of the method and the development of new techniques are ongoing. In whatever application, the method of analysis, experimental protocol, and analysis of results, must be optimised. Huge amounts of information are contained in a single MS acquisition – i.e. ion counts at every mass-to-charge value within a selected mass range are recorded. Therefore, it is important to extract as much relevant information as possible from within a data set to get the most out of an experiment.

Mass spectrometry analysis may be divided into qualitative and quantitative approaches. Qualitative analysis aims only on detecting the presence or absence of analytes of interest whereas quantitative analysis provides also numerical quantities, such as relative or absolute concentrations. For example, qualitative analysis could answer the question like "Which drug metabolites can be observed in a sample?" Quantitative analysis can answer questions like "Is the concentration high enough to be toxic?" Quantitative analysis allows the estimation or prediction of some mathematical model parameters. In addition, for completeness of scientific interpretation, the errors associated with the measurement must be quoted to

determine the level of reliability of the data. Statistical analysis should then play an important role in data interpretation. In order to meet these requirements, this thesis presents a new approach to mass spectrometry data analysis called linear Poisson independent component analysis (LP-ICA) which is demonstrated in Chapters 5 and 6. This approach is based on a quantity estimation of ions generated on mass spectra, with a statistical error model (see Section 3.4). The results of quantitation can then be extracted in terms of proportional quantities associated with the underlying complex mixtures within samples of interest from either non-imaging or imaging data sets. This can be applied in many quantitative problems, including relative quantitation covered in this work and absolute quantitation which will be discussed in the suggested future work, see Section 7.3 of Chapter 7.

3.1.1 Problems in MALDI-MS Quantitation

Quantitative analyses using MALDI-MS is difficult due to the high variability of ion signals which causes uncertainties in measuring abundance of mass-to-charge information in mass spectra. These variabilities are due to the availability of ions formed in individual MS acquisitions which vary between different regions of the deposited sample under what are apparently the same conditions, largely due to the non-uniform spread of sample-matrix crystals, and even shot-to-shot changes at exactly the same position (Duncan *et al*., 2008). Huge differences are also contributed by different sample/matrix preparation and deposition methods, and the optimal method ought to be carefully selected and defined in a protocol for each experiment, as in Section 2.2.8. These significant influences limit repeatability and reproducibility in MALDI-MS experiments. Mass spectrometrists have, for some time, been seeking methods which could provide more meaningful quantitation in MALDI-MS analysis. Approaches that yield significant improvement in MALDI-MS quantitation include those that compensate for both physical and chemical variabilities in the various processes and should overcome some of the systematic and random errors. Techniques are being investigated based on approaches to sample preparation,

instrumentation, calibration using internal and external standards, and mathematical approaches to data processing and analysis.

An effective plume temperature in the early stages of ionisation is one of the parameters which influences ion yield (Bae *et al*., 2013). The ratio of the fraction of protonated analyte yield to the fraction of protonated matrix yield, is known to correspond to an early effective temperature of the plume. This is because the positive charges from the protonated matrix are transferred in order to ionise the neighbouring analyte molecules during the desorption/ionisation process. Moreover, Bae *et al*. (2013) appeared to find that keeping the plume temperature constant during the desorption/ionisation process improved the stability of the ionisation rate.

The heterogeneity of crystal formation also influences the signal intensity variance. This causes lower signal-to-noise values in regions where there are fewer crystals. In contrast, the optimum signal intensity obtained from a crystalline region might result in saturation of the mass spectrum. An automated system can be used to select only the spectra with appropriate quality – i.e. spectra acquired from single laser shots with satisfactory levels of signal-to-noise, but without saturation (Duncan *et al*., 2008). A collection of these mass spectra that pass predefined thresholds are allowed to proceed into the average or accumulative forms.

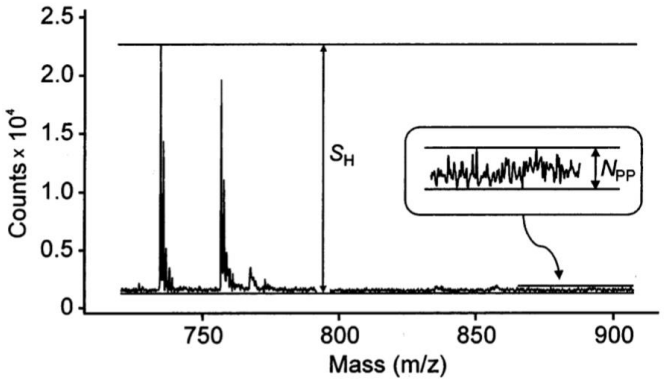

Figure 3.1 Main components of a mass spectrum (Picture from: Müller et al. (2001))

The diagram provided in Figure 3.1 illustrates the main components of a mass spectrum. The peaks represent the associated m/z values that are detected on an MS

sample. The peak's height or relative signal intensity are determined from the ion current. Noise is always generated along with every acquisition, possibly due to chemical and/or instrumental background fluctuations. This can cause random interference with useful signals which affects the ability to quantify mass spectra. Müller *et al.* (2001) defined the signal-to-noise ratio to be

$$\frac{\text{Signal}}{\text{noise}} = 2.5 \times \frac{S_H - 0.5N_{pp}}{N_{pp}} \tag{3.1}$$

Where S_H is the peak height measured from the lower boundary of noise and N_{pp} is peak-to-peak amplitude of noise (as illustrated in the expanded view of the mass spectrum shown in Figure 3.1) measured from the lowest to the highest levels of noise.

3.1.2 Uses of Standards

3.1.2.1 Internal Standards

An internal standard is a selected substance of known concentration added to (and uniformly distributed in) the sample under analysis in order to improve quantitative accuracy of an analyte of interest. A good internal standard should have properties as close to the analyte as possible, allowing it to behave like the original molecules and participate in the same desorption/ionisation events as the analyte but would yield different mass-to-charge peak in the mass spectrum. This is most often achieved using isotopically labelled analyte molecules, where available. A linear relationship is expected between the signal intensity of the analyte normalised to that of the internal standard, and the analyte concentration, seen as the calibration curve in Figure 3.2, given that other experimental conditions are fixed. Hence, the calibration curve yields predictive values of analyte concentration when the analyte/internal standard peak intensity ratio is measured. The signal-to-noise in MALDI mass spectra was observed to increase with analyte concentration (Wilkinson *et al*., 1997). According to Wilkinson *et al*. (1997), two main choices of method can be applied for spectral intensity measurements: 1) linearly average the noise intensity selected from the main informative part of the mass spectrum, eliminate

the averaged noise, and obtain peak intensity via integration, and 2) use the least squares method to fit a local package of spectral peaks at each molecular mass, including the protonated molecular ions, dehydrated molecular ions, and might include metastable decay products and salted molecular ions.

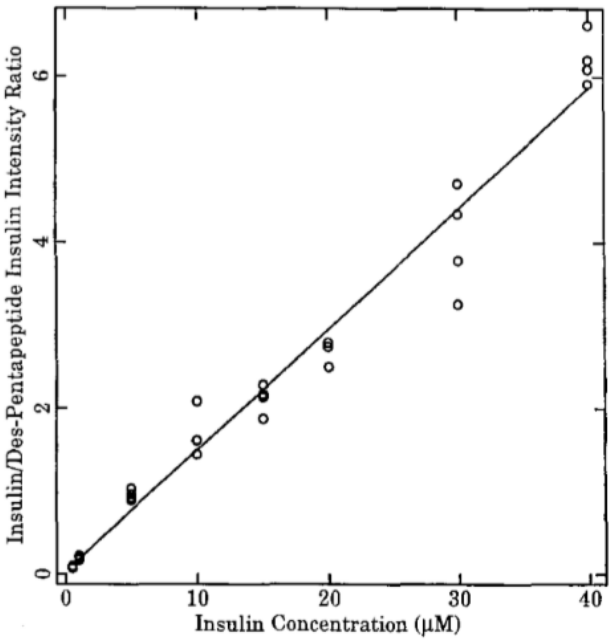

Figure 3.2 Calibration curve for insulin where the internal standard is des-pentapeptide insulin (Graph from: Wilkinson et al. (1997))

The use of isotopic labelling for internal standards works efficiently on lighter molecules (<500 Da) where labels of ≥3 Da are ideally used (Duncan *et al*., 1993). This should generate a distinctive peak outside the distribution of natural isotopes of the original molecules. Available techniques such as isotope-coded affinity tags (iCAT), stable isotope labelling of amino acids in cell culture (SILAC) and isobaric tag for relative and absolute quantification (iTRAQ) are currently in use in quantitative proteomic mass spectrometry research. The techniques could be used to generate biomarkers for diagnosing and staging of diseases (Hultin-Rosenberg *et al*., 2013). For example, iTRAQ is a technique to label the amino acid lysine by attaching an "isobaric tag" to its amine functional group (Hultin-Rosenberg *et al*., 2013). Isobaric tags of almost the same mass are added to different samples to label the same peptide, with apparently the same MS characteristics for mixed sample, but will show distinct

features in MS/MS for low mass fragments (Unwin, 2010). During MS/MS, an isotope "reporter" is fragmented from a labelled molecule of each isobaric species, resulting in separate signals in the MS/MS spectra that allow for relative quantification of the same peptide in each sample following the analysis described by Thompson *et al*. (2003) and the absolute approach as explained in Ross *et al*. (2004).

3.1.2.2 External Standards

An external standard is a chemical with a m/z value selected to match an analyte of interest within the analysing sample. The external standard is prepared at different concentrations in the range that the concentration of the analyte of interest is expected to be in the sample. To construct a calibration curve, the measured ion current at the specific m/z is plotted against its known concentration for a linear least square fitting. Then, the unknown concentration can be determined from its correlation with the observed ion current at the m/z of interest. Note that a series of m/z values can also be observed using the corresponding chemicals as external standards for more robust control over a wide mass range.

3.1.3 Conventional Peak Analysis

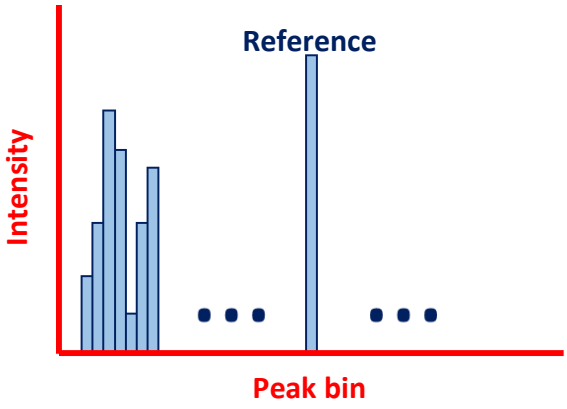

Figure 3.3 Peak detected mass spectrum: A reference peak is selected for peak analysis

Peak analysis methods have been used for quantitative spectroscopy analysis. The method involves some sort of normalisation – i.e. against total spectral intensity or

reference peak intensity. However, lack of signal-to-noise and repeatability problems would result in inaccurate measurements, especially for MALDI mass spectra.

In this work, this single peak analysis approach is used as a conventional method to compare with the linear Poisson ICA method. Where the intensity ratio of a single peak bin to the reference peak is calculated in every mass spectrum in the data set and will be used to quantify the components of the material analysed. Note that the same pre-processing steps (Section 3.3) as for linear Poisson ICA were applied prior to this analysis. Only strong signal peaks with intensities above the noise level will remain in the spectral data set, as ensured by the peak detection (Section 3.3.4). A diagram given in Figure 3.3 illustrates the peaks detected in the mass spectrum with a reference peak selected for relative quantification.

A reference peak should be selected at a peak bin that appears consistent across all spectra in the data set. The peak would be assessed to have relatively no correlation between its signal intensity and the corresponding sample proportions. Usually, one of the largest peaks would be chosen, firstly for stability of intensity values, and secondly for reasonable ratio representation. For example, the appropriate reference peak chosen for every MALDI-MS data sets in Chapter 5 was at m/z 760.5 $[PC(16:0/18:1)+H]^+$ (Deepaisarn *et al.*, 2018). An alternative strategy can be the use of the integral over all data bins as a normalisation factor, e.g. in Chapter 6, which should be a more consistent choice across a large data set, particularly for imaging.

Loss of generalisation is introduced by selecting the one peak, known to be most correlated with the ground truth proportion of the underlying sample components to represent the quantitation of the whole spectral set. In other words, the conventional analysis only relies on a specific molecule.

One of the main problems in conventional MS peak analysis is that natural salt ions (e.g. Na^+, K^+) exist in biological samples and there is no perfect way to purify such samples, especially in imaging experiments. Hence, variation in mass spectral signal intensity between sample deposits, or even between repeat measurements of same sample deposit may be location dependent. The analysis of a single peak is therefore not necessarily advisable when various salted species of the same molecule

contribute to the recorded signals, sharing the signal intensities between those peaks with uncertain proportions.

3.1.4 Supporting Software for Mass Spectrometry Data Analysis

The MALDI-TOF-MS instrument used at the Wolfson Molecular Imaging Centre (WMIC), the University of Manchester is an AXIMA CFR+ TOF^2 model from Kratos (a Shimadzu group company). This instrument has been upgraded to have a 200 Hz laser, effectively making it equivalent to the more recent "Performance" model of instrument. The manufacturer's "Launchpad" software allows selection of positive-negative ion, linear-reflectron, MS, MS/MS, MSI modes with ranges of parameter adjustments, including laser properties, mass range, data processing properties, etc. These primary set-ups allow the users to perform a variety of experiments and to acquire the optimised data with the selected sample-matrix types. However, both experimental results and data analysis processes can be optimised with support of other related software and the semi-automated enhancement of mass spectra is possible with the aid of coding.

MATLAB is a widely used software for statistical and data analysis. As a high-level programming language, it allows simple coding. Also, it is convenient and easy to use for handling and accessing data. It can be designed to suit custom demands with the ability to create graphical user interface format programmes. Moreover, MATLAB has special sets of built-in algorithms called the "bioinformatics toolbox" which provides several useful functions to improve spectral analysis such as baseline subtraction, peak detection, etc., and the "image analysis toolbox" which can be applied for MS imaging (http://uk.mathworks.com/products/bioinfo/; White *et al*., 2005).

In mass spectrometry imaging applications, mass spectral data match spatial voxels to form graphical images of signal distribution throughout the sample (Parry *et al*., 2013). Ranges of software designed for displaying, processing and analysing mass spectrometry imaging data are available to users as open sources e.g. Biomap (https://ms-imaging.org/wp/biomap/), MSiReader (Robichaud *et al.*, 2013; Bokhart

et al., 2018), OpenMSI (https://openmsi.nersc.gov/), or commercially e.g. SCiLS Lab (Bruker). Biomap allows basic interpretation of MS imaging data, including single ion images, averaging of mass spectra in a region of interest. MSiReader (Robichaud *et al.*, 2013; Bokhart *et al.*, 2018) is a Matlab based programme which features conversion between image formats, pre-processing, pixel interpolation, etc. However, the data uploading speed is slow and the computer memory can be a problem for large data files since the data are loaded into a spreadsheet. OpenMSI (Rübel *et al.*, 2013) allows fast data management on a web-based interactive environment, with an interactive view tool function which can represent distribution of 3 different ions on RGB (red-green-blue) image at a time. There are vast number of contributors globally. The commercial software, SCiLS Lab (Bruker) can perform some more sophisticated functions including, correlation analysis, spectral analysis, classification of data, etc.

Available software is easy to use but access to the algorithms that drive the tool is limited. Therefore, it is very difficult to know exactly what the software does to process the data and made worse by the many versions of updated software released. Furthermore, quite often a Gaussian assumption of statistical errors is made (without prior assessment of data). Frequently this is done for the sake of algorithm simplification. There is still a gap that appears common to all available tools, which is the statistical errors in quantitation are not provided. A statistically appropriate chemometric analysis method would be required to solve this matter properly.

3.2 Computational Analysis Methods for MALDI-MS Data

This section gathers together some of the relevant computational methods for data analysis that have been chosen by mass spectrometrists to analyse and report their mass spectral data, particularly in imaging MS. A summary of the methods' basic descriptions and general applications are discussed.

3.2.1 Data Mining

Big data analysis has become one of the topics frequently talked about in the information context including management and interpreting of data in the sciences and social sciences. Currently in scientific research, real-world data generated by state-of-the-art instruments tend to be provided at an increasing size and rate promptly delivering the most relevant available information for studies. The data is therefore 'big' in terms of the amounts and variations in data. This means a lot of hidden information may be there to be extracted. Powerful tools are needed to deal with this aspect properly, to identify useful components and properties of the data.

Modelling tasks for such big data are certainly difficult and require either huge or complicated efforts to sort out specific problems. The techniques for organising data systems and selecting methods to find the optimal solutions that satisfy the question of study, are generically called 'data mining'. Where modelling tasks range from classification, regression, outlier detection, to correlation analysis, data mining can be employed to build an appropriate method which allows multiple types of analysis to uncover hidden information.

***Unsupervised learning*:** By looking into unseen data, features (i.e. unique properties) can be discovered that explain groups, clusters or trends contained in the data set, without prior knowledge.

***Supervised learning*:** A training data set of annotated samples is given. The training data set will contain some associated values to train a computer to perform specific tasks based on meaningful operations as justified in the training. For example, a data set that is known to carry some number of categories and individual samples (already determined as belonging to a particular category) can be utilised to train a classifier that can then perform classification when applied to a new data set.

3.2.2 Computational Approaches

The following computational approaches can be categorised as pattern recognition techniques, which are generally used in machine learning in various applications, e.g. to handle multivariate problems, including MS data analysis. Basic descriptions of these approaches including support vector machines, nearest neighbours, random forests and neural networks are given below. Other machine learning methods, particularly clustering approaches are important in terms of their application on MALDI-MS imaging analysis – i.e. classification and subsequent segmentation. They will be detailed in Section 6.1.3 at the introduction to the imaging experimental Chapter 6 where data analysis approaches for MALDI-MS imaging are compared specifically. Statistical multivariate analysis approaches that involve extraction of linear spectral components (which allows spectral quantitation aimed in this work) are also discussed in Section 6.3.1 with comments on data assumptions.

3.2.2.1 Support Vector Machine

The support vector machine (SVM) was developed as a classifying tool. The method attempts to find the hyperplane that maximally separates the margin of classes in the data in a multidimensional space, where the margin is defined as the (perpendicular) distance from a hyperplane to the closest data point on each side of that separating plane. For a data point, separation from the plane can be written as the function g defining a linear SVM in Equation (3.2).

$$g_{\boldsymbol{w},\boldsymbol{b}}(\boldsymbol{x}) = y(\boldsymbol{w}^T\boldsymbol{x} + \boldsymbol{b}) \tag{3.2}$$

Given that $y'(\boldsymbol{w}^T\boldsymbol{x} + \boldsymbol{b}) \geq g$ for all other data points. The above equation can be normalised by a factor of magnitude $\|\boldsymbol{w}\|$ for vector $\boldsymbol{w}$. This would give the distance from the hyperplane in terms of a unit vector. Therefore, a minimum $\|\boldsymbol{w}\|$ is needed to represent the maximum distance and thus the optimal SVM classifier. Corresponding values for each data point, $\boldsymbol{x}$ can be calculated using $y(\boldsymbol{w}^T\boldsymbol{x} + \boldsymbol{b})$. Note that y indicates the positivity and negativity of a data point according to its side of the hyperplane.

To analyse data with more complicated features (physical properties), a non-linear transform of the linear expression above for each data point, $\boldsymbol{x}$ can also be achieved by multiplying an appropriate kernel of a higher-degree function by the first term in y in order to define more precise boundaries between classes of data.

3.2.2.2 Nearest Neighbours

"k-nearest neighbours" is probably the simplest method amongst all the methods which will be discussed in this section. When data are plotted in a vector space, data might be expected to spatially cluster according to their common properties. A data point of unknown class/value should be more likely to belong to the same class as its nearest neighbour (the data point that is located closest to it). Considering some number of nearest neighbours, k, greater than 1 reduces the effects of noise from measurement. However, a large value for k can lead to problem of regularisation (when trying to fit a model to all data points) if non-relevant data points are taken into account. In classification tasks, the unknown variables take the mode class of the k-nearest neigbours. In regression tasks, the mean distance from an unknown point to the k-nearest neighbours is normally observed, Euclidean distances are measured.

Although the method works with supervision, there is no need to model the data to predict unknown variables. The only parameter that can be freely adjusted is k. This ease of use can be a benefit, but also a problem, as the parametric optimisation is too limited. Sometimes, when the distance relies mainly on a few variables, where there are huge differences in the range of values, appropriate normalisation or weighting techniques can be applied. This is rarely discussed in the literature and there is no definition of the statistical principle involved in training the algorithm.

3.2.2.3 Random Forest

A random forest is a decision tree based method which is used to solve various machine learning problems. A good decision tree should optimally separate samples according to the distinctiveness of their features/variables. In supervised learning,

the method is validated by correctly identifying or estimating labelled samples in the training set. Hence, the prediction in the testing data set is used to decide between logical design choices. The algorithm is relatively fast to operate, therefore, many individual decision trees can be constructed for randomly selected subsets of data to achieve satisfying accuracy with the combined trees, or a “random forest”. The method is very popular, particularly as a great tool for classification, because of its flexibility. It applies little constraints on parametric assumptions of the data compared to other methods, which could simply allow non-linear analysis without adding much complexity to calculation. Random forests can also provide fair solutions to regression problems but are quite limited, as they lack of some important statistical assumptions and may introduce problems due to the model’s randomness. For example, there may be a problem of overfitting the data, or that there is not enough data to train an appropriate regressing estimation.

Random forests have a large application base, extended to dimensionality reduction by ranking the features of data and discarding insignificant ones. Shi and Horvath (2006) has also introduced a use of (semi-)unsupervised random forest where Monte-Carlo sampling is used for training, providing unknown classes.

Random forests use votes and mean values to predict, discrete and continuous variables, respectively. Whist clustering data samplings, optimal performance for each decision tree is achieved when the minimal variance within a cluster, but maximal variance between clusters are achieved. Significant tests used with the method are based upon approaches such as chi-square, analysis of variance.

3.2.2.4 Neural Networks

The concept of the (artificial) neural network is to mimic the some aspects of structure and connectivity of human brain, to learn based on information received and to make decisions on unseen scenarios that comprise similar features. The computer system aims to extract knowledge from training data, and can be used to solve problems like classification, clustering or regression. In order to build a neural network, a number of neurons are connected between layers and define processing

of the input variables with some form of activation function in order to generate outputs – e.g. classified data. The diagrams presented in Figure 3.4 show the structure of a single neuron and a multiple-layer neural network system. A classical neural network equation is given below.

$$h_{\boldsymbol{W},\boldsymbol{b}}(\boldsymbol{x}) = f\left(\sum \boldsymbol{W}^T\boldsymbol{x} + \boldsymbol{b}\right) \tag{3.3}$$

Where an input vector $\boldsymbol{x}$ mathematically expresses underlying feature elements of the weighting factor $\boldsymbol{W}$. As a result of the activation function f, the output h from a layer provides the inputs for the next layer's "neurons". The final outputs are obtained after propagation of these "signals" through all layers in the neural network. $\boldsymbol{b}$ is a bias (intercept) term, allowing for flexibility of the model to fit the data. Inputs and outputs take values of continuous variables.

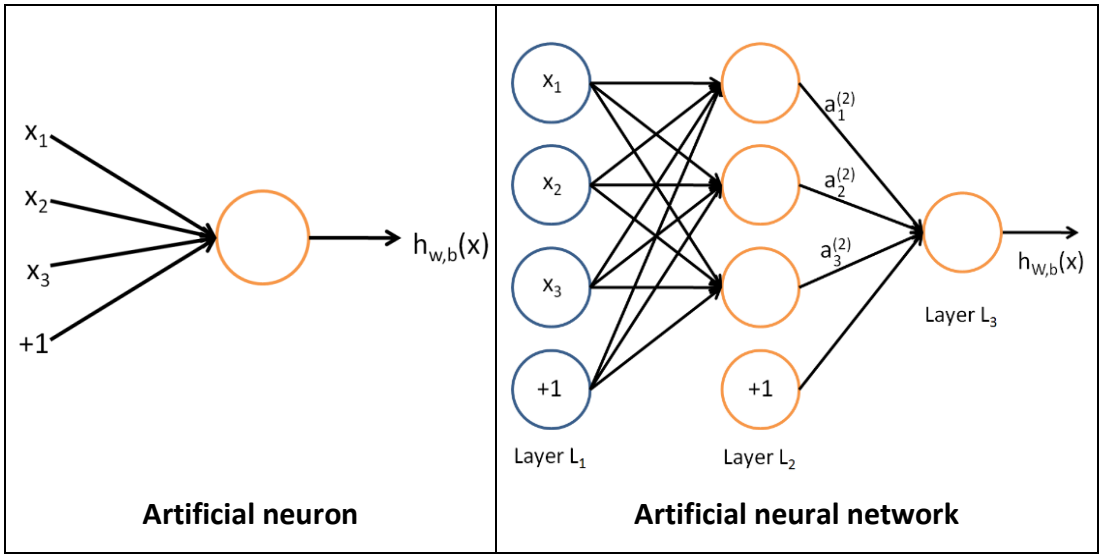

Figure 3.4 Artificial neuron (left), and example of neural network with fully-connected neurons and with an additional bias term indicated +1 in each layer (right) (Diagrams from: http://ufldl.stanford.edu/tutorial/supervised/MultiLayerNeuralNetworks/ (UFLDL Tutorial))

Examples of non-linear functions, that are employed in the transformation Equation (3.3), are Sigmoid functions, hyperbolic tangents (tanh) or other high-degree functions. Neural networks seek the best innate features that need to be carried through the functional network paths into final stage of fitting data. A convolutional neural network, works by multiplying smaller kernels iteratively to different parts in

the network in order to represent the whole network in a practical way – e.g. image and speech recognition.

The drawback of using neural network techniques is the model complexity. It requires in depth investigation of the behaviour of the processed data and selection of suitable functions, number of network layers and elemental features. Moreover, there is quite restricted control over intrinsic parametric updates of the network and training algorithms can be unpredictable.

3.2.2.5 Discussion and Comparison of Some Approaches to MALDI-MS Data Analysis

Mass spectrometry data are very informative and therefore are large in size. Especially, mass spectrometry imaging collects spectra acquired at defined locations across a region of a thin section of sample (with a focus on biological tissue samples in this thesis). Due to the large size and complexity of imaging data, computational methods are often applied in analysis tasks. A simple classification algorithm to segment regions of the tissue section is based merely on a specific analyte, in this case, biological molecules of interest. Spatial distributions of different m/z molecules are contained in the same set of data; therefore, several analyses could be performed, combined, and compared, from the same acquisition session. In medical images, biological structure and its chemical components are usually a known distribution. Problems to be solved often relate to pathological conditions that lead to changes in the tissue sample under examination. Using suitable mathematical methods, it is possible to train a classifier to perform automated diagnoses. As medical images, in classes of interest, usually have regular patterns that might be recognised as class identification, this can be performed by a human; therefore, constraining the training using previous experience, and hence, this is called supervised learning. The alternative approach is referred to as unsupervised, where the learning machine is constructed (without guidance) and is a useful tool for a complex data analysis. Some supervised and unsupervised algorithms are listed in Table 3.1, providing a brief introduction to the use of some techniques for mass spectrometry data analysis.

Table 3.1 Example methods of data analysis that can be applied for classification of mass spectrometry data

Data analysis method	Supervised / Unsupervised	Principle	Example	
			Reference	Application
Principal component analysis (PCA)	Unsupervised	Reduce dimensionality of principal components, and find spectral distributions with optimal difference between groups.	Shao *et al*. (2012)	Classifying serum samples from gastric cancer patients and healthy controls
Probabilistic latent semantic analysis (pLSA)	Unsupervised	Distributions of different target biological cells are expressed by pLSA scores which would then determine mass spectra of components of selected cell types.	Deininger *et al*. (2012)	Providing representative spectra for tumour cells and other cell types, allowing tissue segmentation
Support vector machine (SVM)	Supervised	Bootstrapping resampling method is used for training and testing the SVM where the model is created from the least cross-validation error training data set.	AlMasoud *et al*. (2014)	Differentiating types of bacteria
Random forest	Supervised	Classifier includes series of tree branches with different random m/z features.	Hanselmann *et al.* (2009)	Classification of breast cancer tissues and different tumours
k-nearest neighbours	Supervised	The Euclidean distance is measured between the features of a testing spectrum and every training spectrum to determine the nearest in each comparison and vote for the correct class.	Sanders *et al*. (2008)	Comparing and determining biomarkers for breast cancer based on proteome

In the supervised approach, data points are annotated relative to their pixels in each of the sample images which presumably contain the corresponding target tissue components. Feature information contained in the data points is stored for the purpose of training so that a classification model can be built across a series of sample images via various algorithms such as the random forest method. In the work by Hanselmann *et al*. (2009), random forest classifiers were generated for the classification of breast cancer tissue for mass spectrometry images. This gave a true positive rate for correct classification as high as about 90%. MSI data points (characterised by mass spectra) amongst training samples of known classes are used to build binary decision trees based on a hierarchy of randomly selected features. Spectral information contained within each interval of the full spectrum (responsible for these features) is used to categorise samples into two classes. The classifications are trained sequentially, in a tree using different features until decision paths are obtained that ultimately distinguish the sample between two different classes. The diagram for structure of trees in Figure 3.5 (a) describes this algorithm. Where a tree's node represents a feature (member of a randomly selected subset of the whole set of features) that optimises the separation of the classes with a feature value (e.g. ion counts in a mass spectral interval) determining the class separation threshold (Hanselmann *et al*., 2009) (See also the diagram in Figure 3.5 (b) for graphical boundaries separating data into 2 distinct classes). The tree is grown by splitting each node into 2 branches (representing the classes) starting from the root node. For every child node, it undergoes the same procedure until satisfied at the leaf nodes, where a final class decision is made. Then, a random forest classifier is formed accordingly by combining series of these trees that have been trained randomly and independently in order to achieve good generalisation (Criminisi and Shotton, 2013). In testing, the same data point is classified through every individual decision tree in the forest. In each tree, a decision is made at each node (starting from the root), following an appropriate path until it reaches a leaf node, where a vote is generated for the preferred class. The testing data are then classified as the class with the maximum number of votes as a surrogate for the corresponding class probability. Here, the classifier's sensitivity can be derived from a comparison of the resulting and true class of the test data. Note that the wavelet transform is widely used to

extract useful features with fewer dimensions and more efficient use of data, thus giving better and faster classification performance (Liyen *et al*., 2013).

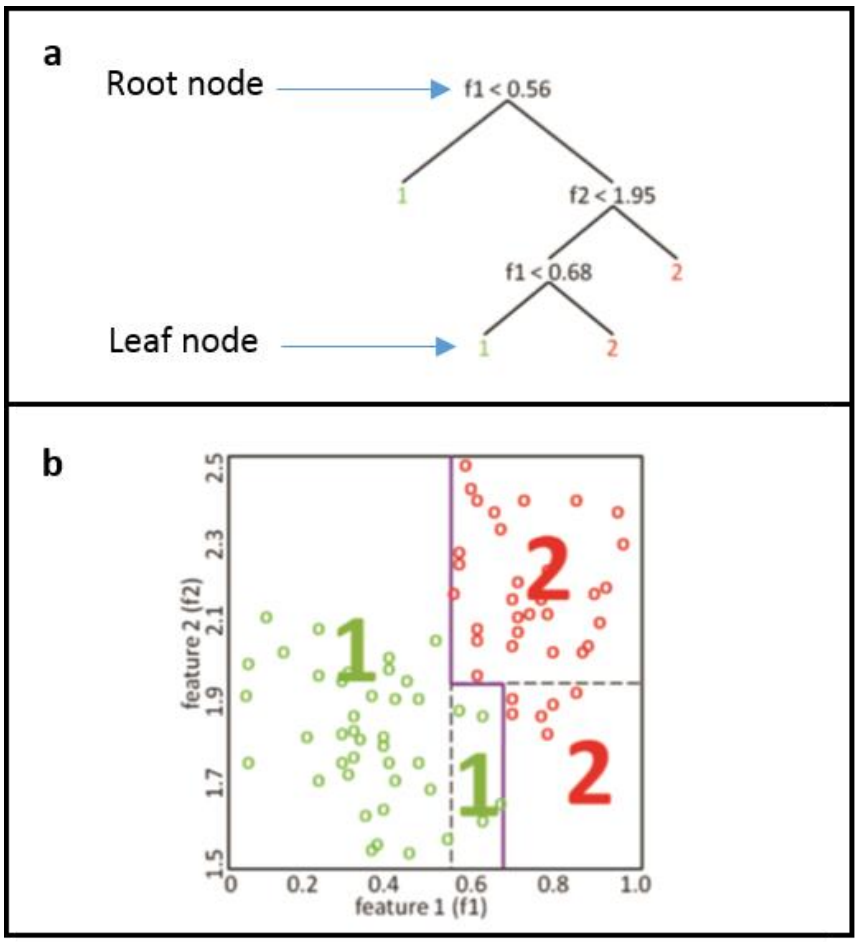

Figure 3.5 (a) Decision tree characteristics where f1 and f2 are feature values of 2 different features at each node used as classification thresholds, and (b) plot of data with decision boundaries being the feature values in the corresponding trees (Adapted from: Hanselmann et al. (2009))

Multivariate analysis allows many measured variables to be analysed simultaneously. Data of high dimensionality are handled using matrix algebra for the convenience of interpretation and computation of the multivariate data (Miller and Miller, 2010). Approaches using linear decomposition of data components used in the mass spectrometry imaging context, e.g. probabilistic latent semantic analysis (pLSA), are discussed in Section 6.1.3. These approaches are usually unsupervised and allow regression measurements. They can be powerful for analysing mass spectrometry

images in terms of dealing with variabilities in signal and noise, and are independent of spatial locations. Therefore, they can also be applied for quantitative classification purposes. For example, principal component analysis (PCA) is a statistical method of handling and simplifying large data sets for further analysis where only the main components of data variance are considered (see details in Section 3.4.2.1). A principal component plot is a graph of data points in a coordinate space with the first principal component axis indicating the direction of most data variance. The complexity is reduced by rejecting the least significant principal components (least variant) until left with fewer dimensions, where data points from a specific class are distributed within certain deviations and can be distinguished from other classes. Note that all principal component axes (the spectral shapes) are orthogonal, as a result of the mathematical form of decompositions. In mass spectrometry, data points are encoded by mass peaks in a set of MS spectra. A PCA algorithm was applied to semi-quantitatively classify MALDI-MS data from different types of bacteria using their relative mass peak intensities (AlMasoud *et al*., 2014). Classification accuracy of 90% was quoted for this specific data set using PCA, followed by further classification using 'support vector machines with a linear kernel' (AlMasoud *et al*., 2014). They also introduced an alternative qualitative approach using principal coordinate analysis (PCoA) where only m/z signals greater than three times a baseline level were considered as peaks (AlMasoud *et al*., 2014). Classification of MALDI-MS proteomic data from serum of (gastric) cancerous and normal tissue samples in humans was successfully performed by Shao *et al*. (2012) using the PCA method. Smaller MS data sets were selected by the most useful proteomic peaks derived from PCA, plotted as in Figure 3.6 with an accuracy in classifying samples in the patient group determined by distribution to be 94.5% (Shao *et al*., 2012).

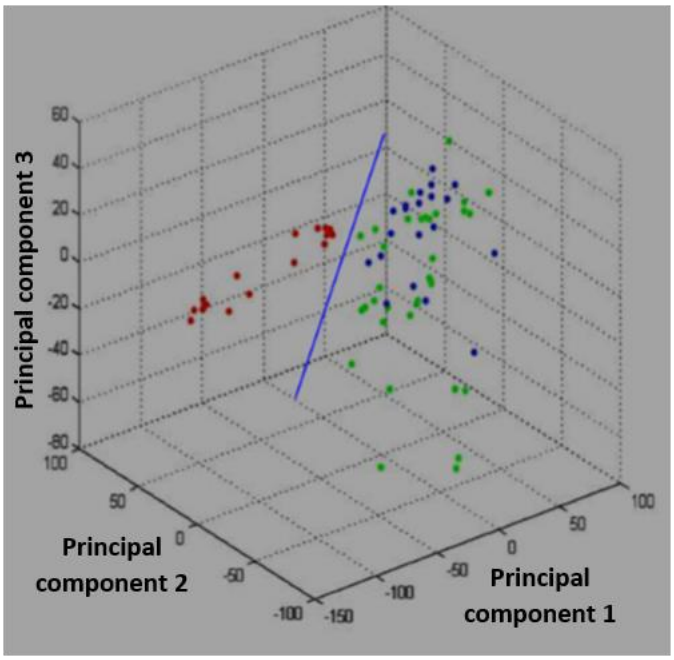

Figure 3.6 Plot of data points on principal components showing clusters of human serum samples using mass spectrometry where red and green spots represent data from healthy and gastric cancer training sets, respectively, and the blue spots represent data from testing sets (all from gastric cancer patients) (Adapted from: Shao et al. (2012))

3.2.3 Understanding Signal and Noise and the Associated Analysis Requirements

Some Definitions

The terms signal and noise are involved in interpreting the contents of digital data, hence, often appear used in data analysis and processing of electrical, imaging, spectroscopy data, and so on.

***Signal*:** A measure of the target quantity, acquired using a specific experimental set-up.

***Noise*:** Errors generated by a measurement system and superimposed onto the actual signal. Note that noise usually refers to random errors.

Errors do exist in every measurement, in other words, recorded signals always contain some sorts of error. Broadly speaking, errors are classed into 2 main types, which are systematic and random errors. Both are expected to occur in several stages of experiments, including instrumental, environmental and man-made errors. The experimental procedure has to be adjusted to optimise the results such that these errors are minimised, giving an accepted level of signal-to-noise ratio (S/N). *Systematic errors* may be recovered by applying some form of function to the data – e.g. constant shifting or scaling throughout the recorded signals. This can generally be dealt with by calibration methods that suit the apparatus. *Random errors* are determined by limitations of instrumental measuring stability (precision) which causes statistically random variations. Pure signals can never be achieved, but averaging the results from repeating measurements is a way to help getting rid of random variations in many scientific problems. However, acquiring multiple measurements may not be possible for some experiments. Attempts to use computational techniques are therefore required at this point to address any serious noise levels.

Identifying noise, and splitting separable noise from signal can improve the interpretation and quantitation of the data, enhancing the S/N. It is important to correctly describe the noise distribution on data as this determines how reliable it can be in a prediction of the noise-free data, leading to appropriate analysis and optimal solutions. Further discussion on Gaussian and Poisson noise characteristics will be noted in Section 3.4.3. There is no explicit role for noise in support vector machines, k-nearest neighbours, random forests, neural networks or clustering approaches, even though it is clearly important for the valid interpretation of data. Appropriate modelling using linear decomposition techniques with correct statistical assumptions is required for a proper characterisation of signal and noise. This therefore motivates the use of linear Poisson independent component analysis which will be described in Section 3.4 and compared explicitly against other approaches for analysis of MALDI-MS imaging in Section 6.1.3 of Chapter 6.

MALDI-MS: Where does the noise come from?

In the particular problem of the MALDI mass spectrometry context, noise comes from many sources as discussed previously in Sections 2.2 and 3.1.1. There are number of instrumental and experimental control parameters that can be optimised to enhance S/N so that it satisfies the requirements for qualitative or quantitative analysis.

***Instrumentation*:** laser power, number of laser shots per profile, pulsed extraction, mass range of interest, pressure in flight tube, detector gain, electronics used for amplification, etc.

***Sample preparation*:** homogeneity of the sample and matrix on surface, the amount and concentration of sample, the matrix type and its ratio to the sample, etc.

There are many other parameters that can also cause difficult concerns to MALDI-MS measurements. For example, the non-planar nature of the sample surface, especially with matrix added can contribute to variation of angles of the incident laser beam. Temperature changes can affect chemical ionisation (heat from the laser pulse raises the energy in the plume) and electrical parts of the machine (heat from the laboratory/instrumental environment). Some uncontrollable fragmentation introduced post ionisation can result in chemical noise that occurs in the mass spectrum apparently at random. This is from matrix clusters and also analytes.

There are also some other instrumental and/or unintended signal variations and systematic errors which interfere with the random noise. Analysis methods that treat the data appropriately from a statistical perspective must be used to maintain the integrity of both signal and noise characteristics so that they can be separated correctly, e.g. via pre-processing, signal decomposition. The MS signals are in the form of ion counts, which are peaks in the current above a certain threshold are counted. These peaks come from ions, for a TOF-MS instrument, some ions arrive the detector at the correct time for their m/z and some are not, hence the mass resolution issues. In the event of two or more ions coinciding at the same m/z within the range of mass resolution, the quantitation task will become even harder to achieve given that a peak is composed of contributions of more than one ion. This is not an issue of noise but the real signal that causes a problem when separate signals

cannot be discriminated (see Section 6.3.5, and the diagram in Figure 6.12 for the analysis solution and discussion). If there is a non-ion induced event at the detector e.g. when hit by a comic ray, or if the ion trajectory leads to a small signal below the threshold for counting, etc., a non-predictable presence/absence of detected signals is expected. However, the statistical assumptions on the data should still be preserved.

All these represent contributions to systematic and random errors whose sources are sometimes too complicated to be modelled, or controlled. The remaining factors that have not been removed via experimental optimisation eventually add up and appear as background noise in the mass spectral readings. Appropriate pre-processing and statistical analysis methods, with suitable assumptions based on the data analysed, can deal with the signal and noise behaviour in the calculation, allowing for a more accurate quantitation of the final results (further quality control is usually required given the complex nature of the MS data discussed above).

3.3 Pre-processing of Mass Spectra for LP-ICA

MALDI mass spectra obtained directly from acquisition are prone to noise and variability. It is common for some pre-processing to be required before any quantification work can be carried out. Pre-processing generally refers to steps of; spectral alignment, background (or baseline) subtraction, and peak detection, prior to analysis.

A complex biomolecule will generate a series of MS features, which undergo correlated variations in intensity and position, depending upon equipment settings and the local sample environment, e.g. Szájli *et al.* (2008), or even suppression effects due to the influences of different molecules on ionisation. Aside from these variations, MALDI mass spectra are approximately linear combinations of sub-spectra from a sample's constituent molecular components. Some sources of variation are reduced through pre-processing. Baseline corrections can remove background by subtracting a smooth function fitted beneath peaks, e.g. Williams *et al.* (2005).

Alignment can be achieved by shifting spectra, with various forms of interpolation applied for sub-bin precision, e.g. Jeffries (2005). Peak detection and integration can be achieved by thresholding, direct summation of m/z bins, or by the fitting of Gaussians, e.g. Yang *et al.* (2009).

For a Linear Poisson Independent Component Analysis (LP-ICA) to be successful, MS data must be presented in the form of a set of histograms composed from (approximately) independent bins containing Poisson-distributed sample quantities. For computational efficiency and convenience, it is desirable to have as few bins as possible whilst maintaining the useful information from the original spectra. Each bin should be well populated. Reducing the full mass resolution of the spectra (10 - 100 thousands of bins each spectrum) to a more manageable size can be achieved using basic pre-processing steps. Additionally, several sources of MS variation can be mitigated against during this pre-processing through some post-acquisition calibration. The following steps are designed to: select an appropriate mass range and resolution, correct misaligned peaks, correct spectral baselines, and integrate significant peaks into individual histogram bins. Full descriptions are provided in previous work, see Thacker *et al.* (2018) for the in-house pre-processing methods for use where Poisson noise is dominant in peaks and Gaussian noise is dominant in background.

An example MALDI mass spectrum before and after applying the following pre-processing steps is shown in Figure 5.2 (see Chapter 5, Section 5.3.1).

3.3.1 Windowing and Resolution Reduction

Low mass peaks are noisy and imprecise, and matrix related ions contain little information regarding the analyte content of samples. As such, the first pre-processing step is to select a mass range containing the analytes of interest.

A basic analysis of correlation between bins is performed in the baseline correction step (Section 3.3.3), the results of which determine the minimum down-sampling required to improve the statistical independence of adjacent bins. Lower resolution

spectra are produced by combining whole bins thereby avoiding the need for interpolation which can introduce aliasing artifacts.

3.3.2 Alignment

A peak alignment procedure, that has been validated for use on Poisson samples, is applied to minimise unwanted shifting of peaks (e.g. due to changes in TOF due to surface height differences, etc.). The algorithm is designed to conserve the pre- and post-aligned integral of each spectrum and also maintain statistical independence of adjacent bins.

A reference spectrum is first created by taking an average of all spectra. Each spectrum is then aligned to this reference individually. A square-root (Anscombe, 1948) is applied to each bin to transform the Poisson quantities to approximately Gaussian variables. Sub-bin alignment is then performed in the Fourier domain by finding the phase shift in data which minimises a least-square difference of each spectrum to the average. The same Fourier description is then used to interpret shifted data.

3.3.3 Baseline Correction

Signal peaks are superposed on a non-uniform but smoothly-varying noisy background. This means that there is no fixed baseline for ion counts across the range of a spectrum. A baseline correction is required which estimates this background, subtracts it, and performs some quality control upon the results. The algorithm chosen to apply assumes that noise on the background is approximately independent and Gaussian with zero mean. Each spectrum is iteratively baseline-corrected, converging when a stable background is found. An initial attempt is made to identify the location of peaks using hysteresis thresholding. A kernel is applied to the identified background that estimates the smooth (noise-free) version and interpolates beneath located peaks. The smooth background is subtracted from the

original spectrum and the root mean square (RMS) between the corrected baseline and new background is computed. The RMS is used to update the hysteresis thresholds, stopping when the RMS converges to a fixed value.

As an additional check, at the solution, the mean run-length – i.e. the mean value of same-signed residuals is computed. This should be 2 if the baseline has been successfully corrected and if adjacent spectral bins are independent. If this is larger than 2, the original spectral resolution can be reduced to improve independence (see Section 3.3.1).

3.3.4 Peak Detection and Integration

The final pre-processing step reduces spectra to a set of histograms containing as few bins as possible, whilst attempting to maintain most of the useful information. Spectral bins between peaks, and small peaks up to a few standard deviations above the noise floor, contain little useful signal. These ranges are also dominated by Gaussian noise (so-called 'background'), whereas Poisson noise must be dominant in signal variation for LP-ICAs to be applied. The peak detection and integration method of Thacker *et al.* (2018) is used to perform this reduction. Significant peaks are detected by applying hysteresis thresholding. Bins associated with each detected peak are summed to give a measurement per peak. Unlike the baseline correction step (which operates on a spectrum-by-spectrum basis) this thresholding is applied to the sum of all spectra, as significant peaks may vary from one spectrum to another. The result is a single common binning across all spectra. The resulting histograms are fed through to a conventional analysis (Section 3.1.3) and the new LP-ICA analysis (Section 3.4.5). As each bin represents a single peak, the terms bin and peak may be used interchangeably from this point.

Once correlated effects have been removed, there are two main sources of random noise that are expected to be present in mass spectra, superimposed on each other. They differ in characteristics as seen in the diagram provided in Figure 3.7 (a). The need for baseline correction is to correct for the background noise which is

introduced mainly by electrical effects of the instrument, which should be uniform across all mass values and explainable as Gaussian noise. On the other hand, the ion counts recorded are a Poisson sampling process, with the noise level proportional to the square-root of signal. The following symbols are used in the rest of this thesis to clearly state the distinction of the (signal variants) Poisson noise σ_p, and the (background) Gaussian noise σ_g. The diagram provided in Figure 3.7 (b) and Equation (3.4) show the effect of the two noise ground to the observed total noise, σ_{tot}.

$$\sigma_{tot} = \sqrt{\sigma_g^2 + \sigma_p^2} \tag{3.4}$$

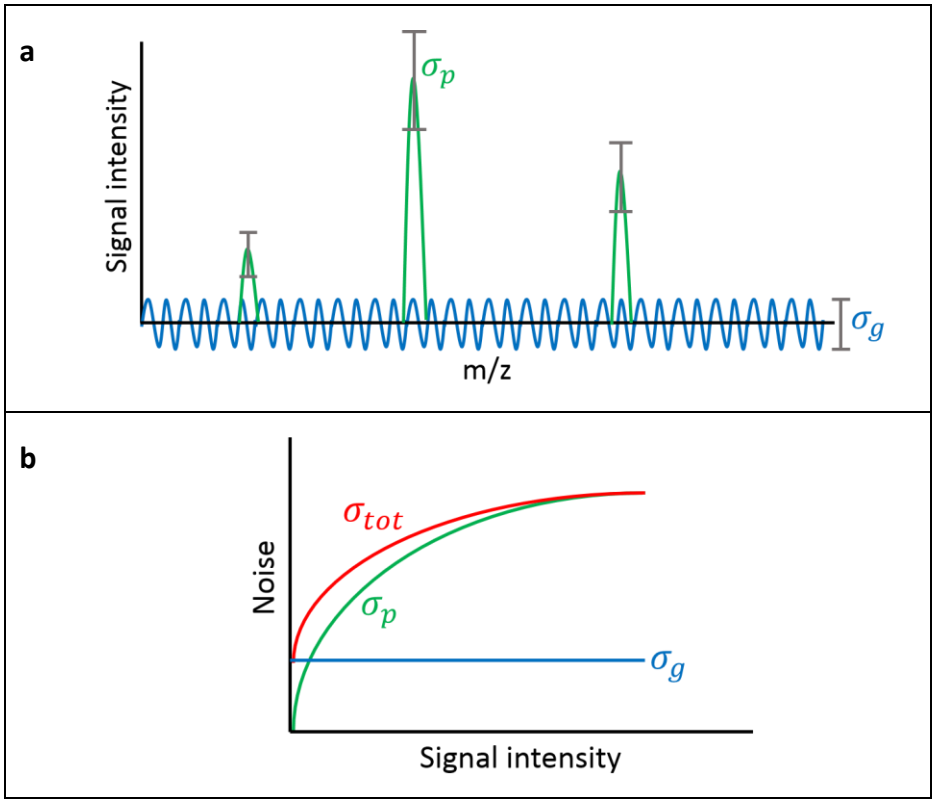

Figure 3.7 (a) diagram and (b) graph showing Poisson vs. Gaussian noise behaviour

σ_g is constant and independent of signal intensity, and is expected to be small in comparison with σ_p. Especially, after baseline correction, σ_g should be small. Therefore, at higher signal intensity as a result of peak detection, the σ_p is dominant in the observed total noise, σ_{tot} – i.e. if $\sigma_g << \sigma_p$, σ_{tot} is approximately σ_p (see Figure 3.7 (b) for the illustrating diagram).

3.4 Linear Poisson Independent Component Analysis

3.4.1 Correlation of Numerical Data

This section explains the general correlation properties of numerical data distributions. Note that correlation is an important concept in statistics for description and interpretation of data. The diagram of an example data distribution of two uncorrelated variables is presented as a 2-dimensional plot in Figure 3.8 (a). The original horizontal and vertical axes of the plot indicate the two variables X_1 and X_2 which contribute to the data distribution about their means μ_1 and μ_2. An ellipse indicates the confidence interval of the data points lie within it, with respect to the value for standard deviation, σ_1 and σ_2. Here, the symmetry of the plot about X_1 = μ_1 and X_2 = μ_2 shows that the data distribution on one axis is not predictable using the value on another axis, the data variables are theoretically uncorrelated – i.e. independent. On the other hand, the data variables are said to be correlated if the spread of data given one variable relies upon the value of the other variables. In the plot presented in Figure 3.8 (b), X_1' and X_2' are the direct rotational axes crossing the mean values of the distribution of both variables at μ_1 and μ_2, and it can be seen that the data lie within the corresponding ellipse are not independent.

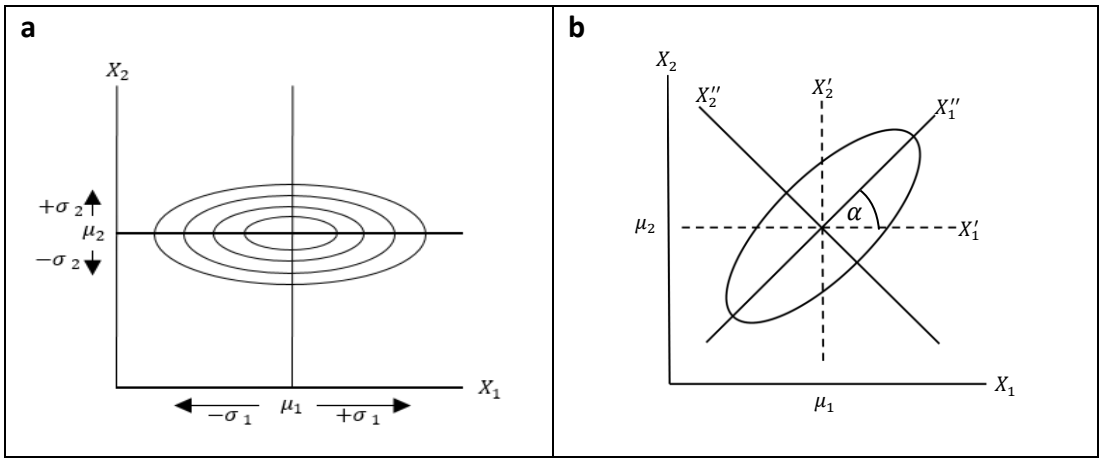

Figure 3.8 Distribution of data on 2-dimensional contour plots of (a) uncorrelated and (b) correlated variables

However, the data shown in Figure 3.8 (b) can be de-correlated mathematically by rotating the axes by an angle, α, so that the new axes X_1'' and X_2'' are aligned on the most separable directions for the given data. The technique of finding most separable directions in higher dimensional data is made useful in a well-known statistical analysis: Principal Component Analysis (PCA).

The next sections will describe and compare the 2 types of multivariate data analysis methods: Principal Component Analysis (PCA) and Independent Component Analysis (ICA) which are often used for the analysis of scientific data.

3.4.2 Standard PCA and ICA

PCA and ICA have some commonalities in the basis of their principles, both aim at simplifying multivariate data. The data are interpreted as a matrix of linear combinations derived from the observed variations within data, following the selected assumptions for each approach. Such methods involve dimensionality reduction into a smaller number of components which best describe the original data. Hence, further problems can be solved using fewer parameters.

3.4.2.1 Principal Component Analysis (PCA)

X is an M-dimensional vector of the underlying variables, each of which contributes different amounts of variation into the data. Y is a vector representing the principal components, where N is the expected number of principal components to be extracted. X and Y are functions of some parameter t that contain information about the origin of variants.

$$X = [x_1(t), x_2(t), \dots, x_M(t)]^T \tag{3.5a}$$

$$Y = [y_1(t), y_2(t), \dots, y_N(t)]^T \tag{3.5b}$$

In order to work out Y from X, a matrix, $A_{N\times M}$ containing eigenvalues a_{nm}, needs to be determined for the weighting of the linear combinations as in the following

Equation (3.6). Note that m and n are the indices for the original and the reduced principal component dimensions, respectively.

$$Y = A\,X \tag{3.6}$$

Orthogonality is assumed in PCA for convenience, as it simplifies the interpretation and optimisation processes. Each element of vector X of underlying parameters are then separated onto orthogonal directions expressed in Y as principal components. This means that a set of data composed of a number of underlying parameters can be transformed into principal components, instead of looking for the variation in each parameter individually. The ability to calculate a covariance matrix and rank the principal components in accordance with their variance, makes PCA a useful method for extraction of features of interest from a data set. However, physical data generators are rarely orthogonal.

3.4.2.2 Independent Component Analysis (ICA)

ICA analysis is capable of modelling higher-order functions to describe underlying variables according to the behaviour of the given data. Unlike PCA, ICA can attempt to extract base compositions that were simultaneously produced within the measured signal. Also, orthogonality of these components is not required in ICA.

The structure for elements of independent component analysis can now be substituted in the linear formulation in Equation (3.6) where Y is the vector containing the modelled independent components, and X is the vector containing underlying source signals, each comes with an associated weighting factor a_{nm} which needs to be estimated. The original signals produced from individual sources (generators) are seen as independent components. The measured signal, contains the mixed characteristics of the source signals, which could be statistically interdependent. A non-parametric assumption can be made for the distribution of each of the source signals, which allows a more reliable modelling of real-world problems. As the independent components are constructed from several signal generators, they are often assumed to be Gaussian distributed and conventional ICA is justified on the basis of the central limit theorem. When a single or too few

underlying variables exist in a component, the validity of this Gaussian assumption is questionable.

ICA has important applications in signal processing/analysis. The early development of the method was so-called “Blind Source Separation”. It was introduced and interpreted by solving the “cocktail party problem” where a mixture of sound signals (observed by the party goers) can be decomposed into its independent sources. The problem was addressed in a speech recognition study by Cherry (1953) where listeners had to try to distinguish 2 messages sent at the same time using one or both ears. The development of the ICA method has brought interest in developing its application in different fields, including the work done by Herault and Ans (1984) that recorded neural activities and processed the signals using an unsupervised extraction of linear parametric components within the acquired signal. Other later applications are, for example, separating signal and noise in complex data from functional magnetic resonance imaging data of brain activation (McKeown *et.al.*, 2003), electroencephalograms (Krishnaveni *et.al.*, 2005), and planetary image analysis (Tar *et.al.*, 2015).

Note that many of experimental devices producing count signals can be described as a Poisson sampling process. Neither conventional PCA nor ICA are based upon this statistical model. However, the ICA algorithms may be adjusted using alternative cost functions, to approximately suit these characteristics of the data. Hence, a wide range of research that involves analysis of data containing multiple variables, has made use of ICA, particularly in, chemometrics, bioinformatics, image analysis, and speech recognition.

3.4.3 Distribution of Data: Gaussian vs. Poisson

The Gaussian distribution, also known as the normal distribution, is the most common probabilistic distribution used to describe measurements of continuous random variables, where the outcomes turn out symmetrical in variance with maximum probability occurring at the mean of the distribution. The distribution of

the variance (mean square deviation from the mean of measurements) is uniform and random throughout regardless of the measurement values. Although, a Gaussian distribution is often assumed for convenience in solving statistical problems, based on a central limit theorem justification, it is not always applicable for all data sets. Hence, there is a need to ensure suitability of the data, especially before quantitative analysis in experimental work.

Poisson noise, instead of being uniform, depends on the value of a particular measurement. This type of probability distribution is typical for histogrammed (count-based) data. Poisson processes include counting the number of occurrences of some (random and independent) events within a definite space or time. Ideally, the variance on a measurement is proportional (or equal) to the measurement value, which indicates that more measurement variation is predicted for higher counts or signals.

The plots provided in Figure 3.9 (a) and (b) show simulated error distributions for Gaussian and Poisson types, presented as Bland-Altman plots (plot of model fitting residual against signal intensity) which respectively have uniform error and power-law error with regard to the measurement values.

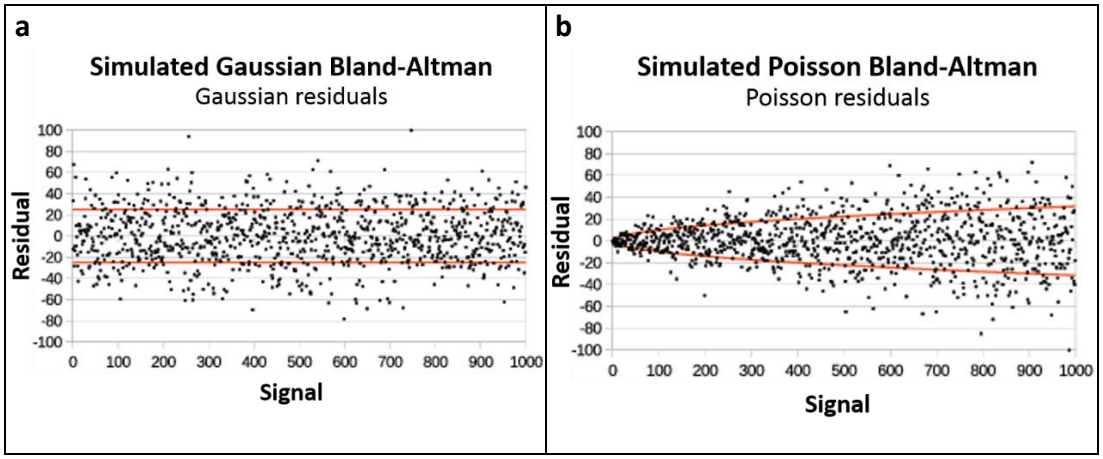

Figure 3.9 Simulated (a) Gaussian and (b) Poisson Bland-Altman plots

The formulations of standard PCA and ICA algorithms are based upon uniform independent Gaussian errors, often conveniently leading to closed-form solutions. However, MALDI may not be compatible with these assumptions. In particular,

Poisson statistics may better describe the counting of ions. Evidence of MALDI's Poisson nature has been highlighted in the literature, for example, Harn *et al.* (2015) and Piehowski *et al.* (2009). A number of modifications of standard methods have been made in order to allow for data suitability. Properties of data corresponding to the choices of modelling method are shown in Table 3.2, and compared with the expected MALDI data properties. These include the standard PCA (Jolliffe, 1986), the standard ICA (Comon, 1994), PCA/ICA with square-root transform converting Poisson noise into approximately Gaussian noise (Anscombe, 1948), Non-negative ICA (Plumbley, 2003; Plumbley and Oja, 2004). And finally, the new Linear Poisson ICA (LP-ICA) method was originally developed by Tar and Thacker (2014), where the ICA method was derived for data with Poisson sampling characteristics: originally called Linear Poisson Modelling (LPM). The method has been applied to planetary and medical images (Tar *et al.*, 2015; 2017; 2018). The method is also proposed as appropriate for the analysis of MALDI data. The properties assessed are noise characteristics (either independent, identically distributed (iid) Gaussian noise, or Poisson noise), linearity of signal components x with weighting factors α, component orthogonality, and the coefficient (positive/negative) on extracted component signals.

Table 3.2 Modelling options, with statistical and signal assumptions available for varied data properties

Model	Noise	Signal	Orthogonality	Coefficients
PCA	iid Gaussian	$\sum \alpha x$	Yes	+/-
PCA with Anscombe	Poisson	$\sum \alpha \sqrt{x}$	Yes	+/-
ICA	iid Gaussian	$\sum \alpha x$	No	+/-
ICA with Anscombe	Poisson	$\sum \alpha \sqrt{x}$	No	+/-
Non-negative ICA	iid Gaussian	$\sum \alpha x$	No	+ only
Poisson ICA	Poisson	$\sum \alpha x$	No	+ only
MALDI data	≈ Poisson	$\approx \sum \alpha x$	No	+ only

3.4.4 MALDI-MS Data Characteristics

The time-of-flight measurement of ions in mass spectrometry is potentially a Poisson process. Where ions of each specific mass-to-charge ratio (m/z) are grouped together with near identical velocity. They drift apart in space from ions of other m/z values in the time-of-flight tube before arriving at the detector a certain point in time. The flight-time can be written in terms of square root of m/z, and the time intervals for ions of specific m/z values to hit the detector can be converted into m/z bins on the horizontal axis of a mass spectrum.

In principle, it is expected that a MALDI spectrum would have Poisson-like signal-to-noise. That is the measurement error (spectral noise level) increases with signal intensity by a power of ½. In reality, a MALDI mass spectrum consists of underlying generators, each of which follows Poisson statistics (and the sum of Poisson's is Poisson). Therefore, the intention of this work was to create a model of mass spectra based upon these signal generators (so-called components), assuming the model parameters are consistent from spectrum to spectrum within a data set. Furthermore, there are a number of complex processes involved in the MALDI-TOF-MS signal generation that give rise to noise. For example, the signal could well be contaminated by suppression effects, from chemical compounds of high proton affinity, sample-matrix preparation, surface, or electrical noise generated within the instrument, etc., not necessarily purely of Poisson type. Therefore, a well approximated model is required – i.e. fits every spectrum, so that the noise accompanied by each component can be interpreted by the Bland-Altman analysis as described in Chapter 5, Section 5.3.5.

The MALDI-TOF mass spectral data has been assessed and found to follow Poisson statistics by observing data distribution via Bland-Altman plot as seen in Figure 5.6 (Section 5.4.2 of Chapter 5). The generic nature of LP-ICA analysis method is detailed in the next Section 3.4.5) and its numerical performance will be presented in later chapters (Chapter 5 for discrete MS data and Chapter 6 for imaging MS data).

Taking appropriate account of the Poisson noise in data should maximise the performance of the analysis of the MALDI mass spectra. In addition, the algorithm

can automate extraction of modelled components and can seek to identify any components that have no association with true sample signals. These extra components representing parts of signals that happened to appear in spectra, without correlation to analyte quantities, are then called 'background'. The background components found in the spectra can then easily be rejected from the spectral analysis.

3.4.5 Linear Poisson Independent Component Analysis (LP-ICA) Modelling

The in-house Linear Poison Independent Component Analysis (LP-ICA) modelling algorithm (see also LPM in TINA vision) has been designed specifically to quantify histogram data which conforms to a Poisson distribution (Tar and Thacker, 2014; Tar *et al.*, 2015). While the standard Independent Component Analysis (ICA) algorithm assumes Gaussian-distributed noise.

An LP-ICA modelling determines the necessary probability mass functions required to describe the distribution of spectra. This process is a linear Poisson compatible form of Independent Component Analysis. The training is achieved using Expectation Maximisation (EM) to optimise the following Extended Maximum Likelihood (Barlow, 1989), see Equation (3.8).

Cost Function

A histogram, H can be modelled by a LP-ICA probabilistic model, M, with K linearly independent components, indices k, with their associated component of quantities, q. Where i is the histogram index and m is the histogram bin. A probability mass function, $P(m|k)$ defines the underlying signal generator for a component to contribute to each histogram bin. This probability is assumed common throughout all histogram samplings of a data set.

$$H_{mi} \approx M_{mi} = \sum_{k} P(m|k) q_{ki} \tag{3.7}$$

When applied to mass spectra, H_{mi} is the histogram bin recording the frequency of observed ions of mass m within spectrum i; M_{mi} is the frequency predicted by the LP-ICA model; k is a label indicating an LP-ICA component (sub-spectrum); $P(m|k)$ is the probability of observing an ion of mass m from source k (note that there is no i subscript here, as an LP-ICA model uses a common set of PMFs to describe multiple histograms); and q_{ki} is the quantity of component k contained in spectrum i. Given a set of N spectra, $i \in \{1,2,\dots,N\}$, an LP-ICA model is used to provide Likelihood estimates for the unknown terms: $P(m|k)$ and q_{ki}. Sub-spectra representing different modes of variation are encoded as the probability mass functions, $P(m|k)$, with the amount of each present within each spectrum being determined by their quantities, q_{ki}.

A log likelihood, $ln\mathcal{L}$ is maximised for this modelling scheme to find the best model fit resulting from the additive sum of the quantities of the extracted components, see Equation (3.8). The cost function required to be minimised is therefore the negative log Likelihood, $-ln\mathcal{L}$. This is based on the Extended Maximum Likelihood which has a renormalisation term added to the standard Maximum Likelihood formula to correct for the circumstance where a data quantity varies. In this case, the data quantity varies according to the Poisson statistics (where the Poisson sampling events are the counts on detected ions). Therefore, the likelihood estimation on data is multiplied by the probability at which a certain number of Poisson events occur, hence the second term in Equation (3.8) when the logarithm is applied.

$$ln\mathcal{L} = \sum_i \sum_m ln\left[\sum_k P(m|k)q_{ki}\right] H_{mi} - \sum_k q_{ki} \qquad (3.8)$$

During training, this function is jointly optimised for a set of example histograms giving a set of $P(m|k)$ components (sub-spectra). The number of components required to describe each class is determined by adding additional components until the goodness-of-fit, χ^2 per degree of freedom (Equation (3.11)) between the model and example histograms approaches a stable value (ideally unity).

In order to find the best linear trend for the underlying sample in the mass spectral data, the model was finalised by putting in extra weighting factors, w_k to the

extracted components. w_k also models efficiencies, etc. which are needed to relate measured values to sample quantities. This gives the following relationship for the overall component contribution, Q_{Ti}. Where T contains a class of components that contribute to describe an underlying sample proportion.

$$Q_{Ti} = \sum_{k \in T} q_{ki} w_k \tag{3.9}$$

Note that suitable w_k values were initially obtained from linear regression optimising the accuracy for some component combinations to predict concentrations of known ground truth samples. (See the method of experimental Chapter 5)

Expected Poisson Error

Propagated error covariance calculated on the $P(m|k)$ of model components is expressed in the equation below, with a and b are different model components. Where available, this can be compared with the measured error (the residual between model prediction and ground truth values). (See the results of Chapters 5 and 6)

$$C_{ab} = \sum_{m} \left[\left(\frac{\partial q_a}{\partial H_m} \right) \left(\frac{\partial q_b}{\partial H_m} \right) \sigma_{H_m}^2 \right] \tag{3.10}$$

A chi-square per degree of freedom, χ_D^2 determines the goodness-of-fit. The degree of freedom, D takes values of total number of training histogram examples. The adequacy of the model to describe the match score histograms is quantitatively testable, unlike many alternative machine learning methods. The number of PMFs, $k \in \{1,2, \dots, K\}$, required to sufficiently approximate the data (i.e. to accuracies within the level of Poisson sampling) is determined to minimise χ_D^2:

$$\chi_D^2 = \frac{1}{D} \sum_i \sum_m \frac{(\sqrt{H_{mi}} - \sqrt{M_{mi}})^2}{\sigma_{mi}^2} \tag{3.11}$$

For a large spectral data set, particularly in imaging, the LP-ICA modelling process can be time consuming and require heavy computational effort. Therefore, maximally compressed data sets should be used. This was achieved by carefully selecting data

to keep only the most useful pieces of information, with less time and memory consumed. The discussion of this topic is covered under pre-processing methods (Section 3.3) designed specific for LP-ICA, and the background to the mass spectrometry imaging data formats (Section 2.4.2).

3.4.6 Maximisation Separation (MAX SEP)

The Likelihood estimates of ICA components and weighting factors need not be unique. Due to the possibility of linear degeneracies in the $\sum_k P(m|k)q_{ki}$ terms, there can be multiple equally good solutions, i.e. different sets of PMFs, which combined in the right way can yield the same value for $ln\mathcal{L}$ (and correspondingly equivalent values for χ_D^2). It can be argued that, given a choice between multiple equivalent Likelihood models, the better models are those which have better physical meaning.

What constitutes physical meaning is dependent upon the system being modelled. In the case of mass spectra, the components should map onto the correlated appearance of different molecules associated with different types of biological sample. If this is achieved then q_{ki} coefficients will be proportional to the quantities of different materials present, i.e. amount of brain or liver. However, the data fitting process guarantees only that the extracted linear model passes through a best fit hyper-plane; the ICA components themselves are linearly degenerate. ICA components may therefore be linear combinations of the underlying biological samples. Typically, the components extracted might require modification (via subtraction of a common structure) to remove unwanted components of the spectra.

In order to rectify this problem, it is reasonable to assume that certain molecules will exist within some biological materials but not others. This should result in some m/z values being zero in one sample and finite in another. Subtracting the maximum amount of each ICA component from all others increases the chance of finding unique stable solutions and makes model structure ‘simpler’. The criteria for defining

components with simple structure were first suggested in Thurstone (1947) with respect to unit vector models in Factor Analysis (FA), the first three of which are that:

- each row [data vector/histogram] contains at least one zero;
- for each column [factor/component], there are at least as many zeros as there are columns (i.e. number of factors kept);
- for any pair of factors, there are some variables with zero loadings on one factor and large loadings on the other factor;

are consistent without observation of mass spectral behaviour. The 'loadings' in unit-vector models are equivalent to histogram bins found within LP-ICA models. The 'factors' are components, equivalent to probability mass functions in models. When using unit-vector models, the above criteria can be achieved using rotations, e.g. varimax (Kaiser, 1958). In the case of LP-ICA models of histograms, the criteria can be achieved using MAX SEP.

The most popular rotation for unit vector-based linear models (e.g. PCA, FA) is varimax, which maximises the sum of the variances of factors' squared loadings. Such an approach is inappropriate for LP-ICA modelling, as PMFs cannot be rotated in the same way unit vectors can, due to the need to maintain positive only values. In contrast, the MAX SEP algorithm attempts to achieve the 'simple structure' criteria by maximising the differences between PMF components to make them as separate and unique as possible. If a weighted amount of a PMF can be subtracted from another unweighted PMF, such that no probability goes below zero, then a 'new PMF', can be computed:

$$P'(m|k) \;=\; P(m|k) - \alpha P(m|l) \tag{3.12}$$

$$\arg_\alpha \max P'(m|k) := \{\alpha | \forall m : P(m|k) - \alpha P(m|l) \geq 0\} \tag{3.13}$$

A renormalisation step, followed by further application of the model's ICA EM loop can converge upon the simplified components. Varimax solutions do not change the linear space that can be reached by original unit vectors; they only provide components that may be easier to attribute to physical measurements. MAX SEP, however, not only provides components which may map better onto physically meaningful measurements, it also widens the reach of the linear space available for

describing data with positive loadings. The introduction of a greater number of zero bins (loadings) pushes back the origin for data on the hyperplane, permitting data points to be reached that would otherwise require negative weights. It also makes components more orthogonal (They can never be fully orthogonal when there is a spectral overlap).

MAX SEP is expected to be especially useful for separating sub-spectra when a finite quantity of each possible sub-spectrum exists within training data. If a finite amount of each molecule is always present, it is more difficult to determine the location of zero loadings needed to identify unique components. In these cases, there are no Likelihood constraints to force extracted components to be capable of describing compositions of data with zero amounts of some sub-spectra. Satisfying the 'simple structure' criteria, via MAX SEP, should produce more repeatable components.

Chapter 4

Optimisation of Experimental Parameters

4.1 Introduction

As shown in Section 2.2 of Chapter 2, it is clearly seen that MALDI mass spectra comprise the signals of interest with a large number of underlying variables. Even though there is no way of controlling all of the complex characteristics, nor completely removing contamination in MALDI-MS experiments, adjustment of some parameters is still possible in order to optimise MS data acquired from a specific instrument in terms of the signal-to-noise.

The sources of the variability in mass spectra are mainly from the sample preparation method and the mass spectral data acquisition. The former introduces chemical contamination (something that is not interesting measuring), however, it might well be deterministic to some extent and could consistently show up in every mass spectrum. The latter is more complex to handle as variations may be introduced at many stages of the MS process. Different ionised species appear in the mass spectra with uncertain abundance, with suppression, unwanted fragmentation, matrix and electrical effects all combining to add to signal variance. All these sources of unwanted variability add up and appear as an inseparable combination of noise and baseline in the measured mass spectra. This represents a significant challenge for the

quantitation of real variations in signal quantities. Therefore, when it comes to quantifying the amount of a substance of interest using MALDI mass spectra, approaches relying on the relative abundance of a single peak (see Section 3.1.3) are often utilised. If the intensity of the strongest peaks are highly correlated with the amount or concentration of an underlying substance in a sample, the unwanted variability might be so negligible that it does not necessarily need to be removed. The technique seems a good way to simplify quantitation by avoiding complicated pre-processing. However, capturing only one or few peaks will never be good representatives of the entire data set and will introduce bias and random errors to the analysis. This work has developed an alternative method called the linear Poisson ICA analysis in which all mass peaks are used (the method is applied in Chapter 5 and 6). A process of acquiring well-behaved mass spectra is still needed in order to allow the linear Poisson ICA tool to detect real variations.

This chapter defines standard protocols to ensure that the quality of the entire mass range of the mass spectra acquired is satisfactory for use in quantitative analysis, which will be the basis for data acquisition in later chapters. The properties tested include; signal intensity, signal-to-noise and mass resolution, to be optimised against laser power. An appropriate amount of sample-matrix solution and a method of deposition must be selected for the MS instrument used, in order to improve signal-to-noise and repeatability of the measurements. The resultant mass spectral data must be in an appropriate format suited to the requirements of the analysis tools (linear Poisson ICA, TINA tool: Tar and Thacker (2014)). Note that the parameter adjustments recommended in this chapter are general guidance for the process to optimise conditions in MALDI mass spectral data acquisition. Another aspect of this chapter is that it provides a better understanding of the performance of the instrumentation and techniques used, including their quantitative capability. Slight alterations were made in order to finalise the set of parameters for each particular experiment in upcoming chapters.

4.2 Instrumentation

Two different MALDI mass spectrometer models, a Kratos AXIMA and Kratos 7090 were used in non-imaging and imaging experiments, respectively. The MALDI-TOF-MS instrument used at the Wolfson Molecular Imaging Centre (WMIC), the University of Manchester is an AXIMA CFR+ TOF^2 model from Kratos (a Shimadzu group company). The 7090 MALDI-TOF^2-MS instrument is available at the Kratos Analytical Laboratory based in Manchester. Both models are capable of imaging acquisition. This section gives general specifications of both models and the standard parameter settings used for acquiring lipid MS profiles in the remaining parts of this thesis.

4.2.1 The AXIMA

The AXIMA model was the instrument used to perform all non-imaging experiments. The MALDI laser was a neodymium-doped yttrium lithium fluoride (Nd:YLF) laser, frequency tripled to a wavelength 349 nm. This instrument can operate at 200 Hz laser repetition rate, with beam diameter of about 100 µm. In each experiment, the laser power was adjusted such that the signal to noise is optimised, and kept constant throughout the experimental session. Note that only the AXIMA was used in this chapter, since only non-imaging experiments were performed at this stage.

4.2.2 The 7090

The 7090 model was used to perform the MS imaging experiments (See later in Chapter 6). It has a 2 kHz laser pulse rate (solid state UV laser, frequency tripled Nd:YAG), wavelength 355 nm. It has tunable laser beam diameter which was set to be 50 µm when acquired data in the experiment.

4.2.3 Standard Apparatus Settings

In lipid MS acquisition, the mass range 1 – 1500 Da was selected and pulsed extraction was optimised at molecular mass of 750 Da. (mass range 1 – 2500 Da, and pulse extraction optimised at 1250 Da for calibration)

4.3 Sample Preparation

4.3.1 Materials

Samples

Milk samples were used because they are examples of complex lipid mixtures and were selected to set out protocols for MALDI-MS targeting of lipids that might also be found in tissue sections. They are easily purchased and expected to have fewer numbers of lipids present in mass spectra than in tissues. Strategies to obtain optimal conditions and parameterisation for lipid MS experiments were justified. Note that specific lipid identifications are not of particular interest here.

Chemicals

Table 4.1 List of chemicals used in experiments

Chemical	Molecular Formula	Description	Manufacturer
2,5-Dihydroxybenzoic acid (DHB)	C_7H_6OH	Matrix (recrystallised)	LASER Biolabs, France
Acetonitrile (ACN)	CH_3CN	Solvent	Sigma-Aldrich, UK
Trifluoroacetic acid (TFA)	CF_3CO_2H	Strong acid	Sigma-Aldrich, UK
Methanol	CH_3OH	Solvent	Sigma-Aldrich, UK
Chloroform	$CHCl_3$	Solvent	Sigma-Aldrich, UK
Ammonium acetate	$NH_4C_2H_3O_2$	For washing brain tissue	Sigma-Aldrich, UK
Deionised water (dH_2O)	H_2O	Solvent	PURELAB Ultra ELGA, UK
Reserpine	$C_{33}H_{40}N_2O_9$	Calibration standard	Sigma-Aldrich, UK
Angiotensin II	$C_{50}H_{72}N_{13}O_{12}$	Calibration standard	Sigma-Aldrich, UK
ProteoMass™ $P_{14}R$ MALDI-MS Standard ($P_{14}R$)	$C_{76}H_{112}N_{18}O_{16}$	Calibration standard	Sigma-Aldrich, UK

All chemicals are stored as recommended by manufacturers.

Equipment

- Indium Tin Oxide (ITO) coated glass slides from Sigma-Aldrich (dimensions 25 × 75 × 1.0 mm)
- Normal glass slides from Menzel:Gläser Superfrost Plus (dimensions 25 × 75 × 1.0 mm)
- Metal targets (Fleximass target made of stainless steel, part number: TO-483R00) from Shimadzu Kratos Analytical

4.3.2 Preparation of Milk Samples

Fresh cow's milk (Sainsbury's British Whole Milk) and fresh goat's milk (St Helen's Whole Goats Milk) purchased from a local Sainsbury's superstore were used in all milk experiments. Milk samples were kept in -80°C freezer for storage, and used within 30 days from the date of purchase.

Fresh milk samples were ready to be prepared, or frozen milk samples were allowed to defrost at room temperature for approximately 2 hours before preparation. The same preparation steps for both milk types are as follows:

1.) Milk samples (250 µl) were mixed with methanol:chloroform (2:1) (935 µl) and chloroform (620 µl) in a 2 ml Eppendorf tube.

2.) Vortex each tube containing a milk sample for 15 seconds until the sample and solvents were visually mixed.

3.) Centrifuge all the samples at a frequency of 1,300 rpm, at 20 °C, for 2 minutes. A Heraeus Biofuge Fresco centrifuge was used.

4.) For every milk sample, remove the top aqueous layer and discard the thin solid disc, carefully collect the lipid extract solution present at the bottom layer and transfer into another tube.

5.) Purify every lipid extract by adding 500 µl of water and follow step 2 to 4

6.) Repeat step 5 for a second time

Lipid extract solutions from individual milk samples are thus obtained.

4.3.3 Preparation of Matrix Solution

DHB matrix solution was prepared at a concentration of 10 mg/ml using acetonitrile:water (1:1) as a solvent with the addition of 0.1% TFA.

4.3.4 Sample-matrix Deposition Method for MS Analysis of Milk Samples

Small quantities of sample and matrix solutions (see below for each method) were deposited in a well on a metal target plate and allowed to dry before MALDI-MS analysis. The metal target used has 48 wells as shown in the diagram in Figure 4.3 (see Section 4.4.1), which allows measurements of multiple samples and/or repeats at the same session. Three droplet spotting approaches, described as: matrix top, sample top and pre-mixed methods are defined as follows.

***Matrix top*:**

DHB matrix solution (1 µl) is spotted on top of lipid extract solution (1 µl) in a well.

***Sample top*:**

Lipid extract solution (1 µl) is spotted on top of DHB matrix solution (1 µl) in a well.

***Pre-mixed*:**

Lipid extract solution, DHB matrix solution and methanol were mixed in equal volumes. (2 layers × 1.5 µl of this pre-mixed solution was deposited in a well for equal sample-matrix deposited materials to the matrix top and sample top methods).

Note that extra layers were applied after a previous layer was completely dry.

In addition, an alternative approach using an automatic TLC sprayer (CAMAG Automatic TLC Sampler 4) was tested, to apply more homogeneous sample-matrix materials onto a metal plate and an indium tin oxide (ITO) coated glass slide, where sample and matrix were mixed beforehand (lipid extract solution, DHB matrix solution and methanol in a ratio 1:1:1.5). The device is a nebuliser that can be moved across the sample at a programmable rate of dispense and movement in x and y directions, similar to commercial nebulisers for matrix deposition. The spray builds up thin layers of the sample-matrix solution, until the same amount of materials is deposited as the above methods. This mimics the nature of samples containing complex lipid mixtures, similar to tissue samples (that might be imaged) but where matrix was mixed thoroughly with the sample. See also Section 4.3.5 for the TLC sprayer apparatus details.

4.3.5 Matrix Deposition Method for Imaging Samples

Two different approaches for matrix deposition were tested by spraying matrix solution onto a glass slide surface in order to observe the coating quality under a microscope. The quantity of matrix material deposited on the glass slide was also measured in order to ensure that the parameters used for both deposition techniques resulted in comparable deposited quantities. This was done using high performance liquid chromatography (HPLC) using a calibration curve of known concentration matrix standards (for the detailed procedure, see Deepaisarn (2015), in TINA memos, 2015-016: http://www.tina-vision.net/docs/memos/2015-016.pdf).

SunCollect

The SunCollect (SunChrom, Germany) is a commercial instrument built specifically for use as a matrix applicator for MS imaging samples. The machine generates jet of spray using a pneumatic nebulisation. The nozzle has x–y–z adjustable positioning and spraying dimensions relative to the surface to be coated (where the z-axis is perpendicular to the surface). The number of layers deposited can be programmed and run consecutively.

TLC Sprayer

An instrument designed for TLC sample application (CAMAG Automatic TLC Sampler 4) was assessed as an alternative approach for matrix deposition on imaging samples. The nozzle has x-y adjustable positioning at a fixed spraying distance to the coating surface. It has the ability to vary the spray head temperature, and thereby adjust the solvent content of the droplets. The number of layers can be programmed but the syringe needs to be refilled every 5 successive layers.

4.3.6 Calibration Standard

The standard for mass calibration was a mixed solution of 3 peptides: reserpine, angiotensin II and ProteoMass™ $P_{14}R$ MALDI-MS Standard ($P_{14}R$), as recommended by the manufacturer. The molecular weights for the three standards are 608.68, 1046.18 and 1532.86 Da, respectively.

4.4 Parameter Adjustment for Optimising Mass Spectrometry Data Acquisitions

4.4.1 Initial Tests of Instrumental and Technical Performance

This experiment was carried out using the lipids extracted from cow's milk samples and DHB matrix (see Sections 4.3.2 and 4.3.3 for preparing instructions). In each MS measurement, 200 mass spectral profiles were accumulated with 5 laser shots per profile, whilst the laser was moved at random within the region of interest (within a well of 2.8 mm diameter). In general, very poor quality mass spectra can be visually rejected. These are selected on the basis of poor signal-to-noise level and/or the misalignment of main peaks by more than ± 1 Da. Poor signal-to-noise ratio (S/N) is normally observed when the laser does not fire right on the "sweet spots" (dense accumulation of crystals) of the sample-matrix mixture.

First of all, the standard method of sample-matrix deposition, the so-called "matrix top" method as referred to Section 4.3.4 was used to test for an appropriate thickness of sample-matrix depositions onto the metal surface in terms of homogeneity of the deposited materials and the S/N obtained. Optimal thickness was determined by varying the number of application layers. For a given thickness, laser power was varied to observe S/N, signal intensity and mass resolution of a specific peak, m/z 760.5, (N.B. the scale for laser power in the instrument is uncalibrated and expressed in arbitrary units). This test was performed for each of

the matrix-sample application techniques, i.e. spotting (matrix top) and TLC spraying on a metal plate and an ITO glass slide (see Section 4.3.4 for the application methods). The laser power that gave the most appropriate results (see the discussion below), was selected to be used throughout the repeatability tests in the following experimental Section 4.4.2.

Mass spectra were acquired from calibration spots at various locations on the same target plate to test for systematic errors in mass-to-charge measurements due to plate misalignment or ion extraction field variations.

Thickness of Sample-matrix Materials

The images presented in Figure 4.1 show microscopic appearance of how sample-matrix crystals formed in wells using the "matrix top" method of application with 1, 2 and 3 layers applied.

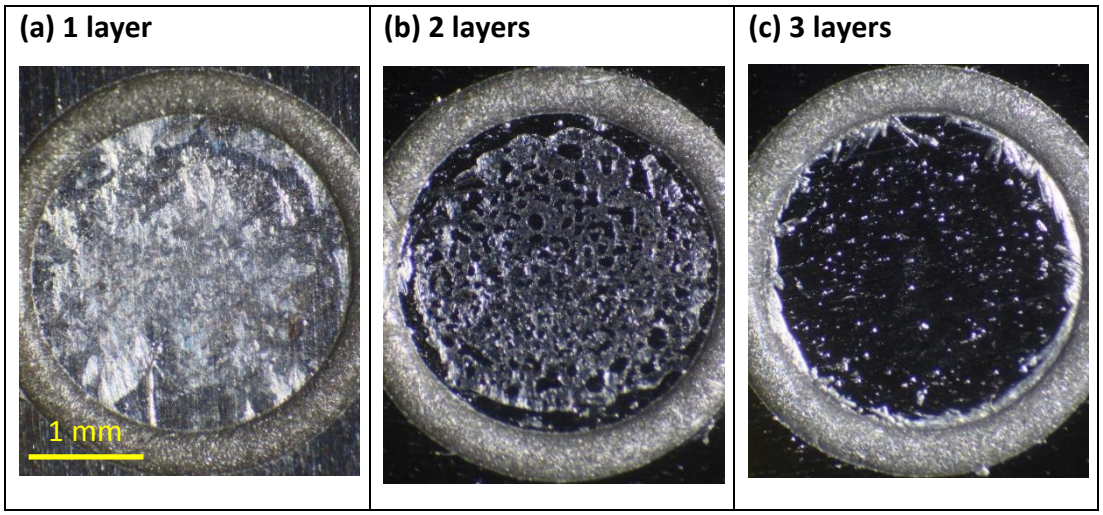

Figure 4.1 Microscopic views of matrix top applications of cow's milk samples with different numbers of sample-matrix application layers (all at the same magnification)

Higher energy was needed to generate a similar ion current when there was a thicker layer coated on the metal surface of the target plate. 1-layer application formed a thin layer of material onto the metal surface, allowing mass spectra to be acquired

at the lowest threshold laser power. The mass spectra produced under these conditions were relatively noisy, which may relate to the fact that not enough analyte was deposited in the well. The image in Figure 4.1 (a) shows also that the crystal size for the 1-layer application was relatively large and distributed unevenly. In comparison, the image in Figure 4.1 (b) shows the 2-layer application to be a more homogeneous distribution through the well as more analyte is present. 3-layer deposition not only increases the chances of spilling of material outside the well, but also generates a higher background noise level compared to the 2-layer method. Thus, the 2-layer application method was selected for use in subsequent experiments.

Laser Power

MS measurements were acquired across a range of laser powers from 90-180 (arbitrary units) for the different deposition techniques, including the "matrix top" spotting on a metal plate, the TLC spraying on a metal plate and the TLC spraying on an ITO glass slide. S/N, signal intensity, and mass resolution (see the definition for FWHM mass resolution in Section 2.2.6) were observed (using Shimadzu Launchpad software of AXIMA mass spectrometer) at varied laser power, for the MALDI-MS peak at m/z 760.5 of milk samples. The influence of laser power on these parameters is discussed below.

For all sample-matrix application methods, the measured signal intensity and S/N increased with increasing laser power to a plateau at higher laser powers as observed at a representative peak (m/z 760.5). In contrast, mass resolution decreased slightly as a function of laser power. This decrease was usually observed approximately at laser powers where S/N was greater than 200. Saturation of ion detection was another factor of concern. On this basis, an appropriate laser power was selected such that the detected signal would not exceed 100 mV. Such a laser power was observed to prevent saturation for this instrument and still generate good S/N for quantitation. The selected laser power of 135 for the "matrix top" method was also

used for all other spotting methods. Whereas those TLC spraying method (applied on metal and glass plates) used a laser power of 137.

Calibration

Calibration standards gave an expected MALDI mass spectrum, allowing 500 mDa tolerance for peak adjustment, as seen in the spectrum in Figure 4.2. This was determined by the precision of the instrument.

The graphs presented in Figure 4.4 shows how the measured m/z of the calibration peaks can vary with the position (see the diagram in Figure 4.3) of the calibration standards deposited on the metal target.

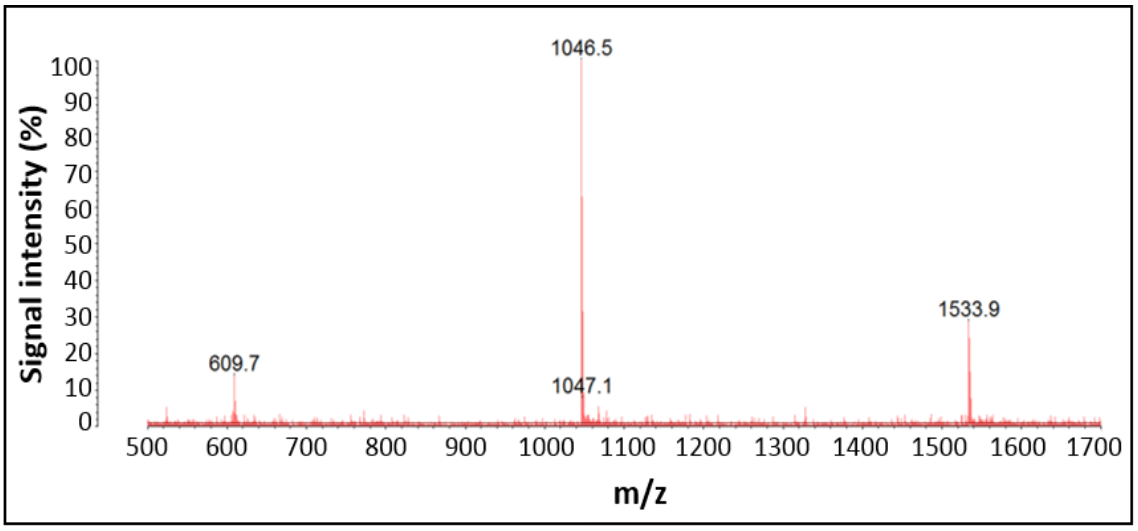

Figure 4.2 Mass spectrum of the calibration standards with peaks m/z 609.7, 1046.5 and 1533.9

The m/z values of the three peaks were observed to vary as a function of horizontal spatial location at which the laser was fired on the metal target plate, as summarised by the graphs plotted in Figure 4.4 (a). Whereas no clear trends were observed by varying position in the vertical direction as seen in the graphs plotted in Figure 4.4 (b), variations for the m/z 609.7 and 1046.5 peaks were within 1 Da (values fluctuate within $\pm$ 0.5 Da from the accepted values). These may arise from the slide alignment

and/or the angle from which the laser beam was fired and/or from variations in the local electric field during ion extraction.

Considering the MS lipid data set's mass range of interest is below m/z 1000, the safest range to allow for alignment of different acquisitions should be $\pm$ 1 Da (as this applied to the calibration standard peaks in the same mass range).

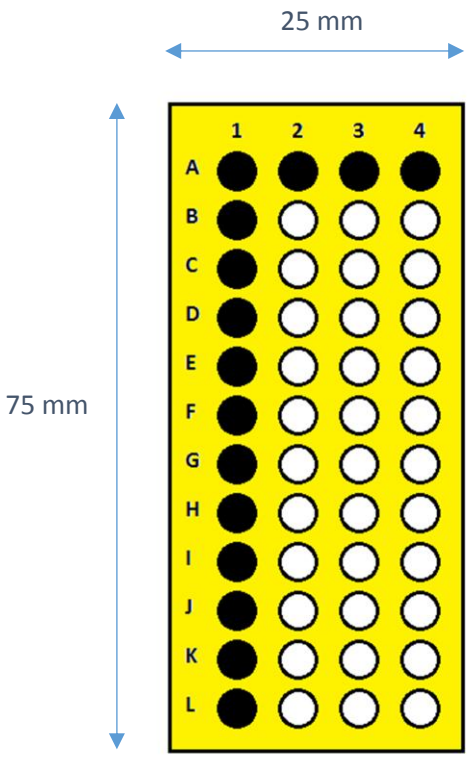

Figure 4.3 Diagram of the metal sample plate indicating well positions (black colour) where calibration standards were deposited for the dimensional variation test. The diameter of a well is 2.8 mm.

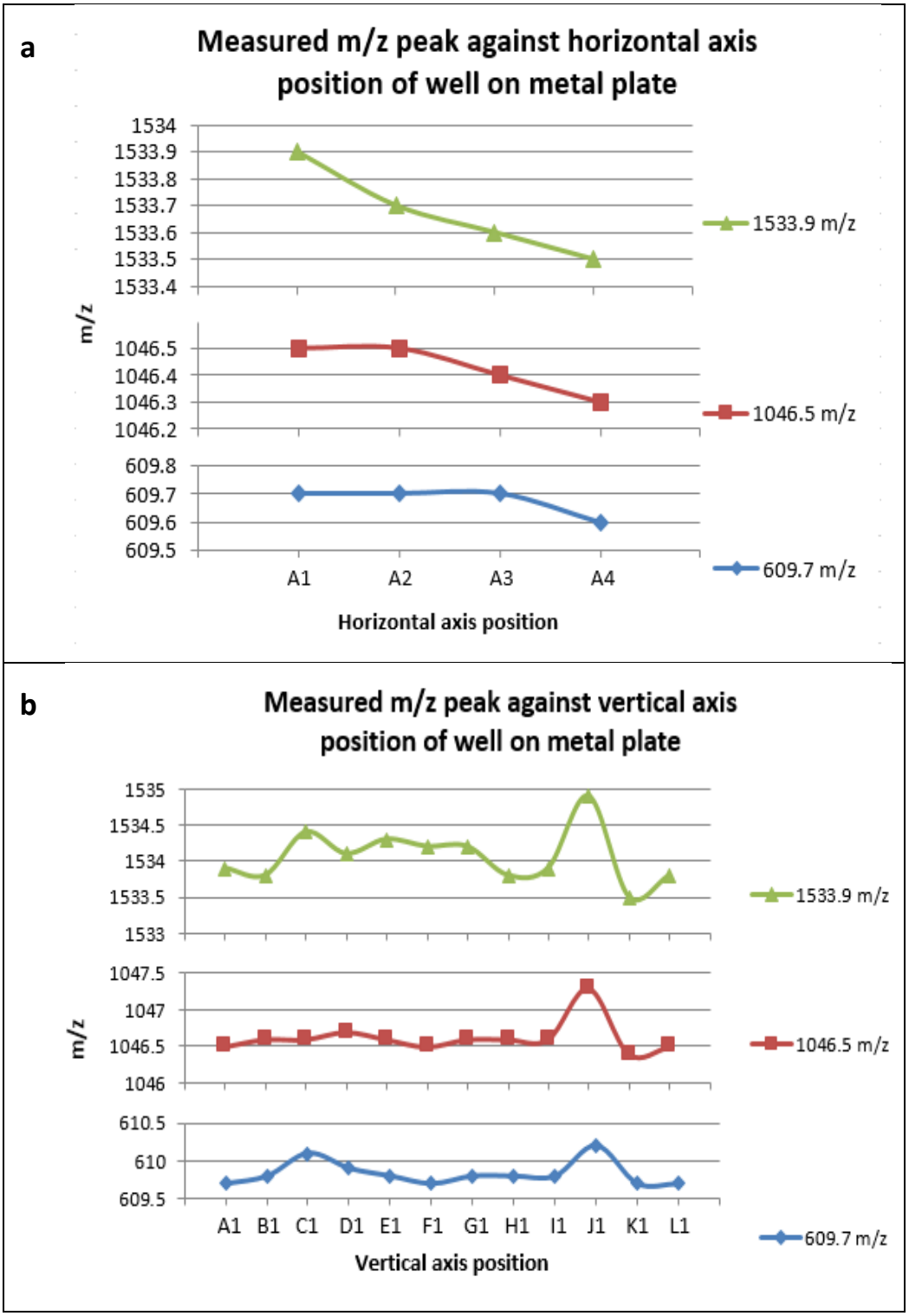

Figure 4.4 Measured m/z values for the m/z 609.7, 1046.5 and 1533.9 calibration peaks vs. (a) horizontal position and (b) vertical position on the metal target plate

Discussion

The fluence (laser energy per unit area) is an important parameter which is a function of laser pulse power and laser spot size. It is not constant across the spot as the intensity distribution is at best Gaussian and at worst very uneven, with hotspots. Therefore, the averaged effect of these local (within spot) fluence variations were seen. Varying the laser power alters the fraction of molecules ionised, and hence leads to variation in ion signal intensities (as observed in mass spectra, recorded as peak height at each m/z value). Relative quantification of peak ratios will be considered reliable if the peaks have their S/N above some threshold. The absorption and dissipation of energy in matrix-sample crystals and the resulting plume involve a variety of possible mechanisms. The energy transfer rates at each step of the process also depend on many factors, such as matrix type, temperature, photon penetration depth. In the case of thick sample-matrix deposition, as with the 3-layer matrix top application, higher laser power is required (the threshold for ion formation is higher), as the laser fluence is known to exponentially decrease with depth (see Equation (2.2)). The energy deposited may be enough to excite a large amount of matrix but not enough to ionise the co-crystallised analytes resulting in a high matrix signal but with poor analyte signal-to-noise (Knochenmuss, 2013). Reduction of ion signal intensity for the analytes could also occur if the deposited materials are heated to some extent, as some matrix might evaporate, especially in the vacuum, due to the fact that DHB is quite volatile. The heat could come from irradiating at too high a laser power or from the ambient temperature inside the instrument (of 45 ± 2 $^{\circ}$C for the AXIMA).

It can be assumed that laser power was approximately of the order of 10^8 W/cm^2 at the threshold for signal detection of most organic molecules crystallised with DHB (corresponding to a laser power of about 135 in the AXIMA instrument used in this study) as this is usually the threshold for completion of the desorption and ionisation processes (Morrical *et al*., 1998). The experiment on varying laser power has illustrated that the signal intensity increases with the laser power, then levels off possibly because of a saturation effect causing a high intensity to be recorded up to a threshold value. Saturation must be avoided because it introduces non-linear

effects on mass spectral signals recorded – i.e. when only the higher intensity peaks are saturated. Mass resolution is also worsened at higher laser power as discussed earlier in this section. The laser power that provides just enough energy to give reasonably good S/N but does not ruin the statistical characteristics of the spectra is therefore preferred for quantitative purposes.

Most of the peaks from the calibration standard spectra at different plate locations varied in mass within ± 0.5 Da from the accepted m/z values as shown in the graphs plotted in Figure 4.4 which was expected from the tolerance limit of the instrument (the figure of ± 0.6 Da was quoted in Yao *et al.* (2014)). Some major causes of the observed mass shift could be due to the electric field inhomogeneity at the surface, given that the sample is not in a perfect infinite parallel plate geometry. Rare cases with greater uncertainty could come from other influences on mass accuracy. One could be inhomogeneity of deposited surface thickness that was not taken into account but can affect flight-time measurements of identical analyte. Another one could be that measuring and detecting very low concentrations of standard at specific points might give poor quality spectra, especially with a distorted distribution of major isotopomer peaks of the calibration standards that may be more concentrated in some deposited region can lead to a wrong peak being picked as an expected calibration peak. It is suggested that mass spectra from a data set acquired by this instrument are allowed up to a 1 Da range to align to account for the fluctuation of up to ± 0.5 Da away from the true m/z values.

4.4.2 Repeatability Tests of MS Spectra from Milk Samples

In this experiment, solvent extracted lipids from cow's milk sample and DHB matrix were used. MS measurement were acquired in the same way as described in Section 4.4.1 (200 profiles of MS spectra, 5 laser shots per profiles). All sample-matrix deposition methods described in Section 4.3.4 were compared. The following 2 sets of MS measurements were considered for every sample-matrix deposition method.

1.) ***Between-well repeatability*****:** A single MS measurement was acquired from each of the 3 repeat depositions of same sample in separate wells. For every MS measurement, laser was fired at random within a corresponding well.
2.) ***Within-well repeatability*****:** 5 repeat MS measurements were acquired from the same deposition of sample in a well. The laser was fired at series of different positions within the well in order to yield good S/N.

Note that when the TLC sprayer approach was used for applying sample-matrix onto an ITO glass slide, repeatability tests were conducted onto similarly-defined well regions as with the metal plate – i.e. the regions on the glass slide, where each single spectrum was recorded, were drawn with equal size and at the same positions as on the metal plate.

Simple Pre-processing and Analysis Approach

This simple approach for baseline correction and the subsequent method to compute peak area ratios were used in this chapter only.

A simple approach for mass spectral baseline correction was performed, where a baseline was estimated by linear interpolation of the minima in each of the 30 data point intervals (determined by the approximate width of a peak), throughout the full range of every spectrum. Then, the estimated baseline was subtracted from the original spectrum. Note that the same approach for baseline correction was also used in the experiment to observe change in peak area ratios as a function of the relative milk concentration (see Section 4.4.3). Integrating over the full-width half maximum region of peaks at a specific m/z in a mass spectrum is used here to determine peak area and hence peak area ratios in both the repeatability and concentration tests.

Mass spectra were recorded as the accumulated signals from all profiles acquired. After pre-processing, the mass spectra of all sample-matrix deposition methods, either the raw data or processed data using spline interpolation (using Matlab to smooth the spectra), were compared to determine the variance of ratios between peak areas of 2 selected ion peaks (see the result in Table 4.2). Where the peaks m/z

760.5 vs. 734.5 were selected from cow's milk spectra because they were observed as major peaks in every acquisition and also in the MSI spectra of rat brain tissue. These peaks appear in the phospholipid mass range as stated in Veloso *et al*. (2011) in a study of lipid distribution in human brain.

Variance Analysis

The appearance of extracted cow milk lipid samples deposited with DHB matrix into wells on metal slides, using the different application techniques are shown in the images provided in Figure 4.5. The "matrix top" approach produced large matrix-analyte crystals with quite a uniform distribution in the well. In contrast, the "sample top" approach deposition has poor uniformity with limited crystal formation. Whereas the pre-mixed sample and matrix gave clear needle-like crystal shapes. Because the sample and matrix are pre-mixed in the solvents, they were allowed to interact more closely and co-crystallise more evenly on the slide. Spraying methods where pre-mixed solution was applied onto both metal and ITO glass surfaces, provided a highly uniform distribution of materials with relatively fine crystal sizes since small amounts were deposited locally using the TLC sprayer with the constant rate of application.

From these, it appeared that the "sample top" method generated visibly non-uniformity of deposited materials relative to other methods. Also, when test acquisitions were performed, it gave mass spectra of very poor repeatability with the worst S/N compared to other deposition techniques. Therefore, the "sample top" approach was rejected from this repeatability test.

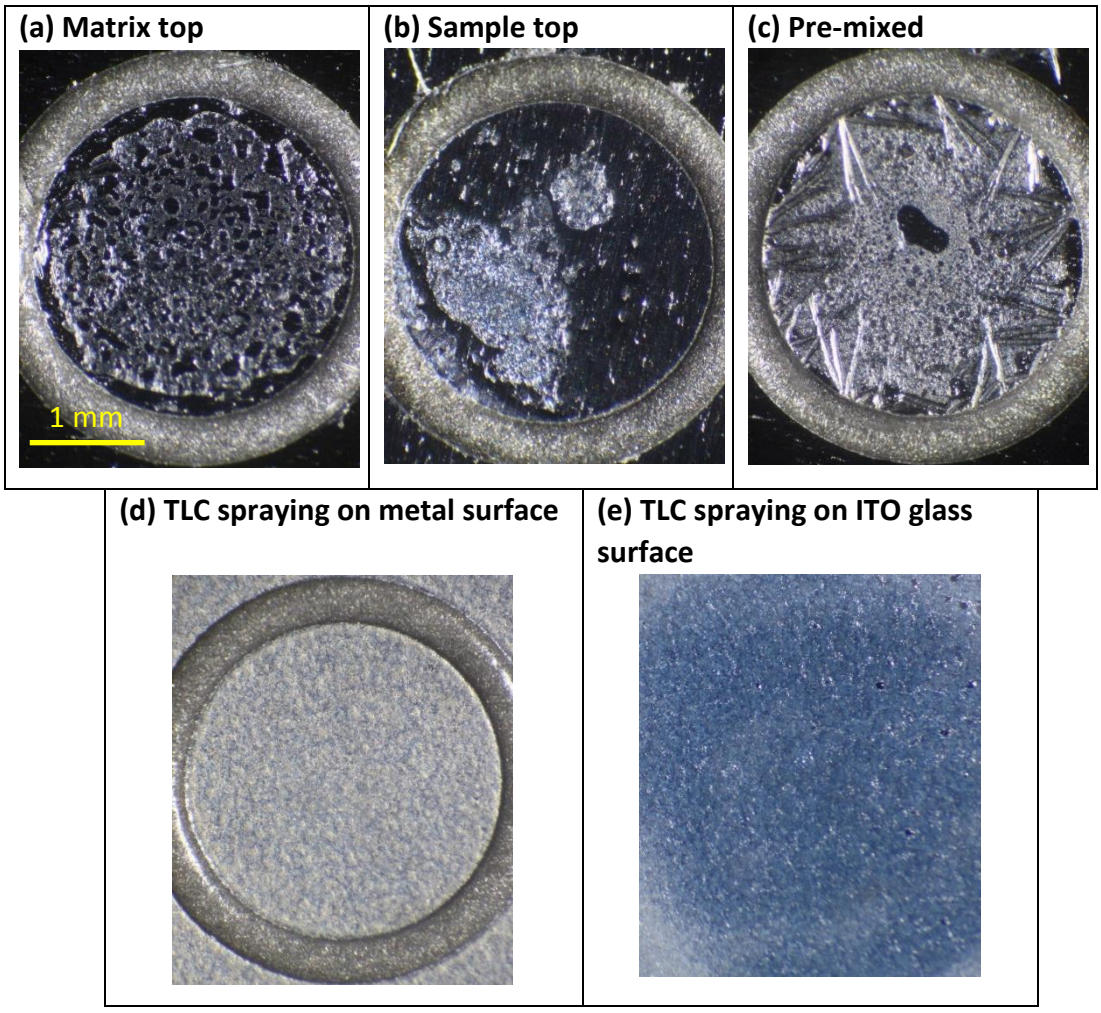

Figure 4.5 Microscopic views of sample-matrix materials deposited using different techniques (all at the same magnification)

All other deposition methods were included in the within-well and between-well repeatability assessments. From the recorded spectra (see examples of pure cow's and goat's milk spectra in Figure 4.6 (a) and (b)), the ratio between m/z 760.5 and 734.5 peak areas (FWHM), was calculated to test for repeatability as the ratio was expected to be constant for every acquisition of samples of the same concentration across deposition positions. These were analysed through the analysis of variance (ANOVA) calculation. The results are summarised in Table 4.2, giving two sets of results which arose from the peak area (FWHM) ratios calculated from the raw data and the interpolated data (smoothen between data points within mass spectral peaks).

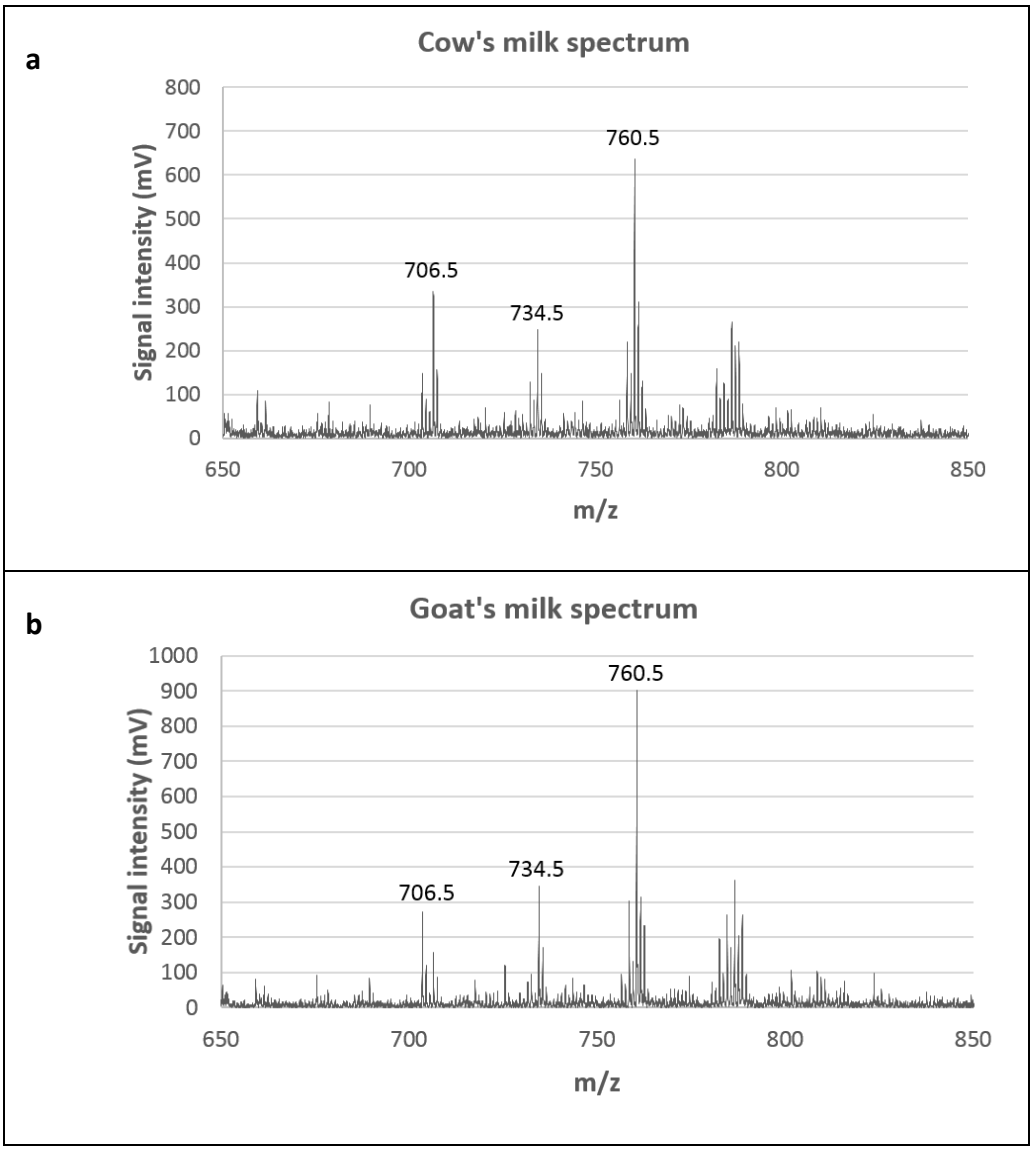

Figure 4.6 Examples of pure cow's and goat's milk mass spectra (acquired using the pre-mixed deposition method)

Table 4.2 Summary of ANOVA for peak area ratios (m/z 760.5 vs. 734.5) resulting from different sample-matrix deposition methods

Method	Raw data				Interpolated data			
	Source of variation	Degrees of freedom	Mean square deviation	F-statistic value	Source of variation	Degrees of freedom	Mean square deviation	F-statistic value
Matrix top	Between-well	2	0.0514	6.94	Between-well	2	0.0497	7.00
	Within-well	12	0.0074		Within-well	12	0.0071	
	Total	14	0.0439		Total	14	0.0421	
Pre-mixed	Between-well	2	0.0066	0.54	Between-well	2	0.0064	0.53
	Within-well	12	0.0122		Within-well	12	0.0120	
	Total	14	0.0443		Total	14	0.0436	
TLC spraying (metal plate)	Between-well	2	0.0099	0.64	Between-well	2	0.0086	0.54
	Within-well	12	0.0153		Within-well	12	0.0158	
	Total	14	0.0561		Total	14	0.0572	
TLC spraying (ITO glass slide)	Between-well	2	0.0083	0.60	Between-well	2	0.0094	0.67
	Within-well	12	0.0137		Within-well	12	0.0141	
	Total	14	0.0499		Total	14	0.0517	

The F-statistic values were determined by dividing between-well and within-well variances. To test the null hypothesis that all wells are identical, the critical value for F with degrees of freedom of 2 and 12 in the first and second sources of variation is given as 3.885 (P=0.05) (Miller and Miller, 2010). Only the "matrix top" method exceeds this value and leads to rejection of the null hypothesis. Whereas all other methods give much lower F-values than the critical value which represent low variations of MS measurements between wells compared to within the wells.

Discussion

It can be suggested that the "matrix top" approach produces quite a uniform spread of sample with a large excess of solvent evaporated (chloroform and methanol) before the application of matrix, making the sample and matrix mix and interact reasonably well in the first sample-matrix application layer. Then, the second layer of sample-matrix application may re-dissolve part of the first layer deposition, and hence leads to more uniform re-crystallisation given a longer interaction between sample and matrix. Different sample-matrix deposition methods led to significantly different surface appearance as seen in the images in Figure 4.5. There appears to be poor sample uniformity for the "sample top" approach – i.e. matrix-analyte crystals were formed only in some places in the well and the acquired mass spectra were not visually repeatable. The preferred crystal structure (needle-like) can be seen in the pre-mixed sample and matrix. Firing laser onto locations with these crystals encourages ionisation and produces a good level of signals. Very uniform deposition was observed when using the spray-based methods to apply pre-mixed solution onto both surface types, however, no clear sweet spot was visually observed due to smaller crystals formed. This supports the observation in Section 4.4.1 where spray-based deposition methods required a slightly higher laser power than spotting deposition methods to give comparable signal levels.

The analysis of variance of the peak ratios (m/z 760.5 vs. 734.5), using the raw data acquired from samples deposited by the pre-mixed spotting method (on metal surface), and the spraying method on metal and glass surfaces have their F-values equal to 0.54, 0.64 and 0.60, respectively. The conclusion was that the MS

measurements did not differ significantly from deposition to deposition when using the same deposition method (P=0.05). Also, the spline interpolation method did not make significant changes in the F-values, hence, only the raw data were used to analyse the milk concentrations in the subsequent experiments. Note that the matrix top method was found non-repeatable according to ANOVA with F-value of 6.94.

So far, it can be confirmed that using pre-mixed sample-matrix solution provides the most repeatable results regardless of deposition method. However, the spraying method is not practically convenient when dealing with large number of samples, and also requires significant effort to prepare. Therefore, the most efficient method for use in non-imaging experiments was the "pre-mixed droplet" deposition.

4.4.3 Matrix Coating and Signal Analysis

Comparison of Matrix Coating Techniques

The appearance of DHB matrix (10 mg/ml, see Section 4.3.3) coated onto normal glass slides using different coating techniques was observed under a microscope as illustrated in Figure 4.7, for the TLC sprayer and SunCollect methods of application (see Section 4.3.5). The sizes and quantities of deposited crystals were comparable in both techniques when the following parameters were set for each instrument.

TLC sprayer: 2 µl per layer, application area 15 x 15 mm

SunCollect: Flow rate 20 ml/min, medium nozzle speed

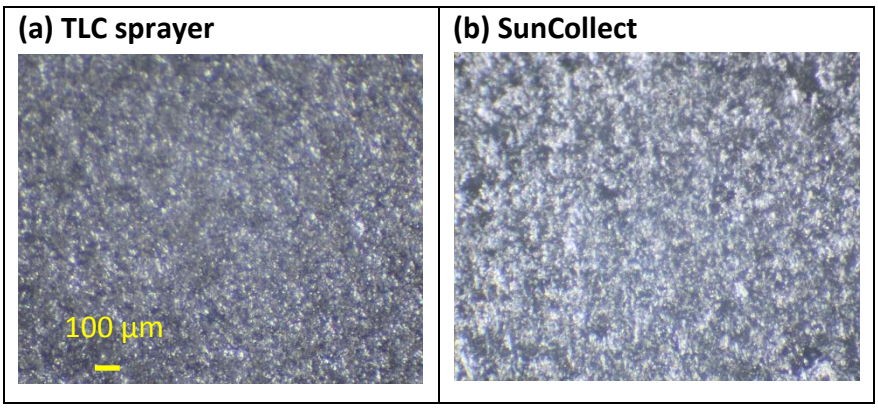

Figure 4.7 Microscopic views with same magnification of matrix coated onto glass slides via (a) TLC Sprayer and (b) SunCollect

Nevertheless, there are a number of factors that prevent the TLC spraying technique from being used as a substitute for the SunCollect. The major problem is the wait time for refilling the syringe which can reduce the smoothness of the deposited matrix as they are allowed to dry for different times between layers. In addition, the speed at which the nozzle moves cannot be adjusted directly but is controlled by setting the application area instead.

Quantifying Milk Concentrations

The pre-mixed sample-matrix solution can be deposited using the TLC sprayer, which is proved to have a good between-well repeatability in Section 4.4.2. It is therefore appropriate to use the TLC spraying approach to trial the quantitative measurement using a similar method of deposition as for imaging (the SunCollect performance was mimicked). Cow's and goat's milk samples were mixed at various concentrations before solvent extraction at ratios 100:0, 75:25, 50:50, 25:75 and 0:100 (cow's milk : goat's milk, by volume). Peak area ratios from each milk concentration were calculated to find correlations with the relative concentration.

The simple quantitative analysis as described in Section 4.4.2 was assessed in this experiment with deposition on both metal and ITO glass surfaces. The best linear fittings of peak area ratio against the known cow's milk concentration in the milk mixtures, observed at peak ratios of m/z 760.5 versus 706.5, are plotted in Figure 4.8.

When using the TLC sprayer method on a metal plate,

$$y = (-0.036 \pm 0.004)\mathrm{x} + (5.439 \pm 0.267)$$

When using the TLC spraying method on an ITO glass slide,

$$y = (-0.042 \pm 0.006)x + (6.069 \pm 0.373)$$

The m/z 760.5 and 734.5 peak area ratios are constant across all concentrations as seen in the plot in Figure 4.9. Where mean ratios from metal plate and glass slide experiments are 2.09 ± 0.16 and 2.11 ± 0.09, respectively – not significantly different.

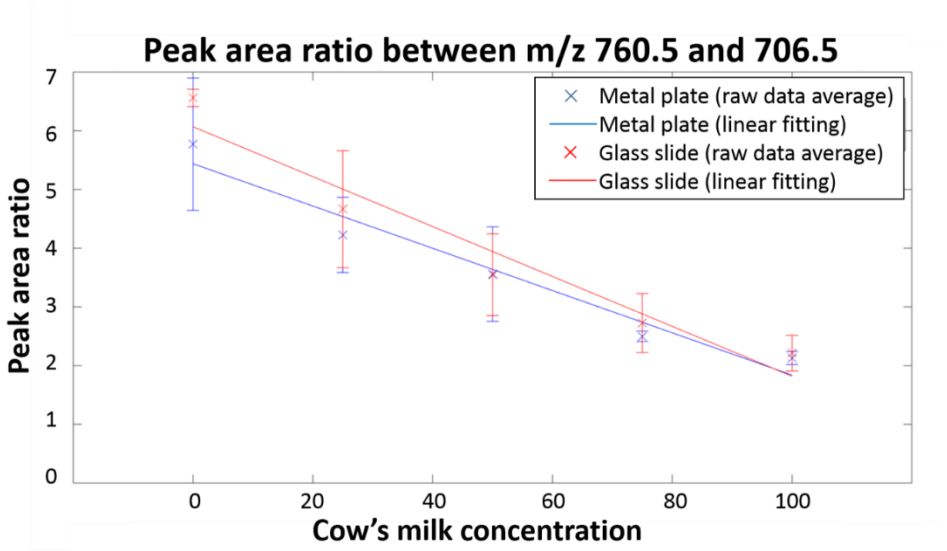

Figure 4.8 Peak area ratio (m/z 760.5 : 706.5) vs. cow's milk concentration (% by volume) using the TLC spraying method of deposition on a metal plate (blue) and a glass slide (red) where error bars represent the standard deviations from the mean of peak area ratios at each concentration from 4 repeated MS measurements from the same sample deposited in 4 different wells – i.e. 1 measurement per well

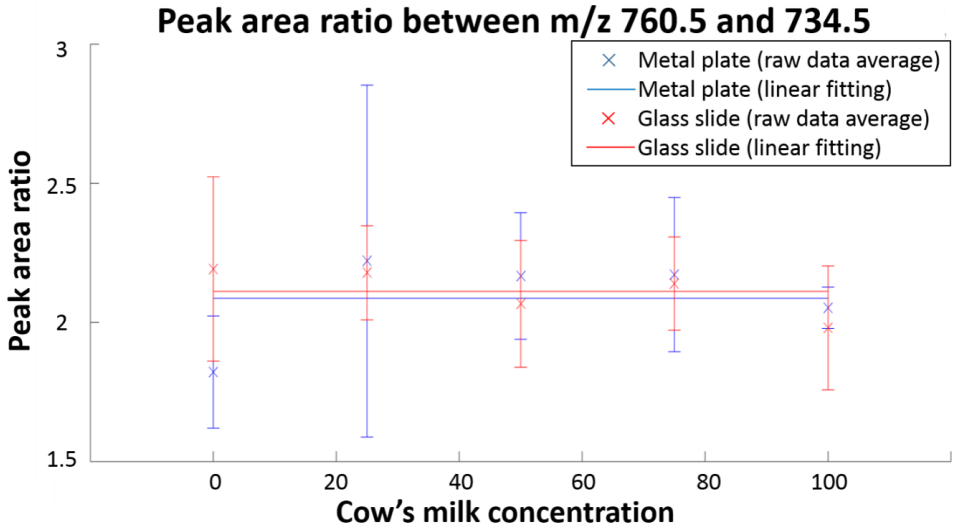

Figure 4.9 Peak area ratio (m/z 760.5 : 734.5) vs. cow's milk concentration (% by volume) using the TLC spraying method of deposition on a metal plate (blue) and a glass slide (red) where error bars represent the standard deviations from the mean of peak area ratios at each concentration from 4 repeated MS measurements from the same sample deposited in 4 different wells – i.e. 1 measurement per well

The quantitative analysis of milk concentrations that results from deposition on both surface types agrees very well, suggesting the similarity of the mass peak determination on either surface. The spraying device coated the surfaces with good adhesion and uniformity. Without clearly seen sweet spots that normally give high signals, the signal levels were nonetheless reasonably high and consistent everywhere.

This strongly suggests that deposition by spraying will prepare samples appropriately for imaging, with a good signal level, given the correct matrix-analyte proportion.

Discussion

The SunCollect apparatus has been shown to be able to generate small matrix crystal sizes, with diameters of less than 50 μm and lead to a very homogeneous matrix layer deposited onto the tissue surface (Römpp and Spengler, 2013). For a simple quantitative milk experiment, TLC spraying parameters were adjusted to perform similarly to the SunCollect system in terms of the amount of matrix applied per unit area per layer. The mass spectra were repeatable as previously observed in Section 4.4.2 and the signals were also reasonably good. In real imaging sample preparation, matrix application rate has an important influence on matrix-analyte interaction while depositing. The sprayed matrix solution should not wet the sample too much so that analytes are not displaced. With the SunCollect sprayer, appropriate distance and the pressure of application can be achieved by adjusting positions of the spraying nozzle and flow rate of the matrix solution, with multiple layers applied continuously, such that the right amount of matrix is applied.

The AXIMA instrument requires long acquisition times, as it is limited by the data transfer rates between the detector and analysis computer, to a sampling rate of about 200 Hz. This affects its imaging capability because an imaging data set contains thousands of mass spectra and therefore it can take a few hours to acquire, depending on the image size and spatial resolution, and the sample should not be left under a vacuum in the instrument for too long. The temperature inside the instrument might cause some matrix evaporation and the vacuum can cause

shrinkage at the edge of the sample section. The superior 7090 instrument acquires the same resolution imaging data set 10 times faster. It can also achieve higher spatial resolution (up to 10 µm), better mass accuracy and the mass resolution (up to 10,000 FWHM vs. 5,000 FWHM for the AXIMA), due to the longer flight path and improvements in the pulsed extraction design.

A linear correlation was found between the specific peak area ratios (m/z 760.5 vs. 706.5) and the proportion of milk types. Thus, given appropriate sample preparation and analysis, MALDI-MS data does allow quantitation of sample proportions. From this basis, in the following chapters, the aim is to improve the analysis with more advanced algorithms that utilise all the useful information contained in an MS data set, and then progress to adapt the method to quantify mass spectrometry imaging data.

4.5 Conclusion

This first experimental chapter addressed the basic aspects of sample preparation and instrumentation used. The capabilities of the instrumentation and the important parameters used to optimise performance have been identified and assessed.

MALDI-MS data acquisition can rely heavily on the experience of the user. Consistency depends on optimising key parameters in each experimental step: from sample washing/extraction, sample-matrix application, to laser power, diameter and beam movement. Important findings that need to be embedded in protocols and carried forward to next experimental chapters are;

- Laser powers with optimal signal-to-noise ratios were determined, giving ion signals of ≤100 mV, to achieve reasonable quantitative data analysis.
- The instrument should be calibrated to an accuracy of ± 0.5 Da to allow for the variation in spectral alignment of within 1 Da range across a data set.
- Repeatability tests for each deposition method for the cow's milk lipid extract samples with DHB matrix were compared by variance analysis. The methods where sample and matrix solutions were pre-mixed showed similar

repeatability regardless of the application techniques. The spotting technique was preferable for analysing multiple (non-imaging) samples in the same session.

- There exists a linear relationship between the ratio of integrated areas of two selected peaks and the concentration of milk mixture. Given that one of the selected peak varies with the concentration and the other peak (normalising peak in this case) is approximately constant throughout the data set. Measurements taken after spraying materials including matrix on MALDI target plates provided very consistent signal intensities from laser shot to laser shot. This confirms the possibility of quantifying MALDI-MS data in both non-imaging and imaging modes.

Chapter 5

Quantifying Binary Mixtures of Biological Samples

5.1 Introduction

In mass spectrometry, the formation of gas phase ions from complex biomolecules typically destroys structures of interest. John B. Fenn and Koichi Tanaka overcame this problem, sharing the 2002 Nobel Prize in chemistry for matrix-assisted laser desorption/ionisation (MALDI) and electrospray ionisation (ESI) (Hillenkamp and Peter-Katalinić, 2007). MALDI co-crystallises complex samples within an easy to ionise matrix. Samples and matrix are vapourised and ionised with a laser, giving a pulsed source of ions ideal for TOF mass analysis. The ability to mass analyse large molecules with high detection sensitivity makes MALDI attractive for biological sample analysis, with applications ranging from milk adulteration detection, e.g. Calvano *et al.* (2013), to cancer studies, e.g. Rodrigo *et al.* (2014). MALDI can also form images by sampling across a 2D lattice (Fülöp *et al.,* 2016), with mass peaks forming pixel values. These data sets are massively rich, with hundreds of mass-specific images able to be generated per acquisition. A method of data mining such images would be a valuable enabling tool, allowing molecular correlations to be identified and mapped upon biological structures. Such a system must quantitatively model the complex variations and attribute them to classes of interest, e.g. tissue

types. This may be achieved using linear modelling approaches, such as Independent Component Analysis (ICA), as in Gut *et al.* (2015). As a step towards a more general data mining system, this work presents an ICA approach that is believed to match well with the properties of MALDI data and therefore provides additional advantages over traditional linear modelling methods, including the ability to build error models.

MALDI mass spectra (MS) are complex and highly variable. Careful preparation and acquisition can mitigate against some factors, e.g. Seeley *et al.* (2008), but requires training, practice and skill. Ideally, a homogeneous specimen might be expected to produce spectra that are repeatable to levels of statistical sampling noise. However, MS exhibits many other modes of variation:

- Ionisation and detection vary depending upon local matrix density, chemistry, laser intensity and duration of acquisition (Astigarraga *et al.*, 2008).
- Fragmentation is not a major process in MALDI. However, long chain molecules can fragment by a number of mechanisms and also have isotopic variations. Matrix molecules which absorb high energy can also fragment in many ways. These would introduce background chemical noise.
- Protonation is not the only process for cation formation. In fact, sodium and potassium ionisation is often observed, even following attempts to wash away soluble salts.
- Suppression effects exist, where the presence of certain chemicals can mask or change the appearance of others due to different affinities for attracting charge.
- Unwanted ions can contaminate mass spectra, including those from the MALDI matrix.
- There is a near-continuous 'chemical noise', from ungated post-source decay processes and ion scattering, superimposed on any inherent instrumentation noise.
- The instrumentation and the detection process involve a series of electronic components which contribute random signal fluctuations – i.e. electrical noise.

A complex biomolecule will generate a series of MS features, which undergo correlated variations in intensity and position, depending upon equipment settings and local sample environment, e.g. Szájli *et al.* (2008). Aside from these variations, MALDI mass spectra are approximately linear combinations of sub-spectra from a sample's constituent chemical components. Some sources of variation are reduced through pre-processing. In previous work, pre-processing methods were developed for use where Poisson noise, σ_p is dominant in peaks and Gaussian noise, σ_g is dominant in background (Thacker *et al.*, 2018). Section 3.3 of Chapter 3 provides a description of these pre-processing methods and the definitions of notation used for the two distinct types of noise are explained in the sub-section, Section 3.3.4.

A basic approach to MS analysis is to inspect single peaks that correlate maximally with the parameters to be measured, e.g. Cahill *et al.* (2016). A peak can be normalised to a second peak (or integral over a total ion current) in order to estimate relative compositions. Peaks may also be artificially added to act as internal standards, such as in Chumbley *et al.* (2016). Signals affected by high levels of ambiguity or confounding variability are thus excluded, at the cost of discarding potentially useful information. More efficient methods, such as Principal Component Analysis (PCA) and Independent Component Analysis (ICA), extract correlated peak variations. These approximate the data as weighted combinations of unit vectors, each representing a correlated set of peaks. Comparisons between linear models can be found in Gut *et al.* (2015) and Nicolaou *et al.* (2011), with evidence that ICA is most beneficial. The formulations of standard PCA and ICA algorithms are based upon uniform independent Gaussian errors, often conveniently leading to closed-form solutions. However, MALDI may not be compatible with these assumptions. In particular, Poisson statistics may better describe the counting of ions. Evidence of Poisson nature of MALDI-MS data has been highlighted by others, e.g. Harn *et al.* (2015) and Piehowski *et al.* (2009), with further investigation by this work.

The behaviour of noise can be assessed using Bland-Altman plots (Bland and Altman, 1986). These plot deviations from expected values as a function of signal strength. Monte-Carlo generated Bland-Altman plots in Figure 3.9 (Section 3.4.3) illustrates

independent, identically distributed (iid) Gaussian noise, giving residuals with a fixed spread, and also Poisson noise, where residuals grow with the square-root of the signal. A square-root transform (Anscombe, 1948) can approximately convert Poisson noise into iid Gaussian noise, but this invalidates any assumed linear model of signal as a consequence. The main modelling options available and their key properties are listed in Table 3.2 of Chapter 3, Section 3.4.3.

Using Bland-Altman analysis, there is evidence that a Gaussian noise assumption of the error on measured signals is inappropriate for MALDI data and that a Poisson noise, σ_p assumption is more realistic. In recent work, an ICA method for data with Poisson sampling characteristics was derived (Tar and Thacker, 2014): Linear Poisson Modelling (LPM). It has been applied to planetary and medical images (Tar *et al.*, 2015; 2017; 2018). This method is believed to provide the best match to the properties of MALDI data (according to Table 3.2 of Section 3.4.3 (see the Poisson ICA)) and is therefore evaluated here on the task of measuring mixtures of complex lipid specimens. This method incorporates a Likelihood estimation procedure and a predictive error theory capable of assessing the effects of Poisson noise, σ_p on measurements. An extension, 'MAX SEP', is designed to reduce degeneracy inherent in linear modelling, aiding interpretation of components allowing them to be attributed to biologically meaningful MALDI sub-spectra. The aim of MAX SEP which is to find a unique solution to the model, is similar to that of the varimax, quartimax and equimax rotations, e.g. Kaiser (1958), but is appropriate for positive only data. This current study uses mixtures of cow's milk and goat's milk; lamb brain and lamb liver extracts; and lamb brain white matter and grey matter extracts, targeting mass ranges associated with the samples' lipid content. In addition to applying the new LP-ICA method, single peak analyses on the same data were performed to corroborate mixture measurements and to compare the attainable measurement precision. The work-flow diagram (Figure 1.1) is provided earlier in Chapter 1, Section 1.3.

5.2 Materials and Methods

Section 3.4.3 previously discussed the noise distribution characteristics of data. The Monte Carlo generated Bland-Altman plots showing behaviour of uniform independent Gaussian noise and independent Poisson noise are compared in Figure 3.9. The modelling options: PCA (Jolliffe, 1986), ICA (Comon, 1994), Non negative ICA (Plumbley and Oja, 2004; Plumbley, 2003), Poisson ICA (Tar and Thacker, 2014), etc. are shown in Table 3.2 (Section 3.4.3) describing statistical and signal assumptions, available for varied data properties. The selected method, linear Poisson ICA, is based upon assumptions matching the properties of MALDI mass spectra. Given that MALDI data has the properties noted in the same table which matches the proposed method.

In this chapter, the use of the linear Poisson ICA is illustrated through application to simple MALDI mass spectral data sets to ensure that the method is appropriate for quantifying MALDI-MS data. These include the analysis of simpler lipid mixtures from milk samples and biological tissue samples which give more complex lipid mixtures – i.e. brain and liver tissues, and brain white and grey matter. Given that brain and liver are two different organs that have very different functionalities, they would be expected to have enough distinguishable characteristics for the algorithm to differentiate. Finally, a more complicated problem was set by working on quantifying mixtures of brain white and grey matter, which moved the study nearer to real clinical questions – where the underlying samples in the mixtures have complex spectra with many common characteristics, and fewer distinguishable mass peaks are expected. The existence of background noise/contamination also blurs the correlation of any mass peaks with the underlying sample proportion. Hence, it is a challenge to confirm the suitability of the linear Poisson ICA method for use as a quantitative tool for analysing MALDI-MS data.

5.2.1 Materials

Biological Samples

- Fresh cow's milk (Sainsbury's British Whole Milk, UK)
- Fresh goat's milk (St Helen's Whole Goats Milk, UK)
- Fresh lamb brain (Worldwide Supermarket, Manchester, UK)
- Fresh lamb liver (Worldwide Supermarket, Manchester, UK)

Chemicals

- Recrystallised 2,5 dihydroxybenzoic acid (DHB)
- Acetonitrile
- Trifluoroacetic acid
- Methanol
- Chloroform
- Deionised water

See Chapter 4, Section 4.3.1 for the manufacturer details, related descriptions and calibration standards used.

Equipment

- Stainless steel plate for MALDI-MS
- Two pairs of curved forceps
- Nylon filters of mesh size 40 μm (Corning^{TM}, UK)

Instrumentation

- AXIMA CFR+ TOF^2 MALDI mass spectrometer
- Power Gen 125 homogeniser (Fisher Scientific)
- Heraeus Biofuge Fresco centrifuge

5.2.2 Sample Preparation

Binary mixtures in differing proportions (e.g. class A : class B) act as ground truth: cow's milk with goat's milk mixtures, chloroform extracts of homogenised lamb brain and liver, and chloroform extracts of lamb brain white matter and grey matter. For each pair, mixtures of lipids were carefully prepared in 11 proportions ranging from 0% A (100% B) to 100% A (0% B), in increments of 10%, with proportions determined by weight.

Milk mixtures were prepared prior to lipid extraction, whereas brain and liver lipids were extracted first, then mixed afterwards. For milk samples, 1 ml at each proportion underwent the lipid extraction procedure. For tissue samples, lipid extraction was done separately using 2 g of homogenised tissue of each type (5 preparations per tissue type were repeated in order to get the amount needed to create mixtures of varied proportions for the analysis – i.e. 5 x 2 g of each tissue type were homogenised and extracted separately as the homogenisation worked well with a small amount of tissue).

5.2.2.1 Brain Dissection

A fresh lamb brain was cut into smaller sections of around 1 cm thick along its coronal axis. In each section, careful dissection for white and grey matter was performed using two pairs of forceps to pull them apart. The brain must be placed on a glass plate with ice beneath it during dissection to keep it in as fresh condition as possible.

There are nearly equal amounts of each of the two tissue types in a brain. Approximately 30 g of each tissue type were obtained for the whole lamb brain used. Where 10 g of each were required for this experiment.

The two tissue types are visually and spatially distinguishable. The image of a coronal brain section is presented in Figure 5.1, with the identification of white and grey matter regions labelled.

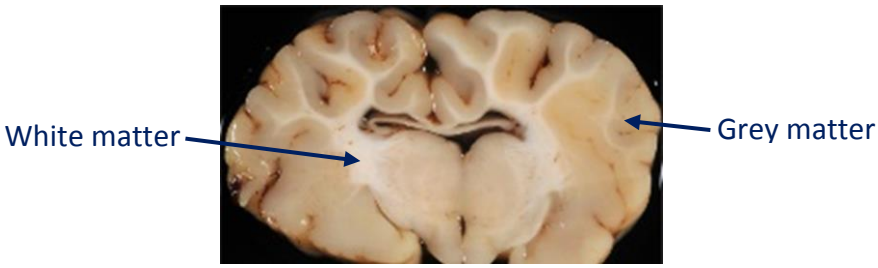

Figure 5.1 Lamb brain white and grey matter as shown in a coronal axis (Pérez et al., 2013)

5.2.2.2 Tissue Homogenisation

10 g of each tissue type – i.e. brain / liver / dissected white matter / dissected grey matter were homogenised prior to extraction of lipids. Note that the homogeniser can only deal properly with a smaller portion of tissue: about 2 g were homogenised at a time. The tissue container was placed in ice during homogenisation to minimise heat building up in the sample.

5.2.2.3 Lipid Extraction

Lipids were extracted by adding 2:1 methanol:chloroform (4.5 ml), chloroform (2 ml) and deionised water (1 ml) to the samples before mixing well. Samples were centrifuged at 1,300 rpm for 2 min at 20 $^{\circ}$C. Levels of natural salts in the resulting lipid extracts were reduced by the addition of 1 ml of deionised water before being centrifuged again.

In the white and grey matter samples, nylon filters of mesh size 40 µm were used to help remove fibrous tissue from the lipid extracts. However, emulsification occurred in white matter, making the lipid extract hard to separate from the water and tissue. The extracting solution of white matter was heated using boiling water to maximise separation between lipid-tissue-water layers. Finally, chloroform was added into the white matter lipid extract to compensate for evaporation.

5.2.2.4 Binary Mixture

For each of the three mixtures mentioned at the beginning of this section, the chloroform based lipid extracts of biological sample (class A : class B) were mixed into 11 different proportions. The binary mixture concentration was varied from pure sample of class A to pure sample of class B, e.g. pure white matter to pure grey matter lipid extracts, with increments of 10%. The Table 5.1 below indicates the exact proportions for these class A : class B binary mixtures which determine the ground truth used in the analysis. Mixtures were made volumetrically but checked for the proportion gravimetrically to account for error associated with pipetting organic solvent – i.e. the proportions of mixtures measured by weight, which are more accurate than those by volume, are taken as actual values. The proportion was calculated as class A concentration versus the total amount of class A and class B in the sample – i.e. for milk, brain:liver and white:grey matter; class A are assigned to be cow's milk, brain, and white matter lipid extracts, respectively.

Table 5.1 Binary mixture proportions as measured by weight

Nominal concentration by volume (Class A %)	**Actual concentration by weight (Class A %)**		
	Cow's milk	**Brain**	**White matter**
0	0.00	0.00	0.00
10	10.74	11.00	8.95
20	19.36	22.41	20.66
30	30.61	32.73	29.12
40	40.11	41.53	38.26
50	49.97	52.34	50.66
60	59.46	63.34	58.73
70	69.35	73.45	71.21
80	80.07	81.94	80.16
90	90.34	91.28	89.54
100	100.00	100.00	100.00

5.2.2.5 Matrix

10 mg/ml of 2,5-dihydroxybenzoic acid (LaserBio Labs) in acetonitrile with addition of 0.1% trifluoroacetic acid was prepared as a matrix solution.

5.2.2.6 MS Sample Preparation and Deposition

The matrix : sample solution was mixed with a ratio of 1:1 for the milk and 3:2 for the tissue samples to form MALDI specimens. Double layers of a MALDI specimen, 1 µl each layer, were deposited into a well of stainless steel MALDI target plate. 8 repeat depositions were applied per mixture proportion to provide repeatability data. The depositing locations of each proportion were randomly positioned on the target plate to avoid correlations between the spatial organisation and the mixture concentration.

5.2.3 MS Acquisition

An AXIMA (curved-field reflectron time-of-flight) mass spectrometer, manufactured by Shimadzu Biotech, was used to acquire the MALDI-MS data. Where the MALDI ionisation system of the instrument is a 349 nm neodymium-doped yttrium lithium fluoride (Nd:YLF) laser of < 5 ns pulse width and approximately 200 Hz repetition rate. Using the positive reflectron mode, an ion extraction energy of up to 24 kV was allowed with an effective drift length of 2.0 m. Launchpad proprietary software was used throughout all of the experiments for controlling acquisition. During acquisition, default settings were adopted (i.e. 200 MS profiles, 5 shots per profile, pulsed extraction 750 Da, mass range up to 1,500 Da). A total of 88 spectra were obtained for each mixture type, one for each of the deposited targets.

5.3 Data Analysis Procedure

5.3.1 Pre-processing

Low m/z MS peaks (e.g. matrix-derived ions) contain little information regarding lipid content. A mass window (m/z) between 650 and 850 was selected for milk mixtures; a window between 690 and 890 for brain:liver mixtures and white:grey matter mixtures. The total quantity of signal gathered per spectrum is difficult to control, making it necessary to pre-filter poor data. Some spectra within this window were rejected on grounds of low signal-to-noise. Spectra containing high signal were also rejected to avoid saturated peaks. A combination of visual inspection and goodness-of-fit tests determined which spectra were kept in order to build satisfactory models. This left 66 milk mixtures, 80 brain:liver mixtures and 82 white:grey matter mixtures, out of the original 88 per group. Pre-processing is performed to ensure that data behaves as linearly additive histograms, with independent Poisson noise (σ_p), as is required for LP-ICA modelling to operate correctly. The methods developed in Thacker *et al.* (2018) satisfy this requirement, see Section 3.3 in Chapter 3. A peak alignment procedure is applied to minimise unwanted shifting of peaks. A baseline correction that assumes noise on the background is approximately Gaussian (σ_g) with zero mean is applied. Finally, histograms are produced containing only bins for significant peaks, with peaks integrated into each bin and inter-peak gaps removed. A total of 102 peaks were retained in the milk spectra, 76 peaks were retained in the brain:liver spectra and 67 peaks were retained in the white:grey matter spectra. The appearance of an example raw spectrum, pre-processed spectrum (after alignment and background/baseline correction), and pre-processed spectrum (after peak detection) are provided in Figure 5.2.

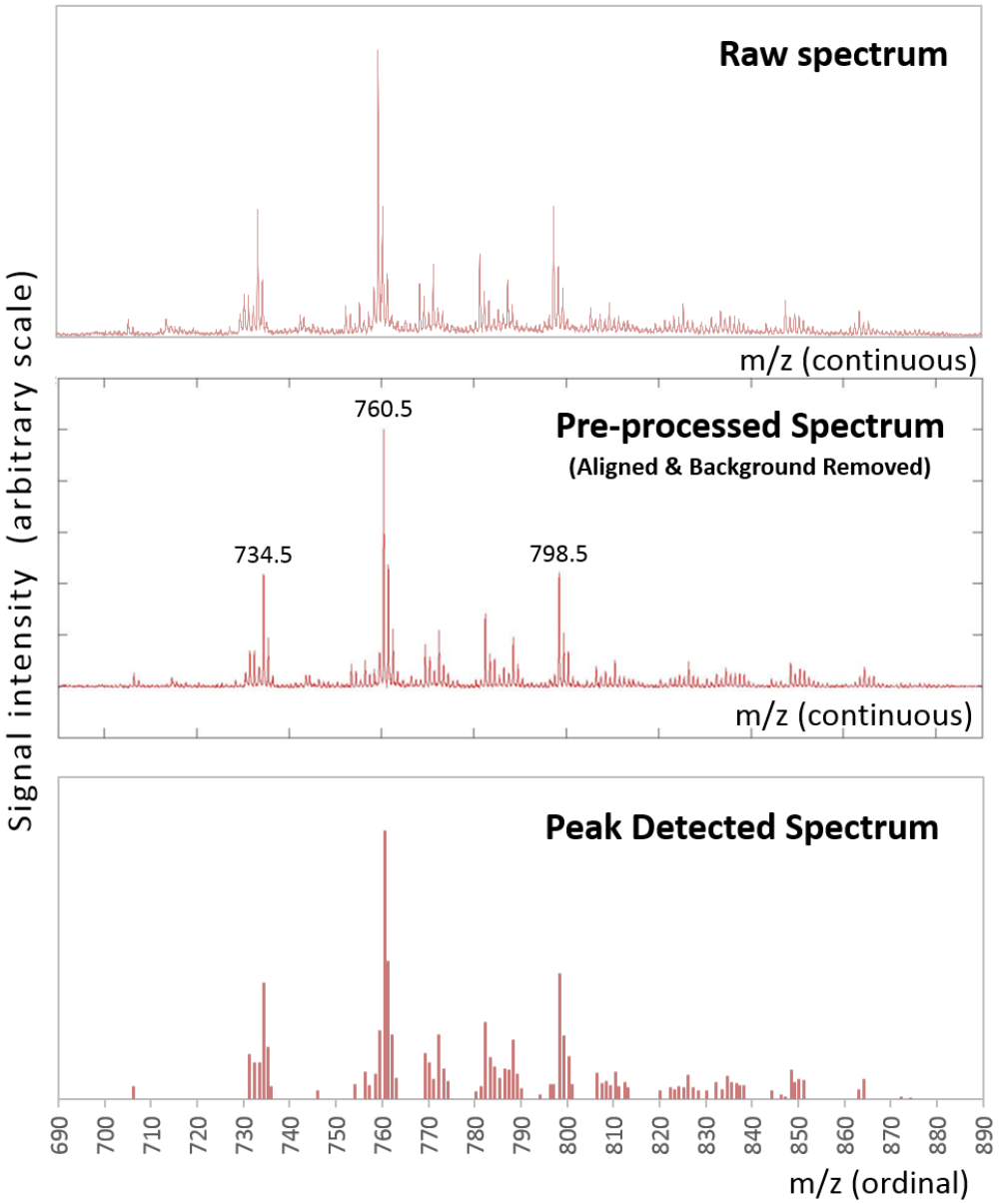

Figure 5.2 Example of averaged raw and pre-processed spectrum before and after peak detection (acquired from the lamb brain lipid extract)

Following pre-processing steps, the resulting (peak detected) spectra for each data set are achieved. The averaged resulting spectra of pure samples are shown in Figure 5.3.

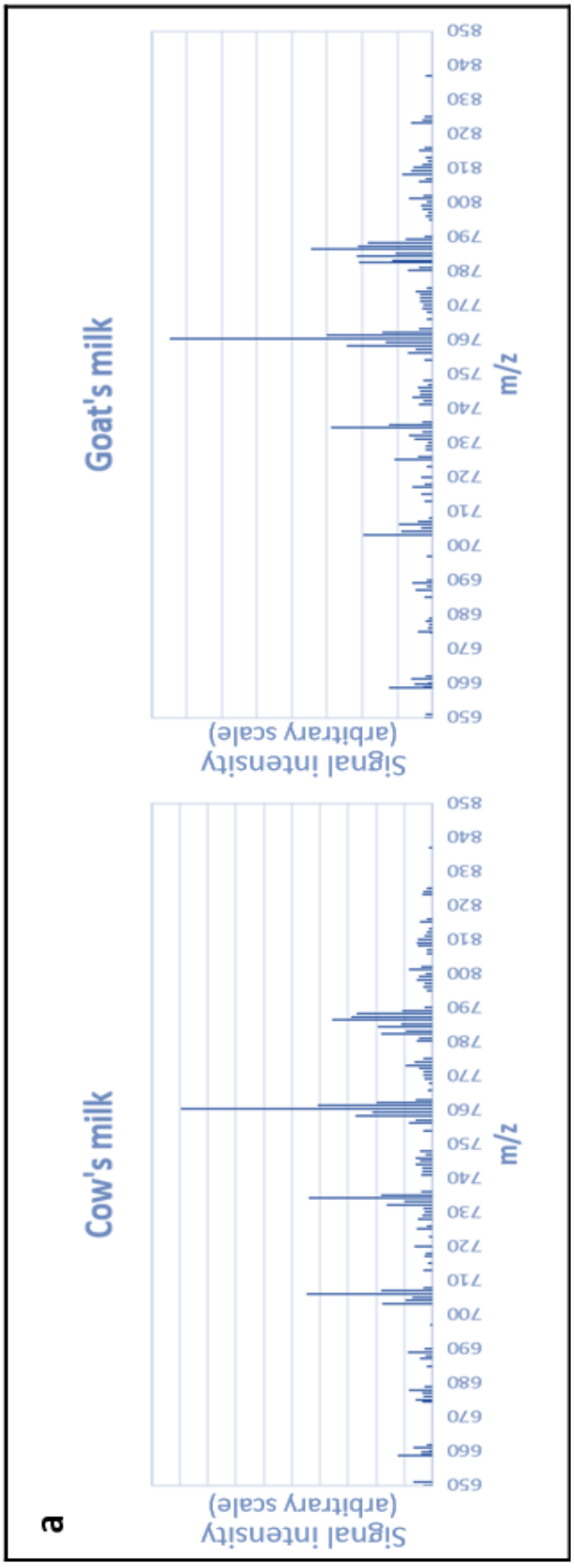

Figure 5.3 Averaged peak detected spectra: (a) cow's and goat's milk, (b) brain and liver tissue and (c) white and grey matter (Part 1 of 3)

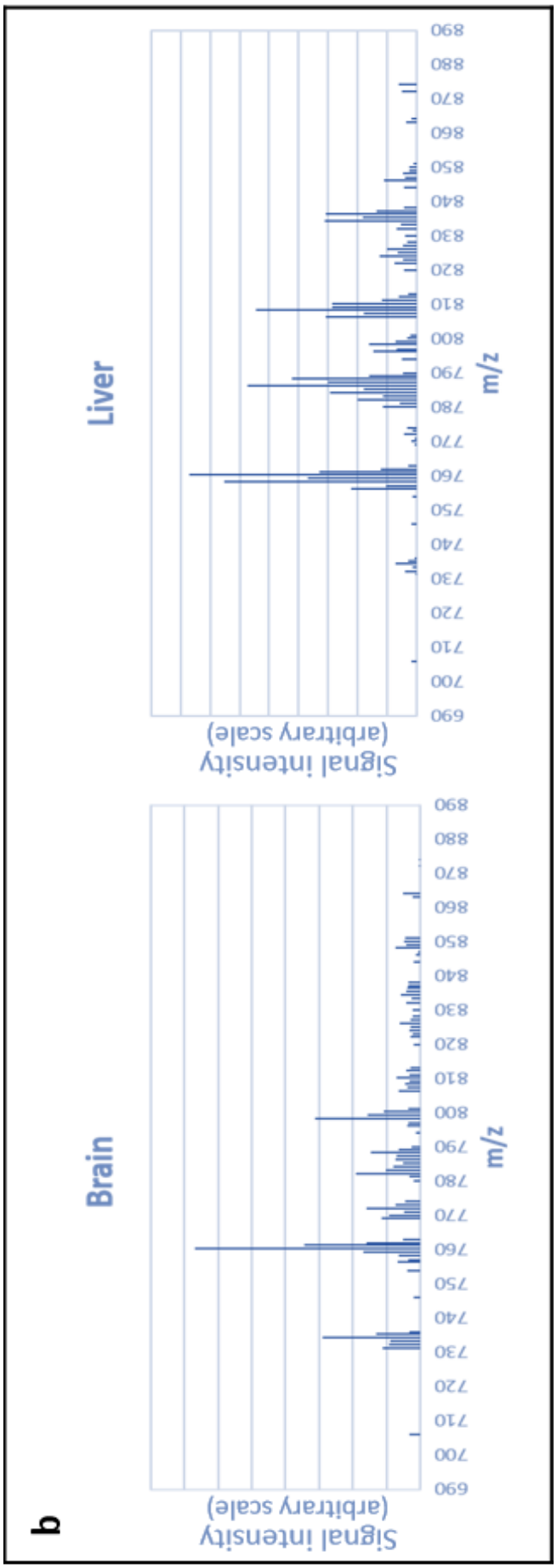

Figure 5.3 Averaged peak detected spectra: (a) cow's and goat's milk, (b) brain and liver tissue and (c) white and grey matter (Part 2 of 3)

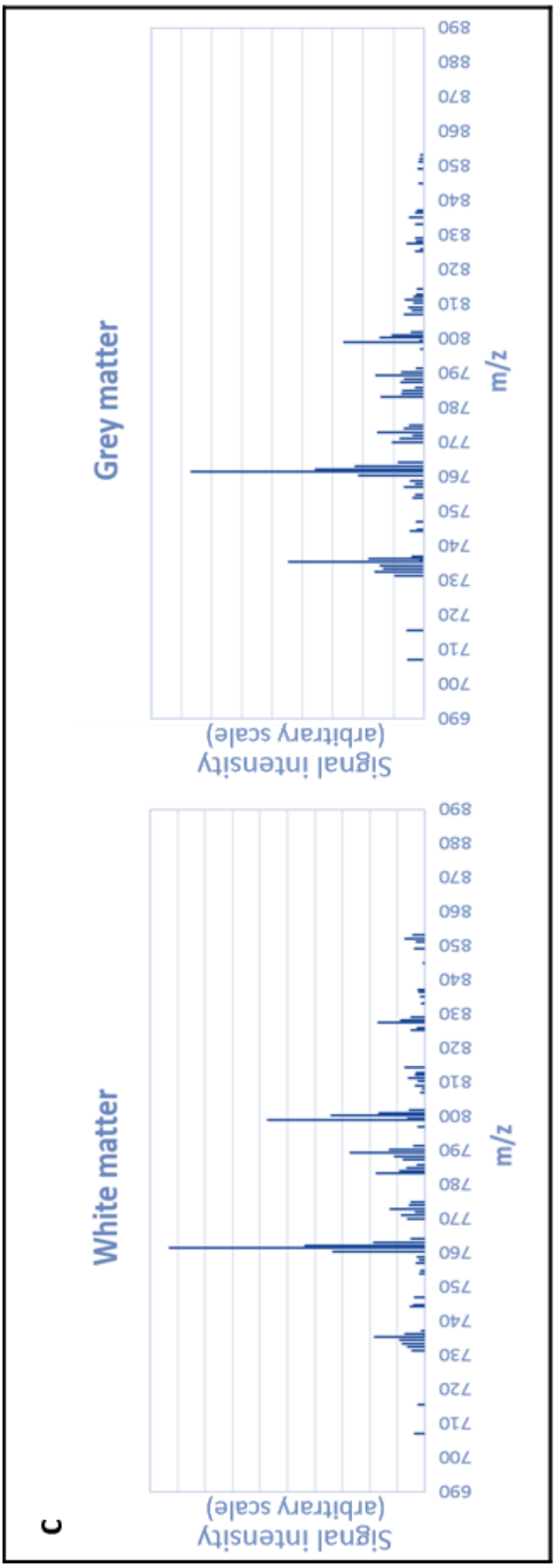

Figure 5.3 Averaged peak detected spectra: (a) cow's and goat's milk, (b) brain and liver tissue and (c) white and grey matter (Part 3 of 3)

5.3.2 Peak Ratio Analysis

A simple peak ratio analysis is applied to estimate mixing proportions for the milk, brain:liver and white:grey matter mixtures as a benchmark against which the new LP-ICA analysis can be compared. Within the lipid window, the largest peak is used for normalisation. This peak is at m/z 760.5 in all three mixture cases, corresponding to a phosphotidylcholine. At each mixing proportion, all peaks are divided by the reference peak, with results for each peak plotted against the known ground truth proportions. A least-squares fit is computed for each peak, which should correlate (or anti-correlate) well with the ground truth if there is useful information present. The most informative peaks (providing smallest errors) were compared to the LP-ICA results. These peaks were at m/z 706.2 for milk mixtures, m/z 786.5 for brain:liver mixtures and m/z 734.5 for white:grey matter mixtures.

Sources of variability, including efficiency losses and possible contamination, make it unlikely that a linear trend extracted from a single peak will have a slope and intercept that exactly predicts ground truth. Rather, the fitted line is used to calibrate a linear predictor that maps normalised peaks to ground truth proportions. The standard deviation of predictions around the calibrated line is used as an estimate of the measurement accuracy attainable from each peak.

5.3.3 Linear Poisson ICA Analysis

LP-ICA models describe the shape and variability of distributions found within histograms using a linear combination of simpler fixed components, with Likelihood estimates of parameters e.g. Barlow (1989) using Expectation Maximisation. Each component can be viewed as a probability mass function (PMF) for a sub-spectrum, representing some correlated set of peaks. Unlike other linear models, LP-ICA models use mixtures of PMFs, rather than unit vectors. This permits positive-only coefficients, appropriate for counting applications such as the ion counting in mass spectra. The mixture of components, fitted on a spectrum-by-spectrum basis,

describes a spectrum as a weighted sum of sub-spectra – see Equation (5.1), adapted from Equation (3.7) in Section 3.4.5 of Chapter 3. The method is illustrated on the schematic diagram in Figure 5.4. An LP-ICA model must determine the necessary PMFs (i.e. sub-spectra) required to describe the distribution of spectra. This process is a Poisson compatible form of ICA, or LP-ICA, which maximises a Likelihood formulation of the problem (Equation (3.8), see Section 3.4.5 of Chapter 3). The number of components required to describe a set of spectra is determined through a model selection process that aims to reach a satisfactory χ_D^2 goodness-of-fit (Equation (3.11), see Section 3.4.5 of Chapter 3). Satisfactory fits are those that either reach a minimum, or lie upon a plateau. In cases of a plateau, failing to achieving a true minimum is compensated for in the error theory, as error covariances are scaled by the final goodness-of-fit. Details of the full method and its validation in other applications can be found in Tar and Thacker (2014) and Tar *et al*. (2015; 2017; 2018).

The Likelihood estimates of LP-ICA components and weighting factors need not be unique. The models created are potentially degenerate, in the sense that different weighted combination of different components could achieve equally good likelihood solutions. The MAX SEP algorithm was therefore designed to reduce this problem by manipulating components to increase their independence – i.e. subtracts quantities of each component from others as far as possible, without generating negative values. The linear components are maximally separated to match individual physical meaning, in this case the correlated appearance of different chemicals associated with different types of biological sample. See Section 3.4.6 for the explanation of MAX SEP algorithm.

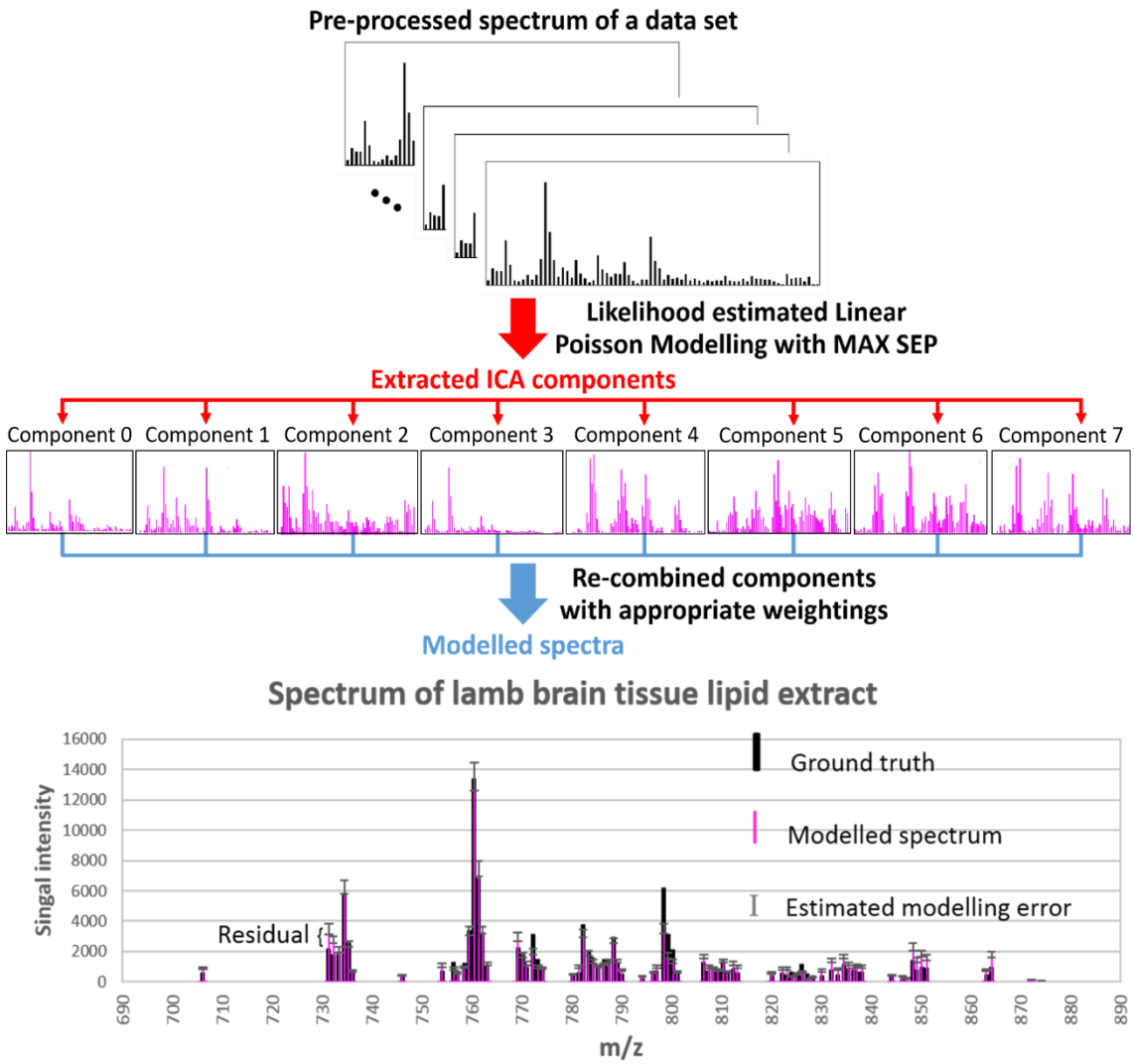

Figure 5.4 Schematic diagram illustrating the linear Poisson ICA modelling method

5.3.4 Mapping Components to Classes

The mixtures of two different biological materials (e.g. brain, liver) will be considered to be composed of proportions from class A and class B. If spectra were stable to within the limits of Poisson sampling and if all molecules within samples were detected with 100% efficiency, there should be only 2 components extracted from such mixtures, i.e. the spectrum for class A and the spectrum for class B. In practice, the numerous sources of variation noted in Section 5.1 lead to multiple components being required to describe spectra. Additionally, the ground truth measurements are based upon the mass of the sample components, which is not, strictly, what is being

measured by the model coefficients. The fragmentation of molecules and their different affinities for attracting charge means only a small fraction of what is in a sample is ever detected, plus the windowing of data and thresholding of small peaks introduces further efficiency losses. As a consequence, the components and their quantities need further interpretation.

Firstly, components must be attributed to classes of material. A component may belong to class A, B, or be contamination belonging to neither class. Secondly, the relative efficiency with which components contribute to the total mass needs to be estimated. These can be solved by the introduction of a new weighting parameter for each component. These weights are optimised in order to achieve the best linear trend between sums of components and ground truth. This is described in Equations (5.1) to (5.3) below.

The contribution to a spectrum, i, containing peak bins, m, from a class, i.e. $class_A$, composed from a subset of components, indices, k, is written as:

$$S_{Ai} = \sum_{m} \sum_{k \in class_A} P(m|k) q_{ki} w_k \tag{5.1}$$

where the total contribution to the class, S_{Ai}, for a given spectrum is a product involving a q_{ki}, dependent upon the component and spectrum, and a further efficiency weight, w_k, dependent only upon the component. To ensure that components are uniquely attributed to classes, a finite weight for one class must correspond to a zero weight for the other. The additional weights, w_k, can be estimated by least squares fitting (via minimisation of root mean square (RMS)) of a line of predicted relative contributions as a function of mixing fractions:

$$F(i) = \frac{S_{Ai}}{S_{Ai} + S_{Bi}} \tag{5.2}$$

$$RMS = \left(\frac{1}{N} \sum_{i=1}^{N} ([\alpha T(i) + \beta] - F(i))^2 \right)^{0.5} \tag{5.3}$$

where $F(i)$ should linearly correlate well with ground truth fractions $T(i)$, given best fitting α, β and set of efficiency weights, w_k. Additionally, the RMS can be scaled to the slope of this line, $\frac{RMS}{\alpha}$ to give an estimate of the predictive accuracy to ground truth.

5.3.5 Spectra Error Analysis

The values recorded within mass spectral bins are expected to be Poisson in nature, as peak heights are proportional to ion counts which are discrete events, occurring in time, consistent with a Poisson process. However, there are additional sources of noise, therefore the Poisson assumption must be checked. The residuals between spectral models and original spectra can be used to assess the validity of the assumption. If binned values are indeed Poisson in nature then the residuals should grow proportionally to the square root of the bin quantity (the signal variance agrees with the Poisson assumption, σ_p). Any fixed scaling of the Poisson process should also be revealed as a scaling factor on the square-root dependency.

Bland-Altman plots, i.e. Bland and Altman (1986), can be constructed and a power-law error model fitted to assess both of these properties. Bland-Altman plots are scatter plots which record expected bin values (i.e. expected peak intensity) on the x-axis versus deviations away from the expected values on the y-axis. The linear model predictions are used as estimates of expected bin values (x-axis), and residuals between model and spectra are the observed deviations (y-axis). A power-law function can be fitted to resulting plots to determine the behaviour. The following function (Equation (5.4)) is fitted to Bland-Altman plots show differences in error behaviour away from the Poisson assumption:

$$\sigma_M = a\left(\frac{H_M}{a}\right)^{\frac{0.5}{b}} \tag{5.4}$$

where σ_M is the standard deviation of model-data residuals; a and b should be unity for non-scaled Poisson bins, and a should be a variance scaling in cases where b is

unity. This variance scaling, a, should also be close in value to the model's goodness-of-fit (χ_D^2), which is an average scaling based upon a χ^2 per degree of freedom. This Bland-Altman approach is a more stringent test than the goodness-of-fit. A value of b deviating too far from unity would suggest that errors are not Poisson. The effects of such a deviation can be evaluated via Monte Carlo if necessary (however, in practice the power-law matches well with the Poisson assumption).

5.3.6 Measurement Error Analysis

Once established, the Poisson noise can be propagated to find its effect on measured values. An error covariance matrix for model coefficients (i.e. estimated quantities, q_i) can be estimated as in Equation (3.10), see Section 3.4.5 of Chapter 3. Assuming independent Poisson errors (σ_p), LP-ICA models provide estimates of quantity errors by summing the effects of individual Poisson bins into quantity error covariances. This is achieved using error propagation. The error covariance can be further scaled by χ_D^2 (goodness-of-fit) computed from model-data residuals to boost errors to better match actual distributions of true residuals, i.e. Poisson scaling factor. Together, the Bland-Altman plots, goodness-of-fits and quantity error covariances summarise the success (or otherwise) of the analysis without any need to refer to ground truth.

Sampling errors in spectral histograms combine to give a level of uncertainty on the estimated quantity measurements. In order to factor these uncertainties into final mixture proportions they must be propagated through the EM algorithm using error propagation, as described in Barlow (1989). This process uses derivative calculations to assess how small changes in inputs (i.e. Poisson noise in data) affects small changes in outputs (i.e. proportion measurements). Equations (3.10) and (5.5b) describe this process.

In a mixture containing 2 sample classes, A and B, the proportion of quantity of class A to the total quantity, $p_A = \frac{A}{A+B}$ has the propagating error, σ_{p_A}.

$$\sigma_{p_A}^2 = \left(\frac{\partial}{\partial A}\left(\frac{A}{A+B}\right)\right)^2 \sigma_A^2 + \left(\frac{\partial}{\partial B}\left(\frac{A}{A+B}\right)\right)^2 \sigma_B^2 \qquad (5.5a)$$

Take square root on both side of the Equation (5.5a)

$$\sigma_{p_A} = \frac{1}{(A+B)^2}\sqrt{B^2\sigma_A^2 + A^2\sigma_B^2} \qquad (5.5b)$$

Where σ_A and σ_B are the standard deviations of estimating values for class A and class B underlying sample, respectively. These final errors, σ_{p_A}, can be compared to actual accuracies computed using knowledge of ground truth values.

Predicted errors (σ_p) via this method can be compared to true measurement errors (σ_{tot}) by dividing the deviations of measured values from ground truth by the predicted errors. These form a Pull distribution, which if unbiased should have a mean of zero, and if precision is correctly predicted should have a width of unity.

In addition to the sampling errors, the Poisson ICA modelling processes is a numerical optimisation method that utilises random initialisations leading to multiple local optima. Local solutions are similar, but do add a level of variability to results. To quantify this, multiple models (i.e. 50) are built to assess the spread of solutions.

5.4 Results and Discussion

5.4.1 Peak Ratio Analysis

The peak ratio approach found that the peak at m/z 706.2 correlated best with changes in milk proportions, m/z 786.5 correlated best with changes in lamb brain:liver tissue proportions, and m/z 734.5 correlated best with changes in white:grey matter proportions. These peaks, for each data set, were normalised to the largest and most stable peak throughout different proportions at m/z 760.5 and the correlation with ground truth via peak ratio analysis is obtained (see the plots

presented in Figure 5.5). The x-axis shows the ground truth proportions. Each cross (data point in the plots) is a peak ratio estimate from a different spectrum, with repeatability data at each 10% increment. Deviations from the fitted line (least square) show typical measurement accuracy. These peaks provide a relative measurement precisions of ± 16%, ± 8% and ± 6%, respectively (see the plot in Figure 5.11 (right)).

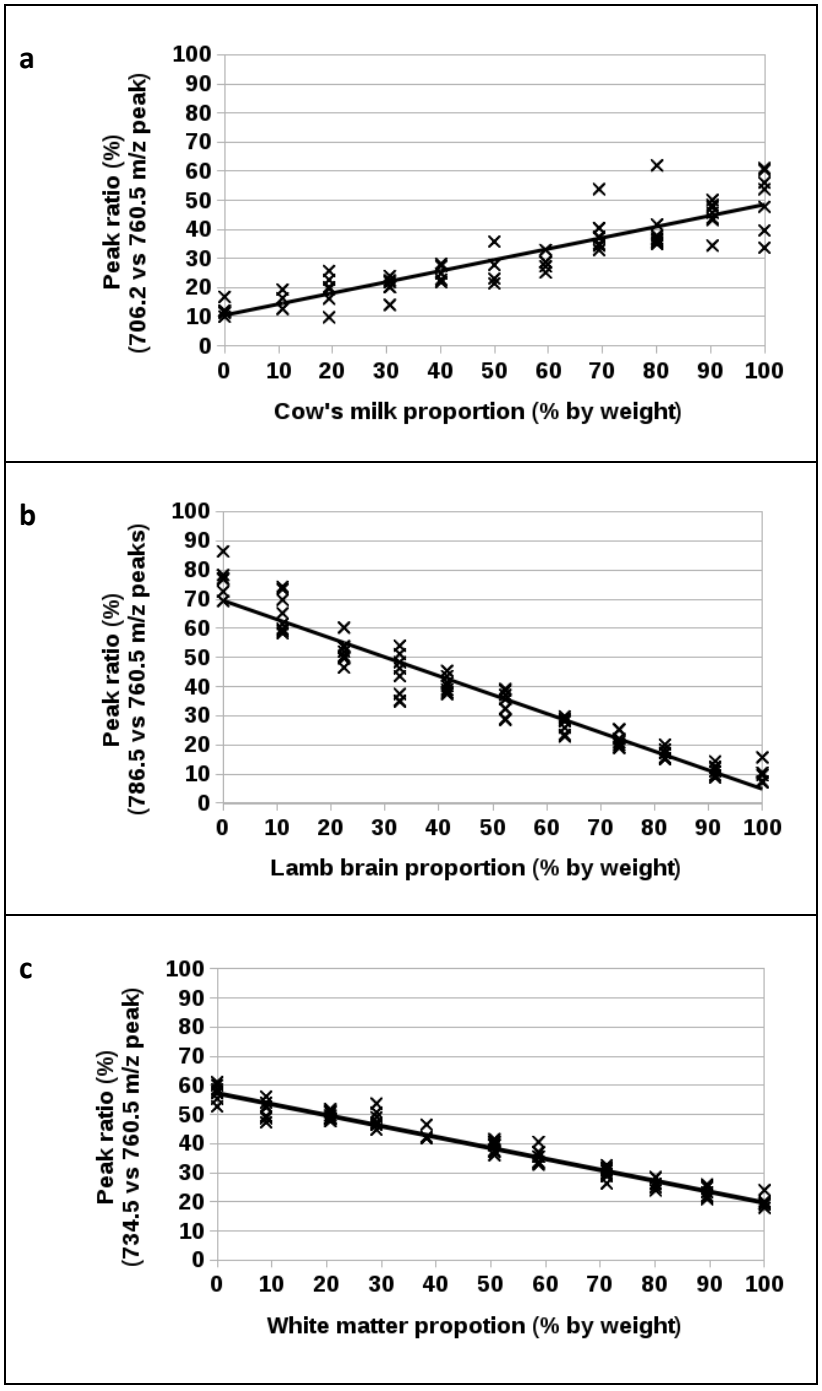

Figure 5.5 Linear fitting for conventional peak ratio analysis results: (a) cow's and goat's milk, (b) brain and liver tissue and (c) white and grey matter

5.4.2 Linear Poisson ICA Analysis

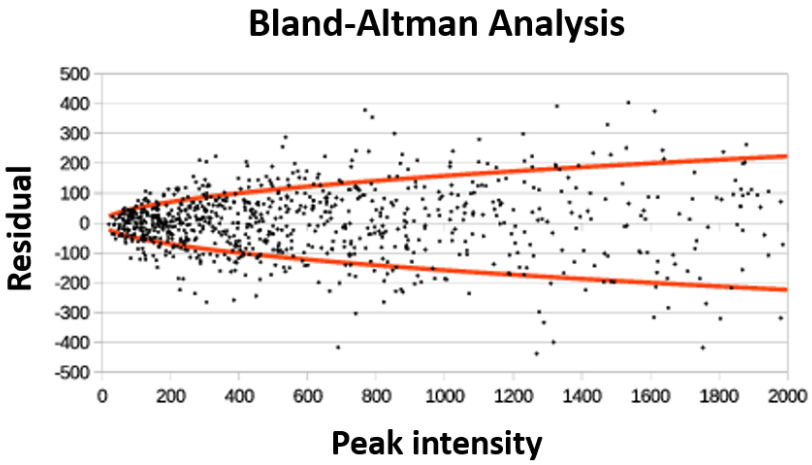

Figure 5.6 Bland-Altman plot showing behaviour of model residuals (y-axis) as a function of peak intensity (x-axis). Each point represents a residual between an LP-ICA modelled spectrum bin and actual spectrum. The fitted curves (power law of Equation (5.4)) show ±1 standard deviation error as a function of peak intensity consistent with Poisson statistics.

Bland-Altman analysis confirms that the pre-processed MALDI spectra are consistent with Poisson statistics (see the Bland-Altman plot in Figure 5.6). The power-law growth parameter (b in Equation (5.4)), was estimated as 1.04 ± 0.02, completely consistent with Poisson style growth in residuals as a function of peak intensity. This justifies the application of Linear Poisson Modelling to perform ICA and mixture quantitation. The power-law scaling parameter (a in Equation (5.4)) was estimated as 23.9 ± 1.4, consistent with the χ^2_D goodness-of-fit, suggesting that each Poisson event is equivalent to an increase of 5 units of signal intensity.

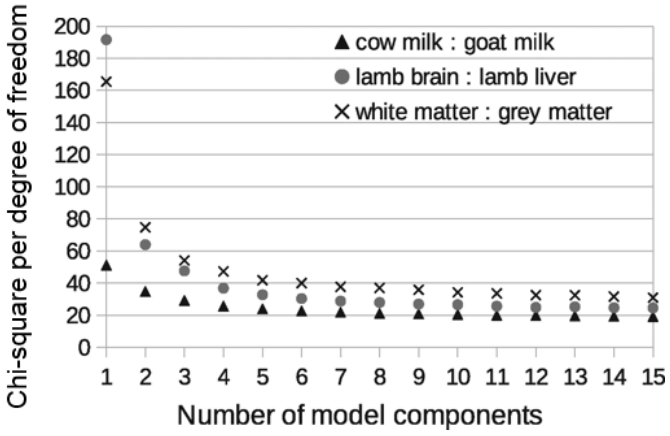

Figure 5.7 Determination of model order for linear Poisson ICA models

In the plot presented in Figure 5.7, the curves show the goodness-of-fit (Equation 3.11 of Section 3.4.5) of linear Poisson ICA models as a function of the number of model components, where each component represents a sub-spectrum that is a mode of correlated spectral variation. A total of six components were found to be required to sufficiently model the milk spectra, at which point the goodness-of-fit begins to plateau (see the plot in Figure 5.7). The lamb brain:liver spectra required eight components and white:grey matter also required eight components. Extracted ICA components (mass spectral components) for milk, lamb brain:liver and white:grey matter mass spectra are presented in Appendix A (see sub-spectra in Figure A.1, Figure A.2 and Figure A.3, respectively). Once attributed to sample classes, one milk component, one brain:liver component and one white:grey component were rejected as being uninformative (due to contamination or ambiguity), with the remaining compositions showing a clear linear trend against known mixtures (see the plots in Figure 5.8, showing composition of spectra in terms of weighted contributions of extracted LP-ICA components). Each 10% increment is shown as a step, where each step contains repeatability data for independent spectra with the same mixing proportions. The black dots show the best fitted trend. Each bar shows the relative proportion of each LP-ICA component present within a spectrum. The error bars are the LP-ICA model predicted errors. The components 'comp 1', etc. are listed in the keys from top to bottom in the same order as they appear in the figure. N.B. The results are also shown as scatter plots with linear fitted line in Figure 5.9 in a comparable manner with the peak ratio analysis results in the plots shown in Figure 5.5. These provided relative measurement precision of around ± 9%, ± 4% and ± 4%, up to approximately doubling that attained via peak ratio analysis (see the plot in Figure 5.11 (right)). Even when the peak known to correlate best with milk mixtures was removed from the LP-ICA analysis, a precision of ± 11% could be achieved.

Pull distribution analysis (actual deviations from ground truth divided by predicted deviations, see the histograms in Figure 5.10) show that LP-ICA model measurements are unbiased (mean consistent with zero) and predicted errors (σ_p) successfully describe the majority of measurement noise (σ_{tot}), with true errors being 1.6, 1.6

and 1.4 times larger than predicted (plotted in Figure 5.11 (left)) in the analysis of milk, brain:liver and white:grey matter data, respectively.

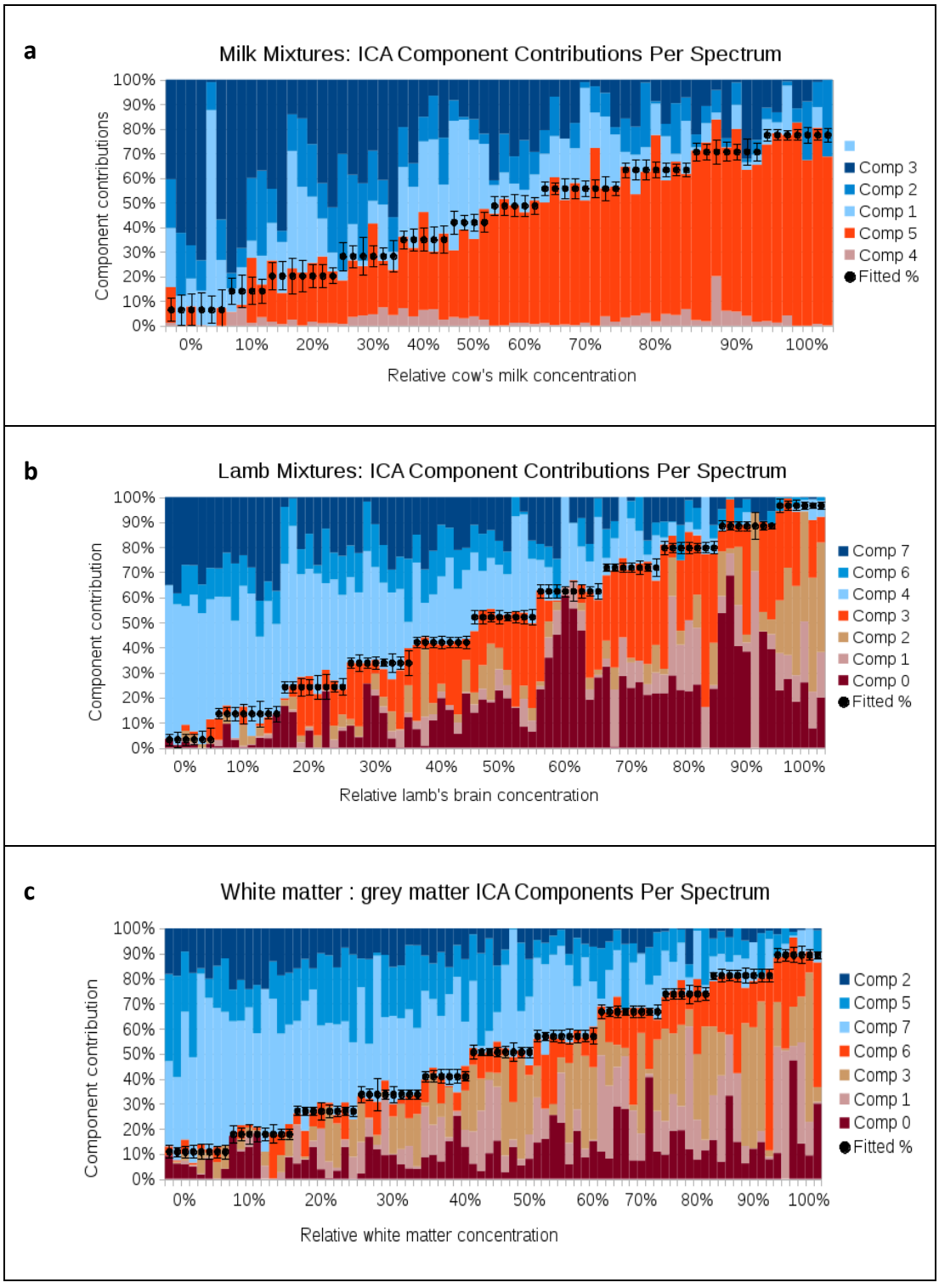

Figure 5.8 ICA component contributions per spectrum: (a) cow's and goat's milk, (b) brain and liver tissue and (c) white and grey matter

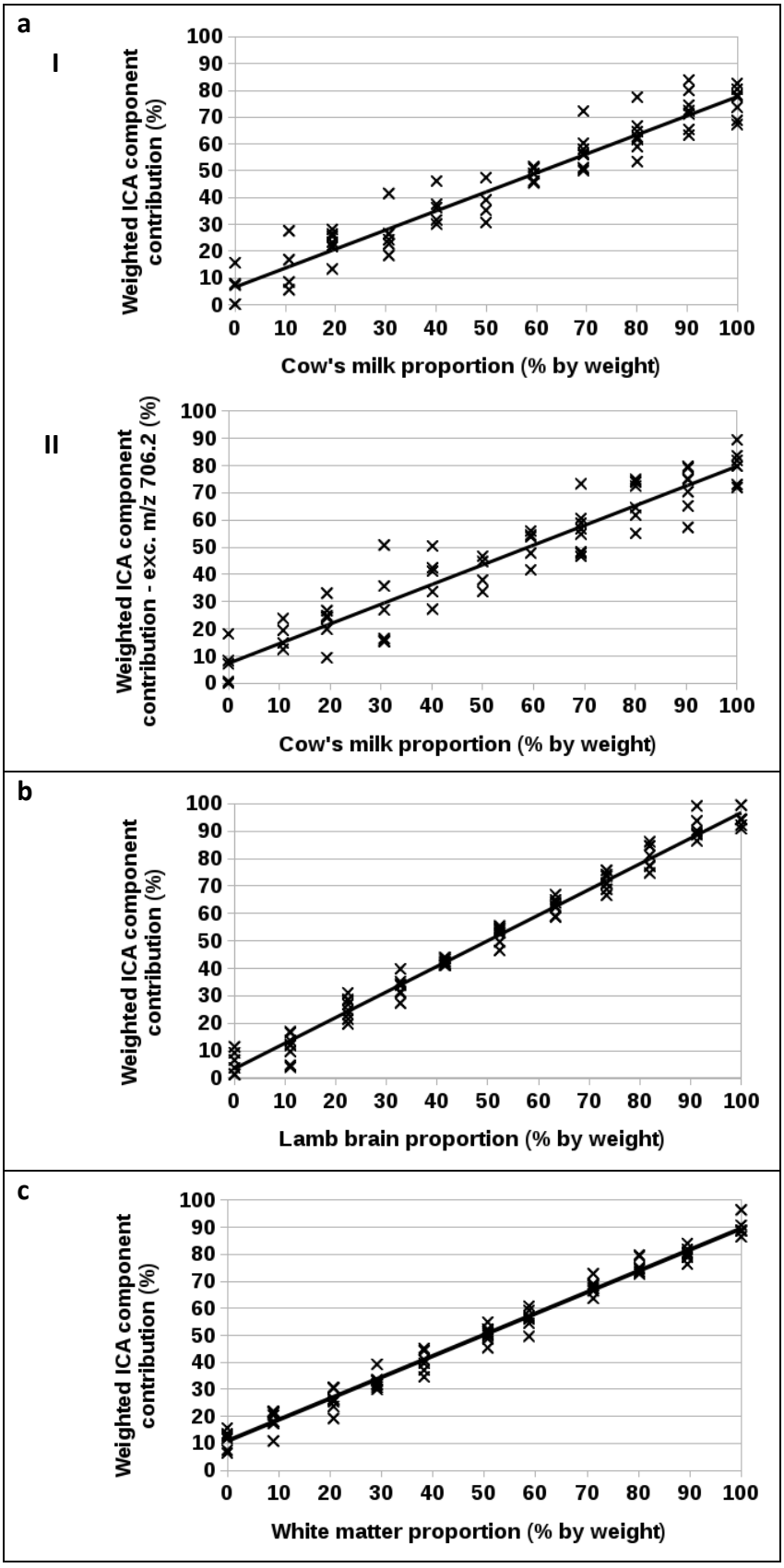

Figure 5.9 Linear fitting for linear Poisson ICA analysis results: (a) I. cow's and goat's milk II. cow's and goat's milk with m/z 706.2 excluded, (b) brain and liver tissue and (c) white and grey matter

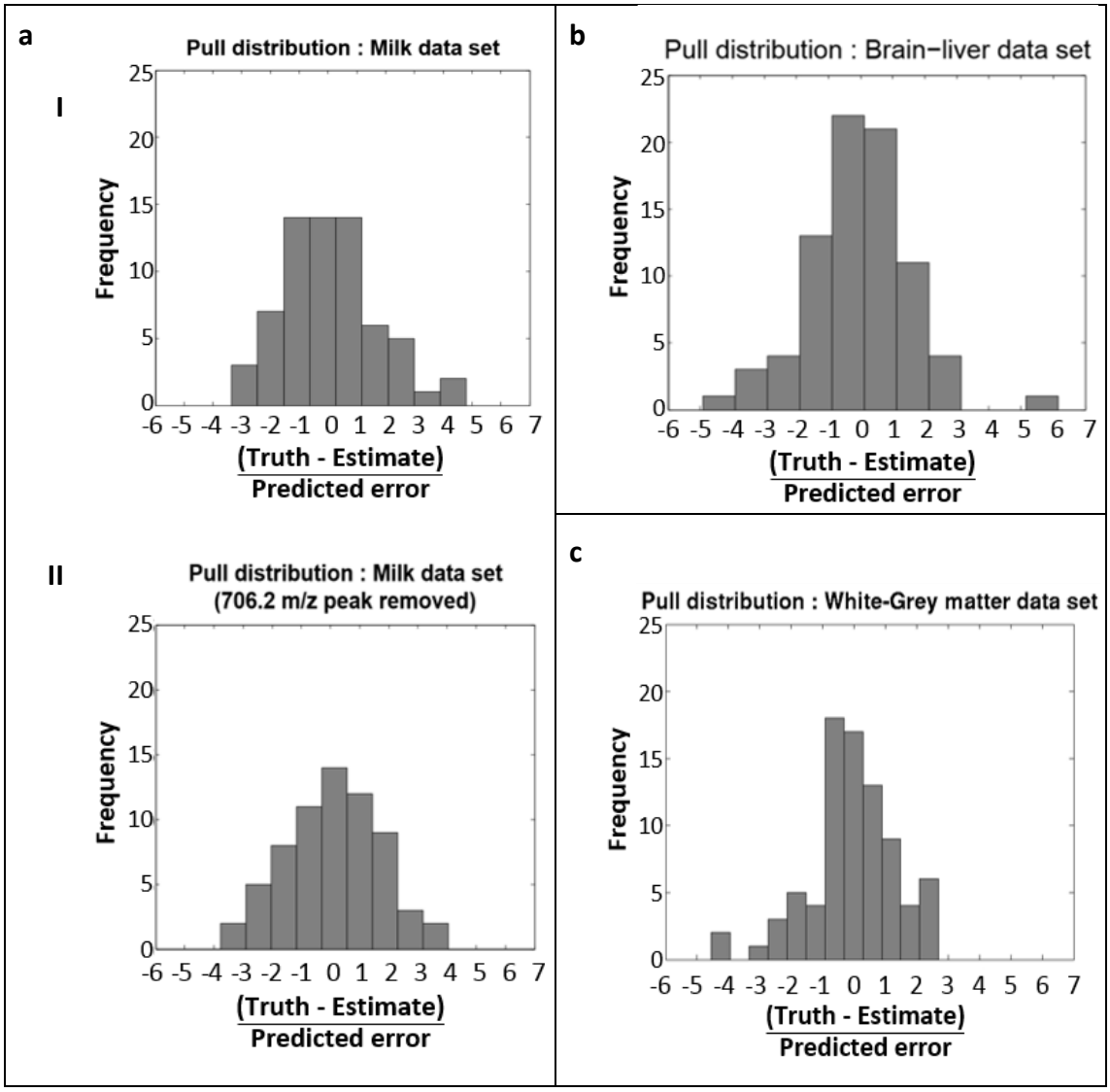

Figure 5.10 Pull distribution histograms: (a) I. cow's and goat's milk II. cow's and goat's milk with m/z 706.2 excluded, (b) brain and liver tissue and (c) white and grey matter, where pull distribution is defined as the actual differences between ground truth and estimated value divided by the predicted error on measurements (sample proportions)

5.4.3 Comparison of the Analysis Approach: Linear Poisson ICA vs. Peak Ratio

Two alternative methods to making quantitative measurements from MALDI mass spectra of biological samples have been presented: peak ratios and Linear Poisson ICA analysis. Both mitigate against confounding variability (caused by local matrix density, chemistry, ionisation field, etc.) and also ambiguity (caused by common

molecular constituents in different samples) using very different approaches. The former avoids problems by simply discarding mass peaks which are adversely affected, selecting those which empirically correlate best with sought measurements. The latter is far more sophisticated, modelling sources of variability, learning correlations between any number of peaks and attributing them to meaningful classes of data. This latter method is far more efficient, as much more signal is retained. The peak ratio method uses only 14% of the total signal available in the pre-processed lamb spectra, whereas the LP-ICA approach uses 90%, which immediately should provide an advantage through sample size alone. The LP-ICA approach achieves levels of measurement precision double that attainable through peak ratio analysis, with 1 standard deviation errors reducing from ± 16% and ± 8% to as small as ± 9% and ± 4%, for milk and lamb tissue mixtures, respectively. Achieving this increased precision using the peak ratios method would require at least quadruple the quantity of data (assuming errors fall with the square-root of sample size). White:grey matter measurement errors reduced from ± 6% to ± 4%, suggesting that most information is already extracted from the single peak at m/z 734.5 (see the plot in Figure 5.11 (right) which illustrates that the LP-ICA method is more precise than the peak ratio method in all experiments).

The efficient use of data is perhaps best illustrated by the LP-ICA method when the most informative milk peak (m/z 706.2) is removed. Despite the ambiguity of remaining peaks, measurements could still be made using the ICA method with errors of ± 11%. If the inverse variance is used as a measure of information content, the LP-ICA analysis precision using all milk peaks (± 9%) is consistent with combining the all-but-one analysis (± 11%) with the conventional peak ratio results from the m/z 706.2 peak (± 16%).

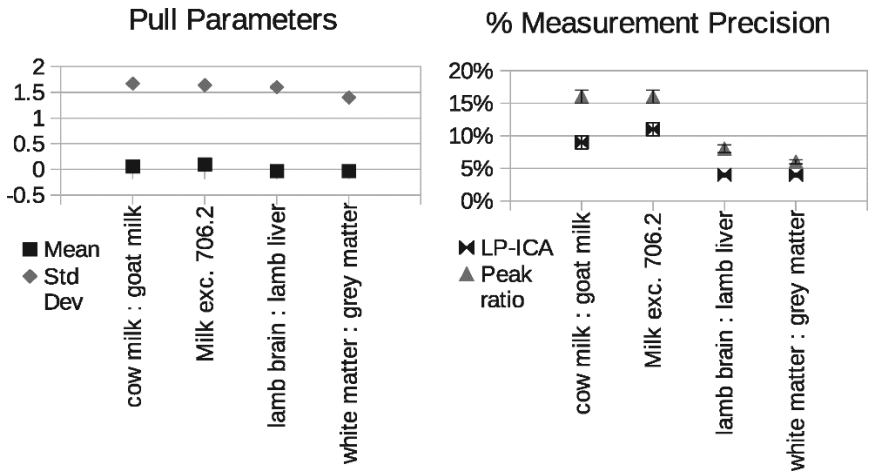

Figure 5.11 Predictive ability of LP-ICA error theory, as measured using Pull distributions (left). Measurement precision of peak ratio analysis versus LP-ICA analysis. Values are 1 standard deviation relative errors, expressed as percentage of quantity measurements (right).

In addition to the increased precision gained using the new method, the LP-ICA error theory (Section 5.3.6) provides the capability to predict measurement errors on a spectrum-by-spectrum basis. These predictions explain the majority of measurement noise, as confirmed by Pull distributions which should have a mean of zero and width (standard deviation) of unity if predicted errors (σ_p) match the observed errors (σ_{tot}). The plot presented in Figure 5.11 (left) shows that there is no bias (mean consistent with zero) and that true errors (assessed against ground truth) are close to those predicted. Error predictions within a factor of 2 are generally deemed sufficient for scientific use, e.g. Barlow (1989) and Press *et al.* (2009). As these errors are predictable from the input data, they do not require ground truth to be computed. These predictive powers provide several advantages, permitting goodness-of-fits to be constructed, such as χ^2_D, and revealing data-specific errors (see variable-sized error bars in the plots shown in Figure 5.8). In contrast, the peak ratio method uses empiricism alone to determine measurement precision. This provides a single error estimate, the use of which relies upon an assumption of uniform errors across all spectra, which logically should not be the case due to differences in normalisation. Furthermore, alternative analyses, such as PCA or conventional ICA do not provide error predictions, and must also rely upon empiricism and ground truth.

Despite the success of the error predictions, observed errors were still larger than expected. The additional sources of unpredictable error include: the spread of local minima in the numerical ICA solutions; the Gaussian measurement noise superposed upon the Poisson sampling process; non-linearity; the potential need for a greater number of linear components; and imperfect pre-processing.

5.4.4 Mean Prediction from Multiple Models

The effect of local optima was assessed by building 50 ICA models. The typical (median) precision attainable for milk mixtures was ± 9.77%, for brain:liver mixtures was ± 4.59% and for white:grey matter was ± 5.15%. The best local solutions found were ± 9.05%, ± 3.96%, and ± 3.98%, from milk, brain:liver and white:grey matter respectively, which are the solutions used in the associated figures. Rather than relying upon a single model (i.e. one local ICA solution) a mean linear mixing prediction can be made from many local solutions, thereby reducing variability. The mean predictions from the 50 model attempts provide precisions of ± 8.72% (milk), ± 3.77% (brain:liver tissue) and ± 4.19% (white:grey matter).

In addition, the mean prediction from multiple models can also help with selection of suitable ICA component combination by comparing this value of models built using different component combinations. Tested using the white:grey matter data set, the plot in Figure 5.12 illustrates that certain number of components would be required for achieving best proportion prediction accuracy. Modelling performance gets improved and maximised with more components extracted before becomes plateau thereafter. From the plot, better prediction accuracy was generally obtained via models that only reject 1 component as contaminating background (i.e. amongst models with the same numbers of extracted components, the RMS error values of individual models that only reject 1 component tends to be smaller and closer in values compared to those with multiple components rejected). However, this effect evens out for the averaged models that account for some more variations in predicting proportion values from individual models – i.e. higher model order.

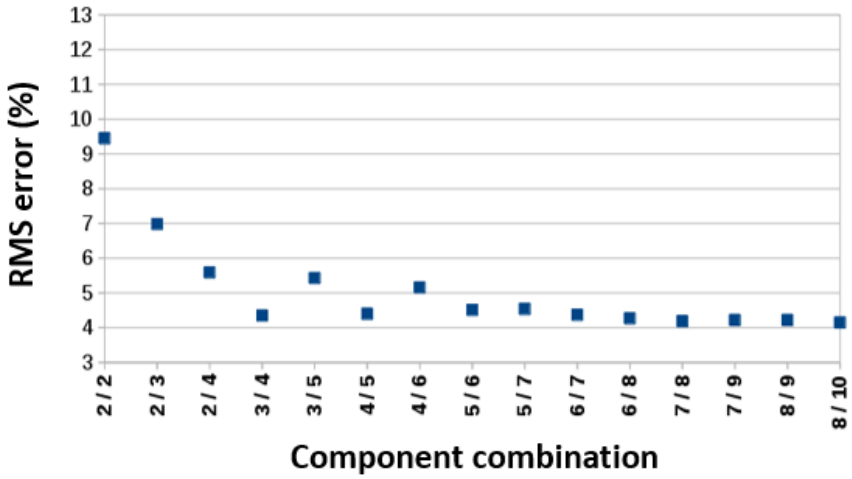

Figure 5.12 Model fitting performance assessed on averaged white:grey matter models built with various number of components

Note that '7/8', as labelled on the horizontal axis of the plot in Figure 5.12, refers to a component combination where 7 out of the total of 8 extracted components were kept for the spectral model fitting and 1 component was rejected as a background/noise component, etc. A small dip at 7/8 component combination is seen in the plot. This confirm that it was a reasonable choice of model.

5.4.5 Validation of the Poisson Assumption and Suitability of the LP-ICA in Modelling MALDI-MS Data

The Poisson sampling assumption was validated via Bland-Altman analysis (plotted in Figure 5.6), showing that errors grow with the square-root of peak intensity (σ_p), with an overall scaling factor of 24. The scaling factor measured is also consistent with the χ^2 per degree of freedom of ICA models (i.e. 24 plateau reached in the model selection curve provided in Figure 5.7). Alternative modelling approaches, such as PCA, and other ICA methods, would be inappropriate due to their Gaussian assumptions and lack of predictive error theories.

If the MS acquisition pipeline was ideal, there would only be two sources of variability: changes in signal due to changing mixture proportions; and random

Poisson sampling noise (σ_p). Despite best efforts to homogenise mixtures, wash away salts and perform basic pre-processing, resulting spectra still contain numerous modes of variation. Six linear components were required to model milk and eight to model lamb tissue. Within these components, one was rejected from each model on account of its inability to provide information regarding mixture proportions. Rejection was on the basis of linear regression applied to map components to classes, Section 5.3.4, when the prediction improved with that component belonging to neither classes. This could be due to either the component representing contamination, or the component could contain common structure indistinguishable between the sample classes. The remaining components are presumed to be modelling those sources of variation noted in Section 5.1, i.e. fragmentation, ionisation modes, isotopic variations, etc. The number of components required to model the data could potentially be used as a measure of data quality. Preparation, acquisition and pre-processing steps could be optimised to minimise the number of required components.

Despite the numerous components required to describe the data, the MAX SEP algorithm (see Section 3.4.6 of Chapter 3) provides the ability to attribute Poisson sampled components physical meaning, allowing their quantities to be used for measurement. The attribution of component quantities to classes of sample are only valid if this physical meaning can be established. An alternative approach, based upon PCA or factor rotations for example, would not have been appropriate due to enforced orthogonality and non-physical negative weightings.

Finally, as a tool for future MALDI image data mining, the LP-ICA approach could potentially improve the information content of images by replacing pixels based on single m/z peaks with pixels based upon LP-ICA component weights. Such images are expected to have better signal-to-noise, as pixels would incorporate information from many peaks. They may also better correlate with tissue types, giving a higher-level interpretation than simply being a map of specific chemicals. And finally, through the LP-ICA error theory, pixel values are made quantitatively meaningful.

The ability to quantitatively assess correlated chemicals and map them onto biological structures will be the focus of the next chapter.

5.5 Conclusion

LP-ICA modelling analysis of MALDI mass spectra has been shown to provide improved quantitative accuracy for the measurement of proportions of biological samples when compared to a conventional single peak approach. There are only a relatively small number of peaks which are applicable to a single peak analysis, as most are adversely affected by high levels of uncontrolled variability. LP-ICAs successfully model this variability, permitting information in any number of peaks to be included in measurement estimation. The accuracy of measuring the proportions of milk, brain and liver mixtures were doubled using this new approach.

In addition, the modes of variation found within MALDI mass spectra, in terms of sub-spectral combinations, can now be extracted and analysed providing physically interpretable models with fewer parameters, marking a step improvement in related ICA work in the field. The high levels of variability, sources of ambiguity and lack of error predictions also suggests that simple single peak ratios are unlikely to be quantitatively trustworthy. The approach demonstrated will be extended in Chapter 6 to data-mine MALDI images.

5.6 Overview: A Bridge to the Next Chapter

The brain is built up from many sub-types of tissues. It can be divided into white and grey matter which are the two main tissue types of the brain that are readily distinguished from one another. They are located in separate sites and are responsible for different tasks but are highly associated and must properly co-operate for the brain to perform normally.

The brain is an important organ in a body which is the main part in the central nervous system (CNS) connected to the spinal cord. The CNS works in conjunction with the peripheral nervous system (PNS) that controls autonomic and somatic nervous systems. The brain gains and recognises information and consists of nerves, in addition to spinal cord nerves, that receive sensation and deliver motor commands.

White Matter

White matter has more variety of cell types, consists mainly of the tails of nerve cells, axons and myelin, lipidic fibres that act as protecting pillow around axons. This is what makes the white matter white/light pink and soft. Neuronal signals are transmitted between nerve cells (neurons) through axons, allowing communication within the complex neuronal network.

Grey Matter

Grey matter is located at the outer part of the brain. Folds of white matter branch into grey matter region, the host for the neurons' cell body, the receptor for neuronal signals. This part of the brain requires most of blood and oxygen supply that comes into the brain. Capillaries surrounded neuronal fibres make the region appear grey/dark brown.

The brain stays shielded inside the skull and under layers of the brain's membranes called meninges. This is an important organ that must be protected as abnormalities of the brain will cause potential risks and damage to other systems all over the body. Degradation of brain tissues or changes in nervous system should be diagnosed rapidly to avoid permanent damage. Detection of the concentration of molecular species within tissues can be performed using mass spectrometry techniques. As with

the other biomolecules, MALDI-MS can detect lipids, which have relatively high concentrations in brain tissue. Regional determination of detected molecules is also capable with imaging MS. Making such analysis quantitative will enable a powerful biomarker identification technique which can be extended to use for *in vivo* (e.g. rapid evaporative ionisation mass spectrometry (REIMS) system for real-time analysis by Phelps *et al.* (2018)) or *in vitro* diagnostics.

In this Chapter, a lamb brain which has many similarities to human brain has been analysed. It has often been used to model the human brain in a variety of study/demonstration contexts. It was therefore selected here for this experiment where the sample proportions of white and grey matter present in the human brain are mimicked. The white and grey matter were expected to show both shared and differing mass spectral lipid profiles. Binary mixtures of the two allowed assessment of the methods introduced for determining proportions within the mixture. As a result of the analysis using the linear Poisson ICA method, all the underlying variations were automatically modelled by extracting independent components that contribute to the spectra, and hence providing accurate estimates of sample proportions. This suggested that the linear Poisson ICA method also has the capability for quantifying MALDI-MS image data, which is to be confirmed in the next chapter using rat brain imaging example data. If so, the method could be seen as an unsupervised approach that can provide quantitative information regarding the spatial distribution of biomolecules of which cells and tissues are comprised. This consequently can take a step closer towards an interpretation of the tissue's biological composition with potential applications in biomarker identification.

Chapter 6

MALDI-MS Imaging Analysis of Brain Tissue Section

6.1 Introduction

6.1.1 Outline of the Chapter

A mass spectrometry imaging (MSI) data set is obtained by acquiring mass spectra across a 2-dimensional array on thin layer of sample. An MSI data set is large in its dimensions (mass bins and spatial locations) and therefore potentially extremely informative. MALDI allows recording of imaging data as the laser moves (usually in discrete steps) through these different spatial locations. However, extracting useful information for quantitative analysis is not straightforward. This is partly caused by the complex nature of the MALDI mass spectra. Moreover, a slight alteration in sample preparation can significantly influence mass spectral behaviour. Unlike normal, discrete sample MALDI-MS acquisition, the imaging approach limits the number of laser shots fired onto a certain area of sample and can lead to fewer MS profiles accumulated into one mass spectrum at a pixel. In order to boost the signal intensity, signals acquired within a larger area may be averaged Chumbley *et al.* (2016). This stabilises the spectra for further evaluation but reduces the spatial resolution. The spatial resolution is determined by the pitch size (equal to pixel size),

the distance between successive locations of the mass spectra acquired (i.e. stages of laser). It is a preferred condition for the quantitative analysis of this work, that the pitch size should be selected to be larger than a laser spot size which determines the sampling area. These sizes are illustrated by the diagram in Figure 6.1. This is in order to maintain the uniformity of sampling area exposed by the laser. Otherwise, there will be overlapping areas (oversampling) between neighbouring pixels where the sample-matrix materials are already used up by the previous laser shots – i.e. although, this improves the spatial resolution, the analytes available in the sampling area are no more evenly spread within a same laser shot, and the height of sample in a sampling area varies. Also, this could physically cause a blurring artifact (images look smoother than reality) due to the common analytes being ionised in the overlapping area.

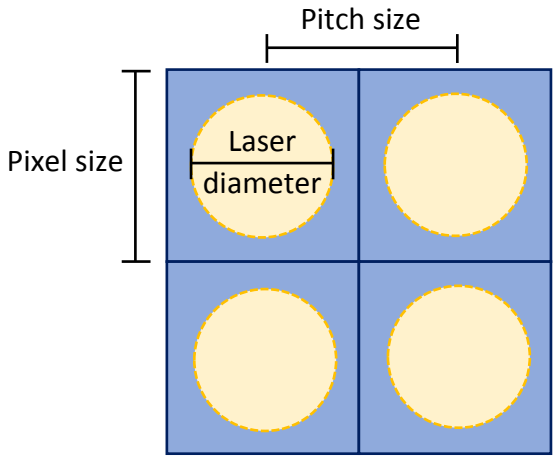

Figure 6.1 Pixels (blue) and sampling areas (yellow)

By emulating the method developed in Chapter 5, linear Poisson ICA (LP-ICA) modelling will extract components from the mass spectra recorded at pixel locations across an acquired MSI data set. The result can then be interpreted as images with LP-ICA component proportions at each pixel, as opposed to the conventional single peak value pixels. The LP-ICA approach works by modelling a more complete set of variations within a data set, with the correct statistical assumptions appropriate to MALDI-MS data as validated in Chapter 5. It also requires expertise in acquiring appropriate MSI data for this method of analysis as well as for binary mixture

experiments. An example MSI data set selected for this analysis is a rat brain section, from a rat stroke model, prepared and acquired under the optimised conditions (Henderson *et al*., 2018) which had been shown to give a good level of signal-to-noise in the mass spectra. Images produced using selected single mass peaks should show clear biological structure within the sample. Such images are used to define an image quality baseline that the data set could produce. Nonetheless, it is expected that more useful images would be formed using the LP-ICA method in terms of biological interpretation due to the added uncertainty information produced by LP-ICA. In this study, the ratios between those m/z peaks with relatively high intensity and their carbon-isotope peaks were utilised as a quality control criteria to differentiate between LP-ICA components that comprise useful signal or simply noise. Where the accepted range of values (taking into consideration the presence of isobaric species) for an isotope ratio can be found in the LIPID MAPS database (http://www.lipidmaps.org/). Other effects including the variation in sodium concentrations across the imaged brain tissue section were also observed. The proportion of molecules ionised as a sodium adduct versus those in the protonated ion form were compared.

At the end of this chapter, the aim is to map the variety of regional tissue types within a brain section, suggesting a method for building a lipid atlas of the brain. A tissue type will be defined by a series of mass peaks in a particular relative intensity ratio that appears in an individual component. They are expected to be distributed across anatomical regions with relative concentrations having biological meaning. These depend on the type and proportion of cells that exist in each tissue at specific location of the brain. The goal is to map all the variations automatically without prior targeting of identified lipids of interest. Instead, the important lipids can be identified from the m/z peaks that appear in the ICA components modelled. Recently, lipids in brain tissues have been actively investigated using MALDI-MS. Given that brain tissues are rich in lipids that perform various tasks, changes in lipid concentrations are often hypothesised to indicate changes and even abnormalities in brain functions. Examples of the earliest work to document the abundance of major lipid species sorted by lipid head groups are the studies on lipids extracted from within specific

tissue types in human brains (O'Brien and Sampson, 1965) and from homogenised regions of rat brains (Chavko and Nemoto, 1992). So far, Delvolve *et al*. (2011) attempted to create complete anatomical segmentation of a rat brain section by observing the concentrations of multiple lipids individually. A number of previous papers (e.g. Astigarraga *et al*., 2008; Murphy *et al*, 2009; Delvolve *et al*., 2011; Mohammadi *et al*., 2016), have listed the identification of important lipids, especially of phosphatidylcholines which are the major species to appear in the imaging mass spectra in this work. Therefore, these can be used as a reference to the data analysed in this thesis.

In this chapter, the method of analysing the imaging MALDI-MS data is described along with a critical discussion of the method and how it could possibly be improved.

6.1.2 The Importance of Quantitation and Error Analysis

Scientific quantitation/quantification is the process of determining the value of a quantity based on experimental measurements or observations, with the ability to quote an error on that value. Every measured value is just an estimate of the true value. Without error estimates, the idea of precision or accuracy of the measurement cannot be discussed meaningfully. Smaller errors on quantitative analysis contribute to lower uncertainties (determined by standard deviations), and therefore greater confidence on determination of the quantity of interest. Here, the quantity refers to 'any quantity' that possesses a value, not only include those with units of gram, metre, or number of counts, etc., but also include ratios of quantities which can be dimensionless. For example, in this work, the ratios of different components across spatial locations are quantified, referring to the relative concentrations of the underlying sub-tissues within the MALDI-MS imaging sample. In other words, the extracted components along with their associated weighting quantities determine the absolute amount of ion counts recorded as peaks in the mass spectrum at each pixel. Because the ion counts come from only a fraction of molecules contained within the sample that were ionised (ideally directly proportional to the amount of that existing molecules), the quantities associated with the extracted components

must be calibrated in order to estimate the absolute concentrations of particular sets of m/z peaks contained in the underlying sub-tissue types (see the future work suggested in Section 7.3).

Segmentation (according to known anatomical structures) is only performed as a general check, in terms of information that is supposed to be extracted as component images, but is not the main purpose for doing this LP-ICA analysis. A quantitative check of these measurements can be based on the error on a physical property, e.g. the ratio of isotope peaks (see Section 6.3.5), where the accepted values are available to compare with the results from the analysis. Therefore, the expected and the measured errors on this quantity can be compared to validate the analysis.

6.1.3 LP-ICA vs. Other Approaches

The intention of this work was to develop a valid statistical method appropriate for the characteristics of MALDI-MS data, to allow the construction of an error model. The LP-ICA described in Chapter 5 was shown to improve the accuracy (over the method that uses only single peak ratios) of measuring the proportions of samples in man-made biological mixtures. In this chapter, the method was then proposed for use in label-free quantitation of real-world MALDI-MS imaging data, where mass spectral signals can be extracted as linear components. The measure of quantity associated with these components can be thought of as the individual contributions of the underlying samples that build up signals forming the imaging data. Each pixel is therefore analogous to a simple mixture sample but with more than two components. LP-ICA provides the spatial distributions of the underlying contributing sources of component mass spectra. In this work, sub-tissue types within a brain section were of interest. To emphasise this further, the usefulness of the approach lies in its potential ability to identify the types of biological tissues (that correspond to the independent components) that are quantified here, rather than the individual lipids contained within each sample. Because tissues are complex mixtures and combinations of biochemicals (such as lipids which are major constituents of brain tissue), they comprise signatures of biological components or tissue types. The

regional structure associated with each component can be extracted, but the LP-ICA's value is not limited only to segmentation, but rather to indicating the relative abundance of each component across the image.

Prior to building a useful algorithm for the analysis of MALDI mass spectrometry data, appropriate assumptions about the input data should be satisfied in terms of their physical/statistical properties. The important assumptions, that accord with MALDI-MS data properties and the intended analysis, include:

1.) The mass spectral signals are in the form of positive counts only,

2.) The signal generation process is linear,

3.) The errors associated with the signal measurements obey Poisson statistics,

4.) Any underlying components can be comprised of some of the same molecules – i.e. the mass spectra of the underlying samples must be allowed to have some signals at the same m/z bins, data correlation is thereby introduced and an orthogonality assumption is not suitable.

Therefore, the LP-ICA method was designed to ensure that all the requirements listed here are addressed. Some other approaches to analysis will be critically discussed with comments in relation to the above assumptions.

There are a large number of existing analysis tools for quantification/classification of mass spectral data. Most of these methods make use of dimensionality reduction in a variety of alternative ways. Many of them are quite similar, with common core principles but are given different names based on variations in the algorithms. These methods may be divided into the following main categories. Note that depending on the purpose of analysis (i.e. what is needed to be known from the analysis), an appropriate method must be carefully selected.

1.) Linear component decomposition approaches, e.g. principal component analysis (PCA), independent component analysis (ICA), non-negative matrix factorisation (NNMF), probabilistic latent semantic analysis (pLSA), Linear Poisson ICA

2.) Pattern recognition approaches, e.g. random forests, support vector machines, k-nearest neighbours, neural-network based methods e.g. t-distributed stochastic neighbour embedding (t-SNE)
3.) Clustering approaches, e.g. K-means, Fuzzy C-means
4.) Normalisation approaches, e.g. linear regression normalisation via peak ratio calculation, total ion current normalisation, calibration using isotopically labelled/internal/external standard (see Section 3.1.2 of Chapter 3), local regression normalisation (Callister *et al*., 2006), quantile normalisation (Callister *et al*., 2006), regional tissue extinction coefficient normalisation (Hamm *et al*., 2012; Taylor *et al*., 2018)

The theoretical foundations of the methods listed in each category leads to differences between them in terms of cost function and optimisation steps. These are selected on the basis of the data characteristics. In mass spectral analysis, statistical properties of data are often ignored and simplified without being confirmed, and components and some properties of the data are therefore lost, compromising appropriate error analysis. Generally speaking, machine learning approaches do not use proper statistical models, rather they identify separable features from the data set and perform arrangements that result in classification of data in most cases. Neural networks are deemed to be the most sophisticated method amongst the pattern recognition machine learning approaches listed and discussed previously in Chapter 3, Section 3.2.2 because of the complexity of the algorithm, involving a large number of connections and the processes of updating parameters. They can perform classification and regression tasks – e.g. Fonville *et al*. (2013) used a neural network-based approach (i.e. t-SNE) to segment anatomical structures within MS images of biological tissues, or Thomas *et al*. (2017), used deep neural networks as a tool for dimensionality reduction prior to performing other classification techniques to increase their performance.

t-distributed stochastic neighbour embedding (t-SNE) has been used often in MS image analysis, e.g. Abdelmoula *et al*. (2018). t-SNE can be applied to a variety of data types because of its loose constraints on the properties of input data. It was not

designed specifically to suit the MALDI-MS data behaviour especially for quantitative analysis. Its optimising cost function (e.g. the 'Kullback-Leibler divergence') is written in a form similar to a standard likelihood function for assessing probability of the extent of similarity between neighbouring spectral pixels. The result allows assessment of the clustering and spread of data on a t-SNE scale and then the full segmentation or soft class-labelling can be visualised (Fonville *et al*., 2013). The data are assumed to have a t-distribution which is very close to a Gaussian distribution. The analysis often applies to data of small sample size, e.g. reduced-dimensional data, which makes this a rapid technique.

Neural networks adjust a set of hidden parameters during computation, whilst learning from known data and can subsequently achieve reasonable classification results when solving scientific questions with unseen data sets. The problem for this type of method is that the separable features may not necessarily reveal the underlying signal generators that give rise to the real variations in the data. These underlying signal generators are of interest, because they are the biochemical tissue components. Some form of additional statistical testing is required to guarantee the suitability of these approaches for quantifying certain tissue/phenotype related chemicals by MALDI-MS.

Clustering methods are relatively rapid approaches, generally used for identification of distinct groups of data. In mass spectrometry, Frank *et al*. (2008) applied clustering of tandem MS data where they grouped MS/MS spectra in the format of packets of m/z peaks that occur as a result of redundant identical peptide spectral generation, to create the representative spectrum, thereby reducing the size of the data set prior to further analysis. This gave better stability with more complete information for molecular identification when using an available database.

The K-means method works by associating a data point with the cluster that has the minimum Euclidean distance between the data point to the centroid of a cluster, where the centroid (centre of the cluster) is located at the mean of data points that belong to the cluster. The position of the centroid can be updated iteratively after adding a point to a cluster. A subsequent design in the clustering method family, Fuzzy C-means, was adapted such that a data point is not restricted to one class.

Instead, it assesses how likely it is that a data point may be belong to different classes. It uses the concept of Fuzzy logic which was introduced in computer science contexts for approximating confidence levels – i.e. an alternative definition of uncertainty that cannot be interpreted using standard statistical probability (Dunn, 1973). Therefore, this is referred to as "soft K-means" as opposed to the K-means where the data are hard-labelled into a specific class. Fuzzy C-means was applied to magnetic resonance imaging data (MRI) where the algorithm was modified such that neighboring voxels (3-dimensional pixels) take part in the classification of individual voxels (Ahmed *et al*., 2002). This produces homogeneous segmentation of brain MRI images since noise levels were reduced (Chuang *et al*., 2006). When applied to MS imaging of myxofibrosarcoma (Jones *et al*., 2011), the Fuzzy C-means reveals superior segmentation compared to PCA, non-negative matrix factorisation or pLSA. Clustering performed well in classification. However, it is not based upon statistically justifiable modelling assumptions and therefore is not appropriate for regression purposes. Consequently, it is not useful in obtaining numerical quantitation. Also, where initial clusters' centroids are defined at the outset, quite significantly affects the resulting classification – i.e. results are not unique.

Non-negative matrix factorisation (NNMF) and probabilistic latent semantic analysis (pLSA) are approaches which are frequently mentioned in the MALDI-MS literature as data analysis tools. The two algorithms have a very close relationship. In fact, NNMF is a broader term describing methods of component decomposition with a non-negative value constraint, and whose result is expressed as a linear matrix equation via a singular value decomposition-like method. It uses an optimisation function (i.e. cost function) to find a matrix of linearly separated factors (components) within the data. The choice of a Poisson or Gaussian assumption can be selected, depending upon the nature of the data (Brouwer, 2016). Therefore, by definition, pLSA is a form of NNMF. pLSA was originally designed for text document classification in linguistics research (Hofmann, 2001). The method was adapted for use in mass spectrometry data analysis e.g. Hanselmann *et al*. (2008), and is also used in commercial software e.g. SCiLS Lab (Bruker). It is not very clear whether there are good links between text and mass spectral data characteristics.

A few options are available in NNMF to address different data types, including pLSA as discussed, and Poisson matrix factorisation (Canny, 2004; Gopalan *et al*., 2014) with similar assumptions, etc. NNMF has shown comparable segmentation results to ICA in the analysis of a mouse brain MALDI-MS image data set, both perform better than PCA (Siy *et al*., 2008). NNMF algorithms are generally unsupervised, however, are modified in Leuschner *et al*. (2018) to be used as a supervised tool with a focus on classification of tumour regions on MALDI-MS image. pLSA is the closest algorithm to linear Poisson ICA in terms of the assumptions made (see Table 6.1 for analysing data properties). Hanselmann *et al*. (2008) has shown use of Expectation Maximisation (EM) in optimisation of a log-likelihood cost function for the pLSA algorithm. This was drawn based on Poisson statistics which has be tested appropriately for simulated data and real-world MALDI-MS imaging data. In addition, the Akaike information criterion was used to calibrate model selection to determine the suitable number of components to be extracted. This is equivalent to the plateau reached in the model selection curved in Figure 6.4 of this chapter using the LP-ICA.

There are many more algorithms built with slight alterations but share core principles, where the assumptions they make on the data analysed or algorithm design are slightly different. Some of the variety is listed in Table 6.1 to compare their main properties which reflect their suitability for use with MALDI-MS data. For imaging tasks specifically, there is no ground truth to train the algorithm and the ability to perform unsupervised tasks is therefore beneficial. A quantitative capability is one of the main issues. Depending upon the objective of the research, a regression or classification approach may be favoured. Regression approaches are required for getting quantitative numerical results (specifying how much things vary between different measurements). Whereas classification approaches aim at grouping the most similar things together and separate dissimilar things (stating to which group something belongs).

The concept of orthogonality applies mainly to the linear component decomposition methods, and also in some other methods which produce equivalent forms of results. In conventional PCA, the extracted (principal) components must be orthogonal. Note that PCA is sometimes used to reduce a number of dimensions of data before

processing clustering methods. In the case of the prior positive only assumption on component spectra (counts cannot be negative), having this orthogonality assumption would mathematically force each and every component to include a different sets of peaks, and therefore prevent components with any degree of commonality from being extracted – i.e. orthogonality means the dot products between components are zero. As discussed before, it is necessary to have non-orthogonal components which means that the same m/z peaks are allowed to appear in multiple components. This can then interpret underlying signals in a more meaningful way. In particular, mass spectra of MALDI-MS imaging data of biological tissues comprise the spectra of various biomolecular mixtures present in the different sub-tissue types at each pixel location. Similar sub-tissue types of the same organ are likely to contain some common biomolecules, but with varied proportions depending on the functional characteristics of those regions. Conventional ICA and its relevant methods e.g. LP-ICA satisfies this criterion. Conventional PCA vs. ICA algorithms were discussed explicitly in Section 3.4.2.

Normalisation approaches are basic techniques of MS data analysis which work by calculating a fraction (ratio) of the interested quantity against a defined reference value. They are simple, with no complicated algorithm involved in the calculation. The cumbersome tasks for normalisation are the additional sample preparation procedures needed with external standards or the selection of appropriate internal standards to suit the analysis (see Section 3.1.2). Individual ion peaks associated with the variation in the sample must be found and validated; therefore, the segmentation and/or quantitation based on this selection process is subjective. More sophisticated normalisation methods, including quantile normalisation, central tendency normalisation, linear regression/local regression normalisation, are reviewed and evaluated in Callister *et al*. (2006).

Alternatively, Hamm *et al*. (2012) and Taylor *et al*. (2018) introduced region-specific normalisation approaches using tissue extinction coefficients to scale mass spectra of tissue regions, between organs and within an organ, respectively. The scaling factors can be determined by the relative signal intensities between regions of a specific molecule that was treated as a calibration standard. Note that spatial regions

based on the different tissue types have to be defined beforehand. The method explained in Taylor *et al*. (2018) employed a clustering approach called 'graph cut' for tissue segmentation. Applying this method can compensate for a problematic inconsistency of ion signals throughout an MS image due to varied degrees of suppression occurred at different tissues.

The common limitation for these normalisation approaches is mainly the potential introduction of bias because the analysis relies only on a few pieces of information contained in a data set, which are sometimes picked manually based on visualisation. Nonetheless, a regression analysis can be constructed using these normalisation approaches, for example, using the conventional peak analysis as demonstrated in Chapter 5 Section 5.4.1. The analysis is very simple, does not require statistical assumptions but errors cannot be predicted.

Although, the available approaches discussed above provide satisfactory results in a number of research studies, they lack a statistical error theory where predicted/expected errors can be estimated. With these methods (and without further error modelling), the associated errors can be calculated only if the ground truth exists for a specific data set. This ideal case is impossible in unseen MALDI-MS imaging data. It is important in a scientific context to be able to estimate errors in measurements because the predicted errors (from theory) and the measured errors (deviation from ground truth) can then be compared and where signals differ, the significance of that difference can be determined. This can test the whole analysis methodology – i.e. the analysis is valid if the agreement or relationship between the experimental error and that predicted by theory is observed, and assumptions used in the algorithm are valid.

In this work, the component images that show reasonable segmentation according to the anatomical structure can be seen as an independent check of the validity of the analysis and are not the primary reason for using LP-ICA. The cost function is derived from the likelihood (see Equation (3.8) of Section 3.4.5). The components extracted by LP-ICA are the ratios of ion counts at a number of m/z peaks represented by probability mass function vectors (of the same size, equal to the number of m/z peaks contained) for each pixel. Associated quantities for components are indicated

per spectrum (at a specific pixel). The algorithm is similar to that of NNMF and pLSA but is more readily formatted as vectors of mass spectrum instead of the matrix format. The use of MAX SEP (see Section 3.4.6) is also another novel part of this work which features maximal separation of components. Error covariances can be calculated for the extracted components.

The algorithm used will automatically find mass spectral signatures that are common to different parts of the brain. The model constructed by quantifying contents of spectra will allow the relative contribution of these signatures (components at each pixel) to be determined. What will be challenging is to relate each of these signatures/components to biological features of the tissue shown by the spectral model in specific ways. It is hypothesised that the components relate to biological features of the tissue, for example, cell types, white matter, extracellular matrix, etc. Referring back to Chapter 5 when binary mixtures of complex lipids were used, cow's milk would be one signature and goat's milk would be another signature in the milk mixture, and also for the brain:liver and the white:grey matter mixtures. Similarly, it is expected that the nerve cells/sub-tissue features as mentioned before are a number of signatures found differentiable in the brain MS image which comprise the underlying tissue phenotypes. Determining the full biological meaning is beyond the scope of the current work. Note that it is clear from the component images shown later in Figures 6.5, 6.6, 6.16 and 6.17 that the spatial distribution correlates well with the tissue anatomy.

The use of an algorithm must suit the purpose of the analysis. In this case, the LP-ICA was selected to perform an appropriate quantitative analysis of the MALDI-MS image data set as discussed. Table 6.1 below compares some available approaches for data analysis that have been used with MALDI-MSI data, with abilities to perform quantitation and/or segmentation. The lists of analysis properties compared include: whether the analysis is supervised or unsupervised, performs classification or regression, what parameter is measured, what typical statistical assumption involved and error model availability. For decomposition methods, the positive/negative and orthogonality constraints of the extracted components are also listed. The references to examples of MS imaging application are also given.

Table 6.1 Comparison of typical properties of some available approaches to analyse MS imaging data including the Linear Poisson ICA

Method	Supervised / Unsupervised	Classification / Regression	Estimated parameter	Typical statistical assumption	Error model	+/-	Orthogonality	Examples of MS imaging application
PCA	Unsupervised	Regression	Linear component	Gaussian	n/a	+/-	Orthogonal	Gut *et al*. (2015)
ICA	Unsupervised	Regression	Linear component	Gaussian	n/a	+/-	Non-orthogonal	Gut *et al*. (2015)
Non-negative matrix factorisation (NNMF)	Either	Regression	Linear component	Either	n/a	+ only	Non-orthogonal	Leuschner *et al*. (2018) Siy *et al*. (2008)
Probabilistic latent semantic analysis (pLSA)	Either	Regression	Linear component	Multinomial	n/a	+ only	Non-orthogonal	Hanselmann *et al*. (2008)
Linear Poisson ICA	Unsupervised	Regression	Linear component	Poisson	Poisson-based	+ only	Non-orthogonal	Deepaisarn *et al*. (2018)
Neural networks	Either	Either	Probability of classification given data	Various and inappropriate e.g. least square, cross-entropy	n/a	n/a	n/a	Thomas *et al*. (2017) Behrmann *et al*. (2018)
t-SNE (neural network-based)	Unsupervised	Classification	Degree of similarities between neighbouring data points	t-distribution	n/a	n/a	n/a	Fonville *et al*. (2013) Abdelmoula *et al*. (2018)
K-means	Unsupervised	Classification	Euclidean distance to the centroid of cluster	None	n/a	n/a	n/a	McCombie *et al*. (2005)
Fuzzy C-means	Unsupervised	Classification	Euclidean distance to the centroid of cluster	None	n/a	n/a	n/a	Jones *et al*. (2011)
Normalisation approaches	Supervised	Regression	Ratio between signal intensities	None	n/a	n/a	n/a	Callister *et al*. (2006) Hamm *et al*. (2012) Taylor *et al*. (2018)

6.2 Methods

6.2.1 MALDI-MS Imaging Data Format

The original MALDI-MS imaging data are recorded as two separate files of type .imzml and .ibd, which is a standard format for many MS imaging instrument outputs. These are readable using commercial software compatible with the instrument used to acquire data. Other software, for example, Matlab based MSiReader (Robichaud *et al.*, 2013; Bokhart *et al.*, 2018) can convert between known MS file types. However, it reads values form the imaging file and writes onto a spreadsheet, taking an enormously long time and may reach the memory limits of the computer before finishing. OpenMSI allows images produced at selected m/z peaks to be viewed instantly on the running webpage, and three m/z peak images can be merged to see the image structure more clearly in RGB colour scale (https://openmsi.nersc.gov/openmsi/client/index.html). The original MS file formats can be converted into H5/HDF5 Hierarchical Data Format (Askenazi *et al.*, 2017) which is a way of simplifying and retaining information from a multidimensional data set, resulting in compression of file size by up to a factor of 8.

Given that .ibd file contains mass spectral information at every pixel of an image, and .imzml file contains header information which directs these mass spectra to specified pixel locations on the image, the image data were loaded into the in-house (TINA) software and then saved in .csv format. This way it can be made certain that the data for this analysis is as “raw” as possible – i.e. extracted as recorded in the original file and has not been pre-processed in any way, as is often done in most instrumental software. The data set in this format is easily manageable and small in size.

6.2.2 MALDI-MS Imaging Acquisition of a Rat Brain Tissue Section

The MALDI-MS image was acquired by Fiona Henderson, PhD as part of her research on post-ischemic stroke studies of a rat brain model comparing diseased and healthy

regions. MALDI-MS was used to image the distribution of lipids whereas PET was used to image biological damage relevant to the disease three-months after the stroke (Henderson *et al.* 2018). Her protocol for sample preparation and MALDI-MS imaging data acquisition is outlined below, see Henderson *et al.* (2018) for the full protocol.

The rat brain specimen with a stroke region was frozen in isopentane, and stored at -80 °C before sectioning. Thin (12 µm) brain tissue sections were cut parallel to the coronal axis. The sections were placed onto indium tin oxide (ITO) conductive glass slides, washed using ammonium acetate solution (150 mM, aqueous). The matrix solution contained 10 mg/ml DHB in methanol:water (70:30), with added 0.1% TFA. 30 successive layers of matrix solution were sprayed onto the thin brain tissue section by the SunCollect matrix sprayer at a flow rate of 25 µl per minute, except the first three layers which built up with lower flow rates in order to minimise the displacement of lipids on tissues.

The data were acquired using the 7090 MALDI-TOF^2-MS (Kratos, Manchester), see instrument specifications in Section 4.2.2 of Chapter 4. The laser beam was adjusted to a diameter of 50 µm. The distance between adjacent pixels, which determined spatial resolution, was 80 µm. At each pixel, 100 laser shots were fired to accumulate a mass spectrum.

6.2.3 Pre-processing

As a result of the white:grey matter experiment in the previous chapter, the same mass range of m/z 690-890 was used for the imaging data set where the major relevant lipid peaks were expected. Also, the narrow range of data was desirable for computational efficiency during method development. Each mass spectrum has 15,539 original bins in the selected mass range. The size of the image was 219 x 118 pixels, comprising 25,842 mass spectra in the entire data set. The raw imaging mass spectra underwent the same pre-processing process as previously used in the binary mixture experiments, with parameters adjusted to suit the data set. Note that the

mass spectra of this imaging data set have double the number of original bins to that of the binary mixture experiments as a consequence of using a different model of mass spectrometer, but still a Kratos model MALDI-TOF^2-MS. Therefore, the mass spectra acquired should have consistent characteristics to the previous ones.

Initially, mass resolution reduction was performed by merging neighbouring bins of the original mass spectra by a factor of one-sixth. Then, all mass spectra were allowed to shift backward and forward by the maximum of 10 bins in order to get a well aligned mass spectral data set. Next, the background was subtracted on a spectrum-by-spectrum basis with mutual parameters: lower threshold, upper threshold and the smoothing parameter, set appropriately according to the protocol for the baseline correction as stated in Section 3.3.3. Finally, peak detection as described in Section 3.3.4 was performed, grouping bins that were expected to contain a single ion m/z peak and integrating them into a single bin, resulting in 67 peaks detected throughout the selected 200 m/z range. Each of the detected peaks has an associated m/z value. Descriptions of the pre-processing algorithm can be found in Section 3.3 of Chapter 3.

6.2.4 Image Formation

Conventional Single Ion Image

A conventional single ion image can be displayed as grey levels representing intensity for each ion m/z in mass spectra, plotted at the corresponding pixel locations. In this brain image data set, 67 different single peak images can be created. A series of single ion images formed using the 20 largest peaks were created. These are used to compare image quality to LP-ICA derived images and also show correspondence between some tissue segmentations using hand-selected peaks verses the automated alternatives.

LP-ICA Component Image

LP-ICA analysis was performed on the brain MS image data set (25,842 mass spectra) – i.e. one per pixel location, with each mass spectrum having 67 bins. Models were built for different numbers of ICA components: 8, 12, 16, 20 and 24. This had been suggested by the model selection curve, see Figure 6.4, that the model fitting started to be near optimal when 12 or more components were extracted. The LP-ICA algorithm was based on an Expectation Maximisation (EM) algorithm with an EM limit being the parameter to control the limit of optimisation divergent point, empirically determined for a sufficiently consistent/accurate model fitting with a reasonable speed, and with the MAX SEP mode applied for a maximal linear separation of components within a model (detailed explanation of the algorithms can be found in Sections 3.4.5 and 3.4.6 of Chapter 3). The use of the LP-ICA modelling method was similar to that used in Chapter 5, which was for the extraction of spectral components, however, the weighting combination scheme was not applied in this experiment as the image data contains much more tissue-related underlying variability. On average, it took 3.5 days to complete 5 attempts to find the best fitted ICA model with this amount of data.

The extracted components are referred to as probability mass functions, which describe a set of variations within the MS image data. Each component shows a mass spectrum of multiple peaks. These peaks must have some degree of correlation in order to appear in the same component. Therefore, better discriminative information is expected using these component-specific mass spectra than using just a single peak. A component image can be formed as a grey level image indicating the variation in each component quantity at different spatial locations.

6.2.5 Image Normalisation

Normalisation is another key to constructing MS images, as well as the ordinary MS data in most of the existing analysis routines. It is used to make all the mass spectra in the whole set of data comparable in terms of the signal intensity scale. MALDI-MS

in particular is very sensitive to systematic artifacts produced, for example, by matrix or contamination enhanced signals (Deininger *et al.*, 2011). With normalisation, such effects are expected to be evened out. However, MALDI mass spectra have a variety of underlying complications.

The input data for the analysis needed to be raw (non-normalised) because any normalisation would lead to the Poisson noise on signals, σ_p being scaled unevenly across the image, as a result of varied normalisation factors from pixel to pixel – i.e. because the signal integral would not be the same in every spectrum. Therefore, raw signal quantities are required in the calculation to correctly optimise the log-likelihood cost function and covariance (see Chapter 3 for Equations (3.8) and (3.10)). As a consequence, normalisation can only be used here for the sake of image presentation – i.e. images can be visually evaluated and compared. For the LP-ICA component images, the mutual dynamic range was used through all the images (ranges from 0 - 100%) so that the weighting for each component can be directly compared with others.

In this chapter, the approaches to normalisation are described below, both for the LP-ICA component images and the conventional single ion images. Each normalisation process was performed on a spectrum-by-spectrum (pixel-by-pixel) basis across the image.

***Non-normalisation*:**

The raw measures of mass spectra in the data set (peak bin intensities as a result of the peak detection) in every pixel were used for the input of MS image data into the LP-ICA analysis tool.

***Normalisation to the signal integral*:**

This is basically referred to as normalisation to the total ion count (TIC) in the literature. The TIC in this case was calculated by integrating across all bins. That is:

- For the conventional single ion images, the signal intensity of the peak of interest in each bin was divided by the integral of total signals for that given pixel.
- For the LP-ICA component images, the signal quantity of the component of interest was divided by the sum over all the component signal quantity in the given model for that given pixel.

6.2.6 Sodium Gradient Analysis

Sodium is an alkali metal that naturally exists in biological tissues. In this specific brain sample, the sodium was at a concentration that led the sodiated ion species $[M+Na]^+$ to be majority for all main molecules in the observed lipid range, whilst the protonated ion $[M+H]^+$ species were the second largest in abundance.

As a first step towards understanding biases in quantitative analysis, the relative sodium concentration across the imaged sample was measured. This was achieved through measurement of sodiated-to-protonated ion peak intensity ratio – i.e. $[M+Na]^+$/ $[M+H]^+$ for 3 major molecules, which are at m/z 756.5, 782.6 and 810.6 versus m/z 734.5, 760.6 and 788.6.

6.2.7 Quality Assessment of the MS Image

This section includes firstly an image segmentation test as an assessment of visual quality of images, and secondly the noise correlation test as an assessment of separation between component images. The following processes were repeated for 8-, 12-, 16-, 20- and 24-component models.

Image Segmentation Test

All LP-ICA component images of a model were computed. For every possible combination of 3 component images, a colour coded image was generated where

intensity scale of three distinct colours: red, green and blue was given to each component image, and then superimposed. This provided an indication of segmentation quality based upon a subset of three images. Some of the colour coded images that enhanced the subjective visualisation of tissue segmentation were noted.

Noise Correlation Test

Some anti-correlation between noises in ICA component images might be evidence of the need to add two or more components together to explain a single tissue type, as was found in the analysis of the binary mixtures. In order to test this, first of all, the noise on each of the component images created was estimated. A noise-free image of a component was estimated through tangential smoothing, which predicts each central pixel using its neighbouring pixels (http://www.tina-vision.net/docs/memos/2016-009.pdf, Thacker *et al*. (2016)). Therefore, the noise estimate can be obtained by subtracting the computed noise-free image from the modelled image of a component.

A correlation plot was then generated for any given pair of the component noise images, where noise on one image was plotted against the other on a pixel-to-pixel basis. Noise correlation patterns were observed for every possible pair of the component images.

6.2.8 Peak Assessment on Individual ICA Component Spectra

LP-ICA models a set of sub-spectra that can be linearly combined with appropriate weighting factors (quantity associated to each component) to approximate the original spectra of the data set. The extracted sub-spectra vary depending on the number of components in a model. Even when the same number of components are extracted, statistical variation leads to differences in those components each time they are calculated, as in real-world data there can be multiple solutions (local optima). The greater the number of components in the model, the more intimately

all the variations in the data are fitted. This is not necessarily a good thing, and when there are too many components, the combination begins to model noise, a situation known as “overfitting”. The opposite would be “underfitting” when too few components extracted leads to failure of fitting enough variations. Continuing from Section 6.2.4, the model selection curve estimated that the appropriate component number was somewhere between 12 and 24 components – 8 components might still be sufficient. Each of these was investigated whether it had modelled the level of variation sufficiently, and that there was no obvious evidence of over- or under-fitting by looking at the sub-spectra and the corresponding component images. This was done as a primary quality control test.

For each of the 8-, 12-, 16-, 20- and 24-component models, individual sub-spectra (component spectra) were examined for the 10 most intense peaks amongst the 67 ion peaks detected. All the m/z values corresponding to these top peaks were labelled as they can potentially be used for further investigation of a link to biological cause, e.g. Sections 6.2.10 and 6.2.11.

6.2.9 Isotope Analysis

The ratios between the different natural isotope permutations in molecules are well known. An isotope peak at one mass unit higher than the monoisotopic peak (all ^{12}C): $[M+1]^+$ for an organic molecule is due mainly to the presence of a single ^{13}C in that molecule replacing any one of the (most abundant) ^{12}C atoms. A small contribution is also due to the existence of ^{15}N. ^{17}O and deuterium can be considered negligible as traced very small abundance in nature, however, they can be significant in larger molecules. The larger the molecule, the higher chance finding these rarer isotopes. The expected isotopic distribution of a molecule, knowing the distribution of the two most abundance isotopes of each atomic type, should follow the general formula for binomial expansion $(a + b)^n$. When a and b are the fractional natural abundance of the two isotopes, and n is the number of atoms in the molecule. The molecular isotopic abundance can be derived by adding up distributions from each atomic

component. Similarly, the $[M+2]^+$ isotope species incorporates two ^{13}C atoms or an ^{18}O within a molecule.

The isotope pattern is therefore a property that determines essential characteristics of mass spectra. This property was used as a basis for assessing mass spectral components extracted by the LP-ICA model – i.e. whether the isotope peak intensity ratio at a selected m/z is consistent with the expected value. Then, any uncertainties observed from the measured values were compared with the theoretical predicted error, see Section 6.3.5. Isotope ratios were calculated from $[M+Na]^+$ and $[M+H]^+$ ion forms of 3 molecules that appears major across every component, which are listed in Table 6.2. Note that regardless of sodium concentration across pixel locations, the isotope ratio is a conserved physical property. It is calculated from spectral components which are derived on a per-pixel basis.

Table 6.2 List of m/z peaks used for the isotope analysis

m/z value	Ion form	Molecular type	Expected ratio	
			$[M+1+H]^+/[M+H]^+$ or $[M+1+Na]^+/[M+Na]^+$	$[M+2+H]^+/[M+H]^+$ or $[M+2+Na]^+/[M+Na]^+$
734.5	$[M+H]^+$	PC(16:0/16:0)	0.46	0.12
756.5	$[M+Na]^+$			
760.6	$[M+H]^+$	PC(16:0/18:1)	0.49	0.13
782.6	$[M+Na]^+$			
788.6	$[M+H]^+$	PC(18:0/18:1)	0.51	0.14
810.6	$[M+Na]^+$			

N.B. These expected isotope ratios were obtained via LIPID MAPS database for mass spectrometry isotopic distribution

6.2.10 Tissue Compositions and Stroke Biomarkers

Component images show different component segments of brain anatomy. Components that display specific regions or the stroke lesion were particularly of interest. The component sub-spectra that relate to each of these were recorded. There must be characteristic chemical (lipid) variations causing differentiation between components which cause these specific tissues types to be separated. Important differentiating molecules (determined by the 10 most intense peaks for

each component, following Section 6.2.8) were identified based on their m/z values with reference to previously identification of those molecules in the similar sample types reported in the literature and also the LIPID MAPS database online resource (http://www.lipidmaps.org/).

6.2.11 Lipid Mapping on Anatomical Brain Atlas

An anatomical atlas of a brain section may be constructed based on chemical labelling (of lipids in this case) at different spatial locations. The construction of colour-coded component images as in Section 6.2.7 shows the segmentation of different brain regions. Component images represents biochemical distributions within the tissue. Tissue-specific functionalities depending on the lipid types observed within the brain regions were explored. These were cross-compared to the rat brain atlas of approximately the same cut of tissue section as presented in The Rat Brain in Stereotaxic Coordinates by Paxinos and Watson (1986).

The list of top 10 major peaks in each component as assessed in Section 6.2.8 can be used at this stage to help identify cell/tissue types according to their biochemical compositions. Therefore, the underlying biology of the brain section can be investigated, although a full biological functional analysis is beyond the scope of this thesis.

6.3 Results and Discussion

6.3.1 Raw vs. Pre-processed Mass Spectra

For the rat stroke brain MS image data set, the mass range of m/z 690-890 was selected for consistency with the previous white:grey matter binary mixture experiment. More importantly, the method of preparation and acquisition favoured phospholipids as the main lipid peaks shown on mass spectra, and they sit mostly

within this mass range (Henderson *et al.*, 2018). An example of a raw spectrum at a single pixel is seen at the top of Figure 6.2.

The MS imaging data set is high-dimensional. The original binning of mass spectra and number of mass spectra acquired are mentioned in Section 6.2.3, creating 219x118 pixels on MS images. Pre-processing steps were applied to the data in order to correct for a number of artifacts and reduce the complexity of the data for more efficient computation/quantification.

Following the parameters indicated in the method Section 6.2.3, the result after pre-processing, which include mass resolution reduction by a factor of one-sixth, alignment, background subtraction, and peak detection; is shown as the resulting spectrum at the bottom of Figure 6.2. The m/z values that correspond to the final 67 detected peaks are listed in Table 6.3.

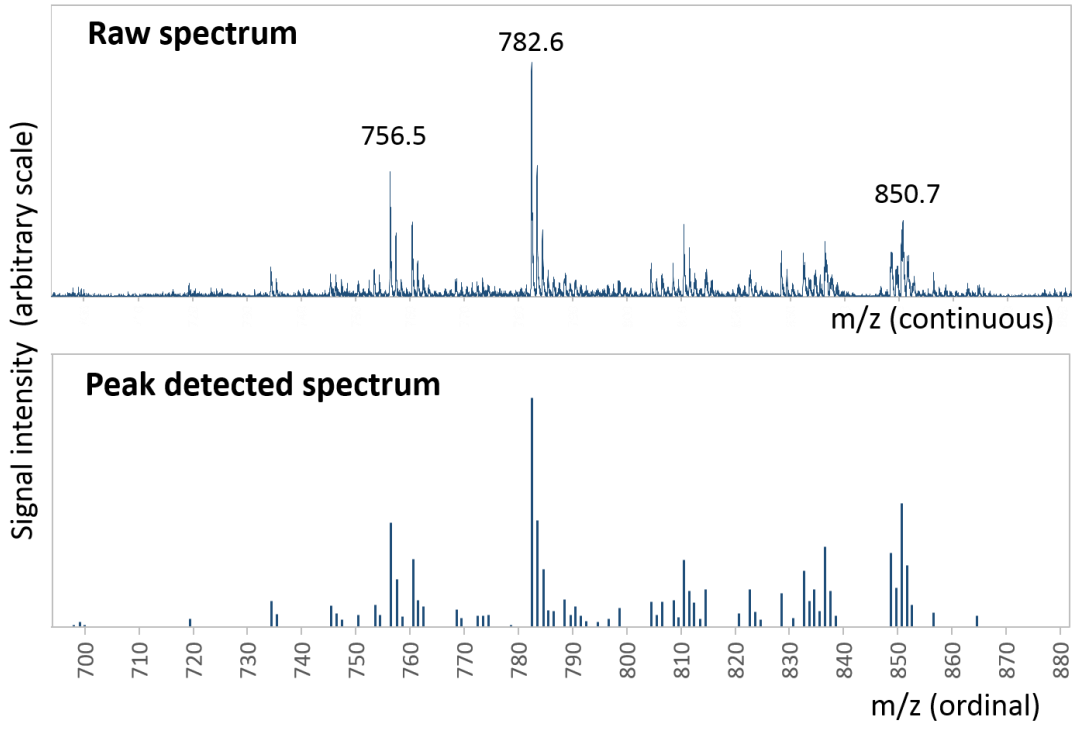

Figure 6.2 Raw vs. Pre-processed mass spectrum (after peak detection) acquired at a pixel of the image data set

Table 6.3 List of peaks detected with the m/z value and the corresponding binning index

Index	m/z value
0	697.98
1	699.12
2	699.97
3	719.39
4	734.50
5	735.45
6	745.50
7	746.46
8	747.41
9	750.49
10	753.65
11	754.47
12	756.53
13	757.64
14	758.60
15	760.67
16	761.48
17	762.51
18	768.60
19	769.57
20	772.46
21	773.51
22	774.48

Index	m/z value
23	778.66
24	782.56
25	783.53
26	784.66
27	785.56
28	786.46
29	788.49
30	789.62
31	790.53
32	791.58
33	792.57
34	794.61
35	796.64
36	798.69
37	804.61
38	805.60
39	806.59
40	808.65
41	809.49
42	810.63
43	811.62
44	812.46
45	813.61

Index	m/z value
46	814.60
47	820.66
48	822.73
49	823.66
50	824.66
51	828.60
52	830.67
53	832.69
54	833.69
55	834.62
56	835.63
57	836.64
58	837.65
59	838.57
60	848.78
61	849.71
62	850.73
63	851.75
64	852.68
65	856.60
66	864.70

Conventional Single Ion Image

Single ion images were formed using the 20 largest peaks from the peak detected mass spectra. The full set of these single ion images are provided in Appendix B-2 (Figure B.4). The image presented in Figure 6.3 below shows an example of these images plotted using m/z 782.6 which is the most intense peak of the image data set. The tissue segmentations derived from these 20 single ion images are highly similar because many molecules are present in common among different tissue regions. This limits the ability of single ion images to represent tissue-specific characteristics.

Figure 6.3 An example of single ion images plotted using m/z 782.6 – the dynamic range has been set to maximise the contrast of the image (the darkest pixel has the highest intensity value)

6.3.2 Model Component Spectra and Images

Primary Model Selection

The primary model selection is assessed using the chi-square per degree of freedom test, as a measure of how well the model fits to the data. A subset of 400 pre-processed mass spectra was used to build models here to speed up computation while preserving the nature of the data set by using mass spectra from 2 rows of pixels horizontally across the middle of the tissue section, thereby typifying most of the variations likely to be found in the sample. The number of ICA components extracted was varied between 2 and 28. The model selection curve in Figure 6.4 demonstrates that the model fitting dramatically improves as component number increases at a small number of components. This improvement starts to change gradually until reaches a plateau. At about 12 components, the rate of improvement of model fitting is considered to be approximately the point where the fitting value begins to level off. This is taken to mean the model should be built with 12 or more components. Given that this test only gives a lower limit on component number, this value and a small set of component numbers beyond this value (12, 16, 20 and 24) were selected for further examination for the rest of the analysis (a model with slightly fewer component numbers (8) was also built for a sake of comparison).

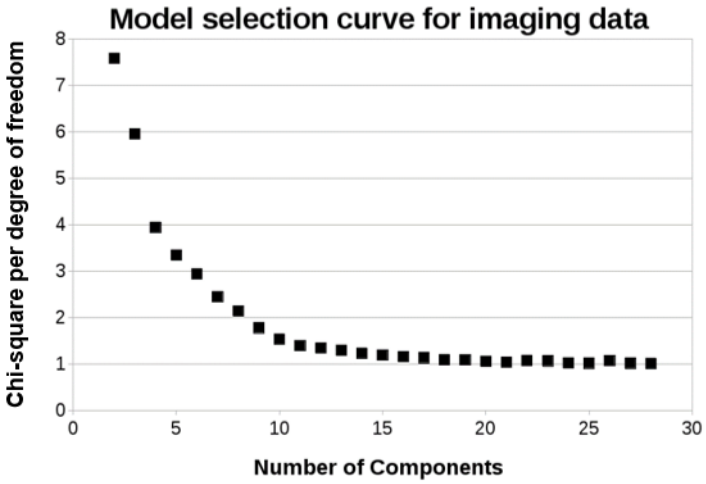

Figure 6.4 LP-ICA model selection curve for the brain MS image data

Component Spectra

Mass spectral components (sub-spectra) extracted from the 12 and 20 component ICA models are shown here in Figures 6.5 and 6.6, respectively, as representative models built in the range of selected component numbers for the illustrative purposes. Other models' component sub-spectra are provided in Appendix B-1 (Figure B.1 to B.3). The peak bins were plotted in the index order and were scaled here according to the m/z values for each component, making them directly comparable with the format of the original mass spectra. For every spectral component of both models (sub-spectra in Figures 6.5 and 6.6), the first 10 most intense m/z peaks were labelled. They were compared against each other. The unique relative concentrations of the major lipid molecules could be associated to some sub-type of tissue (anatomical region). Some lipids were only observed in some of the components and are not present in others. It is therefore of interest to determine the identity of these lipids and then investigate the biological meaning of their presence in that tissue. A comprehensive analysis is beyond the scope of this thesis. For this purpose, individual component images of both models are provided at the corner of the associated plots of component spectra (sub-spectra) in Figures 6.5 and 6.6. All component images were normalised to the integral intensity at each pixel location. Areas outside tissue were masked off to improve visualisation. The grey scale at the bottom of each image represents a relative weighting that each component has to the total signal quantity as a result of normalisation for visualising the LP-ICA component images as described in Section 6.2.5.

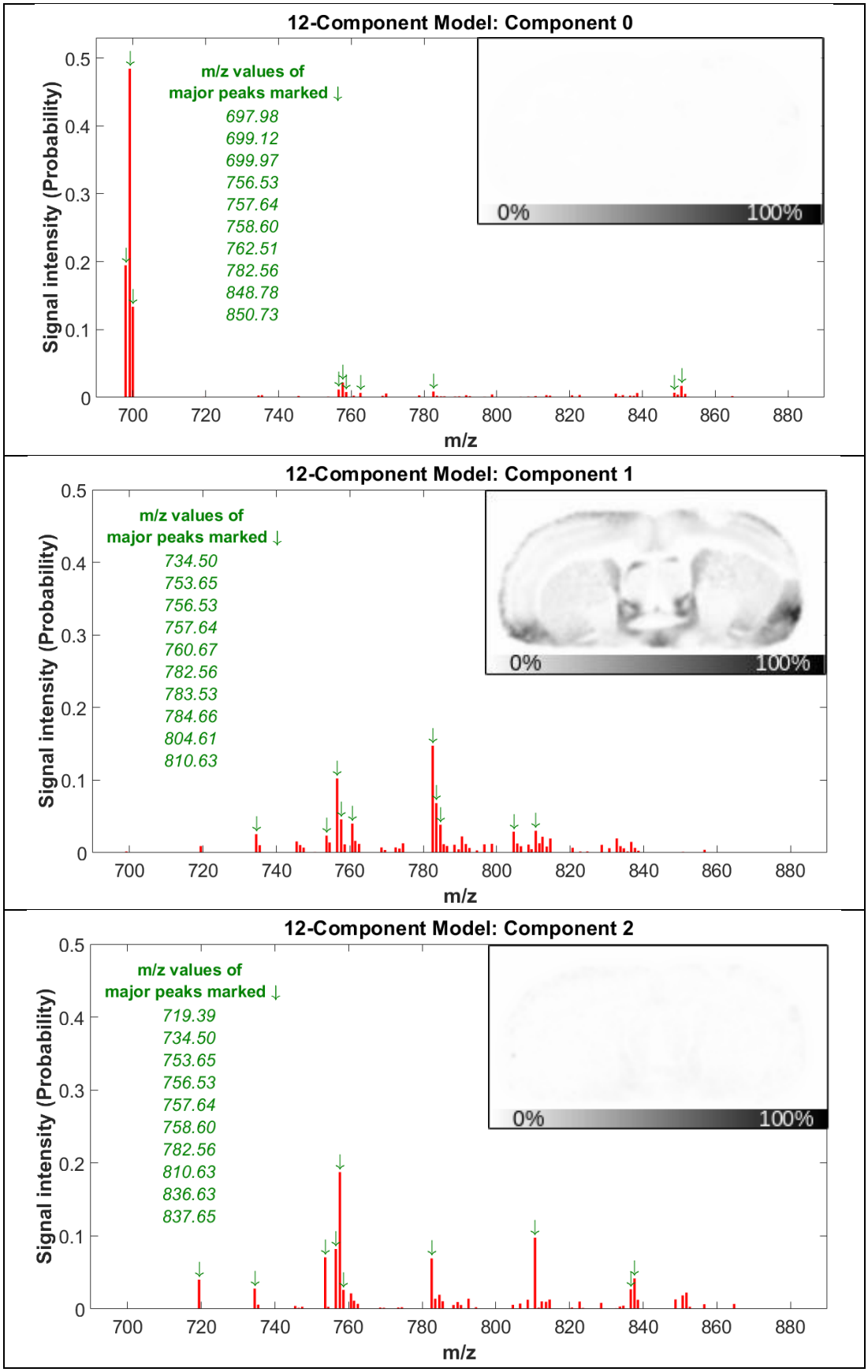

Figure 6.5 12-component sub-spectra with 10 major peaks marked with green arrows (their m/z values are listed in ascending order). The corresponding component images are shown. (Part 1 of 4)

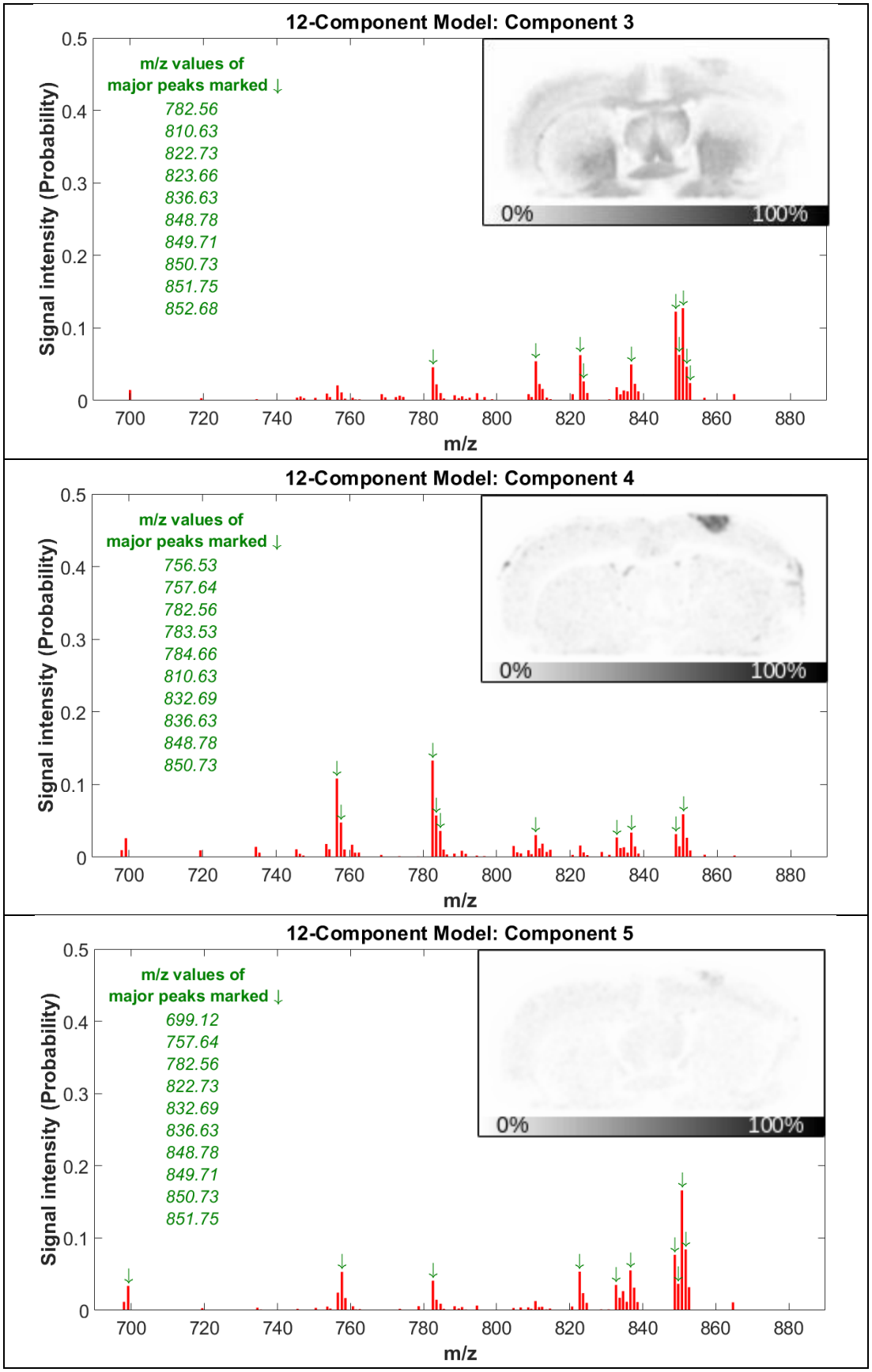

Figure 6.5 12-component sub-spectra with 10 major peaks marked with green arrows (their m/z values are listed in ascending order). The corresponding component images are shown. (Part 2 of 4)

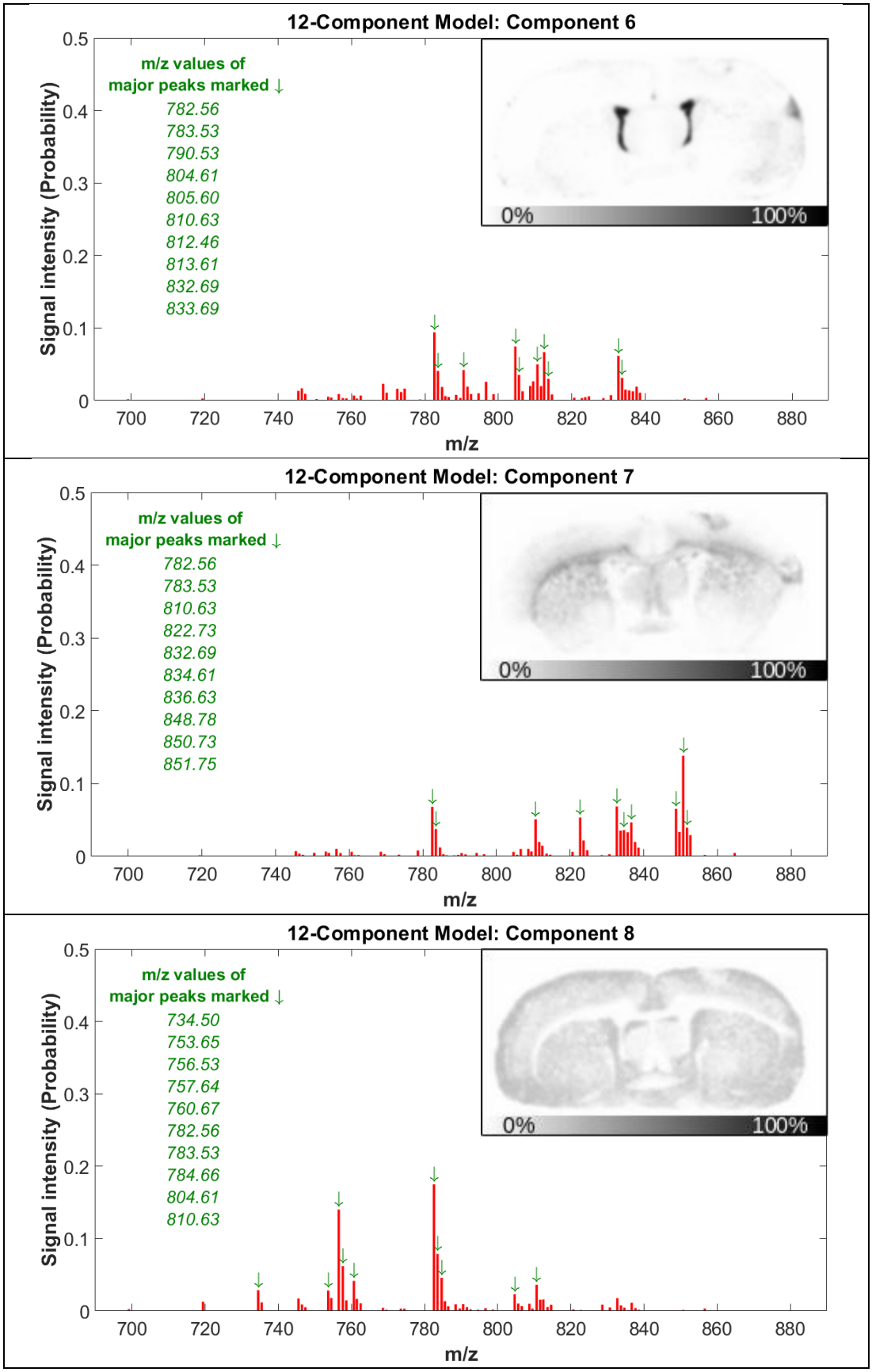

Figure 6.5 12-component sub-spectra with 10 major peaks marked with green arrows (their m/z values are listed in ascending order). The corresponding component images are shown. (Part 3 of 4)

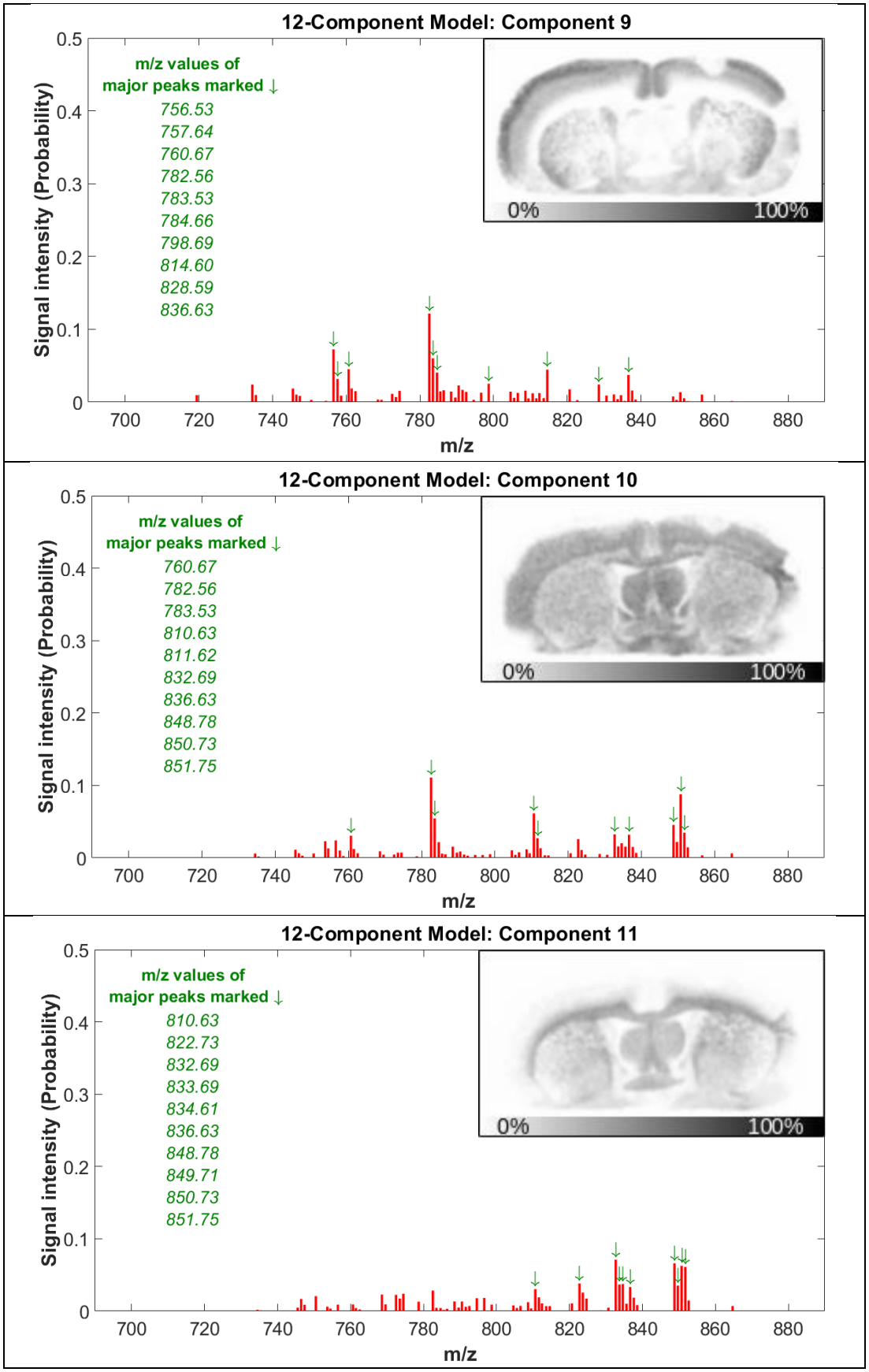

Figure 6.5 12-component sub-spectra with 10 major peaks marked with green arrows (their m/z values are listed in ascending order). The corresponding component images are shown. (Part 4 of 4)

LP-ICA component spectra estimated by the model can be used to generate a number of 2-dimensional grey level plots for each of the extracted components. In a component image, the grey level value at every pixel was determined by the associated quantity of that component spectrum in the pixel which can potentially be interpreted in terms of the common underlying biological variations distributed across the image. The spectra varied slightly when the number of components was altered. These component images show much clearer tissue-specific segmentations compared to single ion images, which can benefit the determination of tissue phenotypes and biomarkers (This will be discussed later in Sections 6.3.9 and 6.3.10).

The 20-component model showed better segmentation of brain tissue, compared to the 12-component model. For example, the stroke region stands out individually in the image corresponding to component number 8 of the 20-component model (see the component image in Figure 6.6). This was not the case for the 12-component model, where the stroke region was not discriminated from the ventricles (see the image corresponding to component 6 in Figure 6.5).

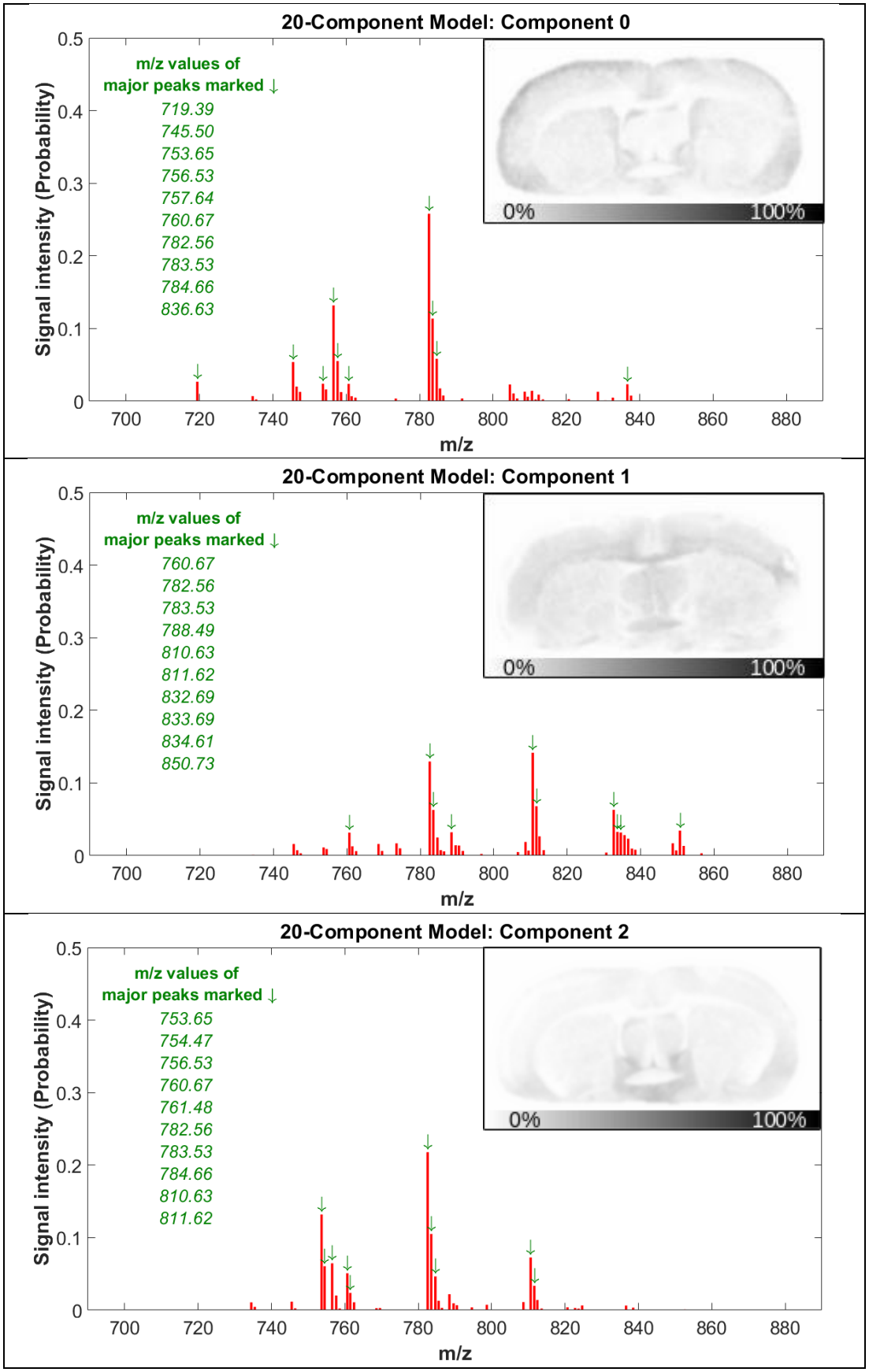

Figure 6.6 20-component sub-spectra with 10 major peaks marked with green arrows (their m/z values are listed in ascending order). The corresponding component images are shown. (Part 1 of 7)

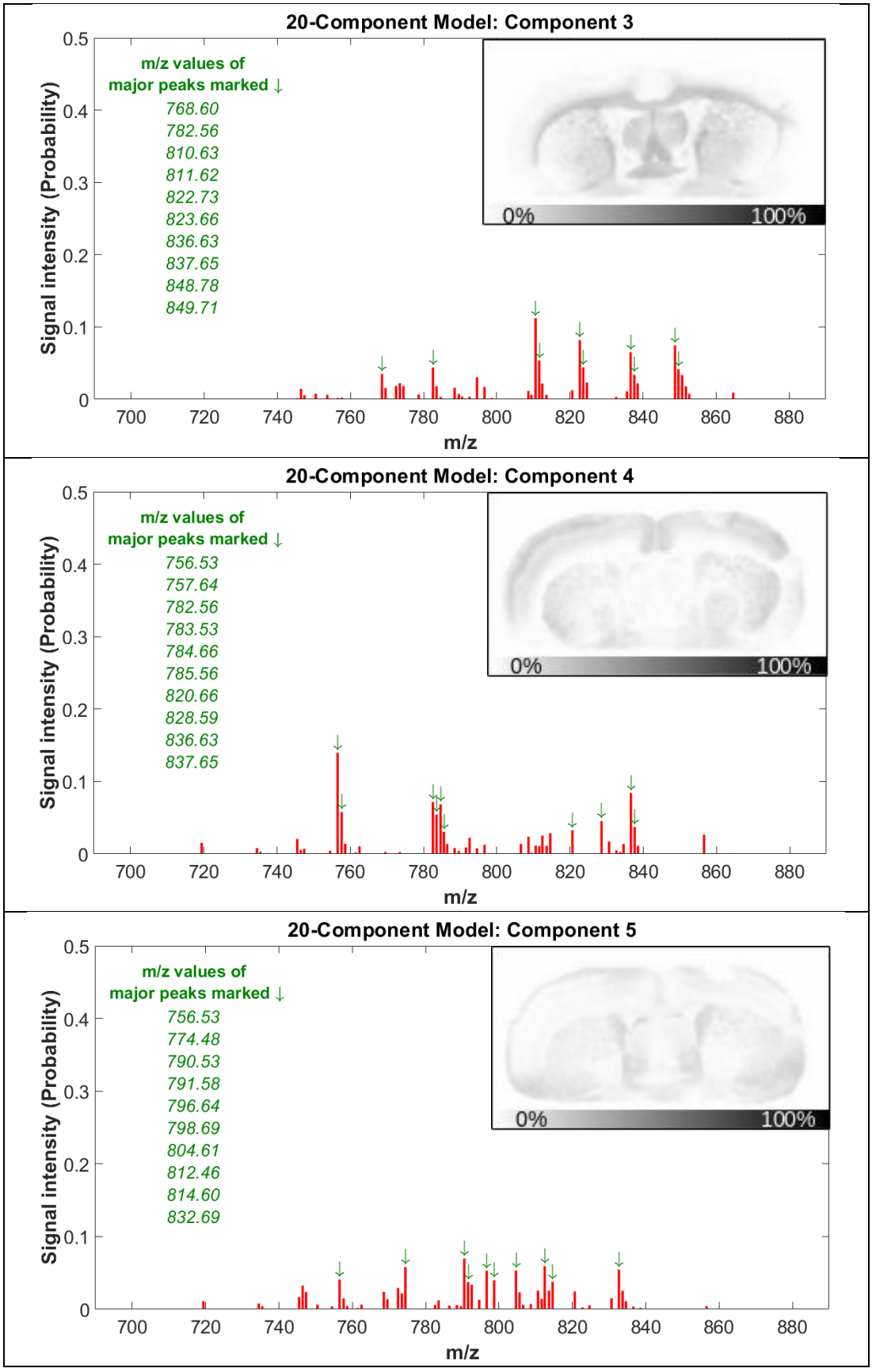

Figure 6.6 20-component sub-spectra with 10 major peaks marked with green arrows (their m/z values are listed in ascending order). The corresponding component images are shown. (Part 2 of 7)

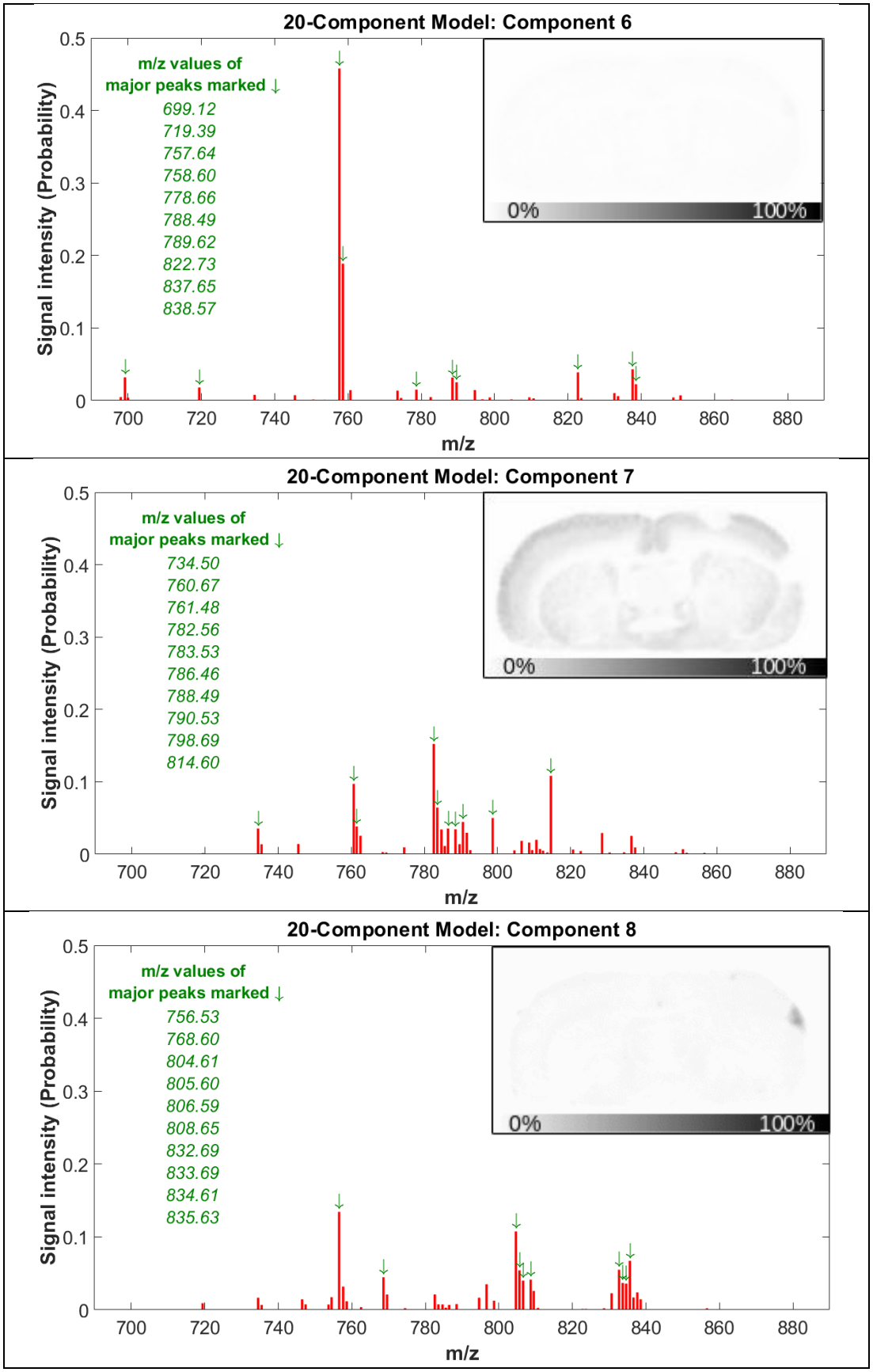

Figure 6.6 20-component sub-spectra with 10 major peaks marked with green arrows (their m/z values are listed in ascending order). The corresponding component images are shown. (Part 3 of 7)

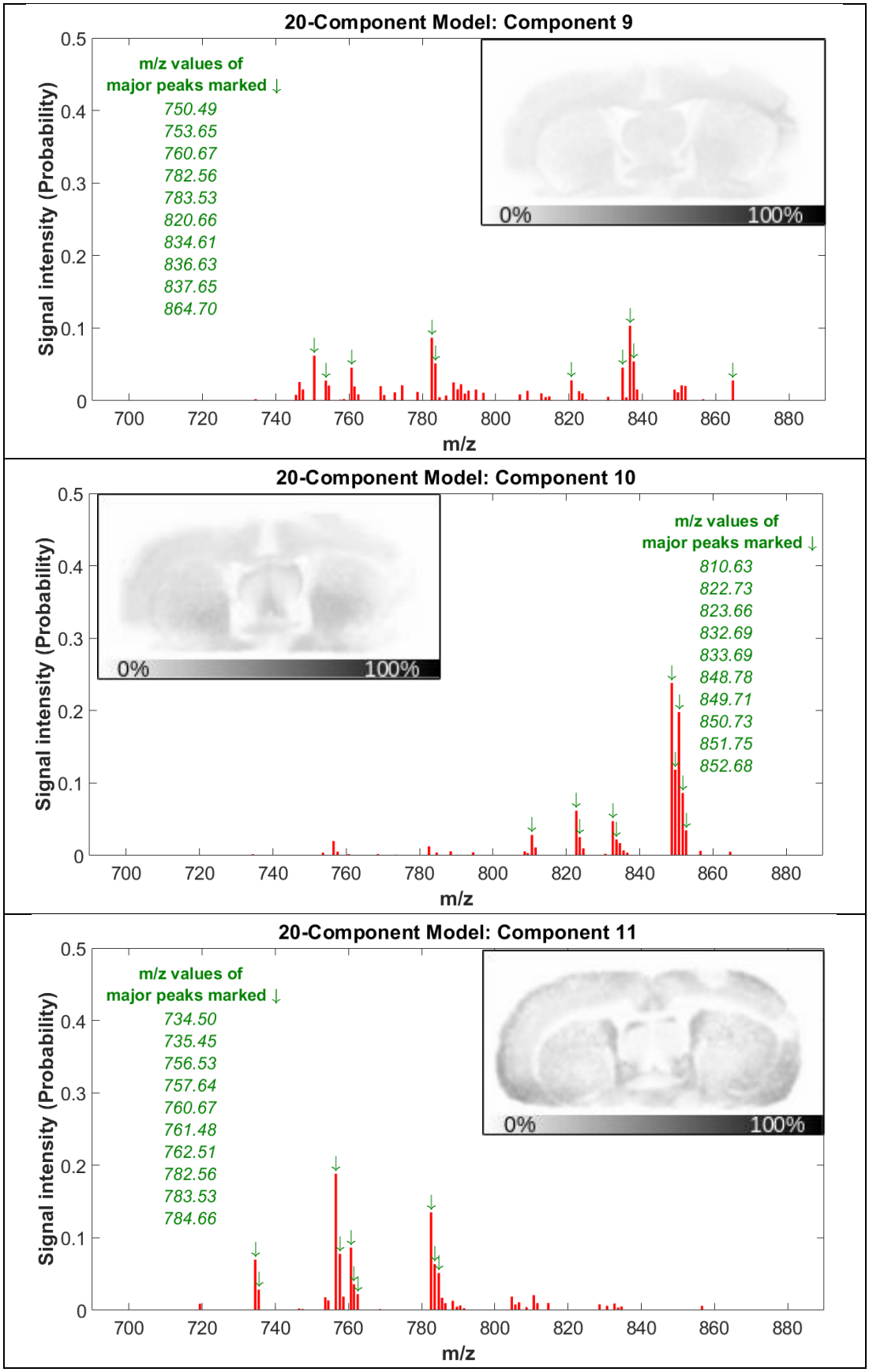

Figure 6.6 20-component sub-spectra with 10 major peaks marked with green arrows (their m/z values are listed in ascending order). The corresponding component images are shown. (Part 4 of 7)

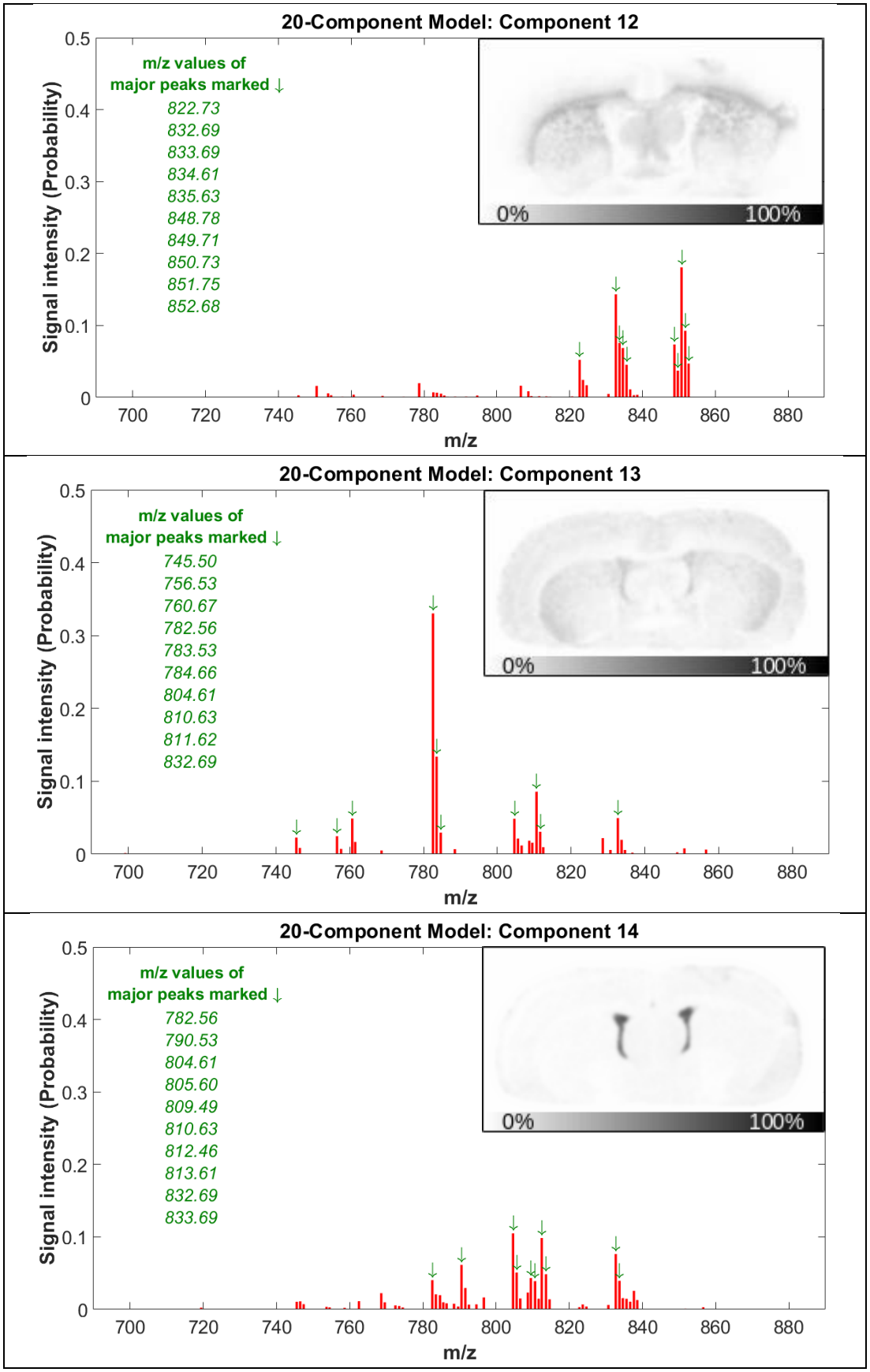

Figure 6.6 20-component sub-spectra with 10 major peaks marked with green arrows (their m/z values are listed in ascending order). The corresponding component images are shown. (Part 5 of 7)

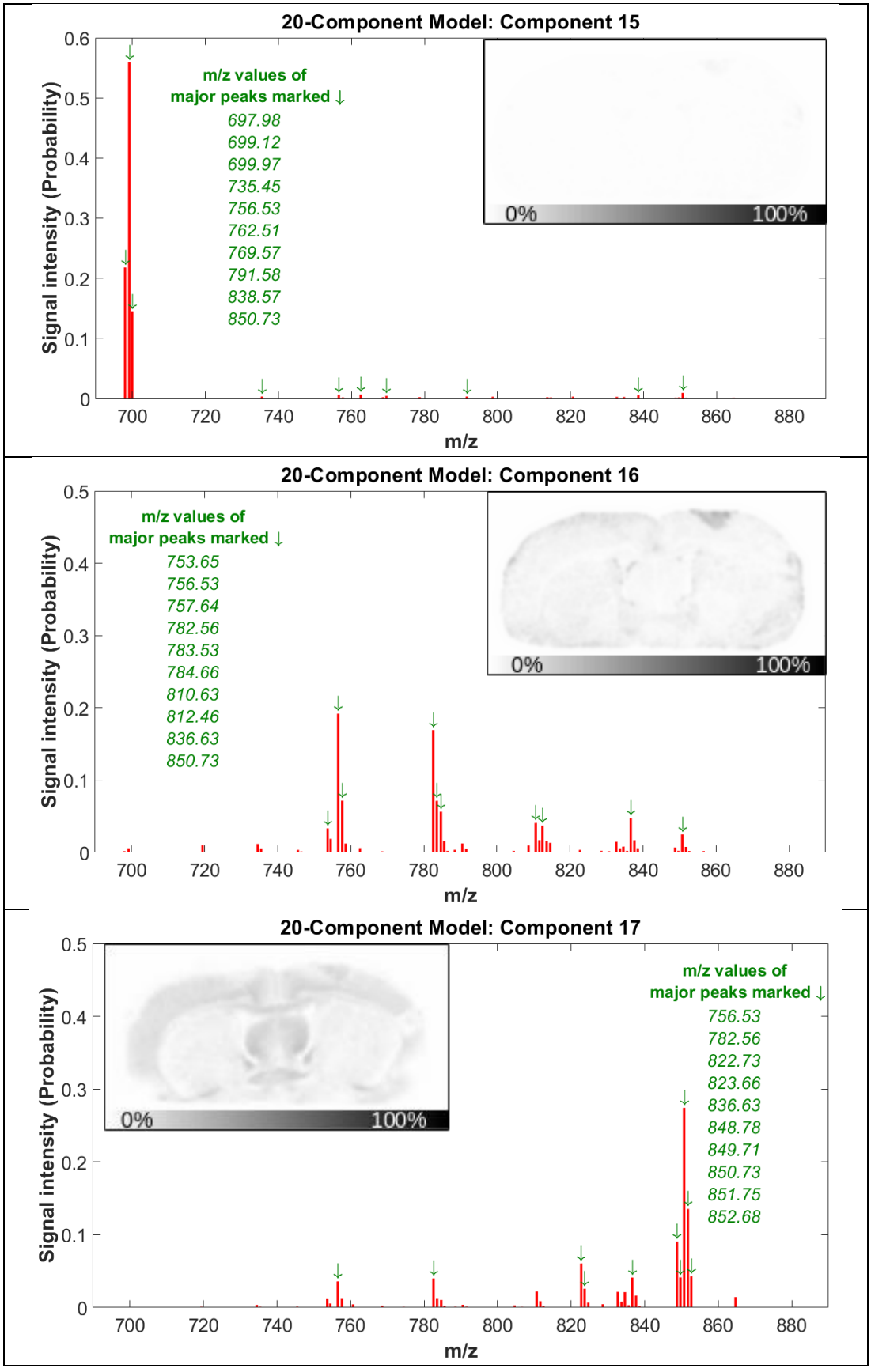

Figure 6.6 20-component sub-spectra with 10 major peaks marked with green arrows (their m/z values are listed in ascending order). The corresponding component images are shown. (Part 6 of 7)

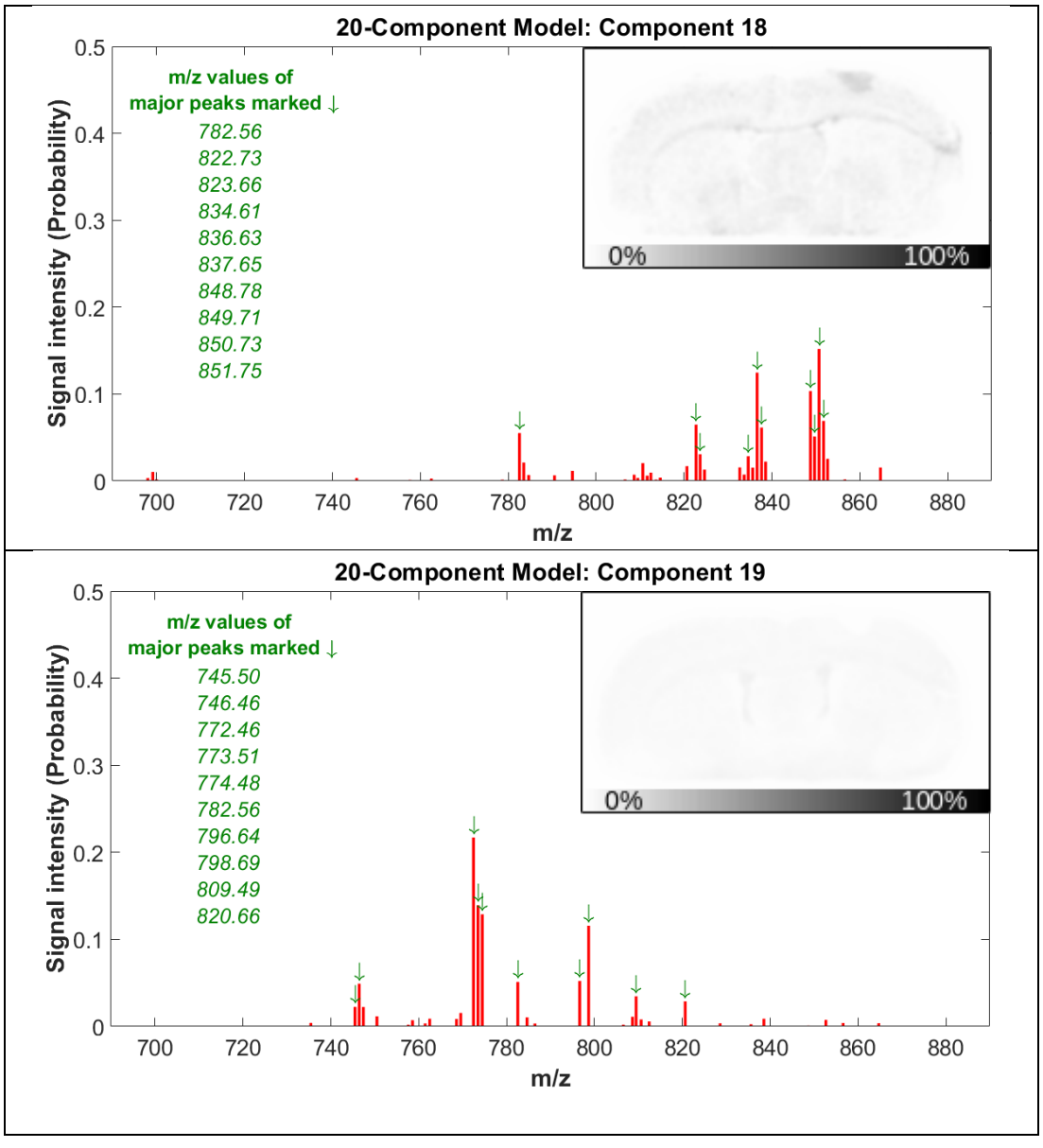

Figure 6.6 20-component sub-spectra with 10 major peaks marked with green arrows (their m/z values are listed in ascending order). The corresponding component images are shown. (Part 7 of 7)

Major Peaks Listed by Component

The 10 most intense peaks observed in each component for the 12- and 20-component models are listed in Tables 6.4 and 6.5, respectively, with bin indices and the corresponding m/z values. A tick indicates the components for which each of these peaks is detected. This information was used to guide identification of lipids of interest. Note that the mass window selected for this analysis was in the phospholipids range. There will very likely be important discriminating lipids outside this range, such as sphingomyelin, cholesterol, etc. These should be included in further work, but would have significantly slowed algorithm development in the current project. Most cell membrane lipids are likely to remain in place when in contact with solutions, whereas lipids of other class may be displaced on the sectioned slice. Additionally, intact phospholipids have a phosphate group which easily binds with a positive adduct, e.g. hydrogen or sodium ions. However, the mass range chosen for this study clearly had sufficient peaks to test the analysis method (as the analysis required a very long computational period: a few days per 5 attempts of building models). When the method is validated, it can be extended to include wider mass ranges – see the discussion on how the computational efficiency can be improved in Section 7.3.

Table 6.4 10 major peaks presented in each sub-spectral component of the 12-component model

Bin index	m/z value	Component index											
		0	1	2	3	4	5	6	7	8	9	10	11
0	697.98	✓											
1	699.12	✓					✓						
2	699.97	✓											
3	719.39			✓									
4	734.50		✓	✓						✓			
10	753.65		✓	✓						✓			
12	756.53	✓	✓	✓		✓				✓	✓		
13	757.64	✓	✓	✓		✓	✓			✓	✓		
14	758.60	✓		✓									
15	760.67		✓							✓	✓	✓	
17	762.51	✓											
24	782.56	✓	✓	✓	✓	✓	✓	✓	✓	✓	✓	✓	
25	783.53		✓			✓		✓	✓	✓	✓	✓	
26	784.66		✓			✓				✓	✓		
29	788.49												
31	790.53							✓					
36	798.69										✓		
37	804.61		✓					✓		✓			
38	805.60							✓					
42	810.63		✓	✓	✓	✓		✓	✓	✓		✓	✓
43	811.62											✓	
44	812.46							✓					
45	813.61							✓					
46	814.60										✓		
48	822.73				✓		✓		✓				✓
49	823.66				✓								
51	828.60										✓		
53	832.69					✓	✓	✓	✓			✓	✓
54	833.69							✓					✓
55	834.62								✓				✓
57	836.64			✓	✓	✓	✓		✓		✓	✓	✓
58	837.65			✓									
60	848.78	✓			✓	✓	✓		✓			✓	✓
61	849.71				✓		✓						✓
62	850.73	✓			✓	✓	✓		✓			✓	✓
63	851.75				✓		✓		✓			✓	✓
64	852.68				✓								

Table 6.5 10 major peaks presented in each sub-spectral component of the 20-component model (Part 1 of 2)

Bin index	m/z value	Component index																		
		00	01	02	03	04	05	06	07	08	09	10	11	12	13	14	15	16	17	18	19
0	697.98																✓				
1	699.12							✓									✓				
2	699.97																✓				
3	719.39	✓						✓													
4	734.50								✓				✓								
5	735.45												✓				✓				
6	745.50	✓													✓						✓
7	746.46																				✓
9	750.49										✓										
10	753.65	✓		✓							✓							✓			
11	754.47			✓																	
12	756.53	✓		✓		✓	✓			✓			✓		✓		✓	✓	✓		
13	757.64	✓				✓		✓					✓					✓			
14	758.60							✓													
15	760.67	✓	✓	✓					✓		✓		✓		✓						
16	761.48			✓					✓				✓								
17	762.51												✓				✓				
18	768.60				✓					✓											
19	769.57																✓				
20	772.46																				✓
21	773.51																				✓
22	774.48						✓														✓
23	778.66							✓													
24	782.56	✓	✓	✓	✓	✓			✓		✓		✓		✓	✓		✓	✓	✓	✓
25	783.53	✓	✓	✓		✓			✓		✓		✓		✓			✓			
26	784.66	✓		✓		✓							✓		✓			✓			
27	785.56					✓															
28	786.46								✓												
29	788.49		✓					✓	✓												
30	789.62							✓													
31	790.53						✓		✓							✓					

Table 6.5 10 major peaks presented in each sub-spectral component of the 20-component model (Part 2 of 2)

Bin index	m/z value	Component index																		
		00	01	02	03	04	05	06	07	08	09	10	11	12	13	14	15	16	17	18	19
32	791.58						✓										✓				
35	796.64						✓														✓
36	798.69						✓		✓												✓
37	804.61						✓			✓					✓	✓					
38	805.60									✓						✓					
39	806.59									✓											
40	808.65									✓											
41	809.49															✓					✓
42	810.63		✓	✓	✓							✓			✓	✓		✓			
43	811.62		✓	✓	✓										✓						
44	812.46						✓									✓		✓			
45	813.61															✓					
46	814.60						✓		✓												
47	820.66					✓					✓										✓
48	822.73				✓			✓				✓		✓					✓	✓	
49	823.66				✓							✓							✓	✓	
51	828.60					✓															
53	832.69		✓				✓			✓		✓		✓	✓	✓					
54	833.69		✓							✓		✓		✓		✓					
55	834.62		✓							✓	✓			✓						✓	
56	835.63									✓				✓							
57	836.64	✓			✓	✓					✓							✓	✓	✓	
58	837.65				✓	✓		✓			✓									✓	
59	838.57							✓									✓				
60	848.78				✓							✓		✓					✓	✓	
61	849.71				✓							✓		✓					✓	✓	
62	850.73		✓									✓		✓			✓	✓	✓	✓	
63	851.75											✓		✓					✓	✓	
64	852.68											✓		✓					✓		
66	864.70										✓										

61 bins have been identified as the major peaks in different components for the 20-component model (Table 6.5) while only 37 bins were observed for the 12-component model (Table 6.4) using the same criteria. This shows that the model managed to extract more variations between components when more components were allowed. For example, when there are fewer components than the underlying variations within a data set, the peak bins that describe minor variations could be hidden by other variations, resulting in peaks not being selected as major contributors to the corresponding spectra. The component images acquired this way would then be ambiguous. In other words, when the number of components is too few, some spectral variations can be merged into a single component instead of being appropriately separated. The peaks that appeared in the main peak list for the 20-component model but not the 12-component model are marked in blue in Table 6.5.

Therefore, the 20-component model was considered a reasonable model to represent the data, providing sufficient unique components to be interpreted as tissue-specific phenotypes. Table 6.7 lists the identified phosphatidylcholines (see later in Section 6.3.6), at each m/z value based on previously reported literature for brain tissues, using MS/MS analysis. These data can be used to determine which molecules are associated with each LP-ICA component and their associated anatomical features.

Overlaid Colour Coded Images

The image segmentation test described in Section 6.2.7 aimed to assess the overall segmentation quality of the component images generated. Even though, some distinguishable structures can be picked out from the grey scale component images (see the images in Figure 6.6), the image constructed using an RGB (red-green-blue) colour scheme to combine any 3 component images, provides visually clearer segmentation and better contrast.

The overlaid colour coded images obtained from various groups of components are presented in Figure 6.7 allowing enhanced visualisation of tissue segmentation. In

other words, this is a clear way of presenting the information seen in the image results analysed using the LP-ICA method. These colour combination images demonstrate how well the components anatomically segment the image into relevant regions, which could support determination of the biological functions each lipid plays.

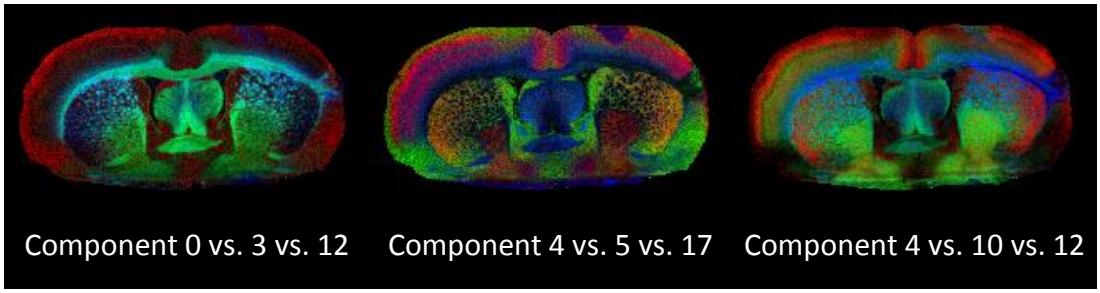

Figure 6.7 Overlaid colour coded images constructed by merging three ICA component images of the 20-component model

Noise Correlation Plots

The technique of using linear combinations of components to describe an underlying variation was previously suggested for binary mixture experiments. However, the previous data sets were restricted to two underlying sample classes per mixture whereas this parameter is completely unknown for the imaging data set. The noise correlation test described in Section 6.2.7 was therefore established to look for pixel-to-pixel cross-correlation of noise in all possible pairs of components. The reason for doing this was to seek components whose noise value could have been counter-correlated with one another – i.e. noise on a pair of components with different signs of residuals shown on a correlation plot as negatively skew data points on the axes. If that was the case, the chance would be these images have to be added together in order to denoise; as evidence for the above component combination suggestion.

Unfortunately, no obvious anti-correlation was observed in any of the plots. An example correlation plot of noise in image pair seen in Figure 6.8 was generated from the 24-component model. They are instead considered (slightly) positively correlated (i.e. when data are positively skew on the axes, resulted from same sign noise on a

pair of components) which means adding the two components together would cause an overall increase in noise, as opposed to the anti-correlation. All other pairs of component in every model built were tested in the same way. They showed more or less similar characteristics. On this basis, it was concluded that components extracted already represent independent variations; there was therefore no need to add multiple components together to correct for evaluation and enhance the contents in MALDI LP-ICA images (for modelling up to 24 components).

Note that tangential smoothing was available to compute an expected noise-free image that could possibly give the closest approximation to this image type where there are full of structural contents, e.g. the brain MS images (Thacker *et al.*, 2016). However, it is not an absolute ground truth and therefore leads to additional random errors during the noise estimation.

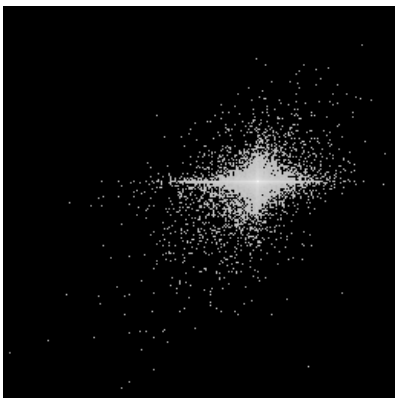

Figure 6.8 Correlation plots of noise on a selected pair of component images (component 7 vs. 12) of the 24-component LP-ICA model – estimated noise on one image was plotted against the other on a pixel-to-pixel basis

6.3.3 Sodium Gradient Analysis

Na^+ and K^+ are common alkali metal ion adducts observed in the brain tissue spectra. Therefore, a single lipid molecule may give rise to multiple peaks separated by known mass differences – e.g. sodiated and potassiated ions, respectively, are placed 22 and 38 m/z units higher than the corresponding protonated ions. With this specific brain

tissue sample used, the Na^+ adduct ion appears to be dominant over the protonated or potassiated forms of same molecule. The distribution of sodiated ions across the sample was therefore assessed.

This section examines whether there is any drift in sodium concentration across the tissue sample. This might arise from the step of washing salts from the tissue section during sample preparation. If so, it can cause problems regarding variations in the model built e.g. an extra component related to sodiated ions may be needed to describe a tissue type. On the other hand, if the sodium variation is only observed from tissue to tissue but is uniform within a same tissue type, there should be no gross change on the number of components due to sodiated ions. The ratio of sodiated to protonated peaks, to be called 'sodium gradient', was calculated throughout the image to look for this as a qualitative check for later model building. In order to look for a sodium gradient in the brain tissue section, the pre-processed spectra with 67 detected peaks were recorded at all the spatial locations. This rat brain sample contained high levels of sodiated phospholipids in the mass range m/z 690-890. Sodium gradient analysis was performed on the three molecules that appeared to produce major sodiated phosphatidylcholines (PC) in this range. This follows an earlier study of complex lipids in rat brain myelin using liquid secondary ion mass spectrometry (Fenselau *et al.*, 1989). The findings also accorded with the rat stroke model MSI data set that the signal strength of sodiated PCs were superior to protonated PCs of the same molecular types. The identification of the pronated form of these molecules is presented below. They were used here as a normalising peak for their corresponding sodiated forms (given that these are the top 3 most common molecular species across the mass spectra of this data set, also with strongest signal intensities).

- m/z 734.5 was identified as $[PC(16:0/16:0)+H]^+$ (Henderson *et al.*, 2018; Jackson *et al.*, 2005)
- m/z 760.6 was identified as $[PC(16:0/18:1) +H]^+$ (Henderson *et al.*, 2018; Ma and Kim, 1995)
- m/z 788.6 was identified as $[PC(18:0/18:1) +H]^+$ (Sugiura and Setou, 2009)

Three images of the sodium gradient were created by computing the ratio of $[M+Na]^+$ / $[M+H]^+$. Where $[M+H]^+$ peaks were observed at m/z 734.5, 760.6 and 788.6, and the $[M+Na]^+$ peaks were 22 mass units higher, at: 756.6, 782.5, and 810.6, respectively. The images were smoothed by applying a median filter once (to stabilise the image with high fluctuation on local pixels, in this case, due to small intensity values), followed by tangential smoothing (Thacker *et al.*, 2016) twice. The images for the sodium gradient calculated from each representative molecule are illustrated in the left of Figure 6.9 (a), (b) and (c). Where the scan lines across the tissue area in the images indicate selected pixels (arranged from left to right) that formed the corresponding intensity ratio plots on the right of Figure 6.9 (a), (b) and (c) – N.B. the same set of pixel locations was selected for all peak ratios.

Table 6.6 below shows the ion types for various PCs in brain tissues (from Sugiura and Setou (2009)). It shows some common masses for different molecular species, observed when cationisation changes. The m/z values highlighted with the same colour are different ion forms that happened to have the same m/z. These indicate that the sodiated and protonated peaks selected do not represent a single lipid species. However, the selected peaks are of the dominant species. Therefore, the characteristics for sodium gradient calculated from them should still be preserved.

Table 6.6 Comparison table for different ion forms of given molecular species of phosphatidylcholine in brain tissues (Reproduced from: Sugiura and Setou (2009))

Molecular species	PC	$[M+H]^+$	$[M+Na]^+$	$[M+K]^+$
PC(diacyl 16:0-18:1)	C34:1	760	782	798
PC(diacyl 16:0-16:0)	C32:0	734	756	772
PC(diacyl 18:0-18:1)	C36:1	788	810	826
PC(diacyl 16:0-20:4)	C36:4	782	804	820
PC(diacyl 16:0-18:0)	C34:0	762	784	800
PC(diacyl 16:0-22:6)	C38:6	806	828	844
PC(diacyl 18:0-20:4)	C38:4	810	832	848
PC(diacyl 18:1-20:4)	C38:5	808	830	846
PC(diacyl 18:0-22:6)	C40:6	834	856	872
PC(diacyl 18:1-18:1)	C36:2	786	808	824
PC(diacyl 16:0-16:1)	C32:1	732	754	770
PC(diacyl 18:1-22:6)	C40:7	832	854	870
PC(diacyl 16:0-20:3)	C36:3	784	806	822
PC(diacyl 18:0-18:2)	C36:2	786	808	824
PC(diacyl 18:1-18:2)	C36:3	784	806	822

(a) m/z 756.5 vs. 734.5

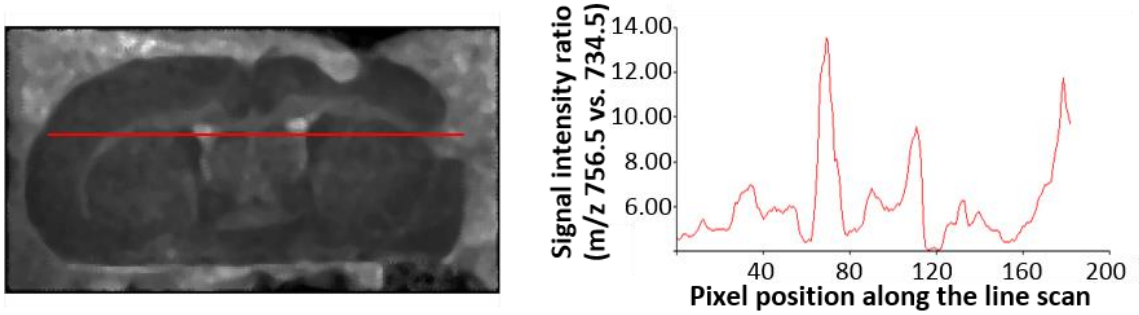

(b) m/z 782.6 vs. 760.6

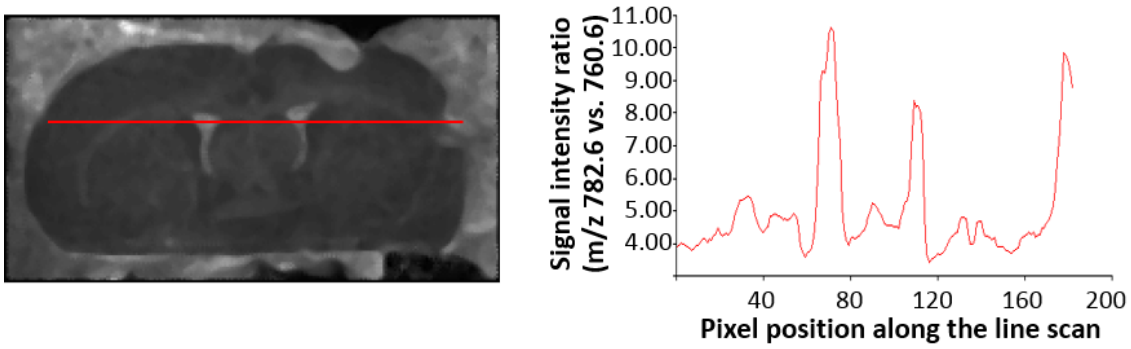

(c) m/z 810.6 vs. 788.6

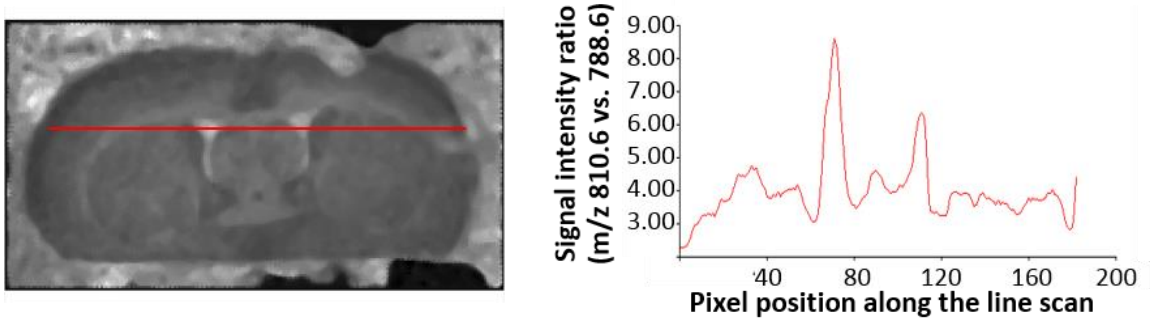

Figure 6.9 Sodium gradient images and the corresponding plots showing the signal intensity ratio of $[M+Na]^+$ vs. $[M+H]^+$ m/z peaks: (a) m/z 756.5 vs. 734.5, (b) m/z 782.6 vs. 760.6 and (c) m/z 810.6 vs. 788.6 at varied pixel positions – the position of the line scan is shown on each image in red

The sodium concentration is region-specific as clearly observed by the three different molecules. Higher sodium concentration regions include the CSF and the stroke scar. The corpus callosum has also moderately high concentration relative to other regions. These probably associate with parts of the brain that have high fluid content, where sodium is more soluble. Conditions such as edema might occur post-stroke where the tissue was damaged, leading to an excess of liquid in the affected site.

Luptakova and co-workers (2018) suggested that the sodium adduct ions measured within areas of edema in a rat brain were significant increased relative to nearby areas, clearly seen in the intensity plots associated to images in Figure 6.9 (a) and (b). The sodiated m/z 810 was observed to appear strongly in the corpus callosum region (Ozawa *et al*., 2015), which agrees with the sodium gradient plot for m/z 810.6 vs. 788.6 shown in Figure 6.9 (c).

Fortunately, the sodium gradient is relatively consistent locally within a same tissue region, although varies in certain anatomical regions as mentioned above, it should not generate extra components due to local sodium concentration.

6.3.4 Isotope Analysis

An independent test to confirm that the LP-ICA method worked was established, and made sure that the biological and physical properties correspond appropriately. In this section, the raw spectra were tested for behaviour of specific isotopes in order to understand the isotopic peaks behaviour on the extracted LP-ICA component spectra, as they should behave similarly, if the model is valid.

The isotope ratio images were generated in a similar manner to the sodium gradient images, assessing the sodiated peak for each of the three major molecules used in the analysis in Section 6.3.3. Two isotope ratio images per molecule were plotted, which are $[M+1+Na]^+/ [M+Na]^+$ in Figure 6.10 and $[M+2+Na]^+/ [M+Na]^+$ in Figure 6.11. Where $[M+Na]^+$ is the most abundant isotope (of the selected isotopic molecular species), and $[M+1+Na]^+$ and $[M+2+Na]^+$ are the next abundance isotopes, respectively.

All the $[M+1+Na]^+/ [M+Na]^+$ plots (Figure 6.10) fluctuate within a small range about the accepted ratios of 0.46, 0.49 and 0.51, for the three molecules in order of mass. Whereas the $[M+2+Na]^+/ [M+Na]^+$ plots (Figure 6.11) vary significantly, showing also region-dependent behaviour. The ratios generally exceed the accepted values of 0.12, 0.13 and 0.14, respectively, for $[M+2+Na]^+/ [M+Na]^+$ of the three molecules. This suggested regional dependency with the variation of isotopomer signal specific

to location. Theoretically, there should be no variation at all. Although for low ion counts, there might be larger influence by multiple variations, any significant spikes that deviate from the expected ratios seen in the plots in Figures 6.10 and 6.11 are likely due to isobaric interference in those regions which will be discussed later in Section 6.3.5. Note that the reference values to the accepted isotope ratios were obtained through http://www.lipidmaps.org/.

(a) m/z 757.5 vs. 756.5

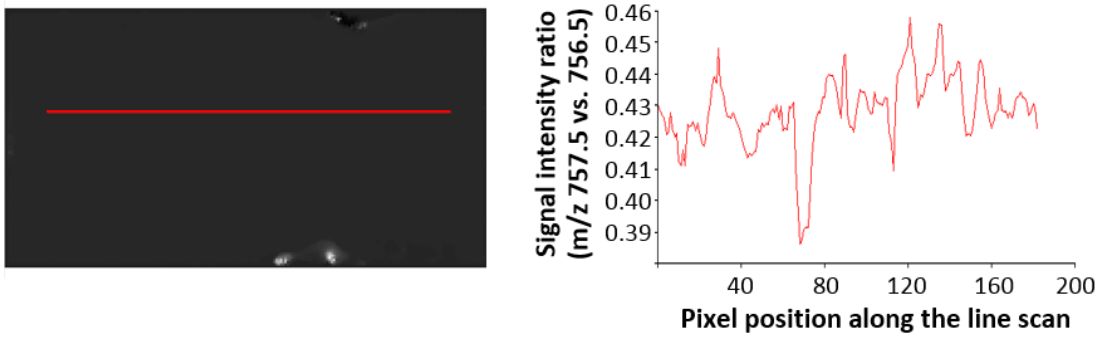

(b) m/z 783.6 vs. 782.6

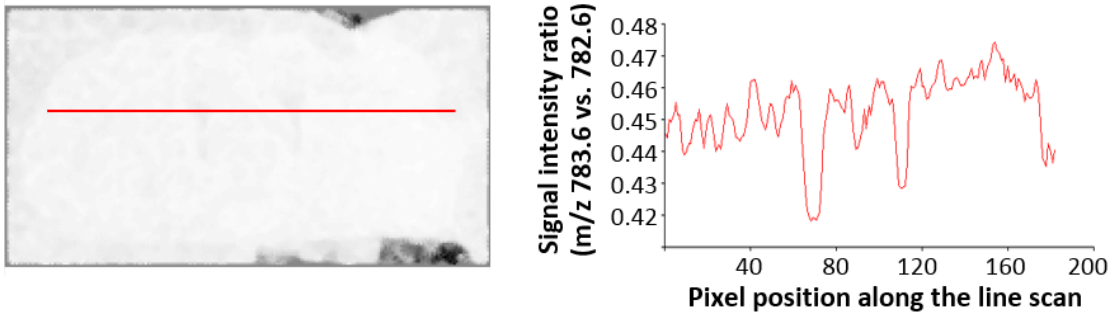

(c) m/z 811.6 vs. 810.6

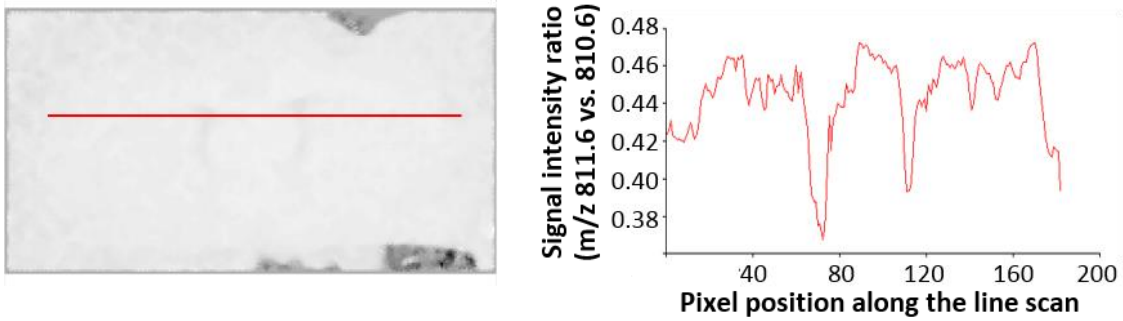

Figure 6.10 Isotope ratio images of $[M+1+Na]^+$ vs. $[M+Na]^+$ m/z peaks: (a) m/z 757.5 vs. 756.5, (b) m/z 783.6 vs. 782.6 and (c) m/z 811.6 vs. 810.6, and the corresponding plots showing their signal intensity ratio at varied pixel positions – the position of the line scan is shown on each image in red

(a) m/z 758.5 vs. 756.5

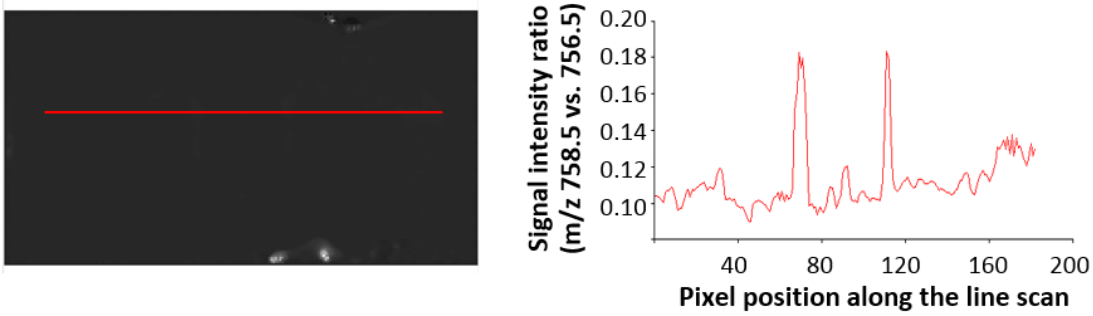

(b) m/z 784.6 vs. 782.6

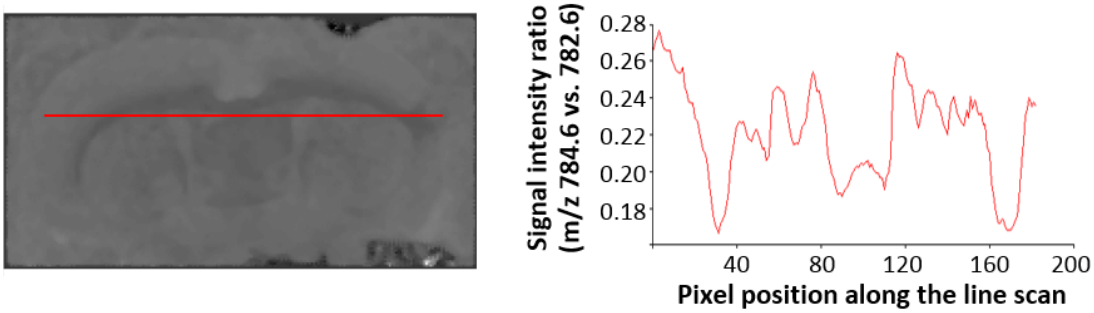

(c) m/z 812.6 vs. 810.6

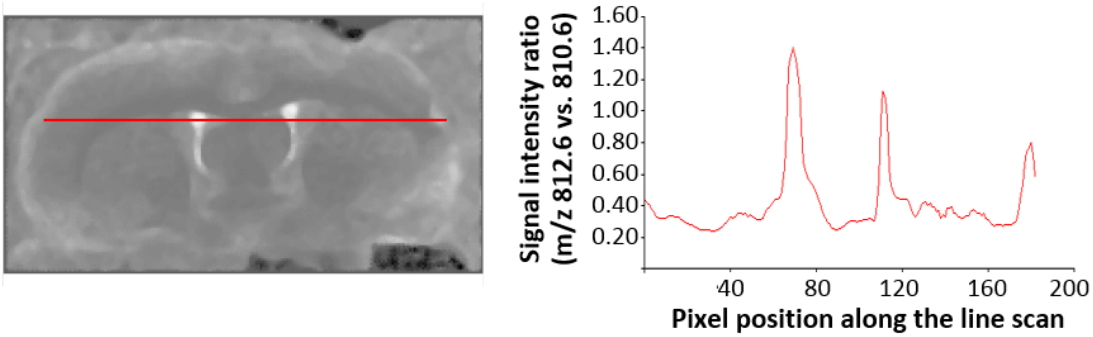

Figure 6.11 Isotope ratio images of $[M+2+Na]^+$ vs. $[M+Na]^+$ m/z peaks: (a) m/z 758.5 vs. 756.5, (b) m/z 784.6 vs. 782.6 and (c) m/z 812.6 vs. 810.6, and the corresponding plots showing their signal intensity ratio at varied pixel positions – the position of the line scan is shown on each image in red

6.3.5 Criteria for Differentiating Signal and Noise Components using Error Distribution on Isotope Peak Measurements

Isobars are different molecules that have the same nominal molecular mass. In a MALDI mass spectrum, peaks with a small mass difference might be seen as a single peak given the limit of mass resolution – i.e. this could be distinguished only if MS/MS

was performed. If the most abundant isotope peaks of the isobaric molecules coincide, then the other isotope peaks should still lie at the same mass positions with more or less the same intensity ratios within errors. As shown in the previous section, the $[M+2+Na]^+$ isotope peaks, however, appear to be contaminated by some other main isotope molecules, for example, at m/z 784.6 and 812.6, as their ratio to the main isotope peaks deviated from the expected values stated in Table 6.2. Their intensity ratios are much greater than their expected abundances and cannot be used directly in the following analysis. Hence, only the ratio between the two most abundant isotope peaks was of interest in this analysis. Furthermore, the three different ion forms (sodiated > protonated > potassiated) also cause complicated overlapping between peaks of different molecules, which affect values of isotope ratios at the measuring m/z.

The following criteria were devised for differentiating between ICA components of signal and noise based on the error pattern on the isotope ratio from 6 pairs of mass peaks defined by $[M+1+Na]^+$ / $[M+Na]^+$ and $[M+1+H]^+$ / $[M+H]^+$ of 3 different molecules quoted above. The simplest way for two molecules to have overlap can be modelled as follows.

There are three common cases that might cause the measured value to be different from the expected value of isotope ratio, see diagrams expressed in Figure 6.12. Possible patterns of isobaric interference that give rise to measuring M_1+1 / M_1 ratio are described in the list below.

1.) ***Upper diagram*****:** M_1 and M_2 are isobars and the abundance of their isotopes should be very close to identical, providing they are PC of similar molecular masses. The ratio of M_1+1 to M_1 is conserved at the expected proportion.
2.) ***Middle diagram*****:** M_2 appears at the M_1+1 position. Only M_1+1 gets increased in intensity. Therefore, the ratio of M_1+1 to M_1 is above the expected proportion.
3.) ***Lower diagram*****:** M_2 appears at one mass unit below the M_1+1 position, adding a small fraction to both M_1 and M_1+1. The ratio of M_1+1 to M_1 is slightly reduced but this should generally be insignificant, given the measurement precision.

Therefore, in the majority of cases the isotope ratio between a large peak and its neighbour should be preserved. When it does differ it can only be larger than expected. This can be used as the basis for a test of ICA components. Such a test also requires an understanding of measurement error.

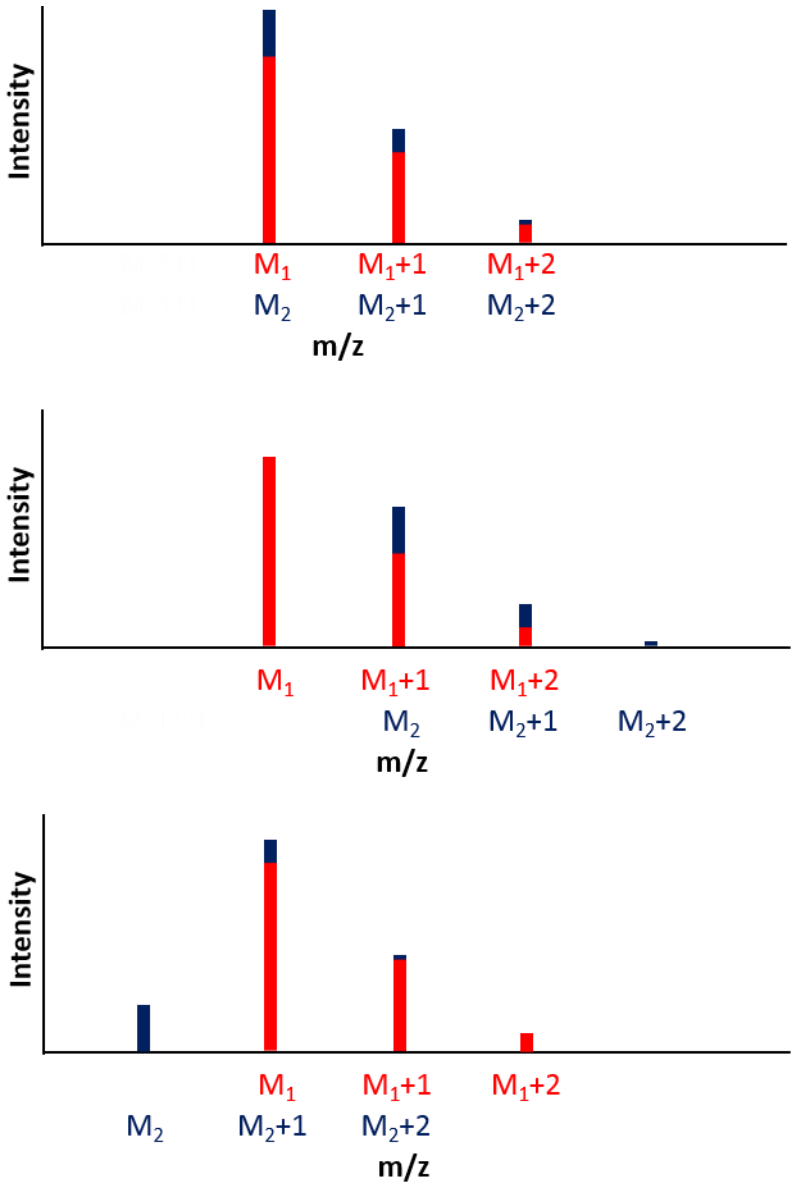

Figure 6.12 Possible arrangements of isotope pattern of molecules that coincide at the same m/z values

The Error Estimates on Peak Ratios of ICA Components

The errors on peak bins' intensity of the ICA components were estimated by computing error covariances through each pair of the probability mass functions (PMF) that describe the component sub-spectra. The method is described in Tar and Thacker (2018), where they corroborated the theory with simulated data (http://www.tina-vision.net/docs/memos/2018-006.pdf). Then, the errors in isotope ratios were calculated on this basis using error propagation.

The stability of each PMF bin, $P(m|k)$, can be estimated using the minimum variance bound applied to the LP-ICA Likelihood function (propagated to give the error estimates on peak ratios). This gives an inverse co-variance between bin order m in component $k = k_A$ and $k = k_B$ as:

$$C^{-1}_{P(m|k_A),P(m|k_B)} \approx \sum_i \frac{Q_{k_A i} Q_{k_B i}}{H_{mi}} \tag{6.1}$$

Where Q is the quantity of the corresponding component contained in spectrum i at a specific pixel, and H is a histogram bin value (equivalent to the ion counts).

The Plots of Predicted vs. Measured Error Distribution of Isotope Ratios

The plots of predicted against measured error distribution of isotope ratios are provided in Figure 6.13 (left). The x-axis in the plot is the measured error (difference between the isotope ratio computed from the probabilistic model component and the expected value as defined in the LIPID MAPS database). The y-axis is the error estimate, defined by the model error covariance calculation, of the corresponding isotope ratio. Adjusted ratio plots (Figure 6.13 (right)) are generated where a fraction equal to some percentage of the main peaks M in an isotope pattern were added to M and M+1 peaks to calculate the new isotope ratio, may compensate for a missing fraction either from instrumentation off-set or from the background subtraction failure, which was found to correct for some negative skew observed in the original ratio plots. A small contribution may also occur when a peak (probably different molecules with different adduct species) is found at a unit mass below the dominant

isotope peak, and hence fractions contribute for M and M+1 are different. In order to define a suitable value of the fraction to be added back into peaks, the mean of measured deviations from the expected ratios (the x-axis of the plot) should be brought closer to zero, hence, the suitable correction – the percentage for these correcting fractions is indicated in each plot (Figure 6.13 (right)).

A line can be drawn to separate noise and signal. For proportional errors, confidence limit takes the form of V-shaped symmetrical lines around zero, where data points that sit within the two lines are consistent with signal, and statistical significance can then be quoted in terms of the p-value. However, a general conclusions can be drawn for this type of plot by looking at the common cases of overlapping peaks illustrated earlier in the diagrams in Figure 6.12. It is possible for a data point to be on the positive side of the x-axis of plots in Figure 6.13. Data points that are too far away from the x-axis in the negative direction should be suspected as modelling errors. Therefore, this method can suggest the suitable number of components to build a model, figure out contamination (background/noise) components, and/or inappropriate parameter estimation (fit failure). Where the plot shows the expected trend, it proved that the LP-ICA model built, according to the procedure and parameters described in Section 6.2.4 e.g. EM, were adequate.

For the plots in Figure 6.13, a value on the vertical axis is proportional to the minimum variance bound estimate of peak ratio error propagated from Equation (6.1). The diagonal dotted lines (on all plots on the left of Figure 6.13, the original ratio) have common slope as a visual aid to highlight the changes in the negative skew of the distributions; these do not constitute error bounds or confidence intervals and are for illustration only.

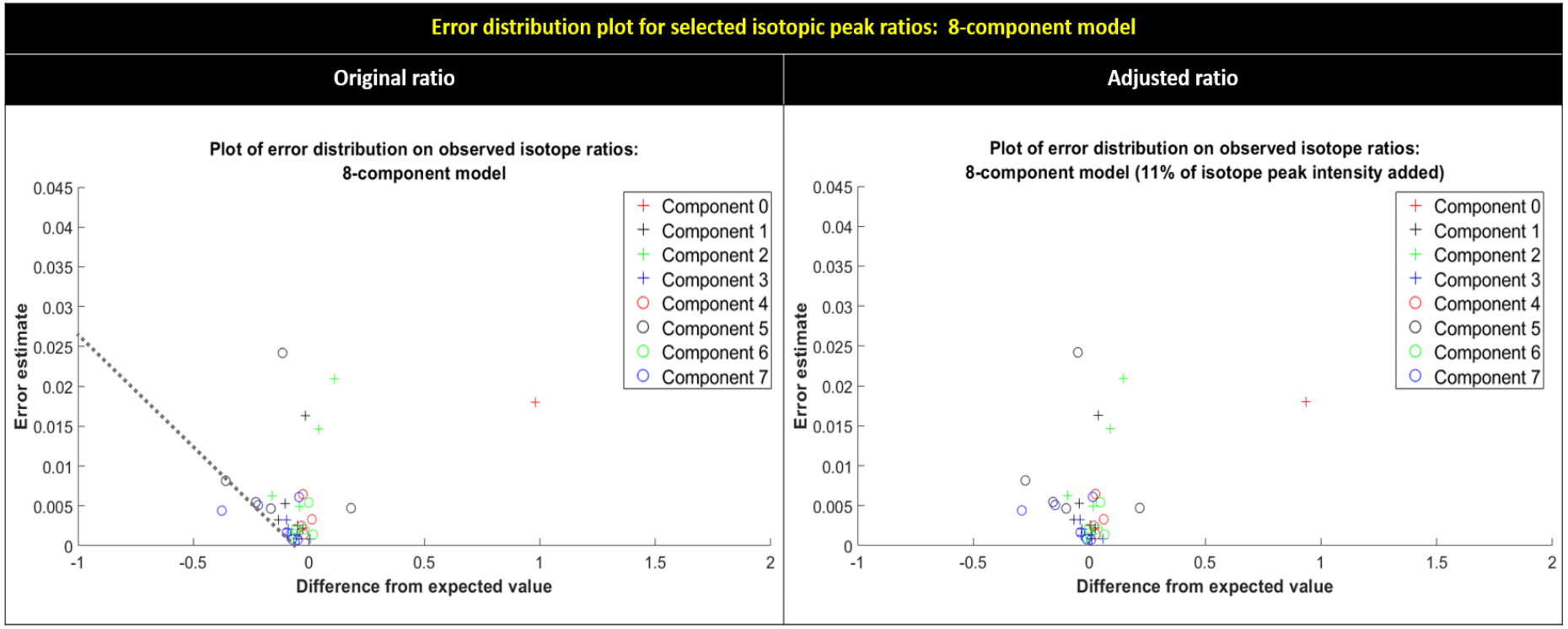

Figure 6.13 Predicted vs. measured deviations from expected ratio for selected isotopic peaks at different model orders, plotted using original ratio (left) and adjusted ratio with added fraction (right). Different symbols indicate the LP-ICA components from which peaks were taken. (Part 1 of 5)

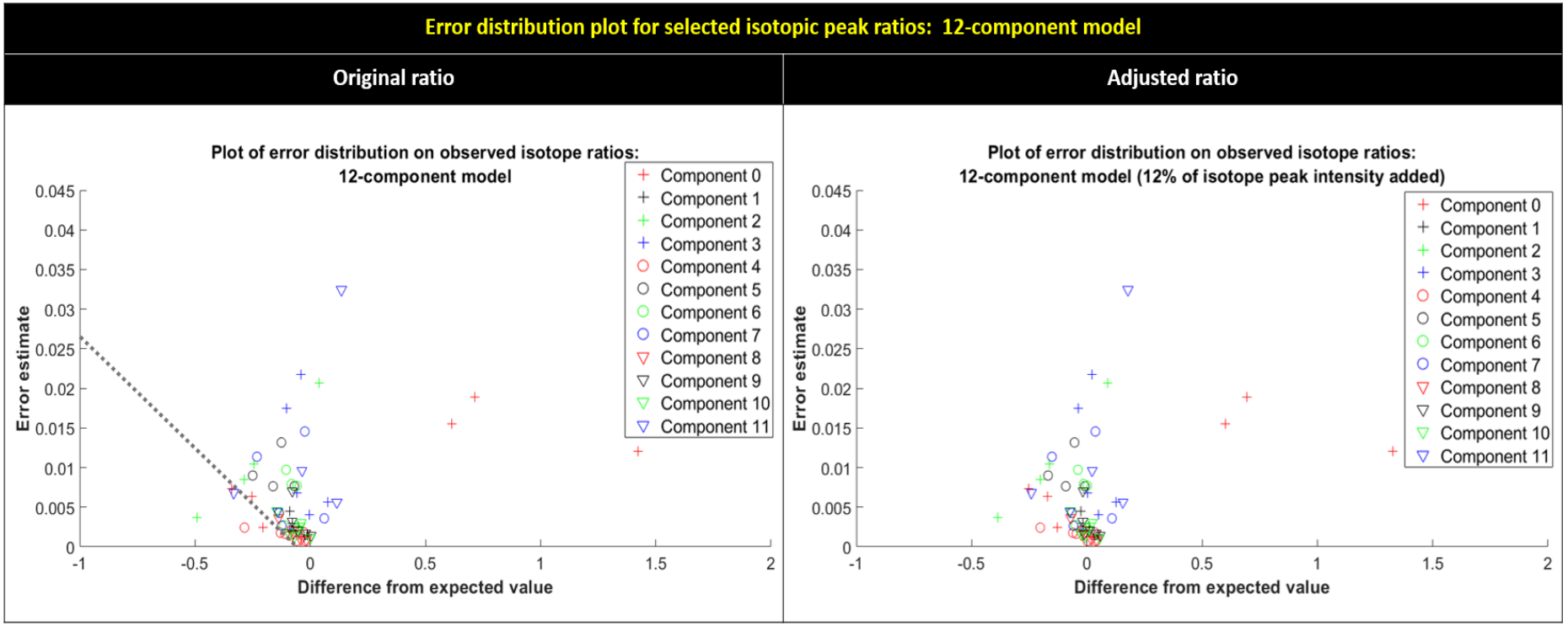

Figure 6.13 Predicted vs. measured deviations from expected ratio for selected isotopic peaks at different model orders, plotted using original ratio (left) and adjusted ratio with added fraction (right). Different symbols indicate the LP-ICA components from which peaks were taken. (Part 2 of 5)

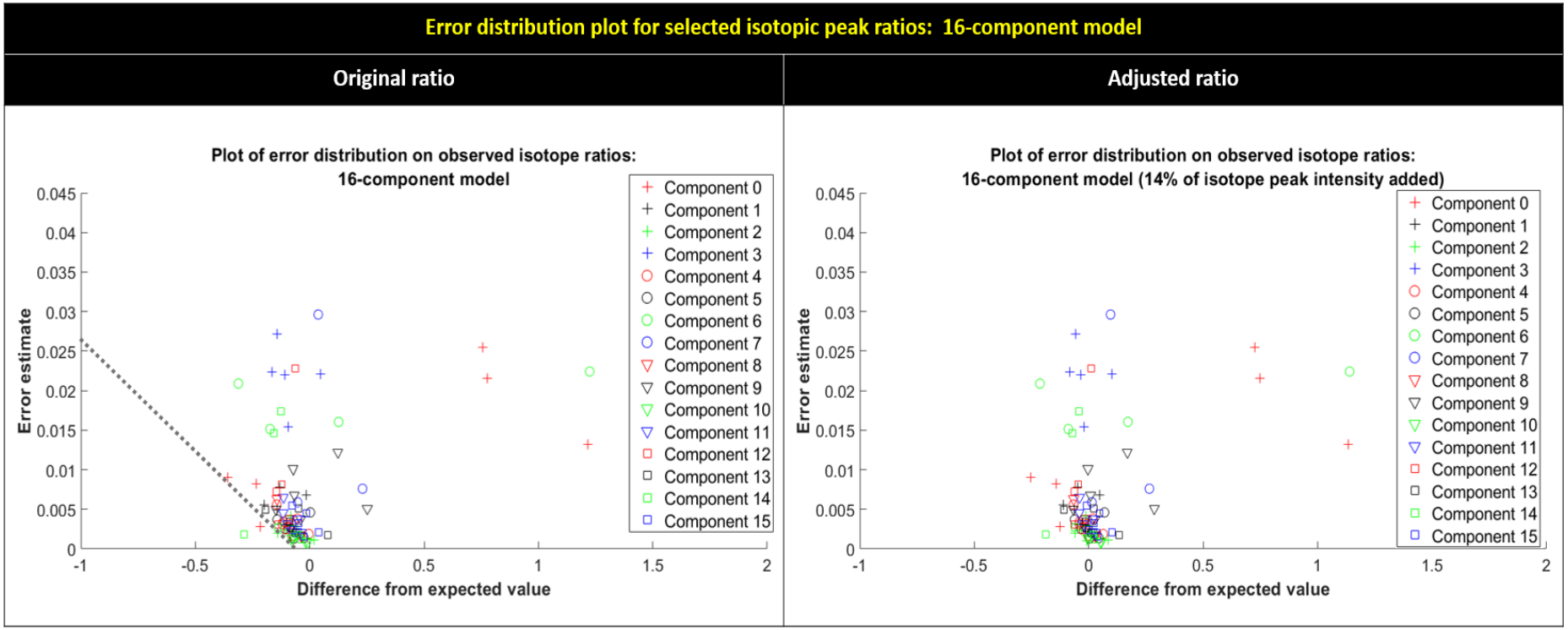

Figure 6.13 Predicted vs. measured deviations from expected ratio for selected isotopic peaks at different model orders, plotted using original ratio (left) and adjusted ratio with added fraction (right). Different symbols indicate the LP-ICA components from which peaks were taken. (Part 3 of 5)

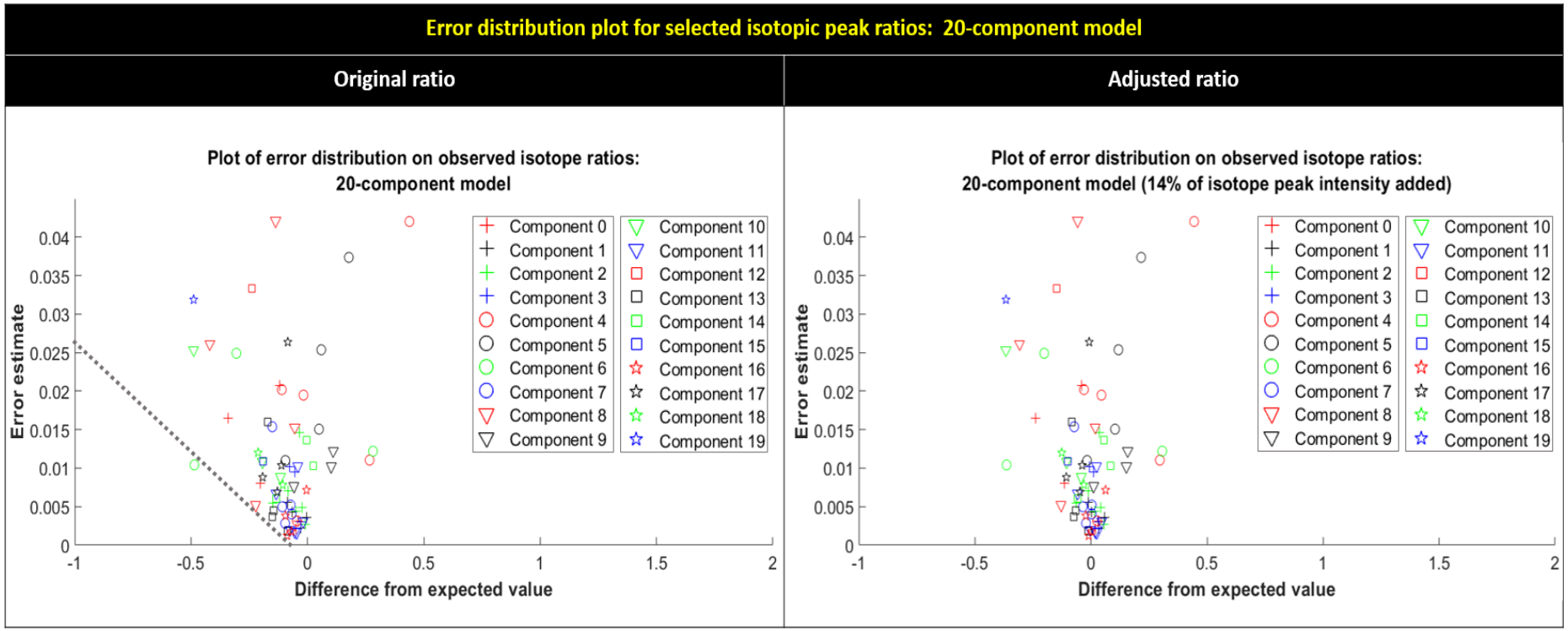

Figure 6.13 Predicted vs. measured deviations from expected ratio for selected isotopic peaks at different model orders, plotted using original ratio (left) and adjusted ratio with added fraction (right). Different symbols indicate the LP-ICA components from which peaks were taken. (Part 4 of 5)

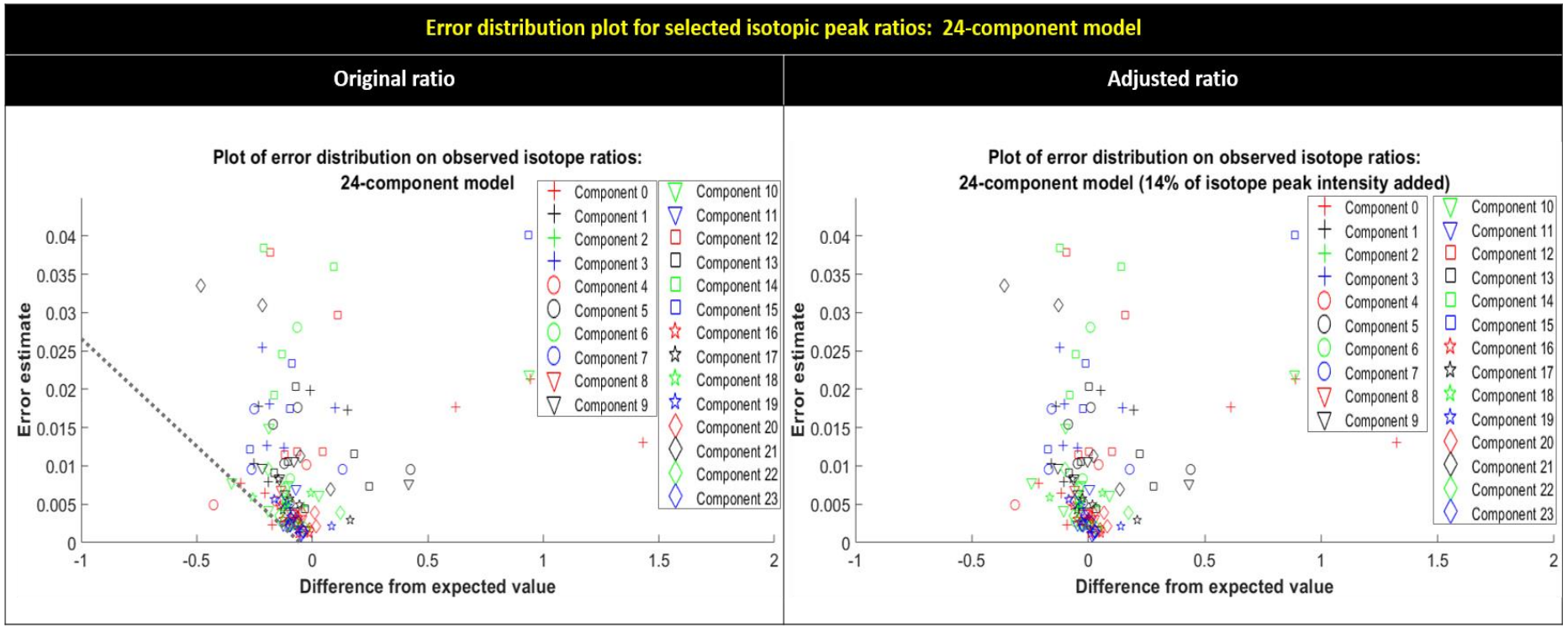

Figure 6.13 Predicted vs. measured deviations from expected ratio for selected isotopic peaks at different model orders, plotted using original ratio (left) and adjusted ratio with added fraction (right). Different symbols indicate the LP-ICA components from which peaks were taken. (Part 5 of 5)

Note that the percentage shown in each adjusted plot above came from the optimally minimised accumulative distance of the x-axis values away from zero for all data points in a reasonable signal range. These error plots could have been improved by appointing appropriate weighting according to the estimated errors on data points to determine the fraction added to peaks more precisely. – i.e. Currently all points are equally weighted to get the optimal correction of peak intensity but more accurate (smaller error) data points could be more strongly weighted in this calculation.

6.3.6 Lipid Identification in Brain Tissue

Rat brains are often used in clinical research as models of pathology and treatment procedures in mammalian brains. Therefore, there are number of available resources for lipid identification from previous MALDI MS/MS studies. The following Table 6.7 gives a list of major lipid peaks found in the rat brain imaging data set that have previously been identified in rat brain tissue, so that important differentiating molecules e.g. the 10 most intense peaks for each component based on the 20-component model (see Table 6.5), can be observed. The m/z values of the analysed data were confirmed to match with the identified lipids within the mass tolerance of ± 0.3 Da based on the LIPID MAPS database (http://www.lipidmaps.org/).

As expected from the results of the ICA models, some of the peaks comprise multiple molecular types. Without access to higher mass resolution, the only way to tell apart those molecular species is to perform MS/MS and identify species based on their fragmentation patterns. The proportion of each species can also be accessed if the fragmentation pattern is known. However, the isotope ratios observed in ICA component spectra can also be used to show the presence of unresolved isobars as discussed in Sections 6.3.4 and 6.3.5.

Table 6.7 List of previously identified phosphatidylcholine species from literature survey (Part 1 of 2)

m/z value	Lipid identification	Reference
697.98		
699.12		
699.97		
719.39		
734.50	$[PC(16:0/16:0)+H]^+$	1,2,5,9
735.45		
745.50		
746.46	$[PC(15:0a/18:1)+H]^+$ $[PC(16:0a/17:1)+H]^+$ $[PC(18:1e/16:0)+H]^+$ $[PC(16:0e/18:1)+H]^+$	5 5 5 5
747.41		
750.49		
753.65		
754.47	$[PC(14:0/18:1)+Na]^+$	9
756.53	$[PC(16:0/16:0)+Na]^+$ $[PC(16:1a/18:2)+H]^+$ $[PC(16:0a/18:3)+H]^+$	1,2,9 5 5
757.64		
758.60	$[PC(16:0a/18:2)+H]^+$	5
760.67	$[PC(16:0/18:1)+H]^+$	1,3,5,9
761.48		
762.51	$[PC(16:0a/18:0)+H]^+$	5,9
768.60		
769.57		
772.46	$[PC(16:0/16:0)+K]^+$	*
773.51		
774.48		
778.66		
782.56	$[PC(16:0/18:1)+Na]^+$ $[PC(16:0a/20:4)+H]^+$	1,3,9 5,9
783.53		
784.66	$[PC(18:1a/18:2)+H]^+$ $[PC(16:0a/20:3)+H]^+$ $[PC(16:0/18:0)+Na]^+$	5 5 9
785.56		
786.46	$[PC(18:1a/18:1)+H]^+$	5
788.49	$[PC(18:0/18:1)+H]^+$	4,5,9
789.62		
790.53	$[PC(18:0p/18:0)+H]^+$ $[PC(20:0a/16:0)+H]^+$ $[PC(14:0a/22:0)+H]^+$	5 5 5
791.58		
792.57		
794.61		
796.64		
798.69	$[PC(16:0/18:1)+K]^+$	6
804.61	$[PC(16:1a/22:6)+H]^+$ $[PC(16:0a/20:4)+Na]^+$	5 9
805.60		

Table 6.7 List of previously identified phosphatidylcholine species from literature survey (Part 2 of 2)

m/z value	Lipid identification	Reference
806.59	$[PC(16:0a/22:6)+H]^+$ $[PC(16:0a/20:3)+Na]^+$ $[PC(18:1a/18:2)+Na]^+$	5,9 7,* *
808.65	$[PC(16:0/22:5)+H]^+$	9
809.49		
810.63	$[PC(18:0/18:1)+Na]^+$ $[PC(18:0a/20:4)+H]^+$ $[PC(16:0a/22:4)+H]^+$	4,9 5,9 5
811.62		
812.46	$[PC(C18:1/C20:2)+H]^+$ $[PC(C18:2/C20:1)+H]^+$	* *
813.61		
814.60	$[PC(18:0a/20:2)+H]^+$	5
820.66		
822.73		
823.66		
824.66		
828.60	$[PC(16:0/22:6)+Na]^+$	9
830.67	$[PC(16:0/22:5)+Na]^+$	9
832.69	$[PC(18:1a/22:6)+H]^+$ $[PC(18:0a/20:4)+Na]^+$ $[PC(16:0a/22:4)+Na]^+$	5 9 *
833.69		
834.62	$[PC(18:0a/22:6)+H]^+$ $[PC(C18:1/C20:2)+Na]^+$ $[PC(C18:2/C20:1)+Na]^+$	5,9 * *
835.63		
836.64	$[PC(18:0a/20:2)+Na]^+$ $[PC(18:0/22:5)+H]^+$	* 9
837.65		
838.57		
848.78	$[PC(18:0a/20:4)+K]^+$ $[PC(16:0a/22:4)+K]^+$	6
849.71		
850.73	$[PC(C18:1/C20:2)+K]^+$ $[PC(C18:2/C20:1)+K]^+$	8 8
851.75		
852.68		
856.60	$[PC(18:0a/22:6)+Na]^+$	9
864.70		

N.B. References to the above table of lipid identification are 1.) Henderson *et al.*, 2018; 2.) Jackson *et al.*, 2005; 3.) Ma and Kim, 1995; 4.) Sugiura and Setou, 2009; 5.) Delvolve *et al*., 2011; 6.) Delvolve and Woods, 2011; 7.) Guo *et al.*, 2017; 8.) Kruft, SCIEX online document; 9.) Löhmann *et al*., 2010. Where * is noted, masses of other ion forms were related based on the identified lipids. The grey shadow indicates the identified lipids from literature at m/z that were not picked up as major peaks as a result of the 20-component model (the 10 most intense peaks for each component).

Lipids of the class sphingomyelin (SM) are important in signalling mechanisms (Delvolve *et al*., 2011). The previous work of this stroke rat brain sample by Henderson *et al*. (2018) reported a specific peak at m/z 725 which was identified through tandem MALDI-MS analysis as SM (d18:1/16:0), to be a marker for the stroke-damaged tissue. However, SM peaks in MALDI mass spectra are usually relatively low in intensity in comparison with PCs. Therefore, it is difficult to find a specific SM peak to analyse, especially when the background level is comparable with small peaks. This situation is quite common in MALDI.

According to the above discussion, approaches for detecting this type of underlying feature is restricted. In other words, small fluctuations might well be missed during the procedure of thresholding and found to be statistically insignificant. The alternative LP-ICA approach introduced here was designed to automatically select a set of peaks that together correlate with the sample biology. This allows systematic quantification even though one peak alone does not stand out as differentiating between tissue regions. This would give molecular compositions for lipids at each location which can then suggest the underlying cell/tissue types.

Davanlou and Smith (2004) performed a microscopic observation of Nissl-stained rat brain sections to differentiate main types of cells in the cerebral cortex. They determined three major cell types; neurons, glial cells and endothelial cells accounting for 47%, 24% and 17% of the overall tissue volume. Endothelial cells had the most distinct optical appearance with heavily stained elongate-shaped nuclei. It was more ambiguous telling apart neurons and glial cells as sizes and staining characteristics vary across their sub-types, ranging between few to tens of micrometres. The study resulted in estimations of cell density by volume. The cell densities quoted in the literature were adopted to proportionally calculate expected number of cells of each type within a pixel's sampling area (area irradiated by the laser in a single pulse) of the rat brain MS image data as expressed in Table 6.8. For this MS image data, the field of view (FOV) was defined by the sampling volume at a spatial location to be 94.2×10^3 μm^3 – i.e. a circular laser beam of 50 µm diameter was fired onto sample tissue section of 12 µm thick.

Table 6.8 Number of cells of main types within the sampling field of view

Cell type	Number of cells within a FOV(*)
Neuron (cell body)	15.11
Glia	11.02
Endothelial	5.75

* Values calculated proportionally from Davanlou and Smith (2004) where rat brain's tissues in the cerebral cortex were examined.

However, the dendrites and axons (myelinated) that connect one neuron to another can branch further away from the cell body. Therefore, whole neurons were not necessarily detected within a single pixel.

6.3.7 Lipid Mapping on Brain Regions

Bregma is a location where coronal and sagittal sutures which are main fibrous joints of the skull/cranium meet at right angle. It is used as a point of origin on the rat brain for referencing to which slice of the brain is referred in the rat brain atlas according Paxinos and Watson (1986). The coronal section of rat brain in this experiment was cut near the bregma. The colour coded image in Figure 6.14 shows regional segmentation as a result of 3 ICA component images, in very good agreement with the overlaid Paxinos and Watson functional brain atlas at the slice position -0.40 mm away from the bregma. Where the atlas drawn (Wistar rats, 270 - 310 g) was stated to have an approximate precision of 0.5 mm. Note that the brain size is a function of age and weight of the rat, however, the atlas scaling should be sufficiently consistent to compare with the acquired rat brain MALDI image (Wistar rat, 350 g).

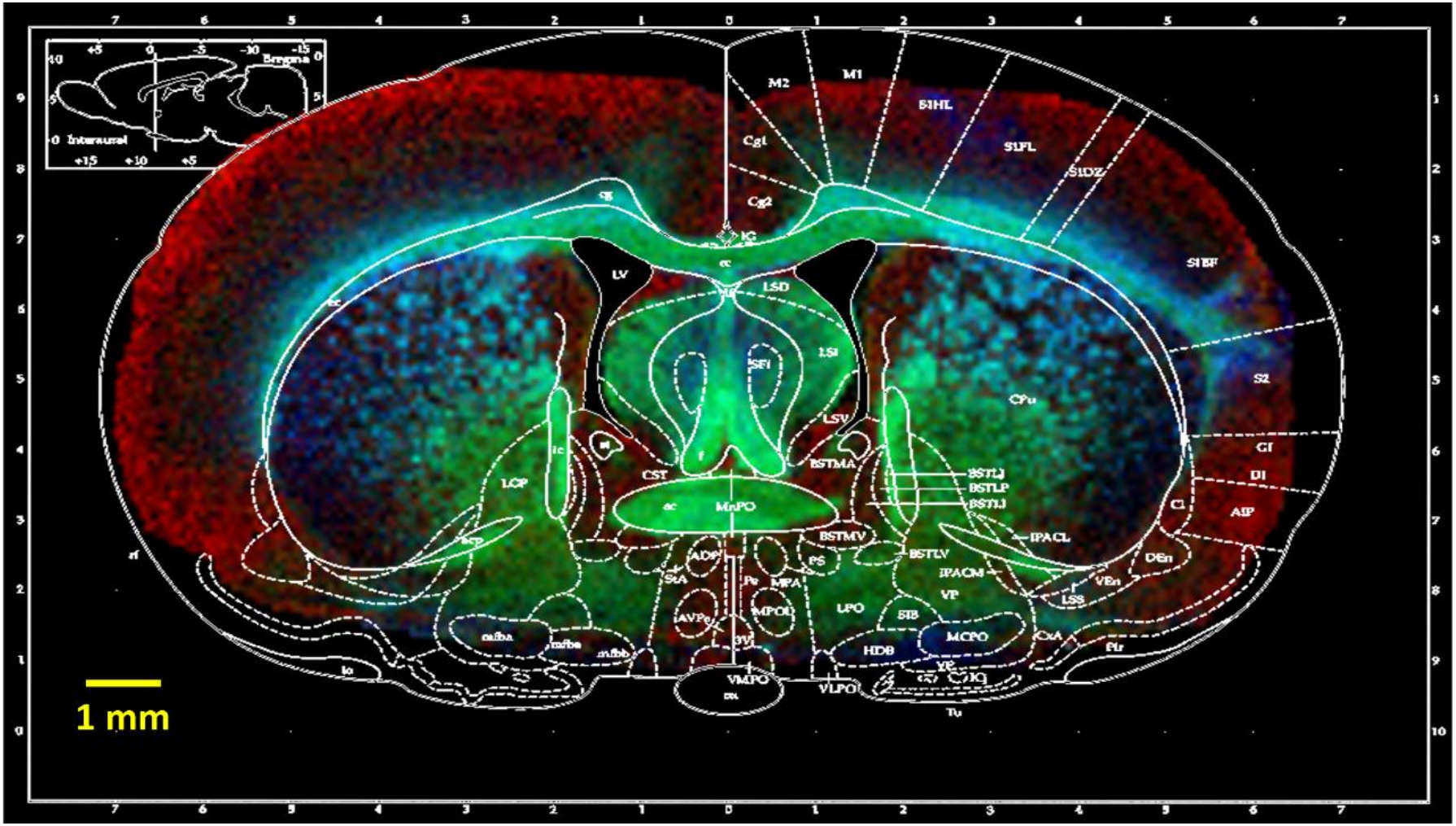

Figure 6.14 Colour coded component image (component 0 vs. 3 vs. 12 of the 20-component model) with the overlaid Paxinos and Watson rat brain atlas (approximate scaling) – see Paxinos and Watson (1986) for a full description of functional rat brain regions

A more generalised brain atlas, indicating only the main anatomical regions with different highlighted colours, is provided in Figure 6.15 (left). This specific coronal cross-section of the rat brain shows the obvious structures of (cerebral) cortex, corpus callosum, striatum, (lateral) ventricles, etc. The cortex is the outermost part of the brain section. It is separated into discrete layers seen as fringes as labelled in the generalised brain atlas in Figure 6.15 (left), due to the density (Skoglund *et al*., 1996) length, size and arrangement of the myelinated nerve fibre that vary radially in the region (Toga, 2015). The ventricles are filled with the 'cerebrospinal fluid' (CSF) which also has pathways through the cranial cavity and spinal canal. Thus, biomarkers can be derived from compositional abnormalities in CSF that report inflammation, infection or disease in the central nervous system. External capsules are located next to the corpus callosum, separating it from the cortex. Internal capsules are found aligned beside the ventricles. The external and internal capsules are considered the efferent projection fibres which means fibres projected from cerebral cortex into other parts of the brain. Therefore, they are expected to have some biochemical correlation with both cortex and their surrounding areas. In addition to the normal structure, the stroke region is situated at the cortex of the right hemisphere of the brain, and is expected to contain differentiable composition compared to the normal tissue nearby.

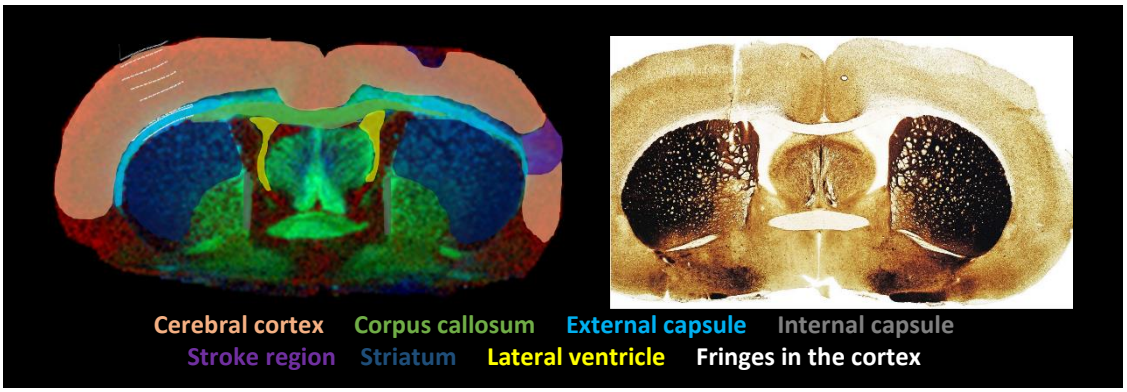

Figure 6.15 Colour coded component image with the generalised rat brain regions labelled (left), compared with microscopic anatomy (right; reproduced from: Paxinos and Watsons (2006))

Detailed anatomical structures in the composite component images are consistent with microscopic images in Figure 6.15 (right), especially for the fringes on the cortex and the granularity of fibre tissues within the striatum areas. They are seen more clearly in some component images. Examples are given in images corresponding to components 4 and 12 of Figure 6.6 which is for the 20-component model. Note that the missing area on the top right side of the cortex is due to a cutting artifact. (N.B. it clearly behaves differently to the infarct region in this analysis).

Looking at grey-scale images created from individual components, the highlighted spatial regions that refer to some specific anatomical structures only appear in certain component(s). As in the 20-component model, a close component-by-component investigation allows tissue segmentation along with information of lipid constituents. The component 3 and 12 display the segmentation of the white matter, whereas component 0, 4, 7 and 11 correspond to the grey matter.

6.3.8 Model Validation

Like all non-trivial analyses, the modelling approach demonstrated requires a level of quality control to ensure results are trustworthy. Data must be pre-processed to ensure statistical assumptions are met; an appropriate model order needs to be selected; and linear degeneracies inherent in initial model builds must be addressed. Failures in any of these areas can invalidate conclusions drawn from identified tissue phenotypes. Quality has been assessed through a combination of Bland-Altman analysis, goodness-of-fit testing and the checking of physical constraints upon possible spectra. The Bland-Altman analysis shows that pre-processed MALDI spectra exhibit Poisson sampling behaviour (see the plot in Figure 5.6 in Section 5.4.2). This is an important result, as it confirms that an LP-ICA approach is appropriate. LP-ICA relies heavily upon a Poisson sampling assumption, in both its Likelihood formulation and its error theory. The errors on peak heights given by Equation (6.1), for instance, is invalid for other distributions. Alternative linear modeling methods, such as PCA and conventional ICA algorithms, make Gaussian noise assumptions (as discussed in Section 3.4.2 of Chapter 3), rendering them less appropriate for this type of MALDI

data mining. In addition to the Bland-Altman results, the goodness-of-fit used during model selection shows that the overall signal distribution successfully describes the total spectra. On average, the sum of the extracted tissues matches the observed spectrum at each pixel to the level of the Poisson sampling noise, σ_p. Whilst the overall model describes the total spectrum at each pixel, the individual model components require further validation. Inspection of isotopic ratios in Figure 6.13 shows that at model order 20 the sub-spectra associated with all components are consistent with the physical constraints expected due to the naturally occurring ^{12}C:^{13}C abundances. An ideal result should show a V-shaped distribution centred at zero, with a positive skew permitted as discussed in Section 6.3.5. Those components that fail these constraints at lower model orders give a negative skew due to poorly described spectra, such as component numbers 0, 2, 4 for the 12-component model and component numbers 0, 14 for the 16-component model. The improved behaviour with higher model order is consistent with the model selection curve in Figure 6.4, where 12- and 16-component models have not quite reached a goodness-of-fit plateau, but the 20-component model has. For this reason, the 8-component model deemed a poor fit to the data. There appears to be a net negative bias for all model orders that can be explained by inappropriate thresholding of low signal during acquisition (a low-level machine setting) and possible biases introduced through pre-processing steps. Despite this, the isotope ratio test proves to be a good quality control tool, giving more confidence that a model order of 20 is sufficient for describing the rat brain data. Note that the 24-component model is considered too complex (see the component sub-spectra and associated component images in Figure B.3, Appendix B-1) and therefore some common biological features starts to split out, and overfitting starts to be an issue.

6.3.9 Tissue Phenotyping

The spatial resolution in MALDI-MSI dictates that within each pixel there will be a number of cells and probably a mixture of cell types. The functionality of each tissue type will reflect its cellular composition. The cell types will include neurons, microglia,

astrocytes and oligodendrites and their various forms. Some of these cells, especially the neurons have processes: the axons that can extend across many pixels and even form a tissue type in their own right: white matter. As tissues are formed from a finite number of these cellular building blocks, one might anticipate that this would be represented in the components extracted. Certainly this is true of white matter.

The LP-ICA automatically extracts measurable correlations between biomolecules that are related to the different tissues, providing soft-segmentations of both wide-spread tissues (see component images and associated spectra in Figure 6.16) and localised structures (see component images and associated spectra in Figure 6.17). Of particular interest is component 8 (of the 20-component model), that highlights the infarct region. In contrast to the LP-ICA 20-component model images, single ion images for the most significant 20 peaks are shown in the Appendix B-2 (Figure B.4). The integral of these peaks across all the data constitutes over 90% of the total quantity, so they may be expected to reveal important information in regions of interest – including the infarct. However, none clearly segment the infarct region, even though these top 20 peaks make up 39% of the integral of component 8. A comparison between images and spectra from different LP-ICA model orders shows that there are some components that are sufficiently unique as to be easily identified across multiple models. In particular, component 6, 12 and 14, respectively, of the 12-, 16-, and 20-component models, are almost identical. A consistent spectrum of chemical noise is also identified in component 0, 0 and 15, respectively, of the 12-, 16-, and 20-component models. In contrast, certain features only become clear at higher model orders. For example, the infarct region (see the associated image in Figure 6.17) is most distinct when 20 components are extracted.

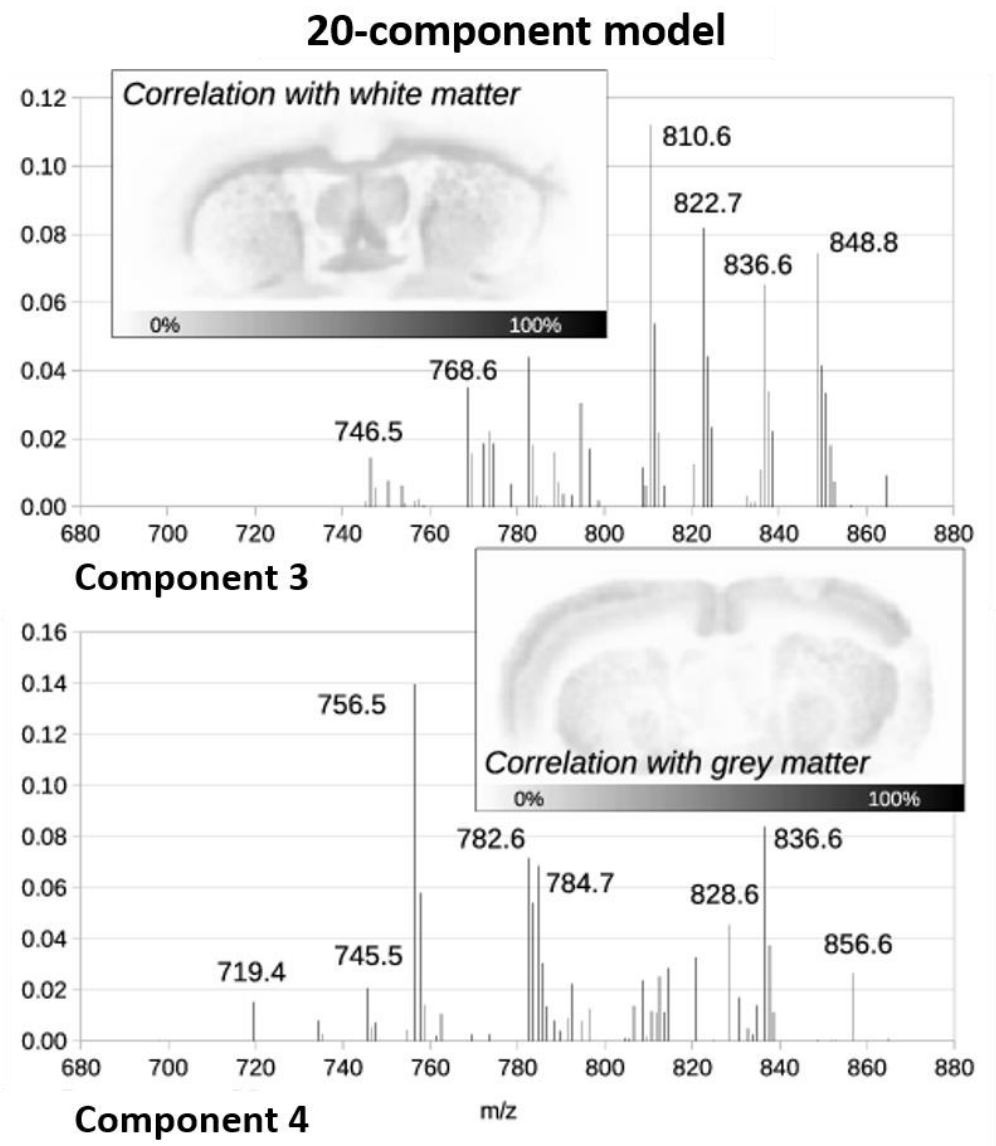

Figure 6.16 LP-ICA component images showing some large-scale structures and associated spectra

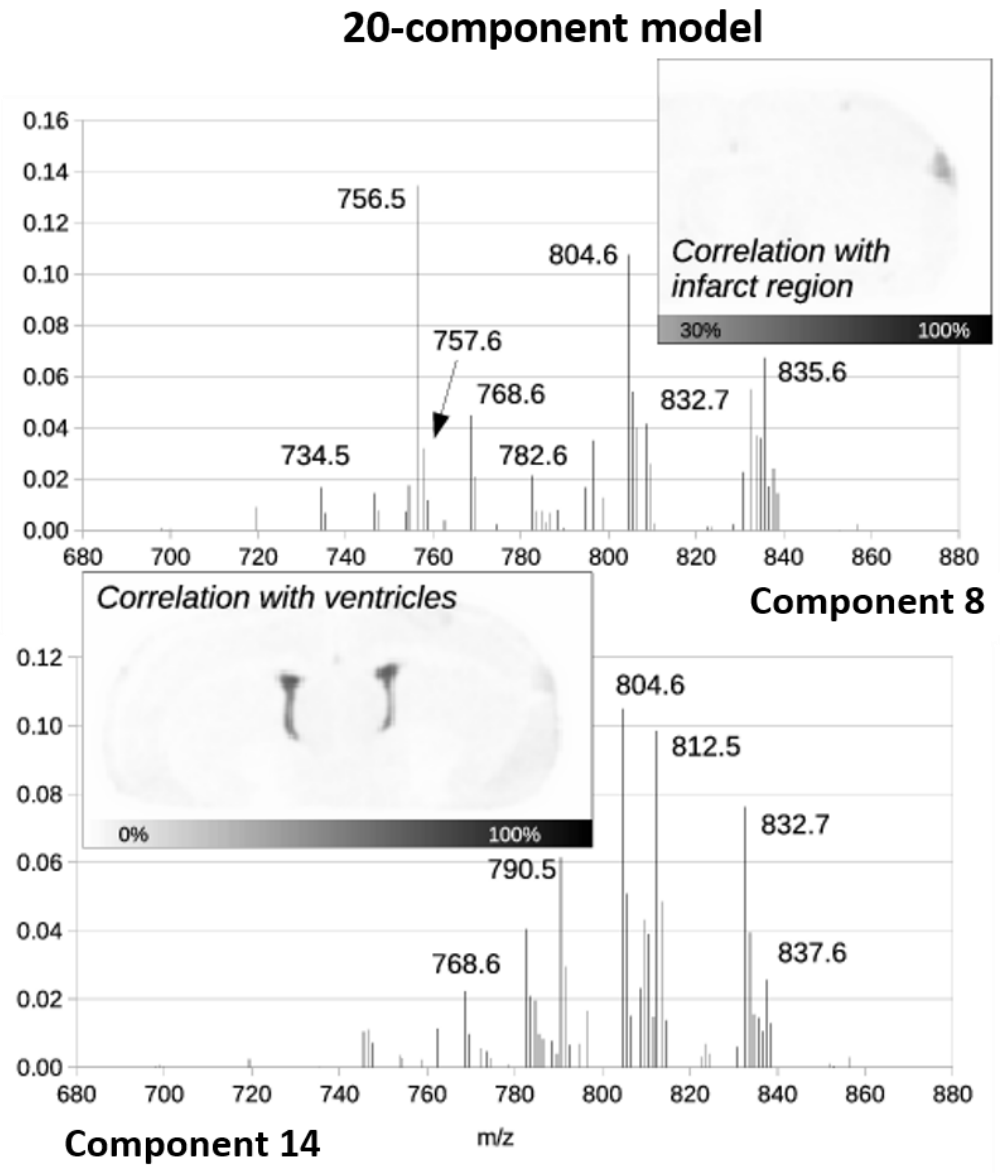

Figure 6.17 LP-ICA component images showing some highly localised structures and associated spectra

6.3.10 Compound Biomarker Discovery

For a single ion image to act as a useful biomarker it must correlate consistently with a tissue or region of interest. It must also not appear in other regions, or only appear in negligible quantities elsewhere. Given that there are many common chemicals found in abundance, distributed throughout the brain and other organs, single-ions that fulfill this criteria can be a minimal contribution to total spectra and thus be

difficult to find. Once found, it is reasonable to assume that the biomolecule discovered plays an important function within the tissue or region of interest that differentiates it from others. But if the biomarker is expressed in very small amounts close to the noise-floor, or 'in the grass', then it may play only a minor role in local biological and metabolic processes. Furthermore, it may only be a byproduct of local processes or be correlated with, but not causally related to them. Whilst there are many biomolecules that are common to multiple regions making them unsuitable as individual biomarkers, they can appear together in unique ratios. A combination of fixed ratios of multiple single ion images can be harnessed as a useful compound biomarker. The LP-ICA components extracted during data mining can be interpreted as such biomarkers. This style of marker has many advantages over single ion images. Firstly, they make use of much more data, including more abundant biochemical with better signal-to-noise. Secondly, a compound biomarker gives a more comprehensive account of the regional chemical environment. The spectrum associated with component 8 of the 20-component model, for example, shows a number of biomolecules that appear in unique ratios (see relative m/z peak intensities of the mass spectrum at the bottom of Figure 6.17), making them candidates for use as naturally occurring biomarkers in stroke damaged tissue (see the image with a highlighted infarct region at the bottom of Figure 6.17). A more extensive study will be required to identify the extent of damage or possibly the ingress of a particular cell type, generation of an astrocytic scar or ingress of CSF. This may answer questions as to the function of this new tissue.

6.4 Conclusion

A MALDI image is a particularly specialised form of hyper-spectral image, as each pixel corresponds to many thousands of masses that can all be visualised simultaneously. Conventional approaches to reducing dimensionality are often inapplicable, as they typically assume independent, identically distributed (iid) Gaussian noise. LP-ICA modelling has been shown to effectively build low dimensional models of orders 12 to 20, whilst appropriately taking into account the

Poisson nature of spectra and variable per-pixel signal-to-noise. The capability of the method to predict errors associated with estimated quantities is useful for model validation. Images constructed from LP-ICA weighting quantities correspond well with biological structures and evidence from associated PMFs is consistent with the discovery of meaningful tissue phenotypes. The discovery of a model component highly correlated with stroke damaged tissue demonstrates the potential for the method to be used in pathology. Through data mining, a new method for potential biomarker discovery has been shown, along with detailed biomolecule correlation analysis and spatial mapping validated using well-understood rat brain data. The success provides confidence that the method may be applied in future work to less well-understood images, including heterogeneous tumours.

Chapter 7

Summary

This final chapter summarises all the main findings of this thesis. Starting from the knowledge that MALDI is a technique for biomolecular analysis widely used in many research fields and industries but is poor at quantitation. The journey through this PhD study was therefore seeking an alternative data analysis approach to quantify MALDI-MS data both accurately and automatically. The experiments were designed to find suitable solutions such that the aims and objectives of the thesis as outlined in Section 1.2 of Chapter 1, were achieved. The detailed background in Chapter 2 explains the various processes, both instrumental and ionisation mechanisms, that affect signal-to-noise in the resultant MALDI-MS spectra. The optimised parameters in preparing samples for analysis and acquiring the mass spectral data with the available instruments were described in Chapter 4. Chapter 2 also discusses the use of MALDI-MS in lipidomics applications (especially the imaging aspect), which is relevant to the samples used in Chapters 5 and 6. Attempts to apply computational or multivariate analysis techniques to mass spectral data are discussed in Chapter 3, which is then followed by the description of the preferred analysis method, namely linear Poisson independent component analysis (LP-ICA), justified by the statistical tests performed on the MALDI data (see the plot in Figure 5.6, Section 5.4.2 for Bland-Altman analysis). The suitability of the method compared to other methods that have been used to analyse MALDI-MS imaging data is discussed thoroughly in Section 6.1.3.

In what follows, the overall conclusions to the thesis will be summarised. This discussion demonstrates the novelty of the work, including the achievements made with the current experimental/analysis approach, and any limitations that have been experienced. Finally, suggestions for future work are provided.

7.1 Overall Conclusions

For every MALDI-MS acquisition, the capabilities of the instrumentation and the important parameters must be identified and assessed for optimal performance, and are kept consistent throughout acquisition of the data set. A number of parameters e.g. laser power, number of laser shots per spectrum, crystal sizes and homogeneity of the prepared sample, affect signal-to-noise ratio and repeatability which are particularly important in terms of getting quantitative analysis. Chapter 4 suggested that a pre-mixed sample-matrix method is the most appropriate way to prepare discrete MALDI samples so that the repeatability is maximised.

This PhD project has developed an analysis method which is capable of relative quantification of underlying biological sub-samples within mixtures for discrete samples, and within spatially located tissues for imaging tissue samples. This new analysis approach is well-suited to the properties of MALDI mass spectra, based upon an independent component analysis derived for Poisson sampled data – i.e. LP-ICA as discussed in Section 3.4.5.

In chapter 5, the proposed analysis method was tested for validation. Lipid-rich binary mixtures of cow's and goat's milk, lamb brain and liver, and also lamb brain white and grey matter were made, and used as examples of complex biological mixtures. These allow measurements of sample proportion and error predictions using LP-ICA to be compared to a known "ground truth". LP-ICA improved quantitative accuracy by up to a factor of 2 for the measurement of these biological samples, when compared to a conventional approach using only single peak ratios. With the LP-ICA, the variations within MALDI mass spectra can be extracted in the

form of sub-spectra, which can be linearly combined to describe mass spectral information of the underlying samples with a reduced set of parameters and lower dimensionality. The results has validated the use of LP-ICA in MALDI-MS data and imply that it can be applicable for larger scale analysis of real-world MALDI-MS data – i.e. imaging.

The final analysis was the application of the LP-ICA method to data mine a MALDI-MS image data set which is built up from thousands of mass spectra at an array of pixel locations. Efficiently extracting the information contained within a large and complex image data is more challenging than the previous binary mixture examples. In Chapter 6, the LP-ICA was performed on a MALDI-MS image of a post-ischemic stroke rat brain tissue cross-section. The results demonstrate an unsupervised extraction of tissue phenotypes, and provide estimates of tissue quantities and biochemical (i.e. lipid) distributions. Automated probabilistic segmentations reveal anatomical structures and their associated mass spectra, which are data-driven, requiring no human annotation or use of brain atlases. Results also include the automatic identification of infarct region and potential associated biomarkers. A range of LP-ICA models of different model order are assessed, with resulting independent components being validated against predicted biological and physical constraints, e.g. known lipids associated with tissues and patterns of adjacent peaks driven by isotopic differences or sodium concentrations.

7.2 Novelty of the Work

Simple analyses have been limited to the use of a small number of mass peaks, via peak ratios, which is known to be inefficient. Most of other peaks have high levels of uncontrolled variability which is difficult to address using a single peak, and therefore large volumes of information are left unused with this approach. Conventional PCA and ICA methods have also been applied, which extract correlations between any number of peaks, but these can be argued making inappropriate assumptions regarding signal sampling noise, i.e. that it is both uniform and Gaussian. The LP-ICA

method successfully models underlying variability within a set of mass spectra, permitting information in any number of peaks to be included in measurement estimation.

7.2.1 Achievements

The statistical behaviour of the MALDI-MS data was shown to fit the assumptions made for the LP-ICA modelling method. Firstly, the raw spectra were pre-processed using the in-house algorithms listed in Section 3.3, assuming that Gaussian noise is dominant in the background, σ_g. The peak detected format of the spectra were analysed using the LP-ICA, and the distribution of the residuals of the model fit confirms that the Poisson noise of sampling process, σ_p was an appropriate assumption. The quantitation using the LP-ICA method resulted in doubled measurement accuracy for the binary mixture experiments. The ratio between measured and predicted errors of modelling ranges 1.4 - 1.6 (see the Pull distribution histograms in Figure 5.10, Section 5.4.2), meaning that most of the variability within the data was successfully modelled. The automation of the method and ability of making suitable error predictions, have made LP-ICA superior to the conventional PCA, ICA, or single peak analysis. The modelled spectral components are unique and refer to the correlated sets of molecular signals in the spectral data set. This provides meaningful interpretations of what are contained in the underlying samples without prior knowledge for both discrete and imaging data.

Tissue-specific mass spectral 'fingerprints' are commonly acquired by either manually selecting regions of interest from an MS image, or through the mechanical separation of tissues. Image region selection can be aided by the use of brain atlases, but this method relies upon subjective expert judgments and can be limited to coarsely shaped annotations designed to avoid contamination from neighboring material. The alternative can involve challenging micro-dissections that necessarily removes tissue from its spatial context. This can increase the complexity of an analysis if both contextual imaging information and tissue-specific spectra are

needed. For certain classes of problem neither of these approaches may be applicable. Atlases may be of limited use in pathological cases that do not follow normal physiology. This includes stochastic structures, such as heterogeneous tumors. Similarly, if the effects of drugs or injury are sought, image annotations or dissections may be impractical due to a lack of knowledge of the spatial distribution of effected regions – indeed, identifying such spatial distributions may be the objective of a study. LP-ICA method for automated tissue phenotyping provides many advantages over these conventional approaches. Primarily, it is a tool that removes human subjectivity from tissue analyses, thus resulting in more objective data-driven outputs. The model selection stage can be used to determine the complexity of the data by identifying how many linear components exist within the spectra. Assuming that non-linearities and chemical gradients are controlled, this number will be indicative of the number of (detectable) unique tissue classes present. The LP-ICA component images present the fractional tissue content of each pixel. Pixels at tissue boundaries are therefore not forced to adopt hard labels and not subject to false-positive or false-negative classifications that can otherwise contaminate spectra. This approach therefore provides complete image coverage via 'soft' segmentations that naturally address partial volume effects. Tissue-specific spectra can be extracted at every location, in images of varying complexity, with no need for atlases or dissections.

7.2.2 Limitations

Every attempt at modelling results in estimate values with some uncertainties. It is almost impossible to capture every process present in the data. The limitations for the current LP-ICA approach are noted here.

- Due to the limited computational efficiency, the data sizes had to be reduced by re-binning the peaks so that the analysis was done on a reasonable time scale. This reduction in mass resolution benefits by evening out the correlation between adjacent bins, but it can hide some finer information

between main peaks – i.e. smaller peaks might be merged into or split between their neighbour peaks.

- Some factors might partly destroy the linearity in the data assumptions made for the LP-ICA modelling method. In reality, the combination of other variability that builds up into signals e.g. the suppression of some ions, (unintended) fragmentations which occur effectively at a random rate, would affect the noise characteristics. However, this is relatively small compared with the signal variability due to the Poisson sampling process, σ_p. In imaging, this problem will become important only if the effects do not occur globally.
- Where a known ground truth does not exist for the imaging data, the ability to test for measurement errors is limited. Although, they may be of quantitative value.

7.3 Future Work

As was demonstrated in the binary mixture analysis in Chapter 5, predicted errors can also be determined for each pixel (each spectrum) of the component images. This allows the determination of the noise floor in the processed images, depending on the signal generators. However, there is no definition of ground truth for real-world MALDI-MS images; therefore, measurement accuracy is difficult to determine. Using a simulated sample would be one of the ways to create a reliable ground truth for the analysis. It is certainly not a simple task in imaging, considering the method and amount of data taken compared with the non-imaging binary mixture approach. A suggestion for the future work would therefore be growing cells (of different types that are contained in an interested organ) in cultures, mixing them in varied proportions, and then using methods such as inkjet printing to produce a simulated sample. Biological materials extracted from separated parts of an organ or cell mixtures can be 3-D printed into a model (Ma *et al*., 2018) with known spatial and chemical distribution for subsequent analysis. This method has an advantage of having full knowledge of input materials (ground truth). However, there is lack of

control over interactions which might occur during the processes after mixing biological materials. This limitation might be overcome by acquiring mass spectrometry data of these mixtures separately prior to forming a simulated sample for comparison. Note that this problem could also exist in a real-world sample environment where every tissue part naturally contains mixtures of various cells/biochemicals as well (probably much more variety than simulated samples). These simulated samples could help with understanding of the associated spectral characteristics, the sources of background noise, and the appropriateness of background subtraction algorithms in pre-processing or the relevance of the background components in LP-ICA. The validity of the LP-ICA modelling method could then be systematically tested. Primarily, these models would combine known biological components and LP-ICA would be expected to re-extract these from the mixture.

In the binary mixture analysis, a weighted combination of sub-spectra was needed to describe a sample class. In contrast, single spectral components were used to explain tissue types in the rat brain imaging analysis and there was evidence (based on the error correlation between components, see the plot in Figure 6.8, explained in Section 6.3.2 and segmentation seen in component images) that single sub-spectra represent unique phenotypes for specific biological tissues. For completeness the same criteria that were applied to the binary mixture experiments, should be applied in the image analysis. The solution requires a mimic ground truth that could be achieved through the use of Entropy and Mutual Information concepts (Bollenbeck *et al*., 2009). These can determine the information content within the image created from weighted component combinations compared to pixel intensities in an independent target image – e.g. a single ion image, an immunohistochemistry image, etc. This could lead to a model refinement, when there is a need for multiple component images to be added together, for a more complete interpretation of the underlying tissues.

A number of methods to extend the quantitative abilities of LP-ICA could be assessed. The current LP-ICA provides an ‘absolute’ measure of the ion counts recorded across the mass spectrum corresponding to each of the components. Alternatively, it can

be viewed as a 'relative' quantitation of the underlying sample quantities – i.e. it quantifies the ratio of tissue sub-types contained in the tissue section expressed in terms of the spectral components that are themselves comprised of mixtures of underlying biochemicals. This enables sample to sample comparison, or between-pixel measurements, in discrete and imaging samples, respectively. Separate steps are required to quantify the things contained in tissue – i.e. to turn LP-ICA into an imaging MS sample quantitation tool (as well as the binary mixtures in Chapter 5). This is a primary step toward the absolute quantitation of samples. This will require calibration with known standards. An internal standard of known concentration can be added evenly across the sample surface (e.g. by spraying along with the matrix solution). This would provide the calibration factor for the extracted components in the absolute sense – i.e. as an approach to measuring the amount of a particular biochemical in the sample. Once established, the calibration factor could then be applied to a data set of same tissue type under the same conditions but without the internal standard. If series of standards are applied to the imaging sample, LP-ICA should be able to extract a component corresponding to these standard molecules. Alternatively, peaks associated with matrix could potentially be used as calibration standards. However, they must be very carefully selected as they are expected to be quite unstable. This is because matrix is highly volatile, forms clusters that subsequently fragment and sometimes bind with some other ions creating random m/z peaks in a spectrum.

The mass spectral range used in this work was limited for the sake of computational speed during development of the methods. It would be interesting to explore the use of a wider mass range to cover a greater number of lipid species and determine associated advantages in terms of overall signal to noise and the number of extracted components. The method developed can also be applied to analyse other classes of molecules, e.g. peptides, proteins, where appropriate for the sample of interest. A LP-ICA component (sub-spectrum) identifies expected ratios between m/z peaks from the associated sub-tissues which is an approach to characterising tissue types. Identification of individual m/z peaks within each component (and therefore within each tissue type) can then be checked with MS/MS.

Component images, as a result of the analysis, give soft segmentation (i.e. the distribution) of the underlying sub-tissues, which could contain useful clinical information (with more biologically interested and informative details than using hard segmentation techniques with definite class labelling). Applications to pathological problems such as identification of tumour sub-types and metabolically distinct regions within tumours are therefore promising. A lipid atlas of the rat brain, which was beyond the scope of this thesis, could potentially be produced. Identification of lipids in specific tissue types corresponding to particular anatomical regions requires collaboration with a range of expertise in biology, medicine and in particular, lipidomics. This will be an extremely valuable resource for the interpretation of MALDI-MS tissue images.

A comparison between the LP-ICA method and some of the other related approaches discussed in Chapter 6 could also be considered for future work – i.e. to assess the power of LP-ICA relative to the other methods in a range of applications, for quantitation, segmentation and classification. However, as already discussed in Section 6.1.3, the LP-ICA produces an error model (which is not available with other approaches) along with the quantitative analysis using appropriate statistical assumptions. The LP-ICA error model, which can be computed from Equation (3.10), will allow error bars to be associated with all measurements (every pixel in an MS imaging data set will have error bars determined on the quantities associated with the extracted components and also on each individual ion count estimate on m/z peak). Therefore, a statistical hypothesis test can be constructed using the uncertainty information from LP-ICA to determine confidence when analysing real-world MALDI-MSI data.

It is almost always possible to improve computational efficiency of every algorithm including the LP-ICA. However, this requires effort and whether or not it is worth doing depends on the objective of the work. The software for this analysis algorithm was written in C. The structure of the algorithm at the moment is not necessary the only way to obtain correct values. There is likely a better way to achieve the same solution using a shorter computational pathway. In order to improve efficiency, it requires a more in-depth analysis of the algorithm, for example, seeking a better

update function, initialising independent components closer to optimum points, etc. Statistical validity was the main aim for this work. Therefore, it was most important to make sure the method worked properly and obtained correct answers to the question of the intended analysis, before considering speeding up the algorithm. Alternative ways of speeding up the calculation is to increase the processing power. This can be done with the help of hardware, using a faster computer and parallel calculations. For example, the computer used to run the present analysis has 6-physical (12-virtual) core processors. However, only one core processor was used, which took a few days (i.e. 3.5 days on average) to complete 5 attempts of running repeating analyses of the same model (equivalent to less than a day for individual attempts). When all the virtual core processors are used in parallel, it can potentially run 12 times faster immediately (reducing computation time to approximately 1.5 hours per attempt). Even with the current efficiency of this approach, the work involved running analyses for multiple models simultaneously, and resulted in multiple models (not only one model) built in a few days. Combining all of these approaches of boosting the computational efficiency and processing power will result in significantly higher analysis speed.

In summary, the issues to be addressed in the future work include:

- Working out how to compute tissue quantities from spectral quantities, e.g. using a calibration against a reference set of internal standards.
- Creating a ground truth for MALDI-MS imaging to test for LP-ICA modelling efficiency (e.g. using simulated samples), and observing noise distribution on the extracted component images.
- Applying the concept of mutual information to an independent target image to find a suitable weighted combination of component images necessary to describe a tissue type.
- Including a wider mass range of spectra into the analysis.
- Confirming ratios of m/z peaks in ICA components that relate to tissue biochemistry. Note that unique m/z peaks can additionally be confirmed and distinguished through MS/MS.

- Extending applications to help answer biochemical questions and identify region of interest, for example, tissue pathology.
- Producing a lipid atlas of the rat brain.
- Performing a statistical hypothesis test on an analysis of MS imaging data using the error model available in LP-ICA.
- Systematic testing of LP-ICA against other approaches for data analysis.
- Improving computational efficiency.

References

Abdelmoula, Walid M., Nicola Pezzotti, Thomas Hölt, Jouke Dijkstra, Anna Vilanova, Liam A. McDonnell, and Boudewijn P. F. Lelieveldt. 2018. 'Interactive Visual Exploration of 3D Mass Spectrometry Imaging Data Using Hierarchical Stochastic Neighbor Embedding Reveals Spatiomolecular Structures at Full Data Resolution', *Journal of proteome research*, 17: 1054-64.

Adibhatla, Rao Muralikrishna, J. F. Hatcher, and R. J. Dempsey. 2006. 'Lipids and lipidomics in brain injury and diseases', *The AAPS Journal*, 8: E314-E21.

Ahmed M. N., Yamany S. M., Mohamed N., Farag A. A., and Moriarty T. 2002. 'A modified fuzzy c-means algorithm for bias field estimation and segmentation of MRI data', *IEEE Transactions on Medical Imaging*, 21: 193-99.

Al-Saad, Khalid A., Vladimir Zabrouskov, William F. Siems, N. Richard Knowles, Richard M. Hannan, and Herbert H. Hill. 2003. 'Matrix-assisted laser desorption/ionization time-of-flight mass spectrometry of lipids: ionization and prompt fragmentation patterns', *Rapid Communications in Mass Spectrometry*, 17: 87-96.

AlMasoud, N., Y. Xu, N. Nicolaou, and R. Goodacre. 2014. 'Optimization of matrix assisted desorption/ionization time of flight mass spectrometry (MALDI-TOF-MS) for the characterization of Bacillus and Brevibacillus species', *Analytica Chimica Acta*, 840: 49-57.

Anscombe, F. J. 1948. 'The Transformation of Poisson, Binomial and Negative-Binomial Data', *Biometrika*, 35: 246-54.

Askenazi, Manor, Hisham Ben Hamidane, and Johannes Graumann. 2017. 'The arc of Mass Spectrometry Exchange Formats is long, but it bends toward HDF5', *Mass Spectrometry Reviews*, 36: 668-73.

Astigarraga, E., G. Barreda-Gomez, L. Lombardero, O. Fresnedo, F. Castano, M. T. Giralt, B. Ochoa, R. Rodriguez-Puertas, and J. A. Fernandez. 2008. 'Profiling and imaging of lipids on brain and liver tissue by matrix-assisted laser desorption/ ionization mass spectrometry using 2-mercaptobenzothiazole as a matrix', *Anal Chem*, 80: 9105-14.

Avanzi, I. R., L. H. Gracioso, M. D. Baltazar, B. Karolski, E. A. Perpetuo, and C. A. do Nascimento. 2017. 'Rapid bacteria identification from environmental mining samples using MALDI-TOF MS analysis', *Environ Sci Pollut Res Int*, 24: 3717-26.

Bae, Y. J., J. C. Choe, J. H. Moon, and M. S. Kim. 2013. 'Why do the Abundances of Ions Generated by MALDI Look Thermally Determined?', *Journal of The American Society for Mass Spectrometry*, 24: 1807-15.

Barber, M., R. S. Bordoli, R. D. Sedgwick, and A. N. Tyler. 1981. 'Fast atom bombardment of solids as an ion source in mass spectrometry', *Nature*, 293: 270-75.

Barlow, R.J. 1989. *Statistics: A Guide to the Use of Statistical Methods in the Physical Sciences* (Wiley).

Bayer, S. A., J. Altman, R. J. Russo, and X. Zhang. 1993. 'Timetables of neurogenesis in the human brain based on experimentally determined patterns in the rat', *Neurotoxicology*, 14: 83-144.

Behrmann, Jens, Christian Etmann, Tobias Boskamp, Rita Casadonte, Jörg Kriegsmann, and Peter Maaβ. 2018. 'Deep learning for tumor classification in imaging mass spectrometry', *Bioinformatics*, 34: 1215-23.

Bennett, Edward L., Marian C. Diamond, David Krech, and Mark R. Rosenzweig. 1964. 'Chemical and Anatomical Plasticity of Brain', *Science*, 146: 610-19.

Benninghoven, A. 1969. 'Analysis of Submonolayers on Silver by Negative Secondary Ion Emission', *Physica Status Solidi*, 34: K169-K171.

Berg, J.M., J.L. Tymoczko, and L. Stryer. 2002. 'Fatty Acids Are Key Constituents of Lipids.' in, *Biochemistry* (W. H. Freeman and Company: New York).

Beynon, J. H., R. G. Cooks, J. W. Amy, Baitinge.We, and T. Y. Ridley. 1973. 'Design and Performance of a Mass Analyzed Ion Kinetic-Energy (Mike) Spectrometer', *Analytical Chemistry*, 45: 1023-31.

'Bioinformatics Toolbox'. The MathWorks, Inc. http://uk.mathworks.com/products/bioinfo/ [Accessed: 06-09-2018].

'Biomap'. Novartis. https://ms-imaging.org/wp/biomap/ [Accessed: 06-09-2018].

Bland, J. M., and D. G. Altman. 1986. 'Statistical methods for assessing agreement between two methods of clinical measurement', *Lancet*, 1: 307-10.

Bligh, E. G., and W. J. Dyer. 1959. 'A rapid method of total lipid extraction and purification', *Can J Biochem Physiol*, 37: 911-7.

Blümel, R. 1995. 'The Dynamic Kingdon Trap - a Novel Design for the Storage and Crystallization of Laser-Cooled Ions', *Applied Physics B-Lasers and Optics*, 60: 119-22.

Bodzon-Kulakowska, A., and P. Suder. 2016. 'Imaging mass spectrometry: Instrumentation, applications, and combination with other visualization techniques', *Mass Spectrom Rev*, 35: 147-69.

Bokhart, M. T., M. Nazari, K. P. Garrard, and D. C. Muddiman. 2018. 'MSiReader v1.0: Evolving Open-Source Mass Spectrometry Imaging Software for Targeted and Untargeted Analyses', *J Am Soc Mass Spectrom*, 29: 8-16.

Bollenbeck, Felix, Stephanie Kaspar, Hans-Peter Mock, Diana Weier, and Udo Seiffert. 2009. "Three-Dimensional Multimodality Modelling by Integration of High-Resolution Interindividual Atlases and Functional MALDI-IMS Data." In *Bioinformatics and Computational Biology*, edited by Sanguthevar Rajasekaran, 126-38. Berlin, Heidelberg: Springer Berlin Heidelberg.

Bonnel, D., R. Legouffe, A. H. Eriksson, R. W. Mortensen, F. Pamelard, J. Stauber, and K. T. Nielsen. 2018. 'MALDI imaging facilitates new topical drug development process by determining quantitative skin distribution profiles', *Anal Bioanal Chem*, 410: 2815-28.

Bordas-Nagy, Jozsef, Dominique Despeyroux, Keith R. Jennings, and Simon J. Gaskell. 1992. 'Experimental aspects of the collision-induced decomposition of ions in a four-sector tandem mass spectrometer', *Organic Mass Spectrometry*, 27: 406-15.

Brouwer, T. A. 2016. "Probabilistic non-negative matrix factorisation and extensions." In. https://www.semanticscholar.org/paper/Probabilistic-non-negative-matrix-factorisation-and-Brouwer/6848045141f67facf171b456b4fe3dd125fa0623 [Accessed: 06-03-2019]: Semantic Scholar.

Bruker. 2018. 'SCiLS lab - The advanced mass spectrometry imaging software solution'. https://www.bruker.com/products/mass-spectrometry-and-separations/ms-software/scils/overview.html [Accessed: 06-09-2018].

Busch, K. L. 1995. 'Desorption Ionization Mass-Spectrometry', *Journal of Mass Spectrometry*, 30: 233-40.

Cahill, J. F., V. Kertesz, T. M. Weiskittel, M. Vavrek, C. Freddo, and G. J. Van Berkel. 2016. 'Online, Absolute Quantitation of Propranolol from Spatially Distinct 20- and 40-mum Dissections of Brain, Liver, and Kidney Thin Tissue Sections by Laser Microdissection-Liquid Vortex Capture-Mass Spectrometry', *Anal Chem*, 88: 6026-34.

Callister, Stephen J., Richard C. Barry, Joshua N. Adkins, Ethan T. Johnson, Wei-Jun Qian, Bobbie-Jo M. Webb-Robertson, Richard D. Smith, and Mary S. Lipton. 2006. 'Normalization approaches for removing systematic biases associated with mass spectrometry and label-free proteomics', *Journal of proteome research*, 5: 277-86.

Calvano, C. D., C. De Ceglie, A. Aresta, L. A. Facchini, and C. G. Zambonin. 2013. 'MALDI-TOF mass spectrometric determination of intact phospholipids as markers of illegal bovine milk adulteration of high-quality milk', *Anal Bioanal Chem*, 405: 1641-9.

Cameron, A. E., and D. F. Eggers. 1948. 'An Ion Velocitron', *Review of Scientific Instruments*, 19: 605-07.

Canny, J. 2004. "GaP: a factor model for discrete data." In *Proceedings of the 27th annual international ACM SIGIR conference on Research and development in information retrieval*, 122-29. Sheffield, United Kingdom: ACM.

Chapman, J. R. 1995. *Practical Organic Mass Spectrometry: A Guide for Chemical and Biochemical Analysis* (Wiley).

Chavko, M., and E. M. Nemoto. 1992. 'Regional differences in rat brain lipids during global ischemia', *Stroke*, 23: 1000-4.

Cherry, E. Colin. 1953. 'Some Experiments on the Recognition of Speech, with One and with Two Ears', 25: 975-79.

Chuang, Keh-Shih, Hong-Long Tzeng, Sharon Chen, Jay Wu, and Tzong-Jer Chen. 2006. 'Fuzzy c-means clustering with spatial information for image segmentation', *Computerized Medical Imaging and Graphics*, 30: 9-15.

Chumbley, C. W., M. L. Reyzer, J. L. Allen, G. A. Marriner, L. E. Via, C. E. Barry, 3rd, and R. M. Caprioli. 2016. 'Correction to Absolute Quantitative MALDI Imaging

Mass Spectrometry: A Case of Rifampicin in Liver Tissues', *Anal Chem*, 88: 8920.

Comon, Pierre. 1994. 'Independent component analysis, A new concept?', *Signal Processing*, 36: 287-314.

Cornish, T. J., and R. J. Cotter. 1993. 'A curved-field reflectron for improved energy focusing of product ions in time-of-flight mass spectrometry', *Rapid Commun Mass Spectrom*, 7: 1037-40.

Criminisi, A., and J. Shotton. 2013. 'Introduction: the abstract forest model.' in A. Criminisi and J. Shotton (eds.), *Decision forests for computer vision and medical image analysis* (Springer: London, UK).

Dagan, S., and A. Amirav. 1995. 'Electron-Impact Mass-Spectrometry of Alkanes in Supersonic Molecular-Beams', *Journal of The American Society for Mass Spectrometry*, 6: 120-31.

Damnjanovic, B., B. Petrovic, J. Dimitric-Markovic, and M. Petkovic. 2011. 'Comparison of MALDI-TOF mass spectra of [PdCl(dien)]Cl and [Ru(en)(2)Cl-2]Cl acquired with different matrices', *Journal of the Serbian Chemical Society*, 76: 1687-701.

Dashtiev, M., E. Wafler, U. Rohling, M. Gorshkov, F. Hillenkamp, and R. Zenobi. 2007. 'Positive and negative analyte ion yield in matrix-assisted laser desorption/ionization', *International Journal of Mass Spectrometry*, 268: 122-30.

Davanlou, Maziar, and Donald F. Smith. 2004. 'Unbiased stereological estimation of different cell types in rat cerebral cortex', *Image Analysis & Stereology; Vol 23, No 1: 1-11*.

Davis, Gwilym G. 1913. *Applied Anatomy: The Construction Of The Human Body* (J. B. Lippincott Company: Philadelphia&London).

de Koster, Chris G., and Stanley Brul. 2016. 'MALDI-TOF MS identification and tracking of food spoilers and food-borne pathogens', *Current Opinion in Food Science*, 10: 76-84.

Deepaisarn, S. 2015. 'First year PhD continuation report: Spectral analysis and quantitation in MALDI-MS imaging', *Internal report, TINA memos*, 2015-016: University of Manchester.

Deepaisarn, S., P. D. Tar, N. A. Thacker, A. Seepujak, and A. W. McMahon. 2018. 'Quantifying biological samples using Linear Poisson Independent Component Analysis for MALDI-TOF mass spectra', *Bioinformatics*, 34: 1001-08.

Deininger, S., K. Meyer, and A. Walch. 2012. 'Concise interpretation of MALDI imaging data by probabilistic latent semantic analysis (pLSA)'.

Deininger, S. O., D. S. Cornett, R. Paape, M. Becker, C. Pineau, S. Rauser, A. Walch, and E. Wolski. 2011. 'Normalization in MALDI-TOF imaging datasets of proteins: practical considerations', *Anal Bioanal Chem*, 401: 167-81.

Delvolve, A. M., B. Colsch, and A. S. Woods. 2011. 'Highlighting anatomical sub-structures in rat brain tissue using lipid imaging', *Anal Methods*, 3: 1729-36.

Delvolve, A. M., and A. S. Woods. 2011. 'Optimization of automated matrix deposition for biomolecular mapping using a spotter', *J Mass Spectrom*, 46: 1046-50.

Dempster, A. J. 1918. 'A new Method of Positive Ray Analysis', *Physical Review*, 11: 316-25.

Dolnikowski, G. G., M. J. Kristo, C. G. Enke, and J. T. Watson. 1988. 'Ion-Trapping Technique for Ion Molecule Reaction Studies in the Center Quadrupole of a Triple Quadrupole Mass-Spectrometer', *International Journal of Mass Spectrometry and Ion Processes*, 82: 1-15.

Duncan, M. W., H. Roder, and S. W. Hunsucker. 2008. 'Quantitative matrix-assisted laser desorption/ionization mass spectrometry', *Brief Funct Genomic Proteomic*, 7: 355-70.

Duncan, Mark W., Gabrijela Matanovic, and Anne Cerpa-Poljak. 1993. 'Quantitative analysis of low molecular weight compounds of biological interest by matrix-assisted laser desorption ionization', *Rapid Communications in Mass Spectrometry*, 7: 1090-94.

Dunn, J. C. 1973. 'A Fuzzy Relative of the ISODATA Process and Its Use in Detecting Compact Well-Separated Clusters', *Journal of Cybernetics*, 3: 32-57.

Dyer, W. J., and Margaret L. Morton. 1956. 'Storage of Frozen Plaice Fillets', *Journal of the Fisheries Research Board of Canada*, 13: 129-34.

Emerson, Beth, Jennifer Gidden, Jackson O. Lay, and Bill Durham. 2010. 'A rapid separation technique for overcoming suppression of triacylglycerols by

phosphatidylcholine using MALDI-TOF MS', *Journal of Lipid Research*, 51: 2428-34.

Fahy, Eoin, Shankar Subramaniam, H. Alex Brown, Christopher K. Glass, Alfred H. Merrill, Robert C. Murphy, Christian R. H. Raetz, David W. Russell, Yousuke Seyama, Walter Shaw, Takao Shimizu, Friedrich Spener, Gerrit van Meer, Michael S. VanNieuwenhze, Stephen H. White, Joseph L. Witztum, and Edward A. Dennis. 2005. 'A comprehensive classification system for lipids', *European Journal of Lipid Science and Technology*, 107: 337-64.

Fahy, Eoin, Shankar Subramaniam, Robert C. Murphy, Masahiro Nishijima, Christian R. H. Raetz, Takao Shimizu, Friedrich Spener, Gerrit van Meer, Michael J. O. Wakelam, and Edward A. Dennis. 2009. 'Update of the LIPID MAPS comprehensive classification system for lipids', *Journal of Lipid Research*, 50: S9-S14.

Fenselau, C., D. N. Heller, J. K. Olthoff, R. J. Cotter, Y. Kishimoto, and O. M. Uy. 1989. 'Desorption of ions from rat membranes: selectivity of different ionization techniques', *Biomed Environ Mass Spectrom*, 18: 1037-45.

Field, F. H., and M. S. B. Munson. 1965. 'Reactions of Gaseous Ions .14. Mass Spectrometric Studies of Methane at Pressures to 2 Torr', *Journal of the American Chemical Society*, 87: 3289-94.

Fjeldsted, J. 2003. 'Time-of-flight mass spectrometry: technical overview', *Agilent Technologies*.

Folch, J., M. Lees, and G. H. Sloane Stanley. 1957. 'A simple method for the isolation and purification of total lipides from animal tissues', *J Biol Chem*, 226: 497-509.

Fonville, Judith M., Claire L. Carter, Luis Pizarro, Rory T. Steven, Andrew D. Palmer, Rian L. Griffiths, Patricia F. Lalor, John C. Lindon, Jeremy K. Nicholson, Elaine Holmes, and Josephine Bunch. 2013. 'Hyperspectral Visualization of Mass Spectrometry Imaging Data', *Analytical Chemistry*, 85: 1415-23.

Frank, Ari M., Nuno Bandeira, Zhouxin Shen, Stephen Tanner, Steven P. Briggs, Richard D. Smith, and Pavel A. Pevzner. 2008. 'Clustering Millions of Tandem Mass Spectra', *Journal of Proteome Research*, 7: 113-22.

Fuchs, Beate, Ariane Nimptsch, Rosmarie Süß, and Jürgen Schiller. 2009. 'Capabilities and Drawbacks of Phospholipid Analysis by MALDI-TOF Mass Spectrometry.' in Donald Armstrong (ed.), *Lipidomics* (Humana Press).

Fuh, Manka M., Laura Heikaus, and Hartmut Schlüter. 2017. 'MALDI mass spectrometry in medical research and diagnostic routine laboratories', *International Journal of Mass Spectrometry*, 416: 96-109.

Fülöp, A., D. A. Sammour, K. Erich, J. von Gerichten, P. van Hoogevest, R. Sandhoff, and C. Hopf. 2016. 'Molecular imaging of brain localization of liposomes in mice using MALDI mass spectrometry', *Sci Rep*, 6: 33791.

Gilmour, J. D., I. C. Lyon, W. A. Johnston, and G. Turner. 1994. 'RELAX: An ultrasensitive, resonance ionization mass spectrometer for xenon', 65: 617-25.

Glish, G. L., and D. J. Burinsky. 2008. 'Hybrid mass spectrometers for tandem mass Spectrometry', *Journal of The American Society for Mass Spectrometry*, 19: 161-72.

Gopalan, P., Charlin L., and Blei D. M. 2014. "Content-based recommendations with Poisson factorization." In *Proceedings of the 27th International Conference on Neural Information Processing Systems*, 2: 3176-84. Montreal, Canada: MIT Press.

Griffith, K. S., and G. I. Gellene. 1993. 'Experimental and Theoretical Evidence for a New Metastable Valence State of O2', *Journal of Physical Chemistry*, 97: 9882-89.

Gross, J. H. 2004. *Mass Spectrometry: A Textbook* (Springer).

Gross, J. H., and P. Roepstorff. 2011. *Mass Spectrometry: A Textbook* (Springer).

Guilhaus, M. 1995. 'Principles and Instrumentation in Time-of-Flight Mass-Spectrometry - Physical and Instrumental Concepts', *Journal of Mass Spectrometry*, 30: 1519-32.

Guo, S., D. Zhou, M. Zhang, T. Li, Y. Liu, Y. Xu, T. Chen, and Z. Li. 2017. 'Monitoring changes of docosahexaenoic acid-containing lipids during the recovery process of traumatic brain injury in rat using mass spectrometry imaging', *Sci Rep*, 7: 5054.

Gut, Y., M. Boiret, L. Bultel, T. Renaud, A. Chetouani, A. Hafiane, Y. M. Ginot, and R. Jennane. 2015. 'Application of chemometric algorithms to MALDI mass spectrometry imaging of pharmaceutical tablets', *J Pharm Biomed Anal*, 105: 91-100.

Hamm, Gregory, David Bonnel, Raphael Legouffe, Fabien Pamelard, Jean-Marie Delbos, François Bouzom, and Jonathan Stauber. 2012. 'Quantitative mass spectrometry imaging of propranolol and olanzapine using tissue extinction calculation as normalization factor', *Journal of Proteomics*, 75: 4952-61.

Han, Xianlin, and Richard W. Gross. 2005. 'Shotgun lipidomics: Electrospray ionization mass spectrometric analysis and quantitation of cellular lipidomes directly from crude extracts of biological samples', *Mass Spectrometry Reviews*, 24: 367-412.

Hanahan, Douglas, and Robert A. Weinberg. 2000. 'The Hallmarks of Cancer', *Cell*, 100: 57-70.

Hanahan, Douglas, and Robert A Weinberg. 2011. 'Hallmarks of Cancer: The Next Generation', *Cell*, 144: 646-74.

Hanselmann, Michael, Marc Kirchner, Bernhard Y. Renard, Erika R. Amstalden, Kristine Glunde, Ron M. A. Heeren, and Fred A. Hamprecht. 2008. 'Concise Representation of Mass Spectrometry Images by Probabilistic Latent Semantic Analysis', *Analytical Chemistry*, 80: 9649-58.

Hanselmann, Michael, Ullrich Köthe, Marc Kirchner, Bernhard Y. Renard, Erika R. Amstalden, Kristine Glunde, Ron M. A. Heeren, and Fred A. Hamprecht. 2009. 'Toward Digital Staining using Imaging Mass Spectrometry and Random Forests', *Journal of Proteome Research*, 8: 3558-67.

Harkewicz, Richard, and Edward A. Dennis. 2011. 'Applications of Mass Spectrometry to Lipids and Membranes', *Annual review of biochemistry*, 80: 301-25.

Harn, Y. C., M. J. Powers, E. A. Shank, and V. Jojic. 2015. 'Deconvolving molecular signatures of interactions between microbial colonies', *Bioinformatics*, 31: i142-50.

Harrison, A. G. 1992. *Chemical Ionization Mass Spectrometry, Second Edition* (Taylor & Francis).

Harrison, AlexG. 1980. 'Chemical Ionization Mass Spectrometry of Hydrocarbons and Halohydrocarbons.' in B. K. Afghan, D. Mackay, H. E. Braun, A. S. Y. Chau, J. Lawrence, D. R. S. Lean, O. Meresz, J. R. W. Miles, R. C. Pierce, G. A. V. Rees, R. E. White, D. M. Whittle and D. T. Williams (eds.), *Hydrocarbons and Halogenated Hydrocarbons in the Aquatic Environment* (Springer US).

Harwood, J. L., and C. M. Scrimgeour. 2007. 'Fatty Acid and Lipid Structure.' in, *The Lipid Handbook with CD-ROM, Third Edition* (CRC Press).

Hazama, Hisanao, Hirofumi Nagao, Ren Suzuki, Michisato Toyoda, Katsuyoshi Masuda, Yasuhide Naito, and Kunio Awazu. 2008. 'Comparison of mass spectra of peptides in different matrices using matrix-assisted laser desorption/ionization and a multi-turn time-of-flight mass spectrometer, MULTUM-IMG', *Rapid Communications in Mass Spectrometry*, 22: 1461-66.

Henderson, F., P. J. Hart, J. M. Pradillo, M. Kassiou, L. Christie, K. J. Williams, H. Boutin, and A. McMahon. 2018. 'Multi-modal imaging of long-term recovery post-stroke by positron emission tomography and matrix-assisted laser desorption/ionisation mass spectrometry', *Rapid Commun Mass Spectrom*, 32: 721-29.

Herault, J., and B. Ans. 1984. '[Neuronal network with modifiable synapses: decoding of composite sensory messages under unsupervised and permanent learning]', *C R Acad Sci III*, 299: 525-8.

Herbert, C.G., and R.A.W. Johnstone. 2002. *Mass Spectrometry Basics* (CRC Press).

Hillenkamp, F., and J. Peter-Katalinic. 2007. *Maldi MS: A Practical Guide to Instrumentation, Methods and Applications* (Wiley).

Hillenkamp, Franz, Thorsten W. Jaskolla, and Michael Karas. 2013. 'The MALDI Process and Method.' in, *MALDI MS* (Wiley-VCH Verlag GmbH & Co. KGaA).

Hofmann, Thomas. 2001. 'Unsupervised Learning by Probabilistic Latent Semantic Analysis', *Machine Learning*, 42: 177-96.

Hu, Q., R. J. Noll, H. Li, A. Makarov, M. Hardman, and R. Graham Cooks. 2005. 'The Orbitrap: a new mass spectrometer', *J Mass Spectrom*, 40: 430-43.

Hulbert, A. J., and Paul Lewis Else. 1999. 'Membranes as Possible Pacemakers of Metabolism', *Journal of Theoretical Biology*, 199: 257-74.

Hultin-Rosenberg, L., J. Forshed, R. M. M. Branca, J. Lehtio, and H. J. Johansson. 2013. 'Defining, Comparing, and Improving iTRAQ Quantification in Mass Spectrometry Proteomics Data', *Molecular & Cellular Proteomics*, 12: 2021-31.

Jackson, S. N., H. Y. Wang, and A. S. Woods. 2005. 'Direct profiling of lipid distribution in brain tissue using MALDI-TOFMS', *Anal Chem*, 77: 4523-7.

Jacobsen, N.E. 2016. *NMR Data Interpretation Explained: Understanding 1D and 2D NMR Spectra of Organic Compounds and Natural Products* (Wiley).

Jeffries, N. 2005. 'Algorithms for alignment of mass spectrometry proteomic data', *Bioinformatics*, 21: 3066-73.

Jolliffe, I.T. 1986. *Principal component analysis* (Springer-Verlag).

Jones, Emrys A., Alexandra van Remoortere, René J. M. van Zeijl, Pancras C. W. Hogendoorn, Judith V. M. G. Bovée, André M. Deelder, and Liam A. McDonnell. 2011. 'Multiple statistical analysis techniques corroborate intratumor heterogeneity in imaging mass spectrometry datasets of myxofibrosarcoma', *PloS one*, 6: e24913-e13.

Kaiser, H.F. 1958. 'The varimax criterion for analytic rotation in factor analysis', *Psychometrika*, 23: 187-200.

Karas, M. 1997. 'Time-of-flight mass spectrometer with improved resolution', *Journal of Mass Spectrometry*, 32: 1-3.

Karas, M., and F. Hillenkamp. 1988. 'Laser desorption ionization of proteins with molecular masses exceeding 10,000 daltons', *Anal Chem*, 60: 2299-301.

Kaya, I., D. Brinet, W. Michno, M. Baskurt, H. Zetterberg, K. Blenow, and J. Hanrieder. 2017. 'Novel Trimodal MALDI Imaging Mass Spectrometry (IMS3) at 10 mum Reveals Spatial Lipid and Peptide Correlates Implicated in Abeta Plaque Pathology in Alzheimer's Disease', *ACS Chem Neurosci*, 8: 2778-90.

Kingdon, K. H. 1923. 'A method for the neutralization of electron space charge by positive ionization at very low gas pressures', *Physical Review*, 21: 408-18.

Knight, R. D. 1981. 'Storage of Ions from Laser-Produced Plasmas', *Applied Physics Letters*, 38: 221-23.

Knochenmuss, R. 2013. 'MALDI and Related Methods: A Solved Problem or Still a Mystery?', *Mass Spectrom (Tokyo)*, 2: S0006.

Köfeler, H. C., A. Fauland, G. N. Rechberger, and M. Trotzmuller. 2012. 'Mass spectrometry based lipidomics: an overview of technological platforms', *Metabolites*, 2: 19-38.

Krishnaveni, V., Sanjini Jayaraman, Prof. Manoj Kumar, K. Shivakumar, and Karthikeyan Ramadoss. 2005. "Comparison of Independent Component Analysis Algorithms for Removal of Ocular Artifacts from Electroencephalogram." In.

Kruft, V. 'MALDI Imaging: Applications to proteins, lipids and small molecules in MS and MS/MS', SCIEX online document. http://www.mobi4health.ug.edu.pl/wp-content/uploads/2014/10/2ndMSW-Volker-Kruft.pdf [Accessed: 23-08-2018].

Lange, V., P. Picotti, B. Domon, and R. Aebersold. 2008. 'Selected reaction monitoring for quantitative proteomics: a tutorial', *Molecular Systems Biology*, 4.

Laskin, J., B. S. Heath, P. J. Roach, L. Cazares, and O. J. Semmes. 2012. 'Tissue imaging using nanospray desorption electrospray ionization mass spectrometry', *Anal Chem*, 84: 141-8.

Laugesen, S., and P. Roepstorff. 2003. 'Combination of two matrices results in improved performance of MALDI MS for peptide mass mapping and protein analysis', *J Am Soc Mass Spectrom*, 14: 992-1002.

Leuschner, Johannes, Maximilian Schmidt, Pascal Fernsel, Delf Lachmund, Tobias Boskamp, and Peter Maass. 2018. 'Supervised non-negative matrix factorization methods for MALDI imaging applications', *Bioinformatics*.

Li, C., D. Ma, K. Deng, Y. Chen, P. Huang, and Z. Wang. 2017. 'Application of MALDI-TOF MS for Estimating the Postmortem Interval in Rat Muscle Samples', *J Forensic Sci*, 62: 1345-50.

Li, L. 2009. *MALDI Mass Spectrometry for Synthetic Polymer Analysis* (Wiley).

Li, Liang, and Randy M. Whittal. 2009. 'Time-of-Flight Mass Spectrometry for Polymer Characterization.' in, *Maldi Mass Spectrometry for Synthetic Polymer Analysis* (John Wiley & Sons, Inc.).

'LIPID Metabolites And Pathways Strategy (LIPID MAPS) Lipidomics Gateway'. http://www.lipidmaps.org/ [Accessed: 06-09-2018].

Liu, R., Q. Li, and L. M. Smith. 2014. 'Detection of large ions in time-of-flight mass spectrometry: effects of ion mass and acceleration voltage on microchannel plate detector response', *J Am Soc Mass Spectrom*, 25: 1374-83.

Liu, S., L. Cheng, Y. Fu, B. F. Liu, and X. Liu. 2018. 'Characterization of IgG N-glycome profile in colorectal cancer progression by MALDI-TOF-MS', *J Proteomics*, 181: 225-37.

Liyen, Wong, MaybinK Muyeba, JohnA Keane, Zhiguo Gong, and Valerie Edwards-Jones. 2013. 'Classifying Mass Spectral Data Using SVM and Wavelet-Based Feature Extraction.' in Tetsuya Yoshida, Gang Kou, Andrzej Skowron, Jiannong Cao, Hakim Hacid and Ning Zhong (eds.), *Active Media Technology* (Springer International Publishing).

Lohmann, C., E. Schachmann, T. Dandekar, C. Villmann, and C. M. Becker. 2010. 'Developmental profiling by mass spectrometry of phosphocholine containing phospholipids in the rat nervous system reveals temporo-spatial gradients', *J Neurochem*, 114: 1119-34.

Lohofer, F., L. Hoffmann, R. Buchholz, K. Huber, A. Glinzer, K. Kosanke, A. Feuchtinger, M. Aichler, B. Feuerecker, G. Kaissis, E. J. Rummeny, C. Holtke, C. Faber, F. Schilling, R. M. Botnar, A. K. Walch, U. Karst, and M. Wildgruber. 2018. 'Molecular imaging of myocardial infarction with Gadofluorine P - A combined magnetic resonance and mass spectrometry imaging approach', *Heliyon*, 4: e00606.

Lou, Xianwen, Joost L. J. van Dongen, Jef A. J. M. Vekemans, and E. W. Meijer. 2009. 'Matrix suppression and analyte suppression effects of quaternary ammonium salts in matrix-assisted laser desorption/ionization time-of-flight mass spectrometry: an investigation of suppression mechanism', *Rapid Communications in Mass Spectrometry*, 23: 3077-82.

Luo, G., Marginean, L., and Vertes, A. 2002. 'Internal energy of ions generated by matrix-assisted laser desorption/ionization', *Anal Chem*, 74: 6185-6190.

Luptakova, D., L. Baciak, T. Pluhacek, A. Skriba, B. Sediva, V. Havlicek, and I. Juranek. 2018. 'Membrane depolarization and aberrant lipid distributions in the neonatal rat brain following hypoxic-ischaemic insult', *Sci Rep*, 8: 6952.

Ma, Jingyun, Yachen Wang, and Jing Liu. 2018. 'Bioprinting of 3D tissues/organs combined with microfluidics', *RSC Advances*, 8: 21712-27.

Ma, Y. C., and H. Y. Kim. 1995. 'Development of the on-line high-performance liquid chromatography/thermospray mass spectrometry method for the analysis of phospholipid molecular species in rat brain', *Anal Biochem*, 226: 293-301.

Macfarlane, R. D., and D. F. Torgerson. 1976. 'Californium-252 Plasma Desorption Mass-Spectroscopy', *Science*, 191: 920-25.

Mamyrin, B.A., Karataev, V.I., Shmikk,D.V. and Zagulin V.A. 1973. 'The mass-reflectron, a new nonmagnetic time-of-flight mass spectrometer with high resolution', *Zh. Eksp. Teor. Fiz. (JETP)*, 64: 82-89.

March, R. E. 1997. 'An introduction to quadrupole ion trap mass spectrometry', *Journal of Mass Spectrometry*, 32: 351-69.

March, R. E., R. J. Hughes, and J. F. J. Todd. 1989. *Quadrupole Storage Mass Spectrometry* (Wiley).

Marshall, A. G., and C. L. Hendrickson. 2002. 'Fourier transform ion cyclotron resonance detection: principles and experimental configurations', *International Journal of Mass Spectrometry*, 215: 59-75.

Marshall, A. G., C. L. Hendrickson, and G. S. Jackson. 1998. 'Fourier transform ion cyclotron resonance mass spectrometry: A primer', *Mass Spectrometry Reviews*, 17: 1-35.

McCombie, Gregor, Dieter Staab, Markus Stoeckli, and Richard Knochenmuss. 2005. 'Spatial and Spectral Correlations in MALDI Mass Spectrometry Images by Clustering and Multivariate Analysis', *Analytical Chemistry*, 77: 6118-24.

McDonnell, L. A., and R. M. Heeren. 2007. 'Imaging mass spectrometry', *Mass Spectrom Rev*, 26: 606-43.

McKeown, Martin J., Lars Kai Hansen, and Terrence J. Sejnowski. 2003. 'Independent component analysis of functional MRI: what is signal and what is noise?', *Current Opinion in Neurobiology*, 13: 620-29.

Menzel, C., K. Dreisewerd, S. Berkenkamp, and F. Hillenkamp. 2002. 'The role of the laser pulse duration in infrared matrix-assisted laser desorption/ionization mass spectrometry', *Journal of The American Society for Mass Spectrometry*, 13: 975-84.

Miller, J.N., and J.C. Miller. 2010. *Statistics and chemometrics for analitical chemistry* (Pearson).

Mohammadi, A. S., N. T. Phan, J. S. Fletcher, and A. G. Ewing. 2016. 'Intact lipid imaging of mouse brain samples: MALDI, nanoparticle-laser desorption ionization, and 40 keV argon cluster secondary ion mass spectrometry', *Anal Bioanal Chem*, 408: 6857-68.

Morrical, B. D., D. P. Fergenson, and K. A. Prather. 1998. 'Coupling two-step laser desorption/ionization with aerosol time-of-flight mass spectrometry for the analysis of individual organic particles', *Journal of The American Society for Mass Spectrometry*, 9: 1068-73.

Mu, Yangling, and Fred H. Gage. 2011. 'Adult hippocampal neurogenesis and its role in Alzheimer's disease', *Molecular Neurodegeneration*, 6: 85-85.

Müller, Matthias, Jürgen Schiller, Marijana Petković, Wolf Oehrl, Regina Heinze, Reinhard Wetzker, Klaus Arnold, and Jürgen Arnhold. 2001. 'Limits for the detection of (poly-)phosphoinositides by matrix-assisted laser desorption and ionization time-of-flight mass spectrometry (MALDI-TOF MS)', *Chemistry and Physics of Lipids*, 110: 151-64.

Münzenberg, G. 2013. 'Development of mass spectrometers from Thomson and Aston to present', *International Journal of Mass Spectrometry*, 349: 9-18.

Murphy, R. C., J. A. Hankin, and R. M. Barkley. 2009. 'Imaging of lipid species by MALDI mass spectrometry', *J Lipid Res*, 50 Suppl: S317-22.

Murphy, Robert C., and Alfred H. Merrill Jr. 2011. 'Lipidomics and Imaging Mass Spectrometry', *Biochimica et Biophysica Acta (BBA) - Molecular and Cell Biology of Lipids*, 1811: 635-36.

Nagornov, K. O., M. V. Gorshkov, A. N. Kozhinov, and Y. O. Tsybin. 2014. 'High-Resolution Fourier Transform Ion Cyclotron Resonance Mass Spectrometry with Increased Throughput for Biomolecular Analysis', *Analytical Chemistry*, 86: 9020-28.

Nemes, P., and A. Vertes. 2007. 'Laser ablation electrospray ionization for atmospheric pressure, in vivo, and imaging mass spectrometry', *Anal Chem*, 79: 8098-106.

Nicolaou, N., Y. Xu, and R. Goodacre. 2011. 'MALDI-MS and multivariate analysis for the detection and quantification of different milk species', *Anal Bioanal Chem*, 399: 3491-502.

O'Brien, J. S., and E. L. Sampson. 1965. 'Lipid composition of the normal human brain: gray matter, white matter, and myelin', *J Lipid Res*, 6: 537-44.

O'Connor, Peter B., and Franz Hillenkamp. 2007. 'MALDI Mass Spectrometry Instrumentation.' in, *MALDI MS* (Wiley-VCH Verlag GmbH & Co. KGaA).

Ozawa, T., I. Osaka, T. Ihozaki, S. Hamada, Y. Kuroda, T. Murakami, A. Miyazato, H. Kawasaki, and R. Arakawa. 2015. 'Simultaneous detection of phosphatidylcholines and glycerolipids using matrix-enhanced surface-assisted laser desorption/ionization-mass spectrometry with sputter-deposited platinum film', *J Mass Spectrom*, 50: 1264-9.

Pacey, D.J. 1976. 'A simple linear scanning system for sector field mass spectrometers', *Journal of Physics E: Scientific Instruments*, 9: 1050-51.

Parry, R. Mitchell, AsiriS Galhena, ChamindaM Gamage, RachelV Bennett, MayD Wang, and FacundoM Fernández. 2013. 'OmniSpect: An Open MATLAB-Based Tool for Visualization and Analysis of Matrix-Assisted Laser Desorption/Ionization and Desorption Electrospray Ionization Mass Spectrometry Images', *Journal of The American Society for Mass Spectrometry*, 24: 646-49.

Passarelli, M. K., and A. G. Ewing. 2013. 'Single-cell imaging mass spectrometry', *Curr Opin Chem Biol*, 17: 854-9.

Paul, W., and H. Steinwedel. 1953. 'A new mass spectrometer without a magnetic field', *Zeitschrift fuer Naturforschung (West Germany) Divided into Z. Nautrforsch., A, and Z. Naturforsch., B: Anorg. Chem., Org. Chem., Biochem., Biophys.*, 8.

Paul, W., and H. Steinwedel. 1960. 'Apparatus for separating charged particles of different specific charges', *German patent*, 944: 19-56.

Paxinos, G. and Watson, C. 1986. *The rat brain in stereotaxic coordinates*. 2nd edition (Academic Press).

Paxinos, G., and Watson, C. 2006. *The Rat Brain in Stereotaxic Coordinates: Hard Cover Edition* (Elsevier Science).

Payne, A. H., and G. L. Glish. 2005. 'Tandem mass spectrometry in quadrupole ion trap and ion cyclotron resonance mass spectrometers', *Methods Enzymol*, 402: 109-48.

Pedder, Randall E., Dennis Lynch, and Jian Wei. 1999. 'Optimizing Quadrupole Transmission for Wide Mass Range to 10,000 amu', *Extrel CMS*.

Perez, V., A. Suarez-Vega, M. Fuertes, J. Benavides, L. Delgado, M. C. Ferreras, and J. J. Arranz. 2013. 'Hereditary lissencephaly and cerebellar hypoplasia in Churra lambs', *BMC Vet Res*, 9: 156.

Perry, R. H., R. G. Cooks, and R. J. Noll. 2008. 'Orbitrap Mass Spectrometry: Instrumentation, Ion Motion and Applications', *Mass Spectrometry Reviews*, 27: 661-99.

Peterson, D. S. 2007. 'Matrix-free methods for laser desorption/ionization mass spectrometry', *Mass Spectrom Rev*, 26: 19-34.

Phelps, D. L., J. Balog, L. F. Gildea, Z. Bodai, A. Savage, M. A. El-Bahrawy, A. V. Speller, F. Rosini, H. Kudo, J. S. McKenzie, R. Brown, Z. Takats, and S. Ghaem-Maghami. 2018. 'The surgical intelligent knife distinguishes normal, borderline and malignant gynaecological tissues using rapid evaporative ionisation mass spectrometry (REIMS)', *Br J Cancer*, 118: 1349-58.

Picariello, Gianluca, Raffaele Sacchi, and Francesco Addeo. 2007. 'One-step characterization of triacylglycerols from animal fat by MALDI-TOF MS', *European Journal of Lipid Science and Technology*, 109: 511-24.

Piehowski, P. D., A. M. Davey, M. E. Kurczy, E. D. Sheets, N. Winograd, A. G. Ewing, and M. L. Heien. 2009. 'Time-of-flight secondary ion mass spectrometry imaging of subcellular lipid heterogeneity: Poisson counting and spatial resolution', *Anal Chem*, 81: 5593-602.

Pirman, David A., Ekem Efuet, Xiao-Ping Ding, Yong Pan, Lin Tan, Susan M. Fischer, Raymond N. DuBois, and Peiying Yang. 2013. 'Changes in Cancer Cell Metabolism Revealed by Direct Sample Analysis with MALDI Mass Spectrometry', *PLoS ONE*, 8: e61379.

Plumbley, M. D. 2003. 'Algorithms for nonnegative independent component analysis', *IEEE Trans Neural Netw*, 14: 534-43.

Plumbley, M. D., and E. Oja. 2004. 'A "nonnegative PCA" algorithm for independent component analysis', *IEEE Trans Neural Netw*, 15: 66-76.

Press, W.H., Teukolsky, S.A., Vetterling, W.T. and Flannery, B.P. 2009. *Numerical recipes in C (2nd ed.)* (Cambridge University Press, New York, NY, USA,).

Rayleigh, Lord. 1882. 'XX. On the equilibrium of liquid conducting masses charged with electricity', *Philosophical Magazine Series 5*, 14: 184-86.

Rinehart, K. L. 1982. 'Fast Atom Bombardment Mass-Spectrometry', *Science*, 218: 254-60.

Robichaud, G., K. P. Garrard, J. A. Barry, and D. C. Muddiman. 2013. 'MSiReader: an open-source interface to view and analyze high resolving power MS imaging files on Matlab platform', *J Am Soc Mass Spectrom*, 24: 718-21.

Rompp, A., and B. Spengler. 2013. 'Mass spectrometry imaging with high resolution in mass and space', *Histochemistry and Cell Biology*, 139: 759-83.

Ross, M. M., and R. J. Colton. 1983. 'Carbon as a Sample Substrate in Secondary Ion Mass-Spectrometry', *Analytical Chemistry*, 55: 150-53.

Ross, P. L., Y. L. N. Huang, J. N. Marchese, B. Williamson, K. Parker, S. Hattan, N. Khainovski, S. Pillai, S. Dey, S. Daniels, S. Purkayastha, P. Juhasz, S. Martin, M. Bartlet-Jones, F. He, A. Jacobson, and D. J. Pappin. 2004. 'Multiplexed protein quantitation in Saccharomyces cerevisiae using amine-reactive isobaric tagging reagents', *Molecular & Cellular Proteomics*, 3: 1154-69.

Rübel, Oliver, Annette Greiner, Shreyas Cholia, Katherine Louie, E. Wes Bethel, Trent R. Northen, and Benjamin P. Bowen. 2013. 'OpenMSI: A High-Performance Web-Based Platform for Mass Spectrometry Imaging', *Analytical Chemistry*, 85: 10354-61.

Sanders, M. E., E. C. Dias, B. J. Xu, J. A. Mobley, D. Billheimer, H. Roder, J. Grigorieva, M. Dowsett, C. L. Arteaga, and R. M. Caprioli. 2008. 'Differentiating proteomic biomarkers in breast cancer by laser capture microdissection and MALDI MS', *J Proteome Res*, 7: 1500-7.

Santos, Claudio R., and Almut Schulze. 2012. 'Lipid metabolism in cancer', *FEBS Journal*, 279: 2610-23.

Schiller, J., R. Suss, B. Fuchs, M. Muller, M. Petkovic, O. Zschornig, and H. Waschipky. 2007. 'The suitability of different DHB isomers as matrices for the MALDI-TOF

MS analysis of phospholipids: which isomer for what purpose?', *Eur Biophys J*, 36: 517-27.

Seeley, E. H., S. R. Oppenheimer, D. Mi, P. Chaurand, and R. M. Caprioli. 2008. 'Enhancement of protein sensitivity for MALDI imaging mass spectrometry after chemical treatment of tissue sections', *J Am Soc Mass Spectrom*, 19: 1069-77.

Shao, Changli, Yaping Tian, Zhennan Dong, Jing Gao, Yanhong Gao, Xingwang Jia, Guanghong Guo, Xinyu Wen, Chaoguang Jiang, and Xueji Zhang. 2012. 'The Use of Principal Component Analysis in MALDI-TOF MS: a Powerful Tool for Establishing a Mini-optimized Proteomic Profile', *American journal of biomedical sciences*, 4: 85-101.

Shi, Tao, and Steve Horvath. 2006. 'Unsupervised Learning With Random Forest Predictors', *Journal of Computational and Graphical Statistics*, 15: 118-38.

Shimadzu, Kratos Analytical Ltd. 2013. "MALDI Mass Spectrometer: MALDI-7090." In. https://shimadzu.com.au/system/files/Brochure%20-%20MALDI-7090%20-%20MO375.pdf [Accessed: 04-09-2018].

Sigma-Aldrich. 2018. "DHA structure." In. https://www.sigmaaldrich.com/catalog/product/sigma/d2534?lang=en&region=GB [Accessed: 03-09-2018].

Simons, Brigitte, Eva Duchoslav, Lyle Burton, and Ron Bonner. 2011. 'Molecular Characterization and Quantitation of Lipids with High Resolution Accurate Mass Tandem MS Techniques', *AB SCIEX, Framingham, MA*.

Sise, O., M. Ulu, and M. Dogan. 2005. 'Multi-element cylindrical electrostatic lens systems for focusing and controlling charged particles', *Nuclear Instruments & Methods in Physics Research Section a-Accelerators Spectrometers Detectors and Associated Equipment*, 554: 114-31.

Siy, Peter W., Richard A. Moffitt, R. Mitchell Parry, Yanfeng Chen, Ying Liu, M. Cameron Sullards, Alfred H. Merrill, Jr., and May D. Wang. 2008. 'Matrix Factorization Techniques for Analysis of Imaging Mass Spectrometry Data', *Proceedings. IEEE International Symposium on Bioinformatics and Bioengineering*, 2008: 10.1109/BIBE.2008.4696797.

Skoglund, T. S., R. Pascher, and C. H. Berthold. 1996. 'Heterogeneity in the columnar number of neurons in different neocortical areas in the rat', *Neurosci Lett*, 208: 97-100.

Smirnov, I. P., X. Zhu, T. Taylor, Y. Huang, P. Ross, I. A. Papayanopoulos, S. A. Martin, and D. J. Pappin. 2004. 'Suppression of α-Cyano-4-hydroxycinnamic Acid Matrix Clusters and Reduction of Chemical Noise in MALDI-TOF Mass Spectrometry', *Analytical Chemistry*, 76: 2958-65.

Soltwisch, J., and K. Dreisewerd. 2011. 'An ultraviolet/infrared matrix-assisted laser desorption ionization sample stage integrating scanning knife-edge and slit devices for laser beam analysis', *Rapid Communications in Mass Spectrometry*, 25: 1266-70.

Standford, Michael F. 2013. 'Mass Analyzers and MS/MS Methods.' in Charles H. Wick (ed.), *Identifying Microbes by Mass Spectrometry Proteomics* (CRC Press).

Stephens, W. E. 1946. 'A Pulsed Mass Spectrometer with Time Dispersion', *Physical Review*, 69: 691-91.

Steven, RoryT, and Josephine Bunch. 2013. 'Repeat MALDI MS imaging of a single tissue section using multiple matrices and tissue washes', *Analytical and Bioanalytical Chemistry*, 405: 4719-28.

Sugiura, Y., and M. Setou. 2009. 'Selective imaging of positively charged polar and nonpolar lipids by optimizing matrix solution composition', *Rapid Commun Mass Spectrom*, 23: 3269-78.

Sun, Y. 2009. *Field Detection Technologies for Explosives* (ILM Publications).

Szajli, E., T. Feher, and K. F. Medzihradszky. 2008. 'Investigating the quantitative nature of MALDI-TOF MS', *Molecular & Cellular Proteomics*, 7: 2410-8.

Takats, Z., J. M. Wiseman, B. Gologan, and R. G. Cooks. 2004. 'Mass spectrometry sampling under ambient conditions with desorption electrospray ionization', *Science*, 306: 471-3.

Tal'roze, V. L., and A. K. Ljubimova. 1998. 'Secondary Processes in the Ion Source of a Mass Spectrometer (Presented by academician N.N. Semenov 27 VIII 1952) (Reprinted from Report of the Soviet Academy of Sciences, vol 86, 1952)', *Journal of Mass Spectrometry*, 33: 502-04.

Tanaka K., Waki H., Ido Y., Akita S., Yoshida Y. and Yoshida T. 1988. "Protein and polymer analyses up to m/z 100 000 by laser ionization time-of-flight mass spectrometry." In *Rapid Communications in Mass Spectrometry*, 3.

Tar, P., and Thacker, N. 2018. 'The stability of probability mass function estimation for linear Poisson modelling', *Internal report, TINA memos*, 2018-006: University of Manchester.

Tar, P. D., R. Bugiolacchi, N. A. Thacker, J. D. Gilmour, and Team MoonZoo. 2017. 'Estimating False Positive Contamination in Crater Annotations from Citizen Science Data', *Earth, Moon, and Planets*, 119: 47-63.

Tar, P. D., N. A. Thacker, M. Babur, Y. Watson, S. Cheung, R. A. Little, R. G. Gieling, K. J. Williams, and J. P. B. O'Connor. 2018. 'A new method for the high-precision assessment of tumor changes in response to treatment', *Bioinformatics*, 34: 2625-33.

Tar, P. D., N. A. Thacker, J. D. Gilmour, and M. A. Jones. 2015. 'Automated quantitative measurements and associated error covariances for planetary image analysis', *Advances in Space Research*, 56: 92-105.

Tar, P.D. 2013. 'PhD thesis: Quantitative planetary image analysis via machine learning', *Internal report, TINA memos*, 2013-008: University of Manchester.

Tar, P.D., and Thacker, N.A. 2014. 'Linear Poisson models: a pattern recognition solution to the histogram composition problem', *Ann. BMVA*: 1-22.

Taylor, Adam J., Alex Dexter, and Josephine Bunch. 2018. 'Exploring Ion Suppression in Mass Spectrometry Imaging of a Heterogeneous Tissue', *Analytical Chemistry*, 90: 5637-45.

Taylor, Geoffrey. 1964. 'Disintegration of Water Drops in an Electric Field', *Proceedings of the Royal Society of London A: Mathematical, Physical and Engineering Sciences*, 280: 383-97.

Thacker, N. A., Deepaisarn, S., McMahon, A.W. 2016. 'Estimating noise models for arbitrary images', *Internal report, TINA memos*, 2016-009: University of Manchester.

Thacker, N. A., P. D. Tar, A. P. Seepujak, and J. D. Gilmour. 2018. 'The statistical properties of raw and preprocessed TOF mass spectra', *International Journal of Mass Spectrometry*, 428: 62-70.

Thomas S. A., Jin Y., Bunch J., and Gilmore I. S. 2017. "Enhancing classification of mass spectrometry imaging data with deep neural networks." In *2017 IEEE Symposium Series on Computational Intelligence (SSCI)*, 1-8.

Thompson, Andrew, Jürgen Schäfer, Karsten Kuhn, Stefan Kienle, Josef Schwarz, Günter Schmidt, Thomas Neumann, and Christian Hamon. 2003. 'Tandem Mass Tags: A Novel Quantification Strategy for Comparative Analysis of Complex Protein Mixtures by MS/MS', *Analytical Chemistry*, 75: 1895-904.

Thurstone, L.L. 1947. *Multiple-factor analysis* (University of Chicago Press, Chicago, USA).

Toga, A.W. 2015. *Brain Mapping: An Encyclopedic Reference* (Elsevier Science), p.138.

UFLDL, Tutorial. 'Multi-layer neural network'. http://ufldl.stanford.edu/tutorial/supervised/MultiLayerNeuralNetworks/ [Accessed: 07-08-2018].

Unwin, R. D. 2010. 'Quantification of proteins by iTRAQ', *Methods Mol Biol*, 658: 205-15.

van den Berg, Jorrit D. J., Nicoletta D. Vermist, Leslie Carlyle, Michal Holčapek, and Jaap J. Boon. 2004. 'Effects of traditional processing methods of linseed oil on the composition of its triacylglycerols', *Journal of Separation Science*, 27: 181-99.

van Meer, Gerrit, Dennis R. Voelker, and Gerald W. Feigenson. 2008. 'Membrane lipids: where they are and how they behave', *Nature reviews. Molecular cell biology*, 9: 112-24.

Veloso, Antonio, Roberto Fernández, Egoitz Astigarraga, Gabriel Barreda-Gómez, Iván Manuel, M. Teresa Giralt, Isidro Ferrer, Begoña Ochoa, Rafael Rodríguez-Puertas, and JoséA Fernández. 2011. 'Distribution of lipids in human brain', *Analytical and Bioanalytical Chemistry*, 401: 89-101.

Weickhardt, Christian, Friedrich Moritz, and Jürgen Grotemeyer. 1996. 'Time-of-flight mass spectrometry: State-of the-art in chemical analysis and molecular science', *Mass Spectrometry Reviews*, 15: 139-62.

Weinkauf, R., K. Walter, C. Weickhardt, U. Boesl, and E. W. Schlag. 1989. 'Laser Tandem Mass-Spectrometry in a Time of Flight Instrument', *Zeitschrift Fur Naturforschung Section a-a Journal of Physical Sciences*, 44: 1219-25.

Wells, J. M., and S. A. McLuckey. 2005. 'Collision-induced dissociation (CID) of peptides and proteins', *Methods Enzymol*, 402: 148-85.

Wenzel, Ryan J., A. Nazabal, and Renato Zenobi. 2006. "Comparison of Sensitivity and Saturation of MALDI-TOF Detectors for High-Mass Ions." In.

White, A. M., D. S. Daly, A. R. Willse, M. Protic, and D. P. Chandler. 2005. 'Automated microarray image analysis toolbox for MATLAB', *Bioinformatics*, 21: 3578-79.

Wien, K. 1999. '100 years of ion beams: Willy Wien's canal rays', *Brazilian Journal of Physics*, 29: 401-14.

Wiley, W. C., and I. H. McLaren. 1955. 'Time-of-Flight Mass Spectrometer with Improved Resolution', 26: 1150-57.

Wilkinson, W. R., A. I. Gusev, A. Proctor, M. Houalla, and D. M. Hercules. 1997. 'Selection of internal standards for quantitative analysis by matrix assisted laser desorption ionization (MALDI) time-of-flight mass spectrometry', *Fresenius Journal of Analytical Chemistry*, 357: 241-48.

Williams, Betsy, Shannon Cornett, Benoit Dawant, Anna Crecelius, Bobby Bodenheimer, and Richard Caprioli. 2005. "An algorithm for baseline correction of MALDI mass spectra." In *Proceedings of the 43rd annual Southeast regional conference - Volume 1*, 137-42. Kennesaw, Georgia: ACM.

Wolff, M. M., and W. E. Stephens. 1953. 'A Pulsed Mass Spectrometer with Time Dispersion', *Review of Scientific Instruments*, 24: 616-17.

Wu, Xinyun, Richard D. Oleschuk, and Natalie M. Cann. 2012. 'Characterization of microstructured fibre emitters: in pursuit of improved nano electrospray ionization performance', *Analyst*, 137: 4150-61.

Yamashita, M., and J. B. Fenn. 1984. 'Electrospray Ion-Source - Another Variation on the Free-Jet Theme', *Journal of Physical Chemistry*, 88: 4451-59.

Yang, C., Z. He, and W. Yu. 2009. 'Comparison of public peak detection algorithms for MALDI mass spectrometry data analysis', *BMC Bioinformatics*, 10: 4.

Yang, J. H., and R. M. Caprioli. 2011. 'Matrix Sublimation/Recrystallization for Imaging Proteins by Mass Spectrometry at High Spatial Resolution', *Analytical Chemistry*, 83: 5728-34.

Yao, J., S. Utsunomiya, S. Kajihara, T. Tabata, K. Aoshima, Y. Oda, and K. Tanaka. 2014. 'Peptide Peak Detection for Low Resolution MALDI-TOF Mass Spectrometry', *Mass Spectrom (Tokyo)*, 3: A0030.

Yost, R. A., and C. G. Enke. 1979. 'Triple Quadrupole Mass-Spectrometry for Direct Mixture Analysis and Structure Elucidation', *Analytical Chemistry*, 51: 1251-1264.

Zaima, Nobuhiro, Takahiro Hayasaka, Naoko Goto-Inoue, and Mitsutoshi Setou. 2010. 'Matrix-Assisted Laser Desorption/Ionization Imaging Mass Spectrometry', *International Journal of Molecular Sciences*, 11: 5040-55.

Zeleny, John. 1914. 'The Electrical Discharge from Liquid Points, and a Hydrostatic Method of Measuring the Electric Intensity at Their Surfaces', *Physical Review*, 3: 69-91.

Appendix A: Extracted ICA Component

Spectra of Binary Mixture Data Sets

Extracted ICA components (sub-spectra) for milk, lamb brain:liver and white:grey matter data sets are presented in Figures A.1, A.2 and A.3, respectively. They are in the form of probability mass functions which describe underlying signal generators within the mass spectra. Each component is stated as having characteristics of either of the underlying sample classes, e.g. of brain or liver for the brain:liver data set, etc., or contamination.

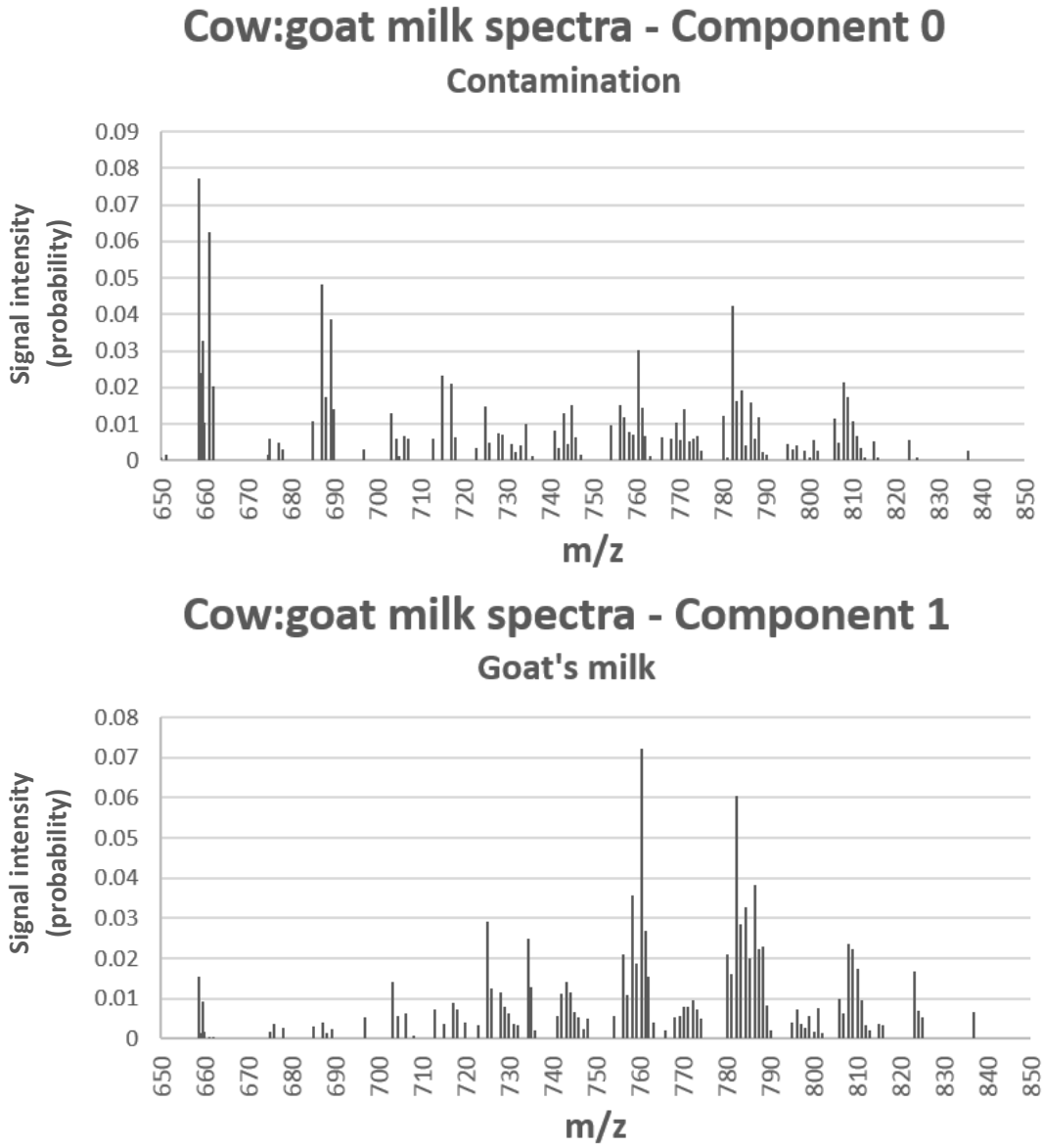

Figure A.1 Extracted ICA component spectra for the milk data set (Part 1 of 3)

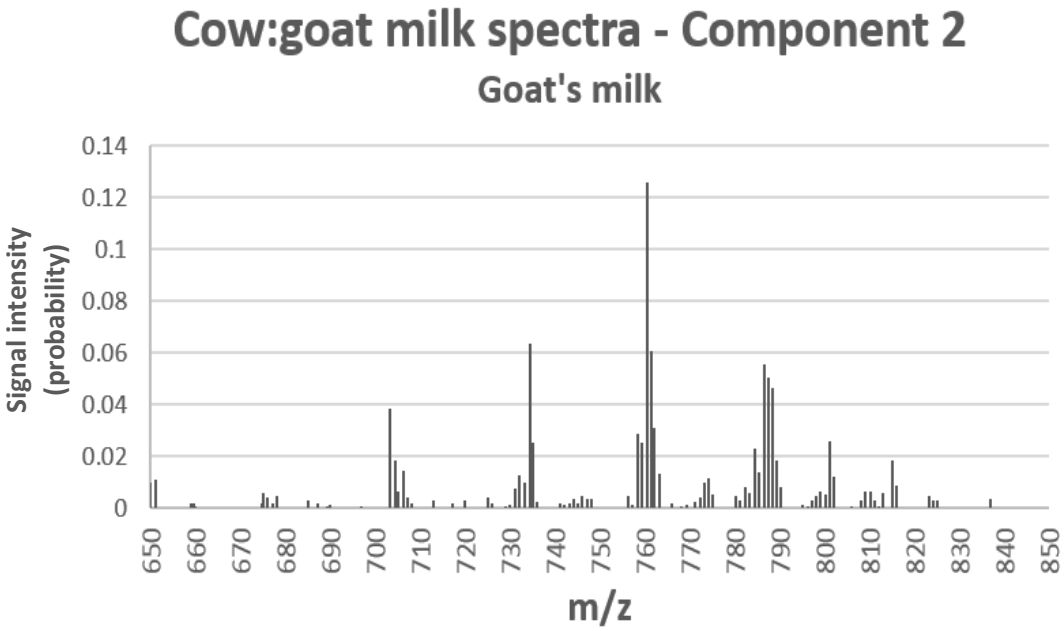

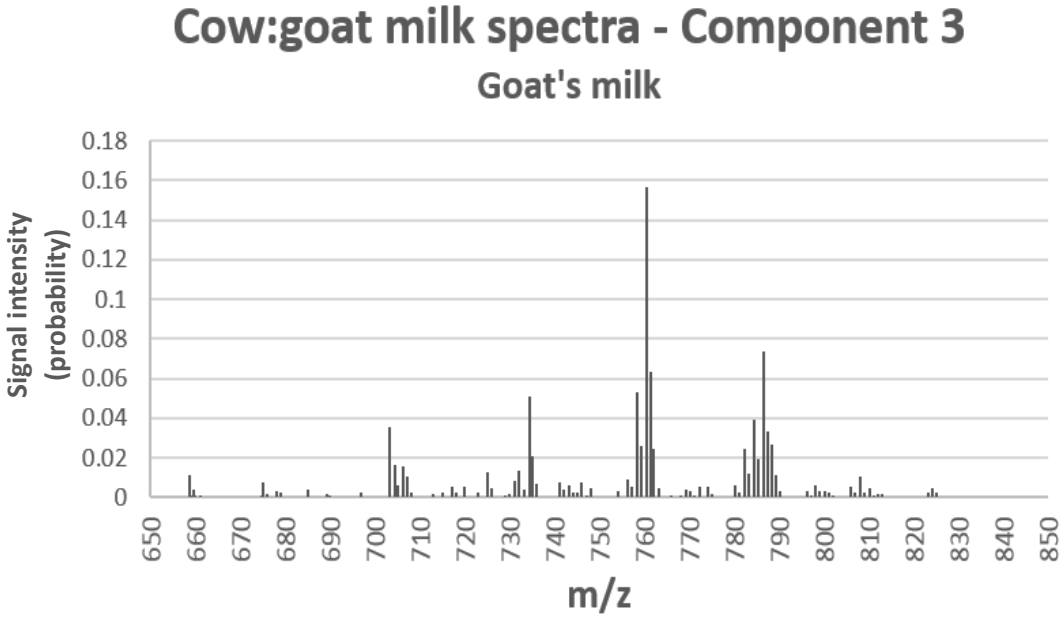

Figure A.1 Extracted ICA component spectra for the milk data set (Part 2 of 3)

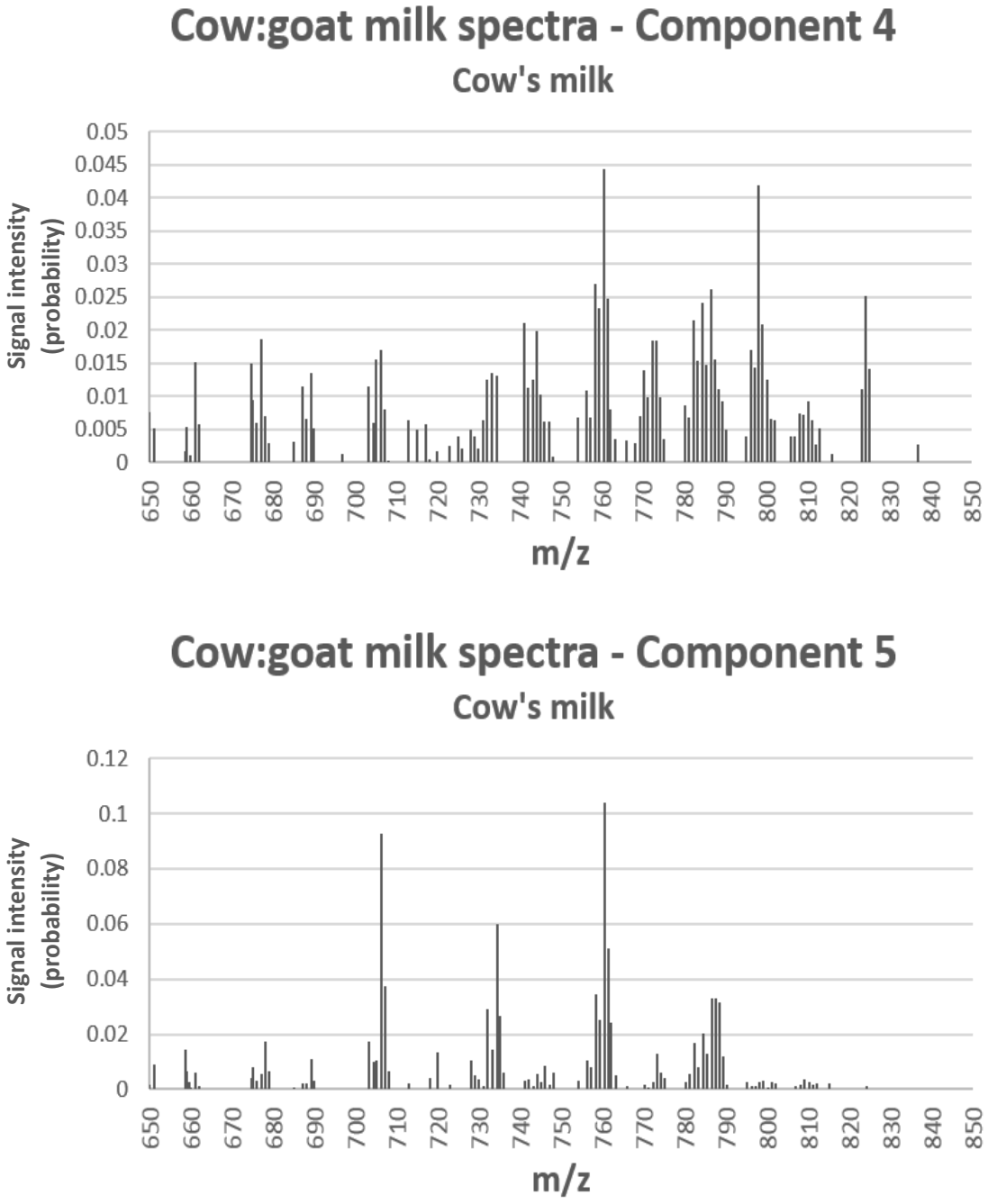

Figure A.1 Extracted ICA component spectra for the milk data set (Part 3 of 3)

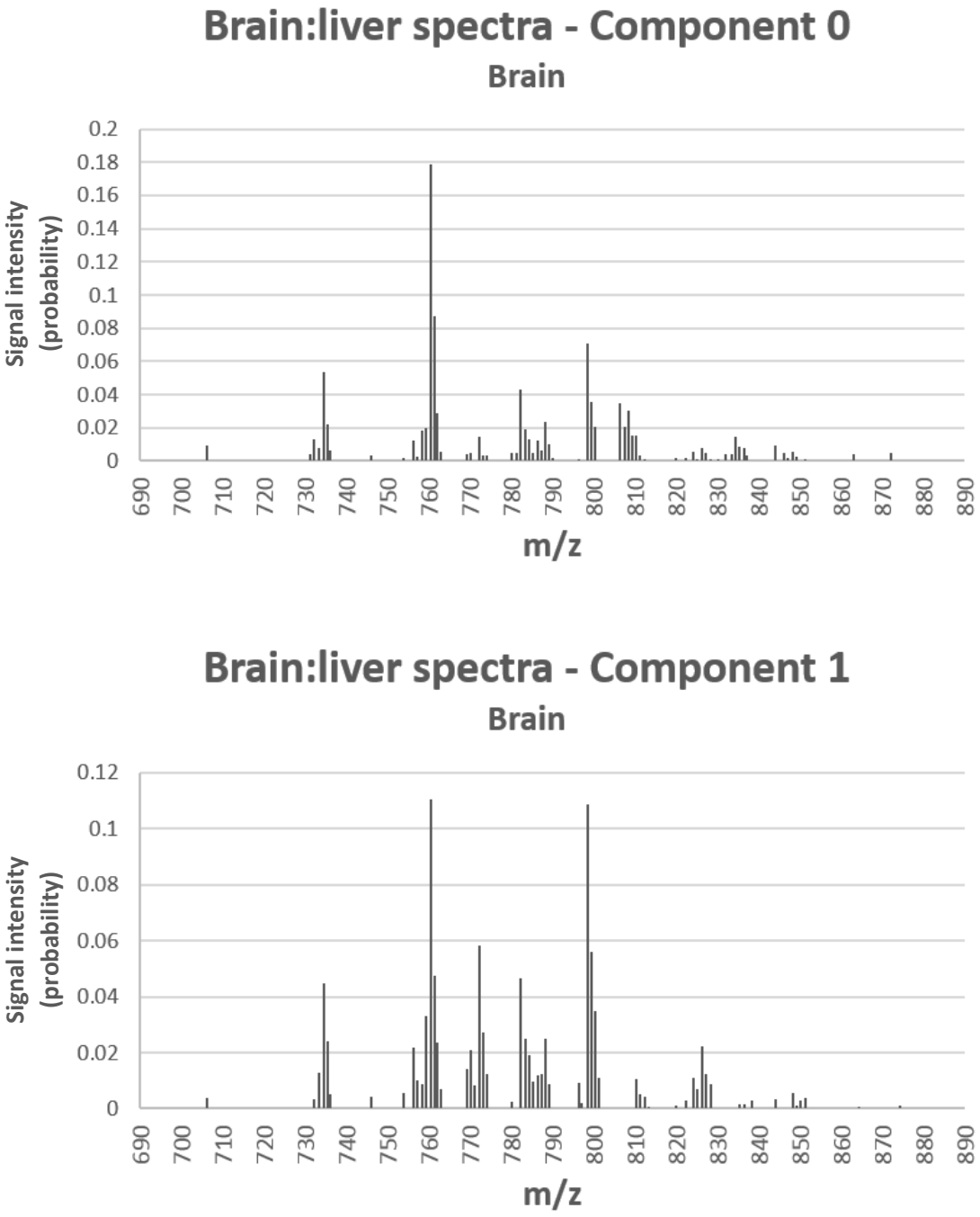

Figure A.2 Extracted ICA component spectra for the lamb brain:liver data set (Part 1 of 4)

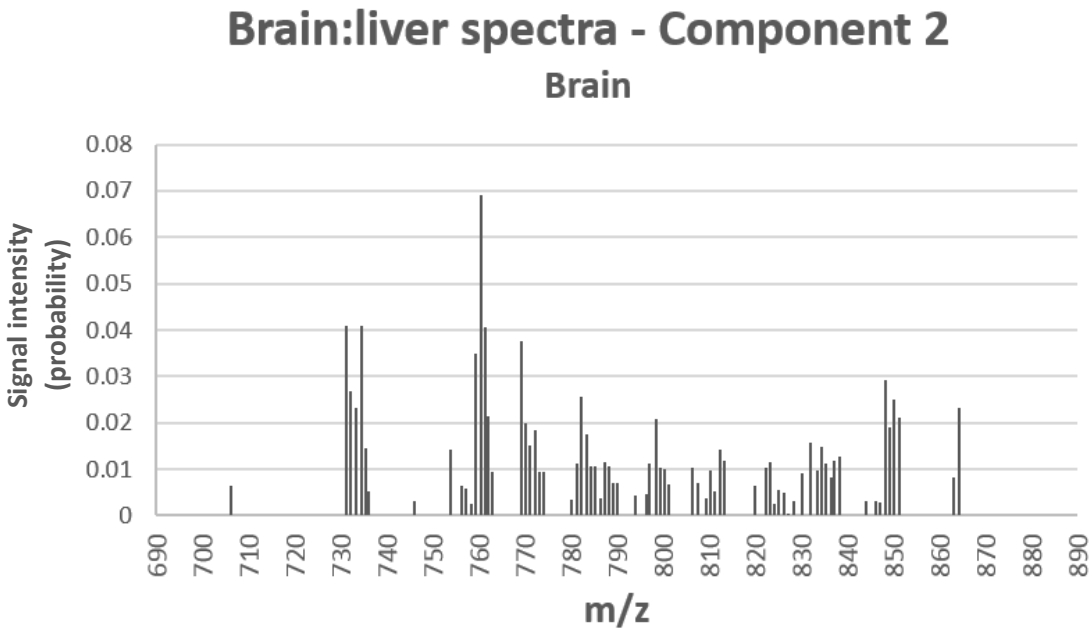

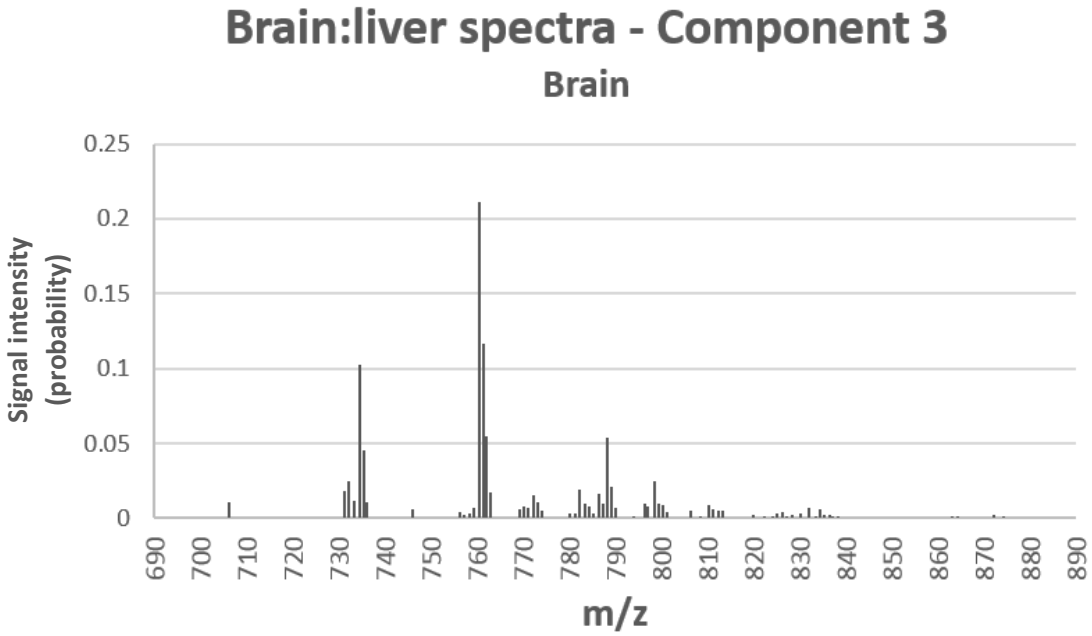

Figure A.2 Extracted ICA component spectra for the lamb brain:liver data set (Part 2 of 4)

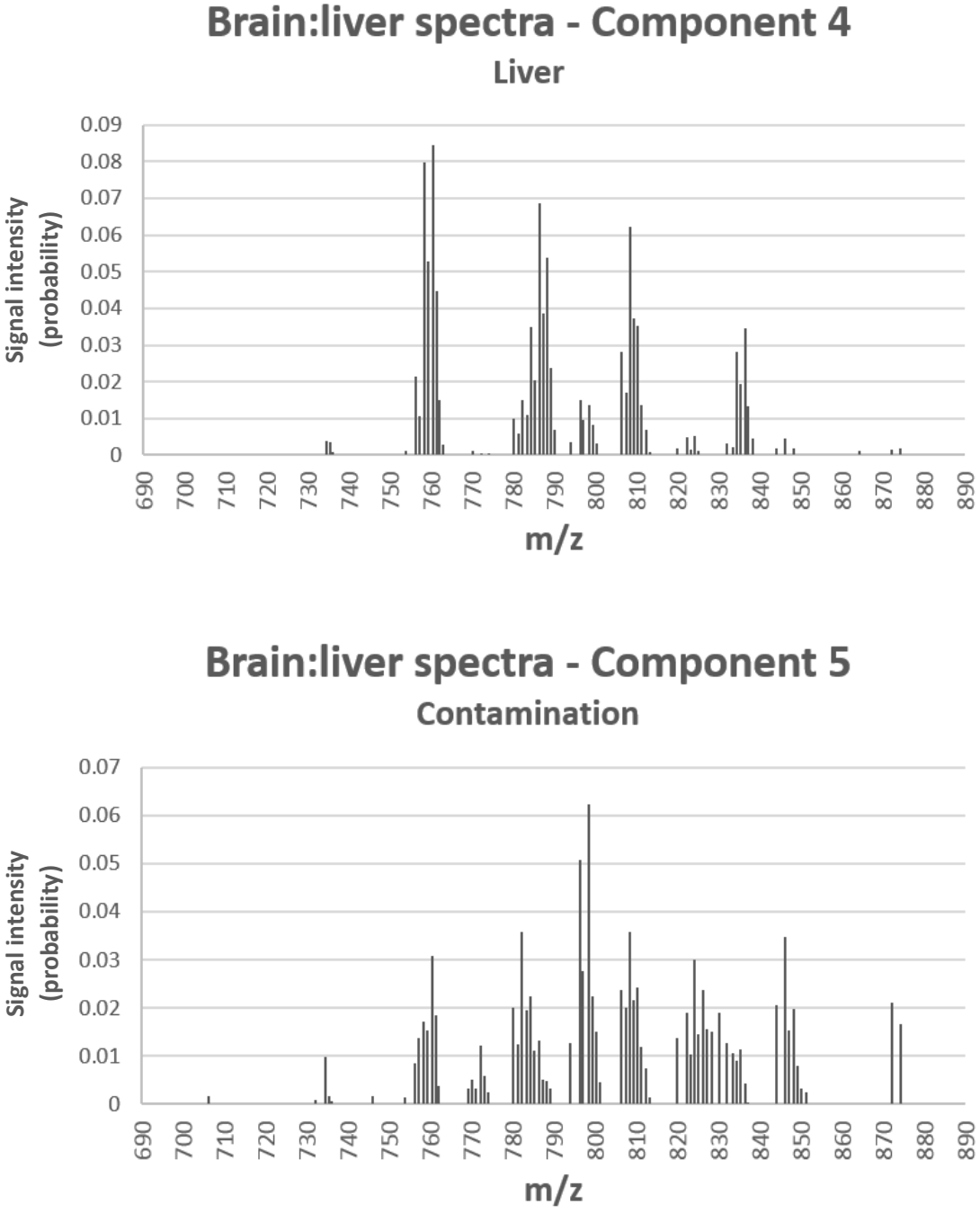

Figure A.2 Extracted ICA component spectra for the lamb brain:liver data set (Part 3 of 4)

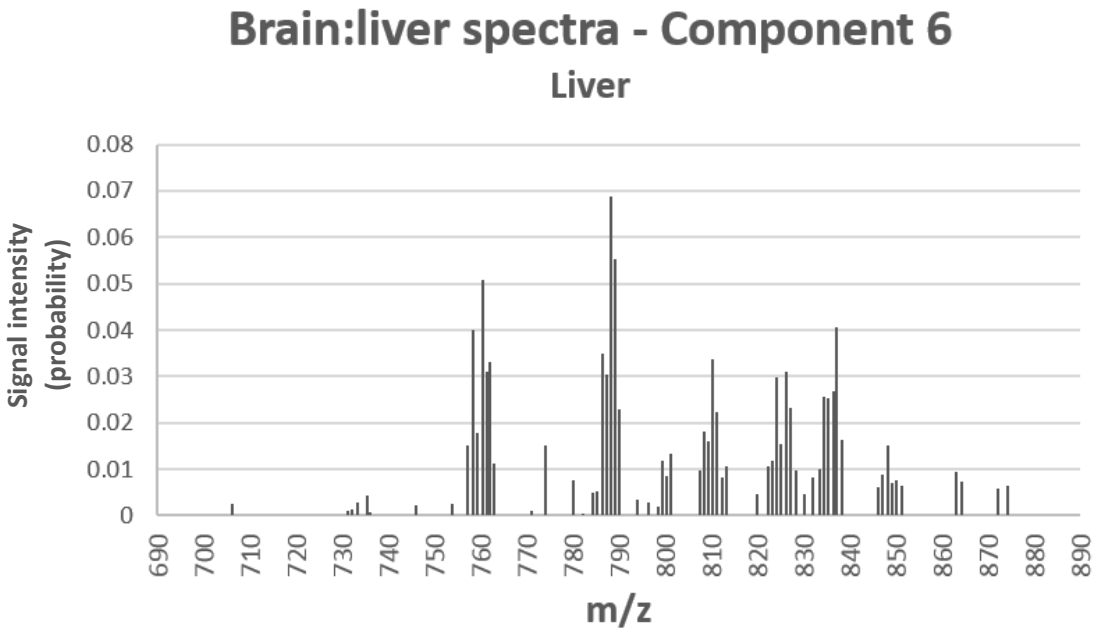

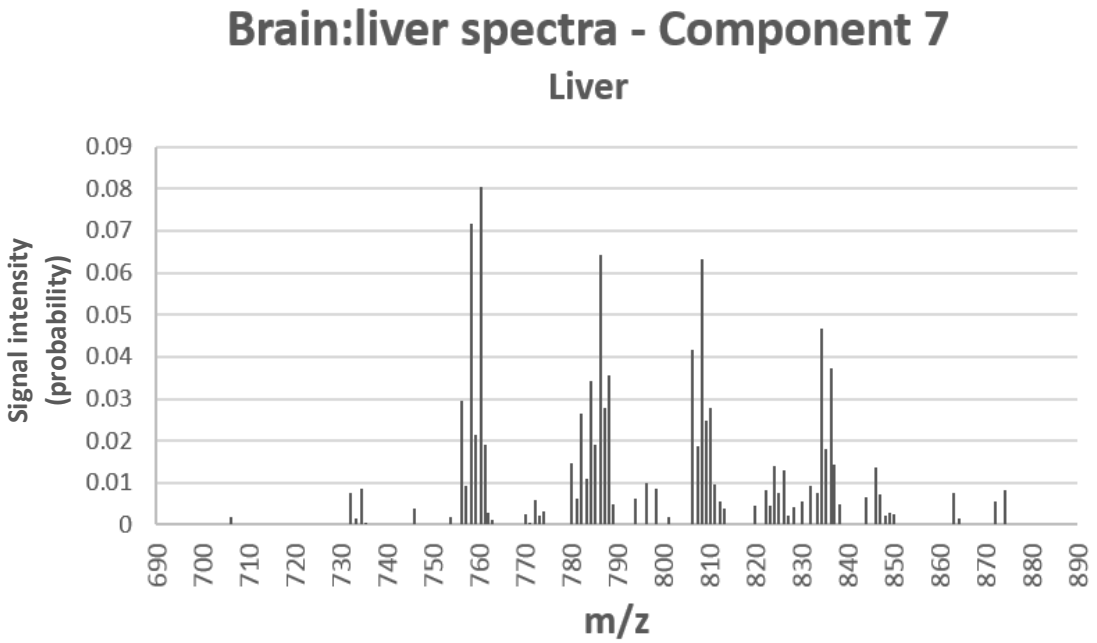

Figure A.2 Extracted ICA component spectra for the lamb brain:liver data set (Part 4 of 4)

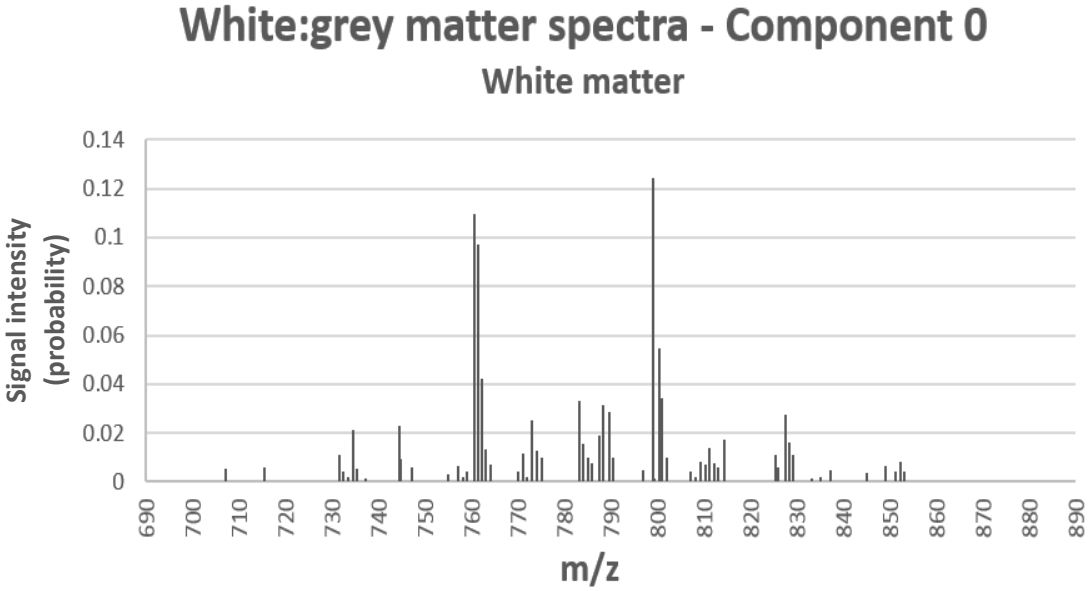

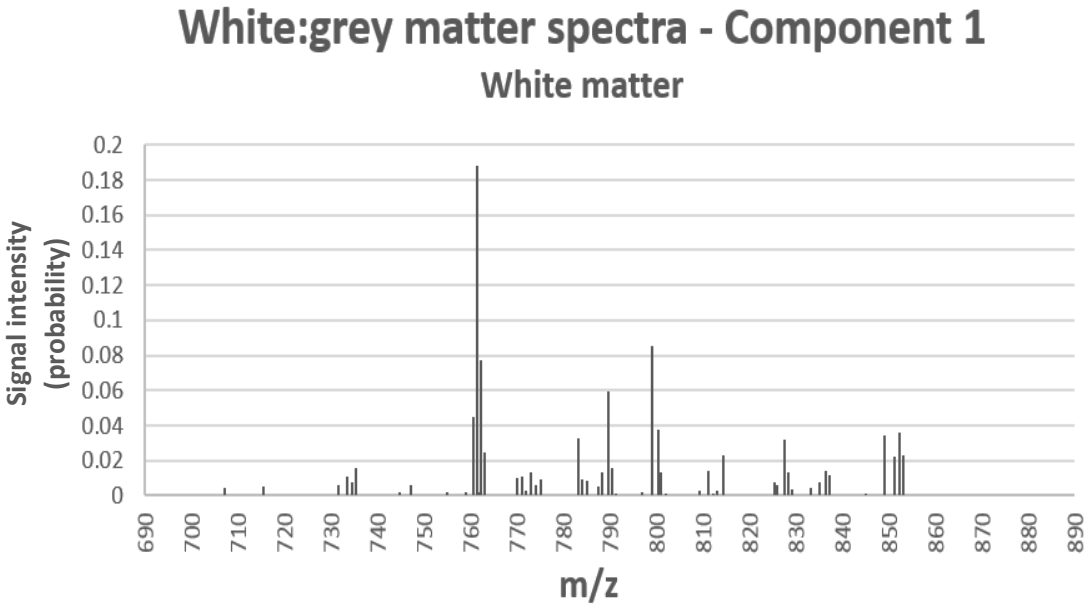

Figure A.3 Extracted ICA component spectra for the white:grey matter data set (Part 1 of 4)

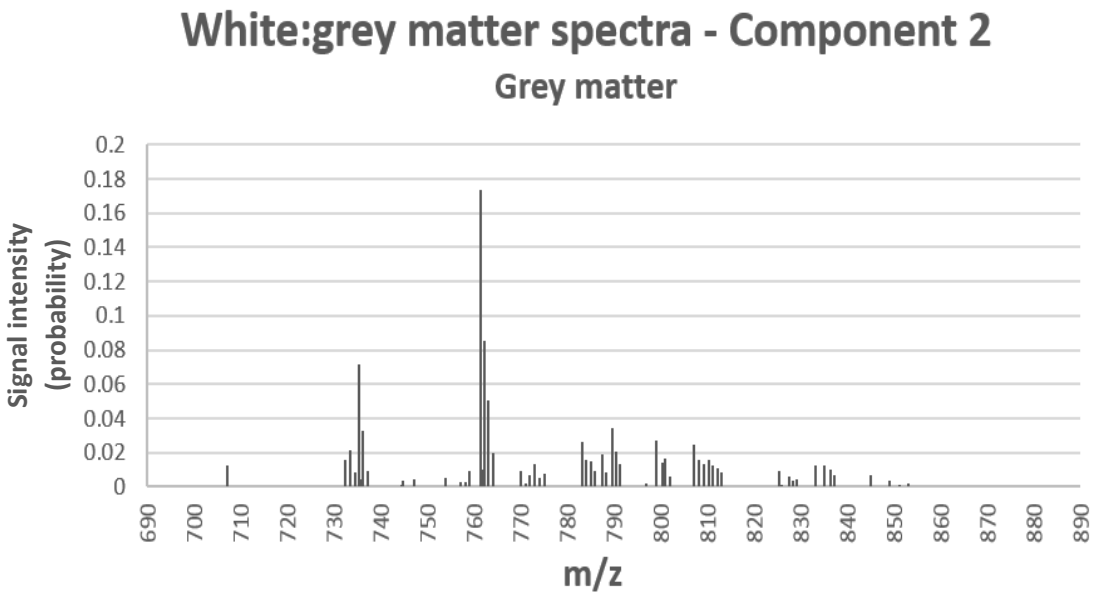

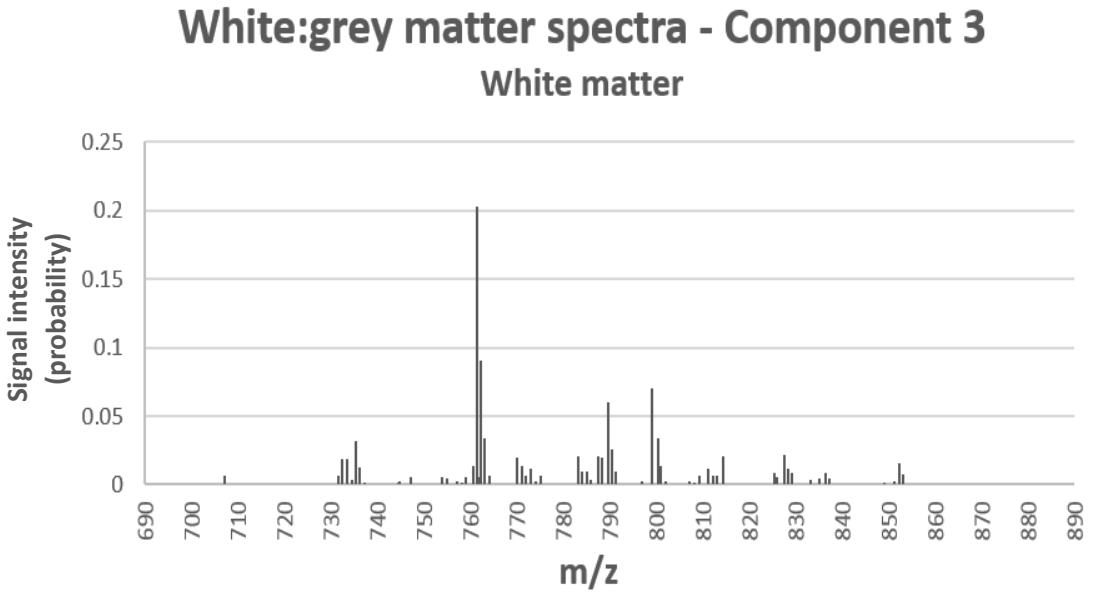

Figure A.3 Extracted ICA component spectra for the white:grey matter data set (Part 2 of 4)

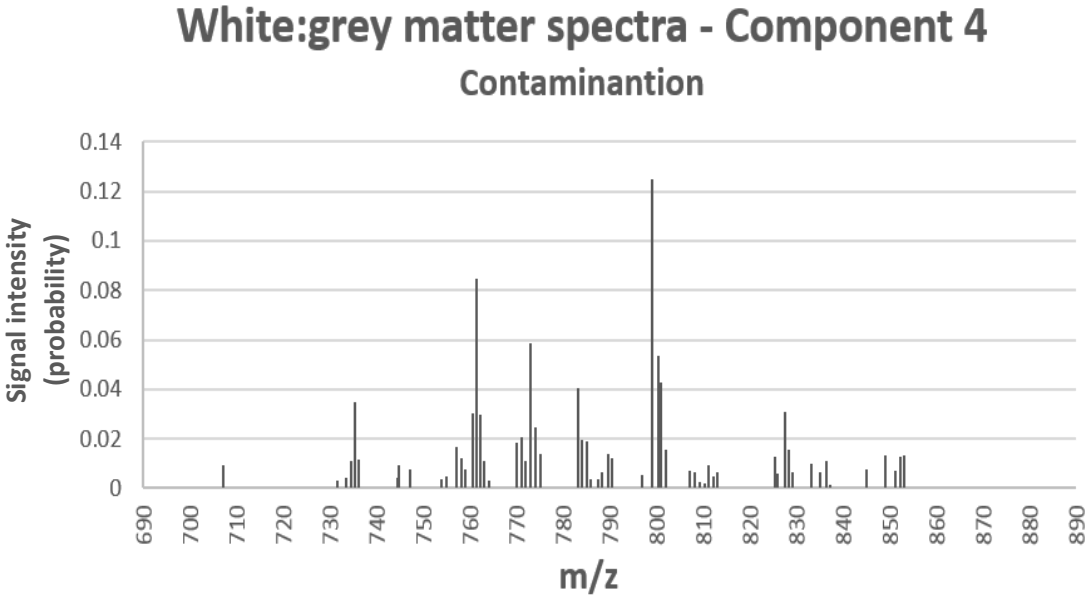

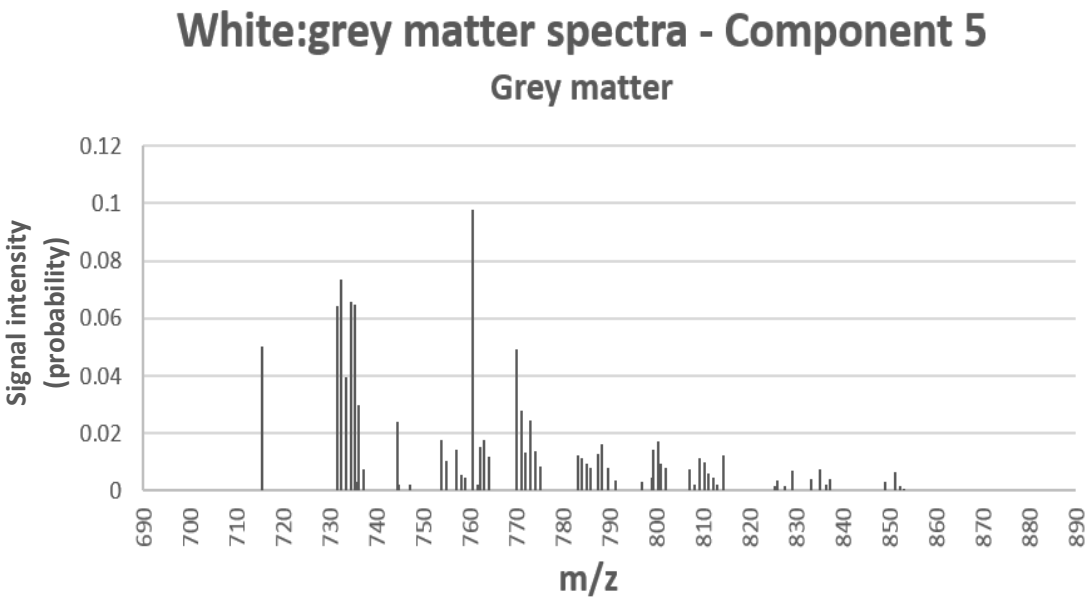

Figure A.3 Extracted ICA component spectra for the white:grey matter data set (Part 3 of 4)

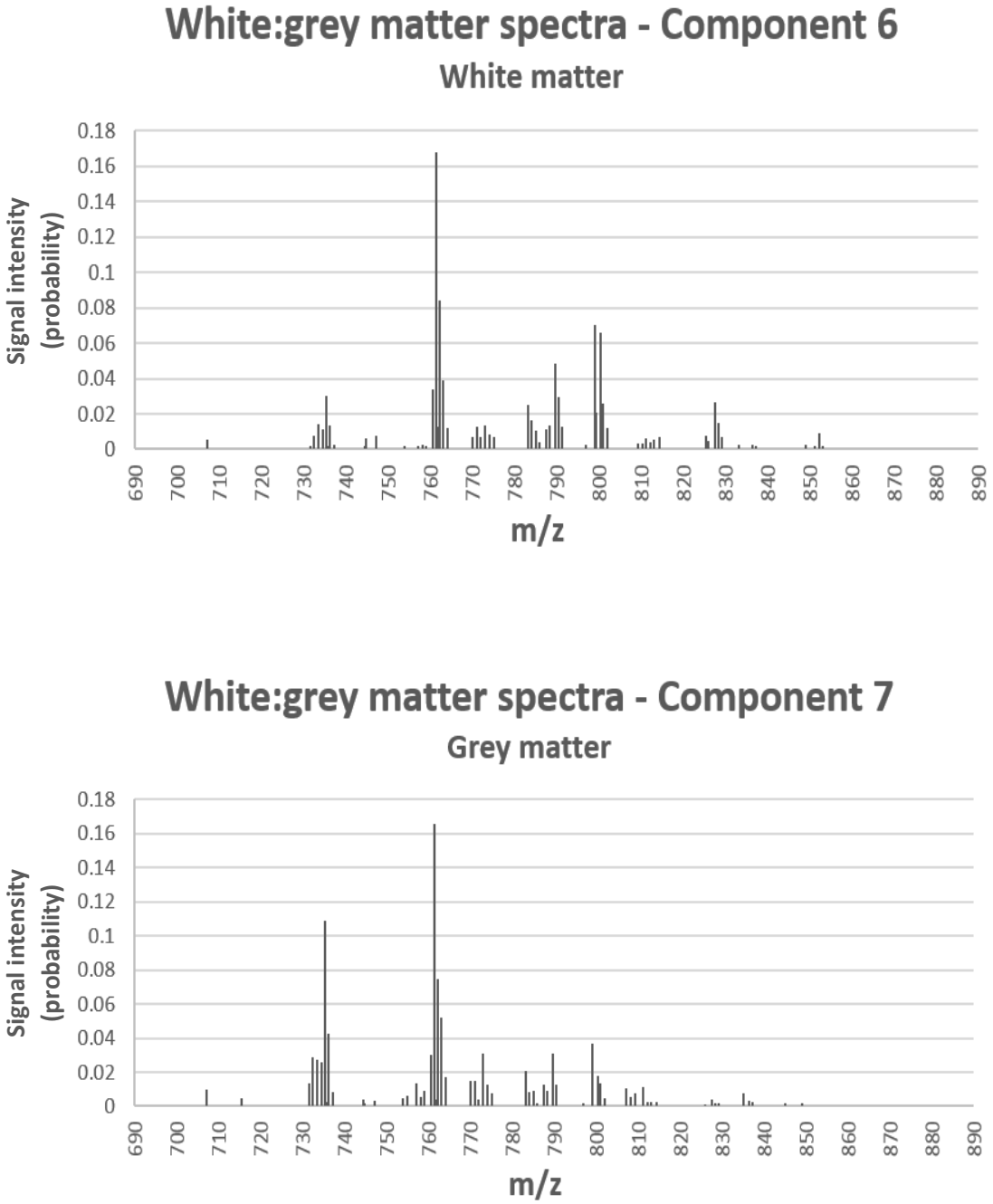

Figure A.3 Extracted ICA component spectra for the white:grey matter data set (Part 4 of 4)

Appendix B: Extracted ICA Components vs. Single Ion Distributions of the Image Data Set

B-1 Extracted ICA Components of the Image Data Set

Extracted ICA components (sub-spectra) for the rat brain MALDI-MS images of 8-, 16- and 24-component models are presented in Figures B.1, B.2 and B.3, respectively. The corresponding component distribution images are also shown at a corner of each component spectrum, plotted with a normalisation to the integral over all the components in the given model. The grey scale at the bottom of each image represents a relative weighting each component has to the total signal quantity. The 10 major peaks of each component spectrum are marked with green arrows, with their m/z values listed in the figures.

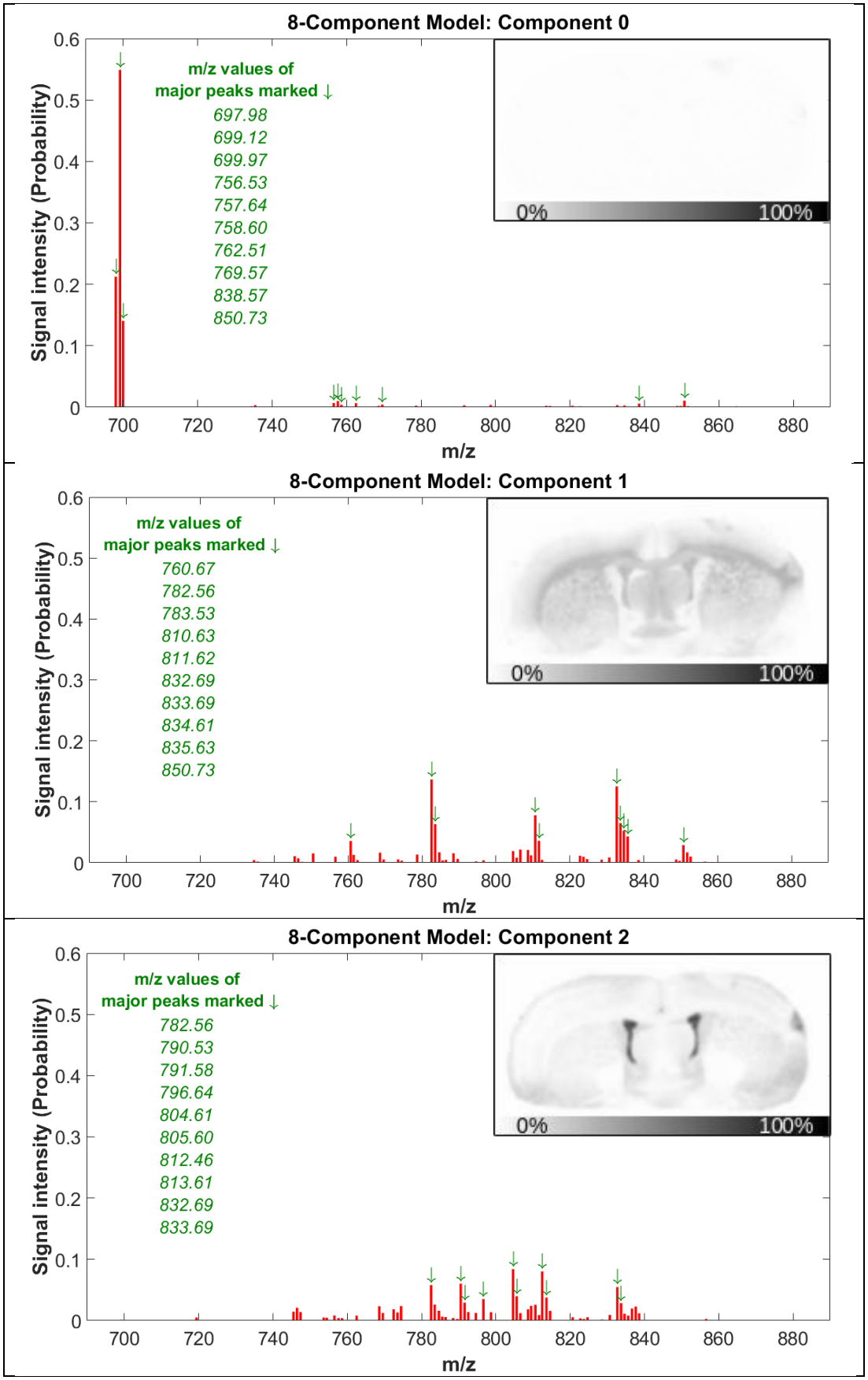

Figure B.1 Extracted ICA component spectra and images for the 8-component model of the rat brain MALDI image data with 10 major peaks marked with green arrows – their m/z values are listed in ascending order (Part 1 of 3)

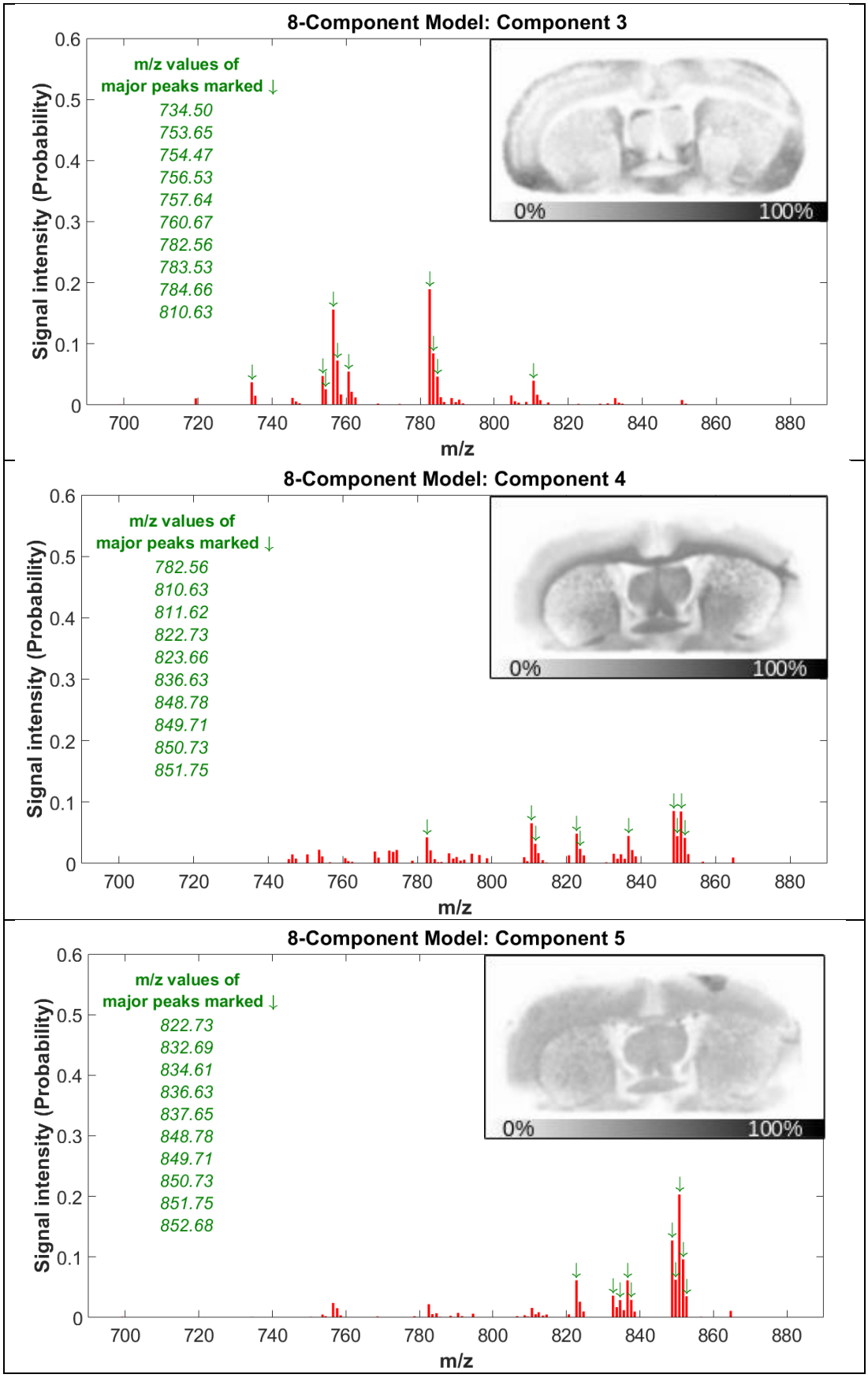

Figure B.1 Extracted ICA component spectra and images for the 8-component model of the rat brain MALDI image data with 10 major peaks marked with green arrows – their m/z values are listed in ascending order (Part 2 of 3)

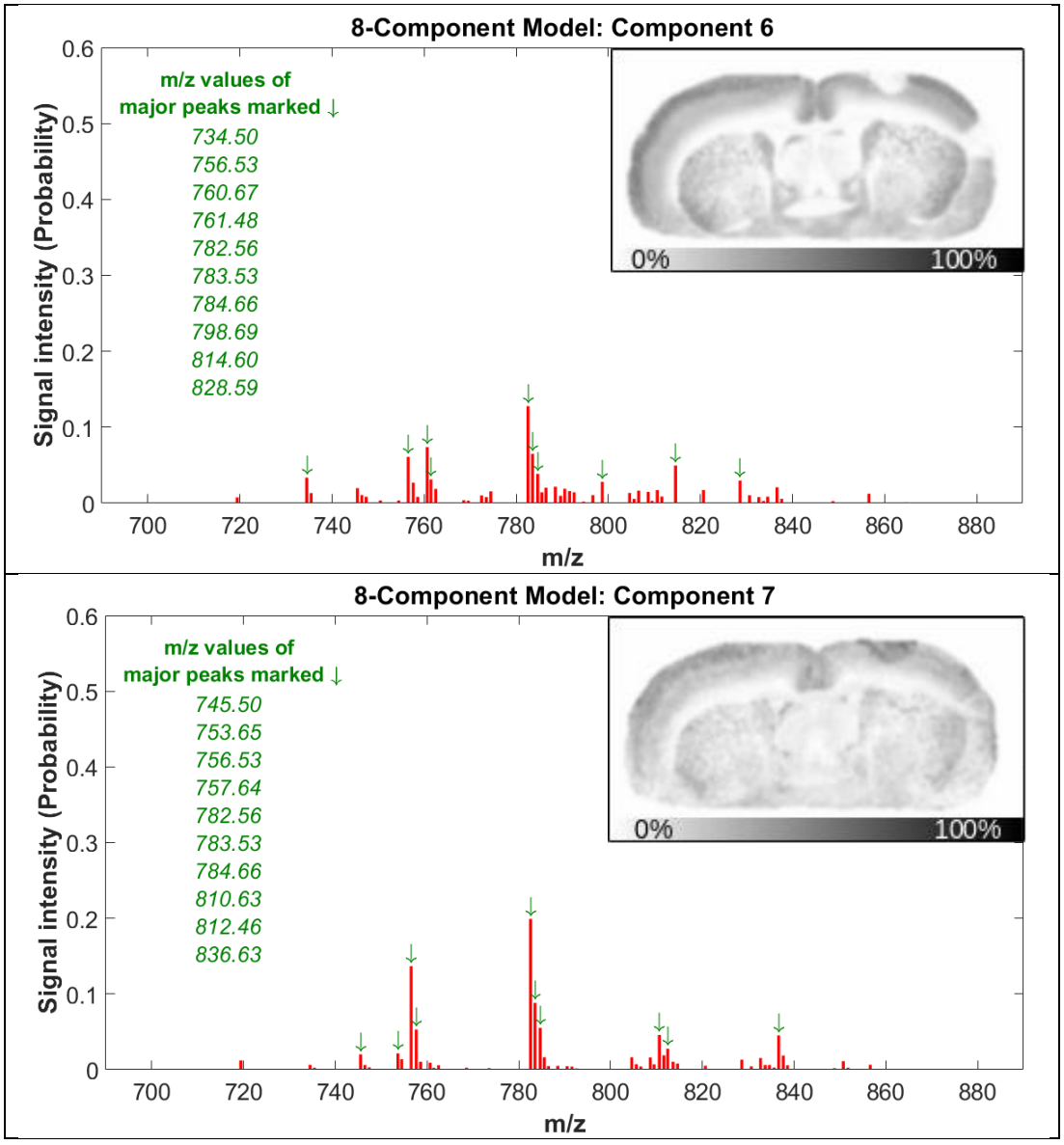

Figure B.1 Extracted ICA component spectra and images for the 8-component model of the rat brain MALDI image data with 10 major peaks marked with green arrows – their m/z values are listed in ascending order (Part 3 of 3)

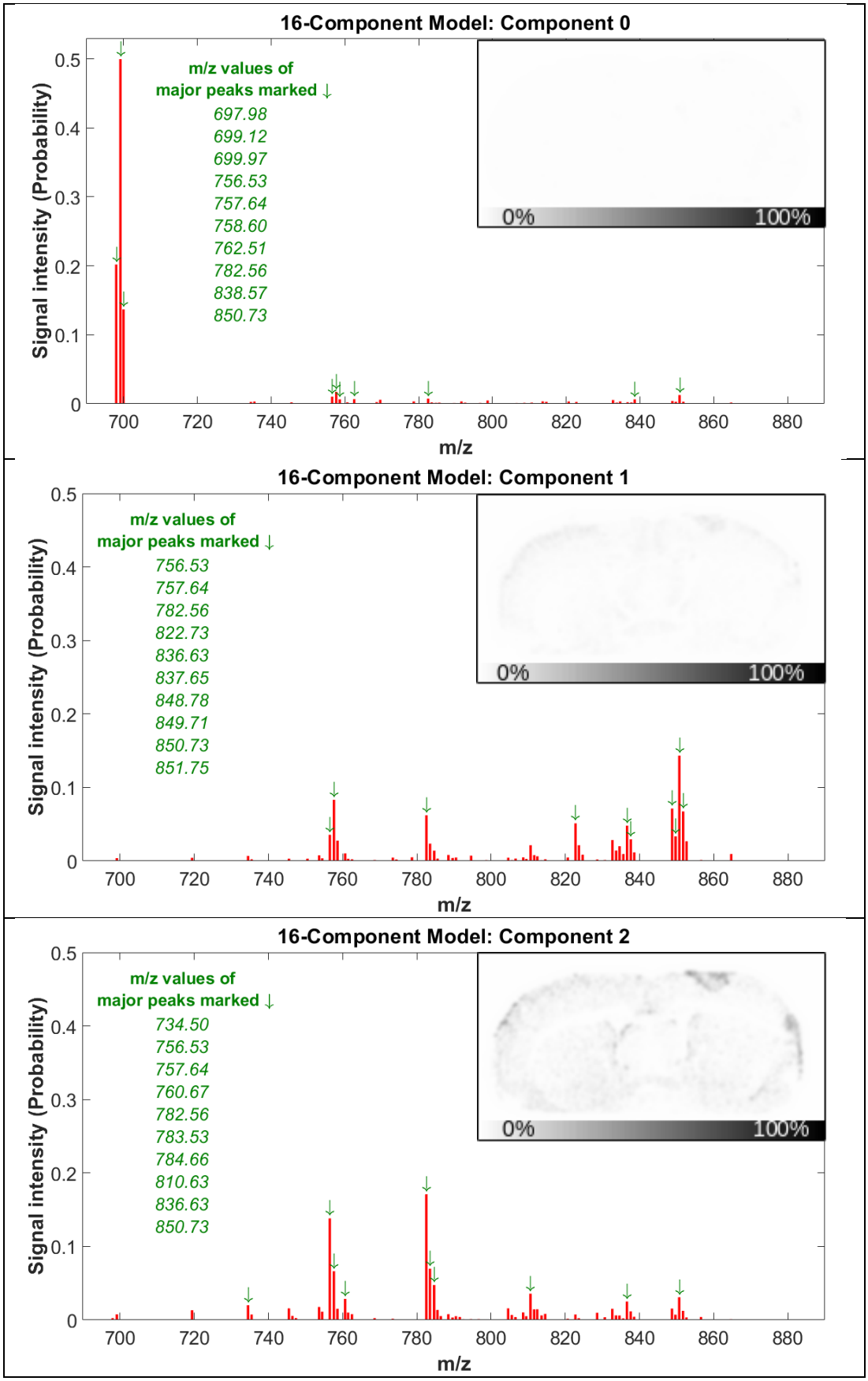

Figure B.2 Extracted ICA component spectra and images for the 16-component model of the rat brain MALDI image data with 10 major peaks marked with green arrows – their m/z values are listed in ascending order (Part 1 of 6)

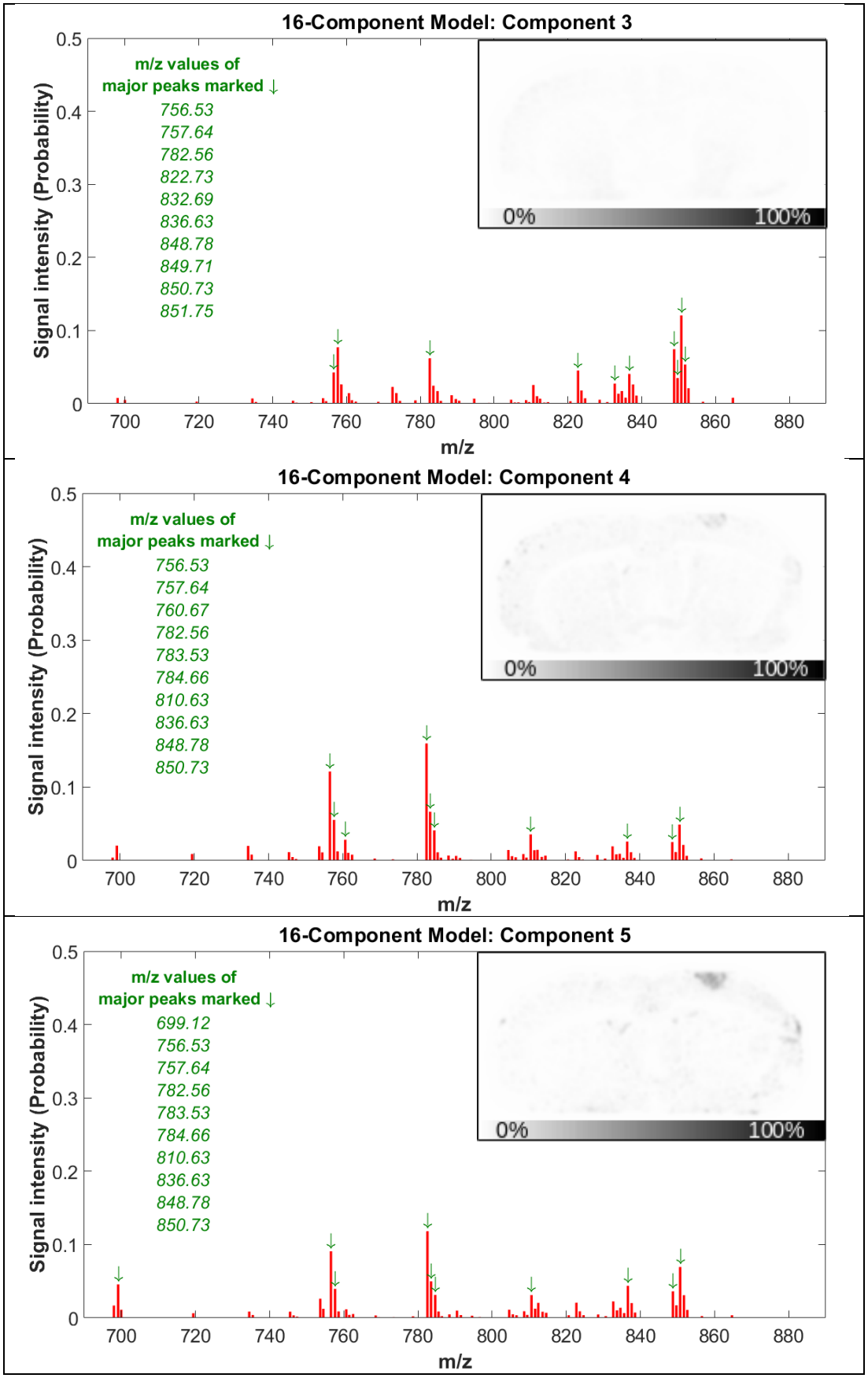

Figure B.2 Extracted ICA component spectra and images for the 16-component model of the rat brain MALDI image data with 10 major peaks marked with green arrows – their m/z values are listed in ascending order (Part 2 of 6)

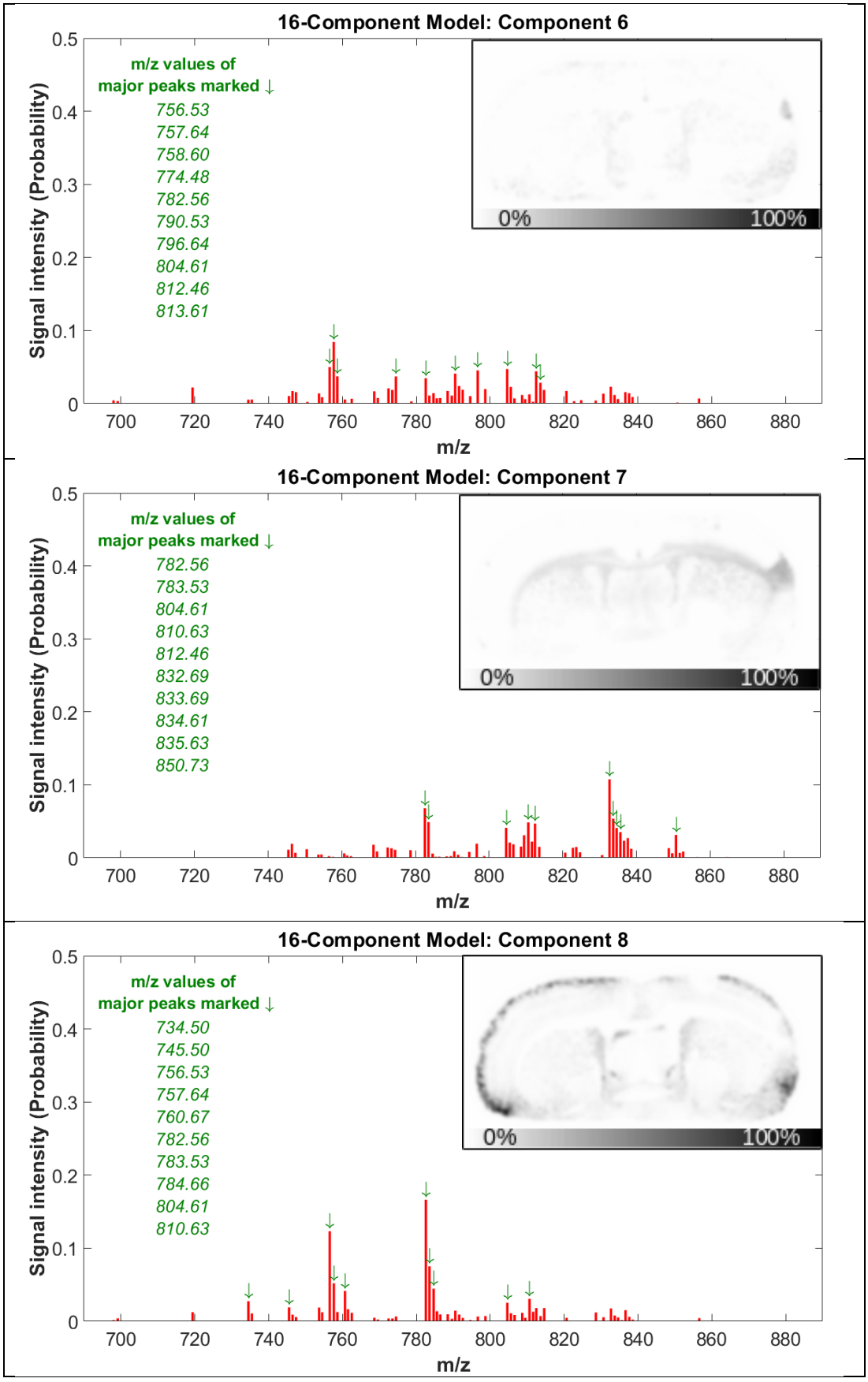

Figure B.2 Extracted ICA component spectra and images for the 16-component model of the rat brain MALDI image data with 10 major peaks marked with green arrows – their m/z values are listed in ascending order (Part 3 of 6)

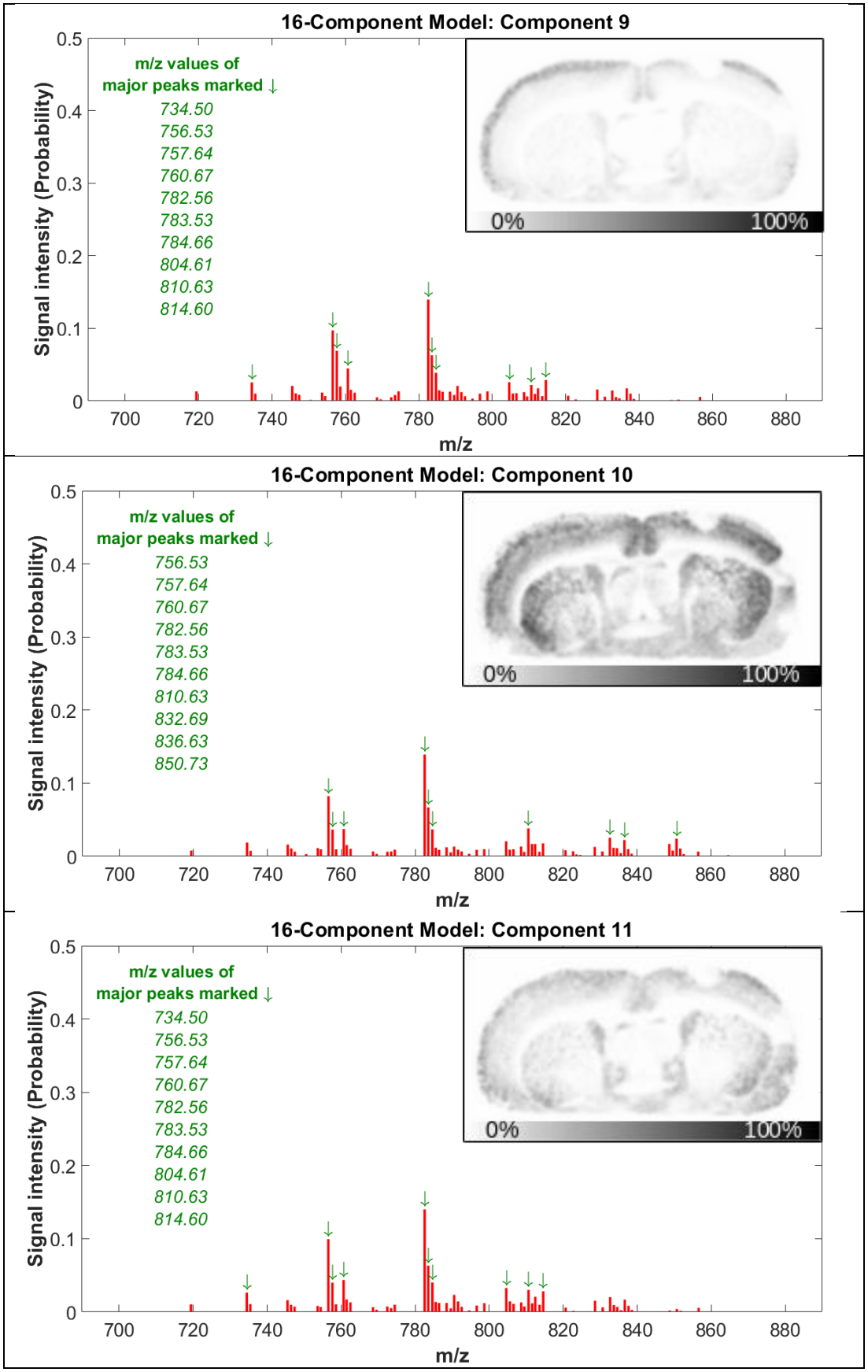

Figure B.2 Extracted ICA component spectra and images for the 16-component model of the rat brain MALDI image data with 10 major peaks marked with green arrows – their m/z values are listed in ascending order (Part 4 of 6)

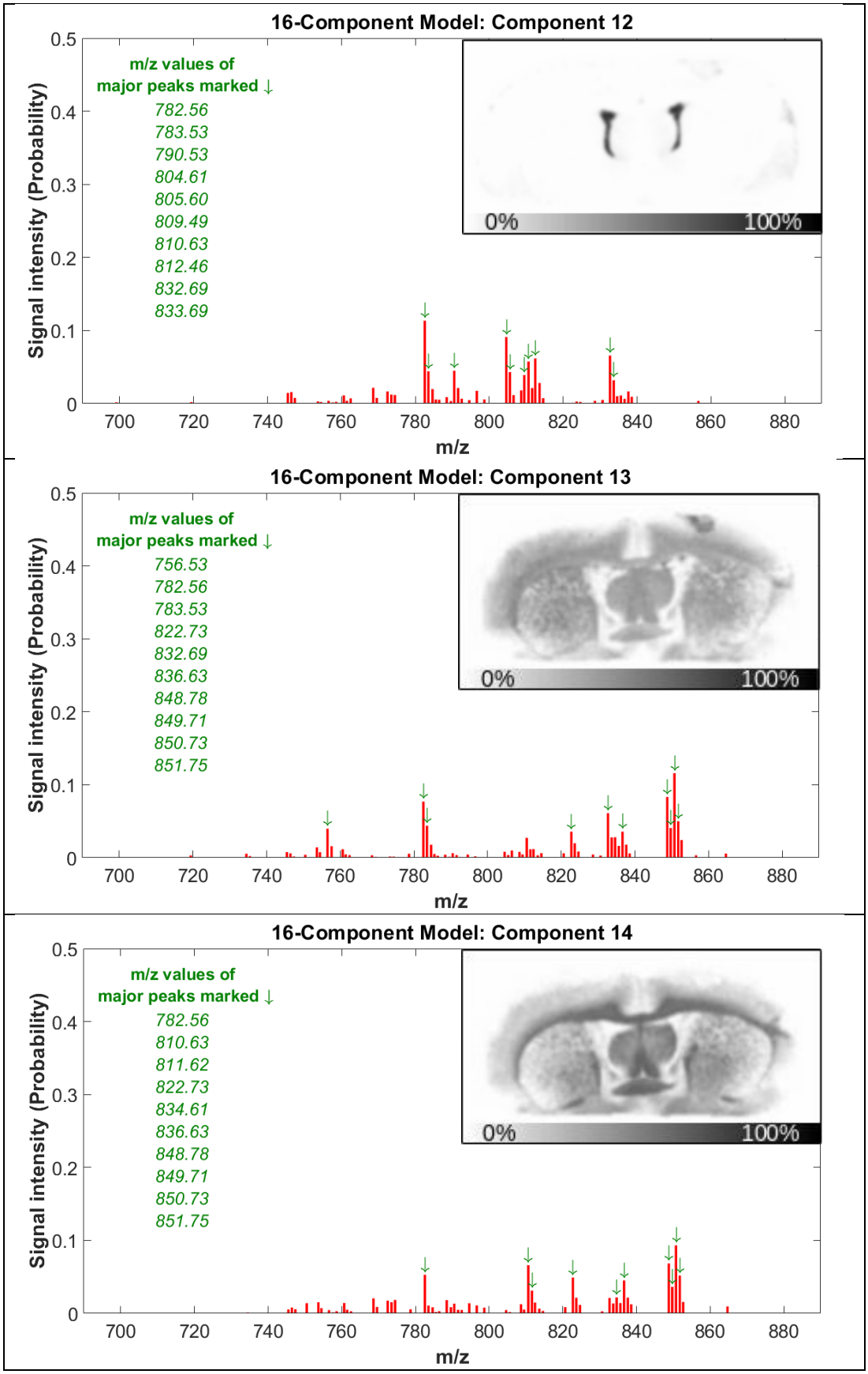

Figure B.2 Extracted ICA component spectra and images for the 16-component model of the rat brain MALDI image data with 10 major peaks marked with green arrows – their m/z values are listed in ascending order (Part 5 of 6)

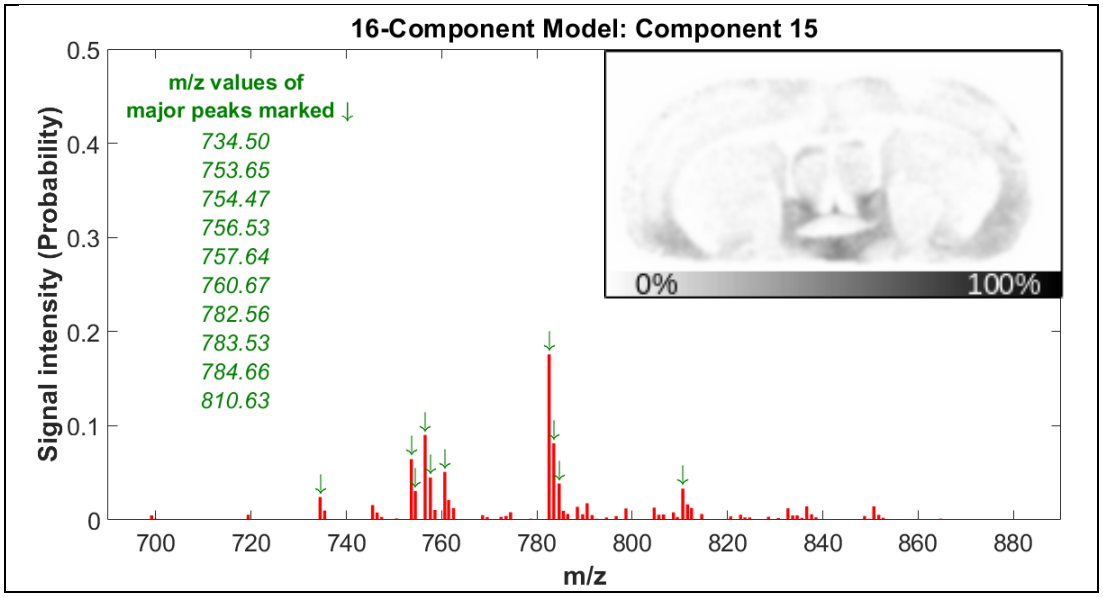

Figure B.2 Extracted ICA component spectra and images for the 16-component model of the rat brain MALDI image data with 10 major peaks marked with green arrows – their m/z values are listed in ascending order (Part 6 of 6)

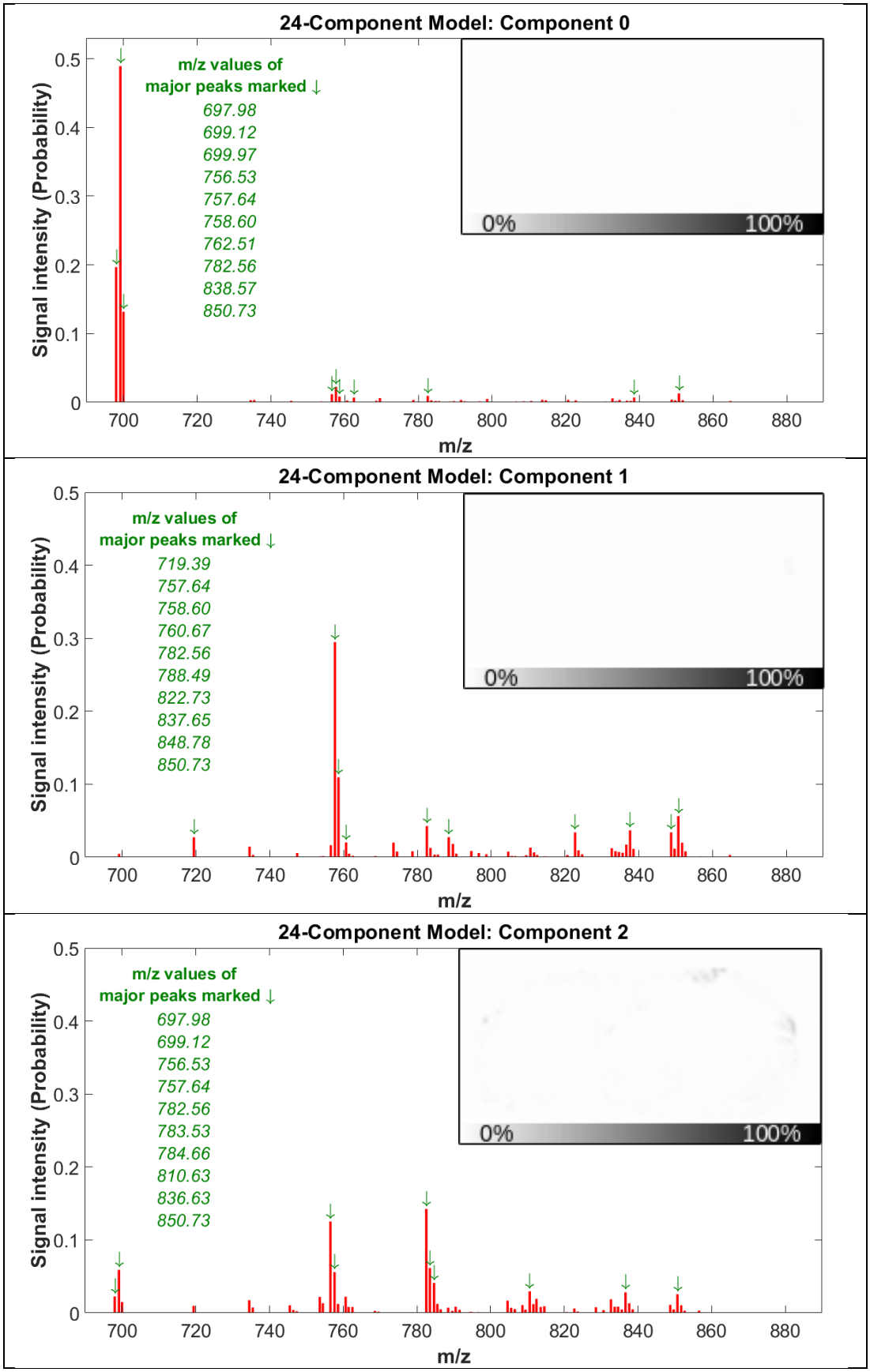

Figure B.3 Extracted ICA component spectra and images for the 24-component model of the rat brain MALDI image data with 10 major peaks marked with green arrows – their m/z values are listed in ascending order (Part 1 of 8)

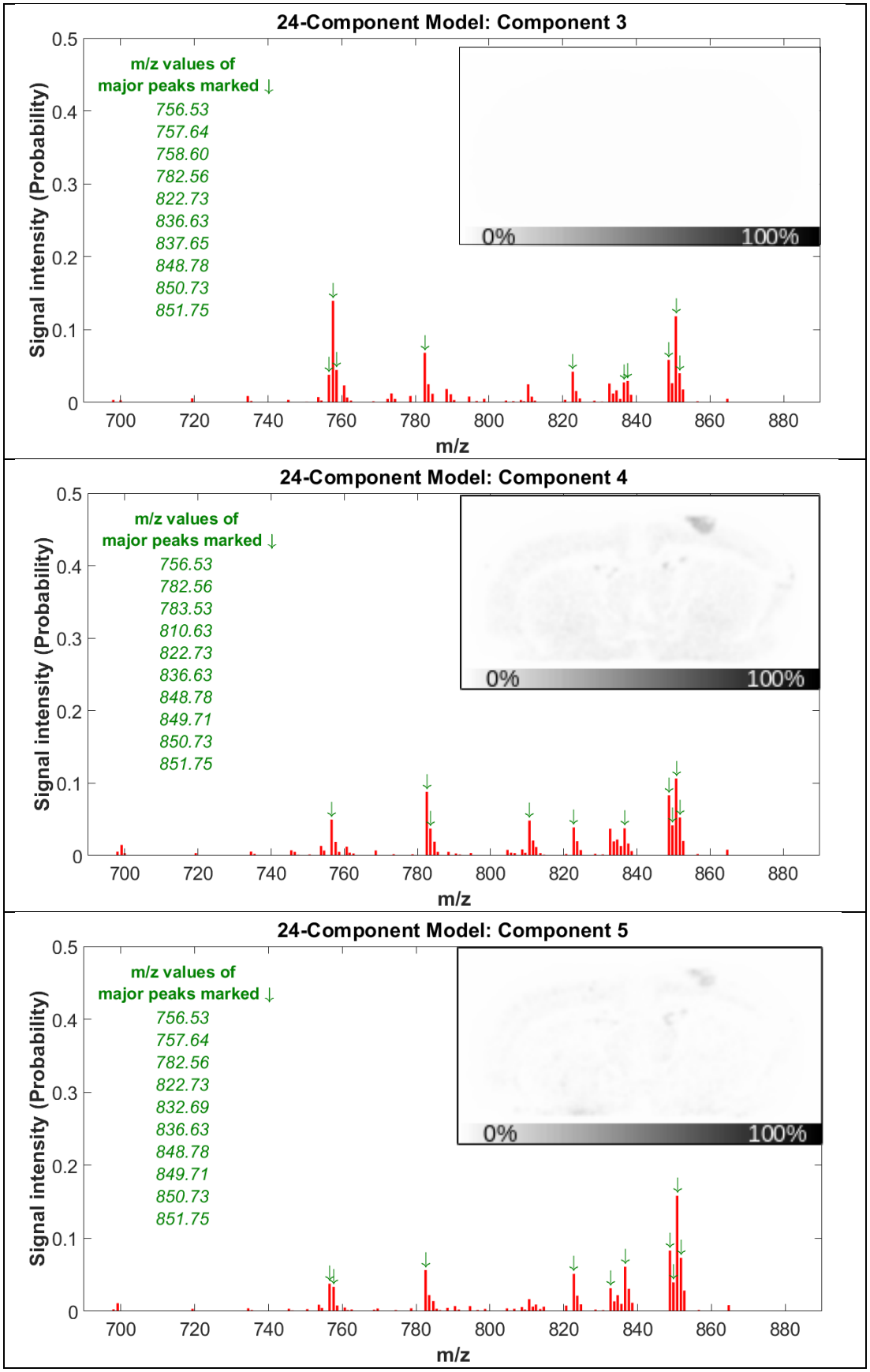

Figure B.3 Extracted ICA component spectra and images for the 24-component model of the rat brain MALDI image data with 10 major peaks marked with green arrows – their m/z values are listed in ascending order (Part 2 of 8)

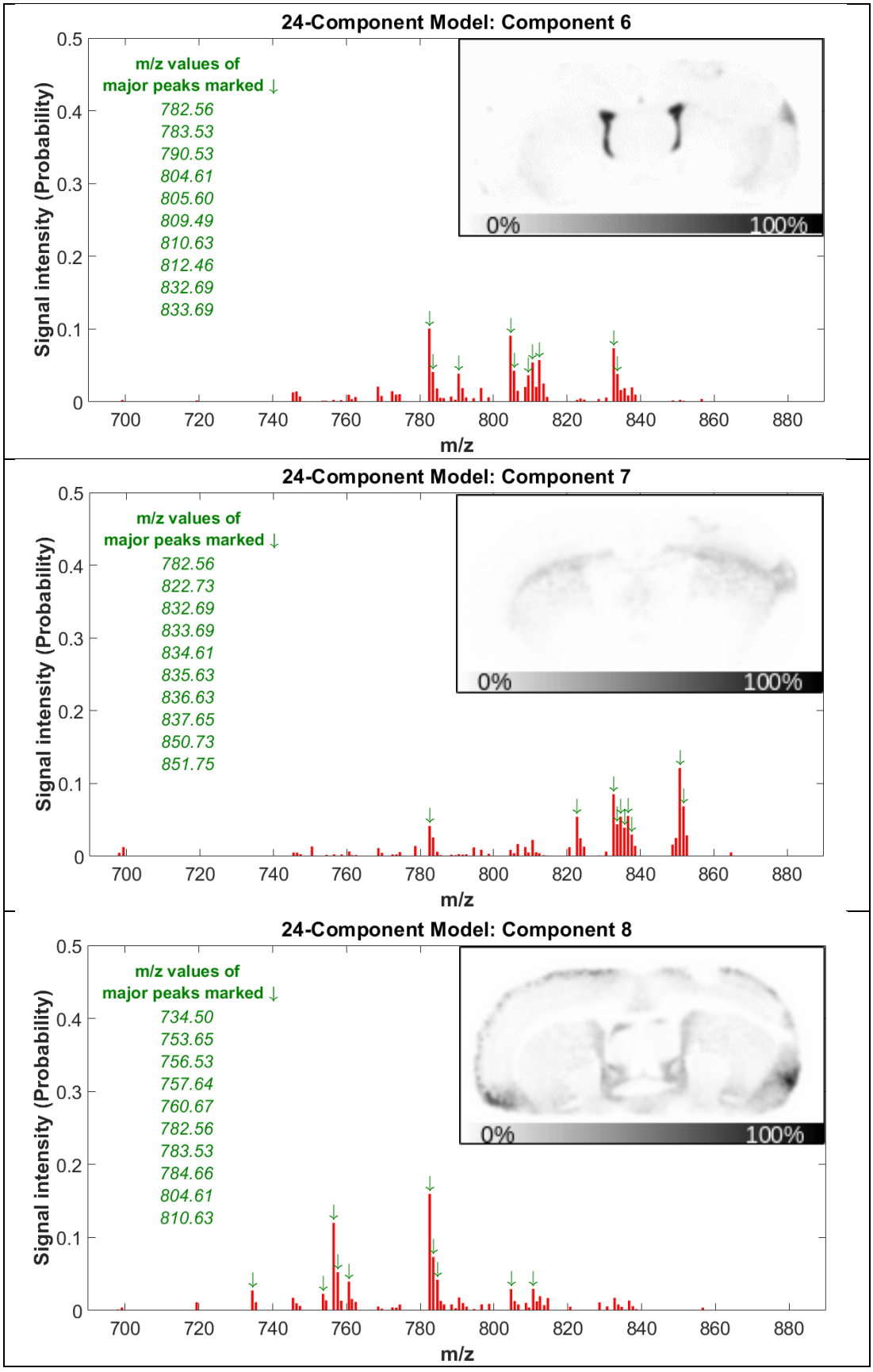

Figure B.3 Extracted ICA component spectra and images for the 24-component model of the rat brain MALDI image data with 10 major peaks marked with green arrows – their m/z values are listed in ascending order (Part 3 of 8)

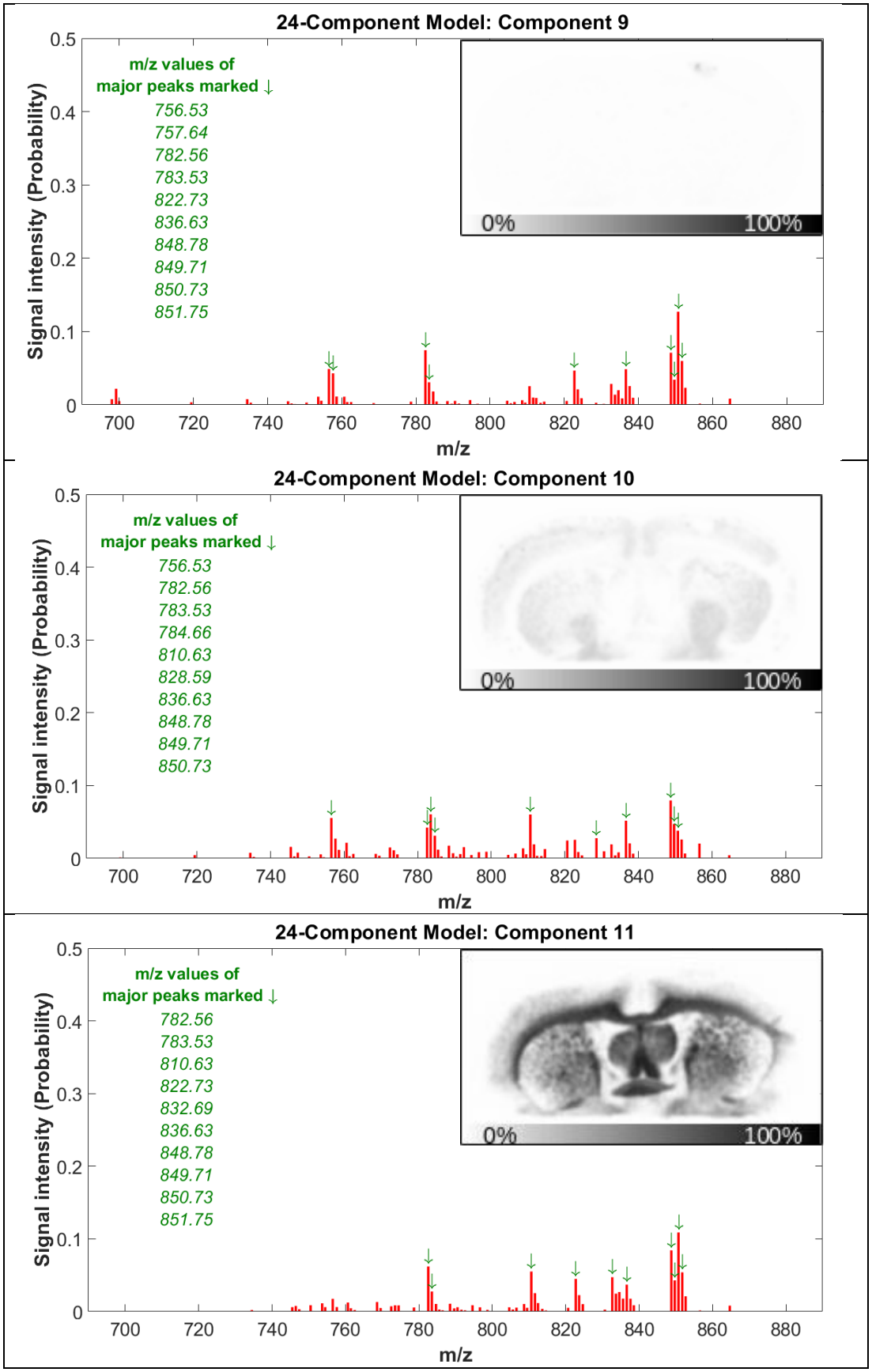

Figure B.3 Extracted ICA component spectra and images for the 24-component model of the rat brain MALDI image data with 10 major peaks marked with green arrows – their m/z values are listed in ascending order (Part 4 of 8)

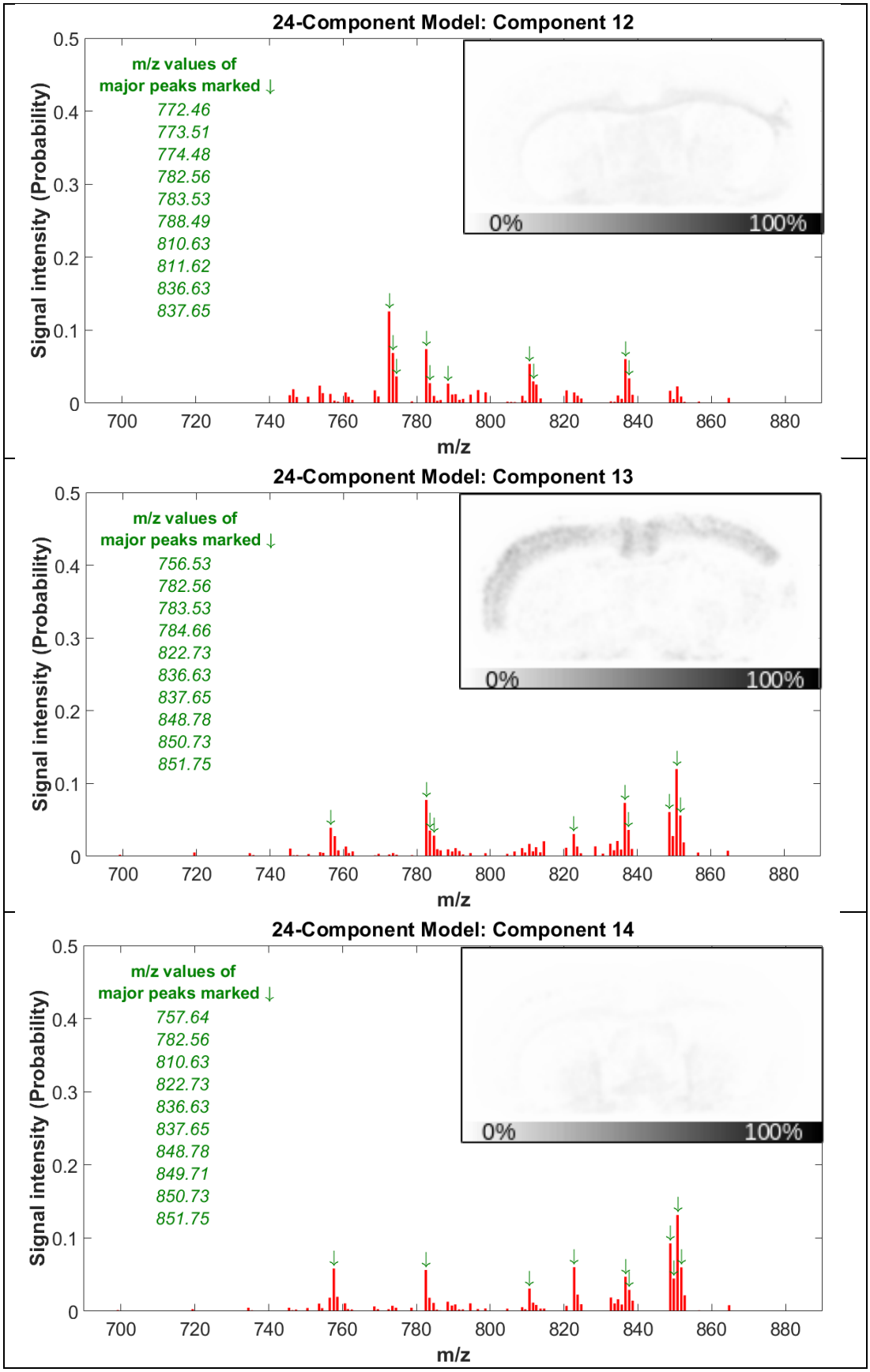

Figure B.3 Extracted ICA component spectra and images for the 24-component model of the rat brain MALDI image data with 10 major peaks marked with green arrows – their m/z values are listed in ascending order (Part 5 of 8)

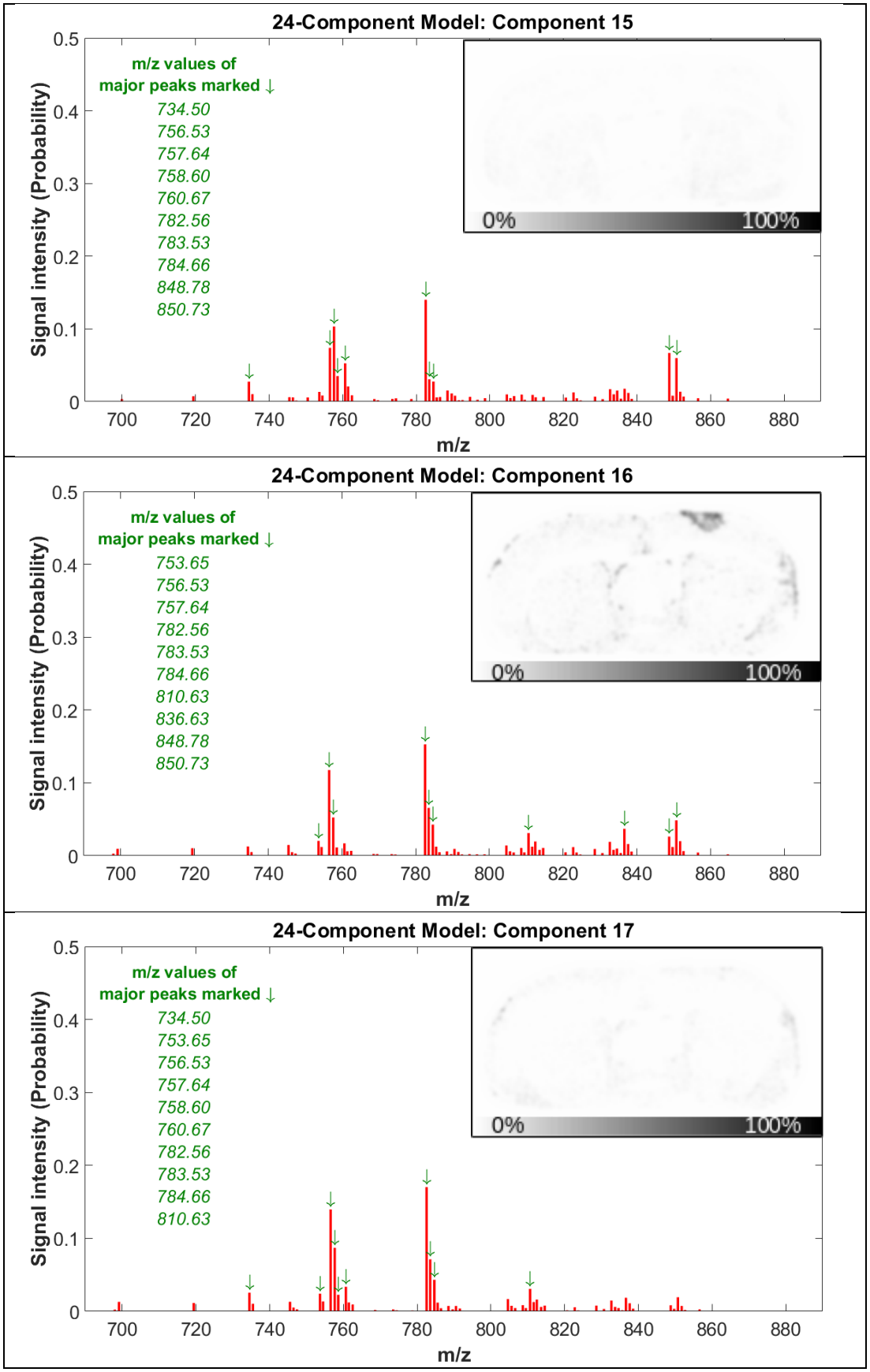

Figure B.3 Extracted ICA component spectra and images for the 24-component model of the rat brain MALDI image data with 10 major peaks marked with green arrows – their m/z values are listed in ascending order (Part 6 of 8)

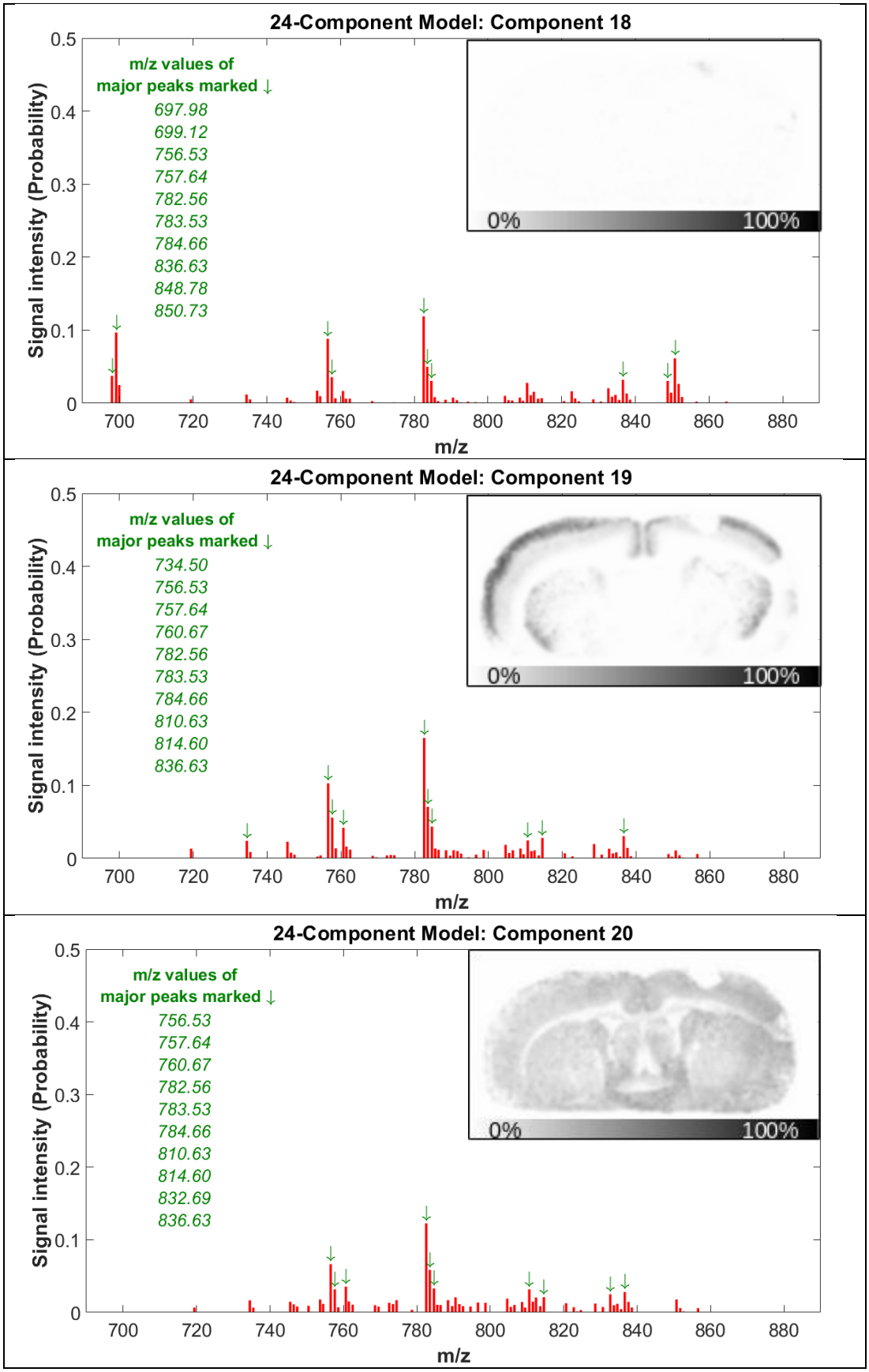

Figure B.3 Extracted ICA component spectra and images for the 24-component model of the rat brain MALDI image data with 10 major peaks marked with green arrows – their m/z values are listed in ascending order (Part 7 of 8)

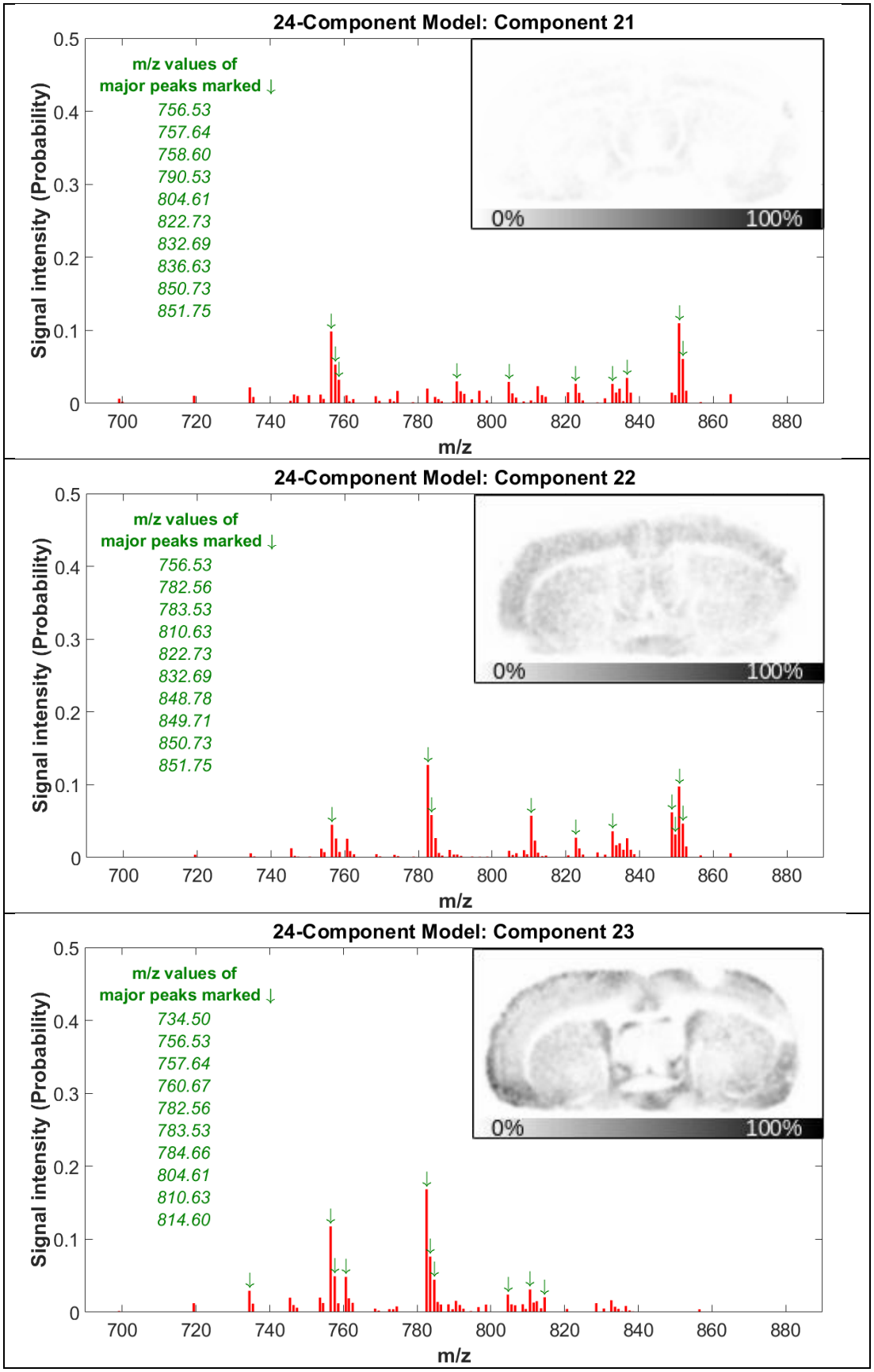

Figure B.3 Extracted ICA component spectra and images for the 24-component model of the rat brain MALDI image data with 10 major peaks marked with green arrows – their m/z values are listed in ascending order (Part 8 of 8)

B-2 Single Ion Images

The single ion images created for the 20 largest peaks as a result of the peak detected mass spectra of the rat brain MALDI image data set are provided in Figure B.4.

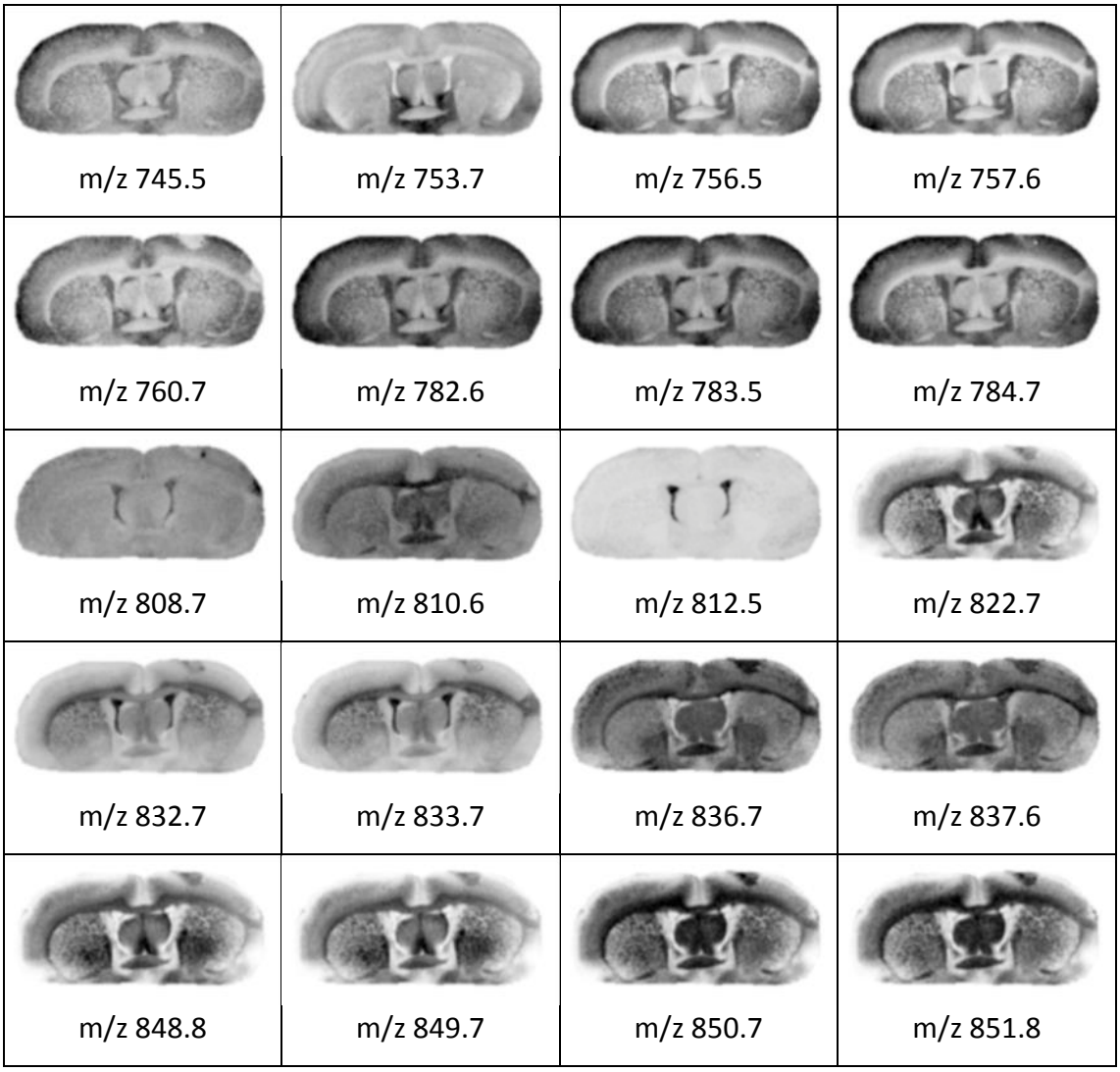

Figure B.4 Single ion images of the rat brain MALDI image data for the top 20 strongest peaks detected – the dynamic range has been set to maximise the contrast of each image where the darkest pixel has the highest intensity value